

**The response of marine carbon-nitrogen-zinc
geochemical cycling to the ~183 Myrs
Toarcian global warming**

Dissertation

der Mathematisch-Naturwissenschaftlichen Fakultät
der Eberhard Karls Universität Tübingen
zur Erlangung des Grades eines
Doktors der Naturwissenschaften
(Dr. rer. nat.)

vorgelegt von
MSc Yunfeng Wang
aus Jining, Shandong Province, VR China

Tübingen
2021

Gedruckt mit Genehmigung der Mathematisch-Naturwissenschaftlichen Fakultät der
Eberhard Karls Universität Tübingen.

Tag der mündlichen Qualifikation:	15.09.2021
Dekan:	Prof. Dr. Thilo Stehle
1. Berichterstatter:	Prof. Dr. Ronny Schönberg
2. Berichterstatter:	Prof. Dr. James H. Nebelsick

Ich erkläre hiermit, dass ich die zur Promotion eingereichte Arbeit mit dem Titel „The response of marine carbon-nitrogen-zinc geochemical cycling to the ~183 Myrs Toarcian global warming“ selbstständig verfasst, nur die angegebenen Quellen und Hilfsmittel benutzt und wörtlich oder inhaltlich übernommene Stellen (alternativ: Zitate) als solche gekennzeichnet habe. Ich erkläre, dass die Richtlinien zur Sicherung guter wissenschaftlicher Praxis der Universität Tübingen (Beschluss des Senats vom 25.05.2000) beachtet wurden. Ich versichere an Eides statt, dass diese Angaben wahr sind und, dass ich nichts verschwiegen habe. Mir ist bekannt, dass die falsche Angabe einer Versicherung an Eides statt mit Freiheitsstrafe bis zu drei Jahren oder mit Geldstrafe bestraft wird.

Ort, Datum

Unterschrift

Acknowledgement

The completion of this work was financially supported by the China Scholarship Council (No. 201706400079).

Foremost, I would like to thank my supervisor Ronny Schönberg for supporting me to apply for the Scholarship, for supervising and motivating me to complete this work, and for all his help throughout my entire PhD period. I was often enlightened from conversations or discussions with him, from which I have acquired a lot of invaluable knowledge and obtained many useful experimental skills. I would like to thank him again for his availability and patience when I was facing difficulties, questions, or problems.

I would like to thank Frantz Ossa Ossa who provided lots of fruitful thoughts, ideas and suggestions for this work, and appreciate his continuous encouragement and motivation especially for the moments when I was at a loss. I am very much thankful to Marie-Laure Pons (Aix Marseille Université) who taught me to familiarize and understand the protocol of Zn isotope analysis and provided me many insightful remarks and comments on my manuscript, to Martin Wille (University of Bern) who shared many great ideas when I was revising my manuscripts, and to Jorge E. Spangenberg (University of Lausanne) who helped to perform the analysis of N isotope compositions. I would also like to thank Elmar Reitter, Bernd Steinhilber, Ilka Kleinhanns and Heinrich Taubald for their useful assistance in the laboratories throughout this work.

Many thanks go to all other members of the Isotope Geochemistry Group: Gülüm Albut, Luise Wagner, Julius Havsteen, Lucile Roué, Markus Gogouvis, Aierken Yierpan, Maria Isabel Varas Reus, Daniel Schöckle, Carolina Rosca, Rachel Bezar, Benjamin Eickmann, Timon Kurzawa and Stephan König. Thank all of them for supporting me and for their companionship during the last years.

Finally, I would like to express my gratitude to my parents and my sisters. Thank you very much for being in my life, and for understanding, supporting and encouraging me.

I had a wonderful experience studying and living in Tübingen because of all of you. Thank you very much!

ABSTRACT

An extreme perturbation of carbon cycle to the global climate arising from the injection of massive amounts of CO₂/CH₄ into the atmosphere-ocean system occurred during the Early Jurassic (Toarcian: ~183 Myrs). This carbon-cycle perturbation was dictated by negative carbon isotope excursions (T-CIEs) of ~3-7 ‰ in δ¹³C, which were globally recorded by the coeval marine carbonate and organic matter reservoirs. The severe Early Toarcian carbon cycle was accompanied by expanded marine anoxia which was dubbed Toarcian Oceanic Anoxic Event (T-OAE), and considerable accumulation of organic-rich sediments especially in the northern European epicontinental shelf-sea region. The T-CIEs on carbonate or organic matter from the Early Toarcian marine sedimentary sections have been widely identified, however, it is not well exemplified how and to what extent local-scale carbon cycles are able to disturb the T-CIE records. Furthermore, the traditionally deemed T-OAE was increasingly challenged by the fact that most of the Early Toarcian sedimentary sections investigated for the argument of global deep ocean anoxia were deposited in hydrographically restricted anoxic basins, which were appreciably isolated from the open ocean. Interestingly, the widespread organic-rich sediments deposited on the epicontinental shelf across the T-CIE interval generally contain high amounts of zinc (Zn) which is a sulfide-forming and bio-essential element. The response of Zn and its isotopic composition to changes in the bioproductivity during the T-OAE, however, has so far remained unexplored.

In this dissertation local-scale carbon cycles were investigated using the combined δ¹³C_{carb} and δ¹³C_{org} for the Dotternhausen T-CIE sedimentary section, SW Germany (see section 3.2.1). A two-step δ¹³C_{carb}-δ¹³C_{org} decoupling – superimposing the general T-CIE trends – was identified, which corresponded to an increase in green sulfur bacteria (GSB) prosperity. This δ¹³C_{carb}-δ¹³C_{org} decoupling was thus related to GSB disturbance, with the larger magnitude second-step δ¹³C_{carb}-δ¹³C_{org} decoupling being further exaggerated by early diagenesis. Local-scale carbon cycles can thus considerably upset the general expression of the T-CIE. Furthermore, this dissertation observed contrasting decoupled δ¹³C_{carb}-δ¹³C_{org} patterns from paleogeographically distinct localities of the Tethys region, demonstrating that the local carbon-cycle perturbations have pervasively and independently impacted the Early Toarcian global carbon cycle.

To address the controversy of the Early Toarcian open ocean redox structure, a combination of $\delta^{15}\text{N}$ of bulk samples and extracted kerogens (expressed by $\delta^{15}\text{N}_{\text{bulk}}$ and $\delta^{15}\text{N}_{\text{ker}}$) from the Dotternhausen T-CIE sedimentary section was used in this dissertation (see section 3.2.2). Both $\delta^{15}\text{N}_{\text{bulk}}$ and $\delta^{15}\text{N}_{\text{ker}}$ values imply enhanced N_2 fixation by cyanobacteria using the molybdenum (Mo)-based nitrogenase enzyme. N isotope compositions of +0.3 to +2.5 ‰ produced by this process are in stark contrast to the typical sedimentary $\delta^{15}\text{N}$ values (> 3 ‰) induced by partial water-column denitrification and/or anammox in oxygen minimum zones of the modern ocean, thus indicating the existence of restricted local oxygen-depleted settings on the northern European epicontinental shelf. Such restricted environments with severe oxygen depletion on the northern European epicontinental shelf are unlikely representative of the open-ocean redox landscape.

The Zn biogeochemical cycling in response to the Early Toarcian anoxia on the northern European epicontinental shelf-sea region, was explored by measuring $\delta^{66}\text{Zn}_{\text{bulk}}$ values for the Yorkshire (northeastern England) and Dotternhausen T-CIE sedimentary sections, respectively (see section 3.2.3). The authigenic $\delta^{66}\text{Zn}_{\text{auth}}$ values of these two sedimentary sections are comparable to that of the modern global deep ocean, indicating that the Zn biogeochemical cycle in the Early Toarcian ocean has already reached present-day conditions. A short-lived ocean oxygenation was likely recorded by a negative excursion of $\delta^{66}\text{Zn}_{\text{bulk}}$ observed in both Yorkshire and Dotternhausen sections, implying changing ocean redox states during the T-CIE. Near-quantitative removal of dissolved Zn from the seawater to early diagenetic minerals in the sediment with minimal isotopic effects is observed under excess hydrogen sulfide conditions, similar to the behaviour of the redox-sensitive element molybdenum (Mo). Compared to molybdenum, however, zinc as a non-redox sensitive element is less prone to local redox effects in restricted basins and thus $\delta^{66}\text{Zn}_{\text{auth}}$ values of euxinic marine sediments bear the potential to accurately record global seawater redox variations through geological time.

ZUSAMMENFASSUNG

Eine extreme Störung des globalen Kohlenstoffkreislaufs durch den Eintrag massiver Mengen von CO₂/CH₄ in das Atmosphären-Ozean-System trat während des Unterjuras (Toarcium: ~183 Myrs) auf. Diese Störung wurde durch negative Kohlenstoffisotopenexkursionen (T-CIEs) von $\delta^{13}\text{C} \sim +3-7 \text{‰}$ begleitet, die weltweit von marinen Karbonaten und organogenen Stoffreservoirs aufgezeichnet wurden. Der Kohlenstoffkreislauf des frühen Toarciums wurde von einer Ausdehnung mariner anoxischer Bereiche begleitet, die als toarcisches ozeanisch-anoxisches Ereignis (T-OAE) bezeichnet werden. Dabei wurden große Mengen an organogenen Sedimenten, insbesondere auf dem nordeuropäischen epikontinentalen Schelf abgelagert. Die negative Kohlenstoffisotopenexkursion in marinen Karbonaten und organisch-reichen Sedimenten des früheren Toarciums ist ausführlich dokumentiert. Jedoch ist der Einfluss lokaler Kohlenstoffkreisläufe auf die Isotopenexkursion nicht abschließend geklärt.

Darüber hinaus wird das traditionell als global angesehene T-OAE und die damit verbundene anoxische Tiefsee zunehmend durch die Tatsache in Frage gestellt, dass sich bisherige Studien größtenteils auf Sedimentabschnitte konzentrierten die in hydrographisch vom Ozean isolierten, anoxischen Becken abgelagert wurden. Interessanterweise enthalten die weit verbreiteten, organogenen Sedimente, die auf dem epikontinentalen Schelf über das T-CIE-Intervall hinweg abgelagert wurden, im Allgemeinen hohe Mengen an Zink (Zn), einem Sulfid-bildenden und biologisch essentiellen Element. Die Reaktion von Zn und seiner Isotopenzusammensetzung auf Veränderungen der Bioproduktivität während der T-OAE blieb jedoch bisher unerforscht.

In dieser Dissertation wurden lokale Kohlenstoffkreisläufe unter Verwendung kombinierter $\delta^{13}\text{C}_{\text{carb}}$ und $\delta^{13}\text{C}_{\text{org}}$ Isotope am Sedimentabschnitt Dotternhausen T-CIE, in SW Deutschland untersucht (siehe Abschnitt 3.2.1). Es konnte eine zweistufige $\delta^{13}\text{C}_{\text{carb}}-\delta^{13}\text{C}_{\text{org}}$ -Entkopplung – welche allgemeine T-CIE-Trends überlagert und während der frühen Diagenese noch verstärkt wurde – identifiziert und einer erhöhten Bioproduktivität von grünen Schwefelbakterien (GSB) zugeschrieben werden. Regionale Kohlenstoffkreisläufe können somit den allgemeinen Ausdruck der T-CIE erheblich beeinflussen. Darüber hinaus zeigt diese Dissertation kontrastierende, entkoppelte $\delta^{13}\text{C}_{\text{carb}}-\delta^{13}\text{C}_{\text{org}}$ -Muster aus paläogeographisch unterschiedlichen Lokalitäten der Tethys-Region auf.

Diese zeigen, dass lokale Störungen in Kohlenstoffkreisläufen einen umfassenden Einfluss auf den frühen toarcischen globalen Kohlenstoffkreislauf hatten.

Um die Kontroverse um die Redox-Struktur des frühen Toarciums im offenen Ozean anzugehen, wurde in dieser Dissertation eine Kombination aus $\delta^{15}\text{N}$ Analysen am Gesamtgestein sowie an extrahierten Kerogenen (ausgedrückt durch $\delta^{15}\text{N}_{\text{bulk}}$ und $\delta^{15}\text{N}_{\text{ker}}$) aus den Dotternhausen Sedimenten verwendet (siehe Abschnitt 3.2.2). Sowohl die $\delta^{15}\text{N}_{\text{bulk}}$ - als auch die $\delta^{15}\text{N}_{\text{ker}}$ -Werte implizieren eine erhöhte N_2 -Fixierung durch Cyanobakterien unter Verwendung des, auf Molybdän basierenden, Nitrogenase-Enzyms. Die N-Isotopenzusammensetzungen von +0.3 bis +2.5 ‰ stehen im großen Gegensatz zu den typischen sedimentären $\delta^{15}\text{N}$ -Werten (> 3 ‰), die durch partielle Denitrifikation und/oder Anammox in Sauerstoffminimumzonen des modernen Ozeans produziert werden. Dies weist auf die Existenz begrenzter lokaler, sauerstoffarmer Umgebungen auf dem nordeuropäischen epikontinentalen Schelf hin. Es ist allerdings unwahrscheinlich, dass solche sauerstoffarmen Umgebungen repräsentativ für die Redox-Struktur des offenen Ozeans sind.

Die Reaktion des biogeochemischen Zn-Zyklus auf die Sauerstoffarmut in nordeuropäischen epikontinentalen Schelfmeerregionen während des Toarciums wurde anhand von $\delta^{66}\text{Zn}_{\text{bulk}}$ Messung an Sedimentabschnitten aus Yorkshire (NO England) und Dotternhausen untersucht (siehe Abschnitt 3.2.3). Die authigenen $\delta^{66}\text{Zn}_{\text{auth}}$ -Werte dieser beiden Sedimentabschnitte sind mit denen der modernen globalen Tiefsee vergleichbar, was darauf hindeutet, dass der biogeochemische Zn-Zyklus im toarcischen Ozean bereits heutige Bedingungen erreicht hatte. Eine negative Exkursion von $\delta^{66}\text{Zn}_{\text{bulk}}$ Werten, sowohl in den Yorkshire als auch Dotternhausen Abschnitten, weist auf eine kurzzeitige, lokale Anreicherung von Sauerstoff hin welche wiederum Hinweis auf fluktuierende Redox-Zustände im Ozean während des T-CIE hindeutet. Ein nahezu quantitativer Entzug von gelöstem Zn aus dem Schwefelwasserstoff übersättigten Meerwasser bis hin zu fröhdiagenetischen Mineralen im Sediment mit minimaler Isotopenfraktionierung, ähnelt dem Verhalten des redox-sensitiven Elements Molybdän. Im Vergleich zu Molybdän ist Zink jedoch, als nicht redox-sensitives Element, in isolierten marinen Becken weniger anfällig für lokale Redox-Effekte und birgt daher das Potenzial, globale Meerwasser Redox-Variationen über die geologische Zeit genau zu erfassen.

LIST OF PUBLICATIONS AND AUTHOR CONTRIBUTIONS

Chapter 1 Published paper

Title: Evidence for local carbon-cycle perturbations superimposed on the Toarcian carbon isotope excursion

Authors: Yunfeng Wang, Frantz Ossa Ossa, Martin Wille, Simon Schurr, Mario-Erich Saussele, Annette Schmid-Röhl, and Ronny Schoenberg

Status: published in 2020 (*Geobiology*, 18, 682-709)

Declaration contributions by author

Position in list of authors	1
Scientific ideas	80%
Data generation	60%
Analysis and interpretation	85%
Writing	90%

Chapter 2 Published online paper

Title: Restricted oxygen-deficient basins on the northern European epicontinental shelf across the Toarcian carbon isotope excursion interval

Authors: Yunfeng Wang, Frantz Ossa Ossa, Jorge E. Spangenberg, Martin Wille, and Ronny Schoenberg

Status: published online in 2021 (*Paleoceanography and Paleoclimatology*, 36, 6. <https://doi.org/10.1029/2020PA004207>)

Declaration contributions by author

Position in list of authors	1
Scientific ideas	75%
Data generation	50%
Analysis and interpretation	85%
Writing	90%

Chapter 3 Ready for submission

Title: Zinc geochemical cycling response to the Early Jurassic (Toarcian: ~183 Ma) marine anoxia and its paleoenvironmental significance

Authors: Yunfeng Wang, Marie-Laure Pons, Angela Coe, Frantz Ossa Ossa, Martin Wille, and Ronny Schoenberg

Status: ready for submission

Declaration contributions by author

Position in list of authors	1
Scientific ideas	90%
Data generation	100%
Analysis and interpretation	85%
Writing	90%

Table of Contents

1. Introduction	1
1.1. Early Jurassic (Toarcian: ~183 Myrs) carbon cycles and ocean redox states ..	1
1.2. Geological setting and materials	4
1.3. The behavior of stable isotope systems in marine environments	8
2. Objectives and Expected Outcomes	13
3. Results and Discussion	14
3.1. Results	14
3.1.1. Element concentrations and carbon, nitrogen and molybdenum isotopes for Dotternhausen samples	14
3.1.2. Element concentrations for Yorkshire samples	19
3.1.3. Zinc isotope compositions for Yorkshire and Dotternhausen samples	20
3.2. Discussion	23
3.2.1. Evidence for local carbon cycles superimposed on the T-CIE	23
3.2.2. Restricted oxygen-deficient basins on the northern European epicontinental shelf across the T-CIE.....	33
3.2.3. Zinc geochemical cycling response to the Early Jurassic (Toarcian) marine anoxia	43
4. References	53
APPENDIX	73

1. Introduction

1.1. Early Jurassic (Toarcian: ~183 Myrs) carbon cycles and ocean redox states

The Early Jurassic period (201.4–174.1 Myrs) was characteristic of multiple intervals of global-scale changes in paleoclimatology and paleoceanography (e.g., Pálffy and Smith, 2000; Bjerru et al., 2001; Bailey et al., 2003; Rosales et al., 2004; Kemp et al., 2005; van de Schootbrugge et al., 2005; Dera et al., 2011). These perturbations are documented by the Early Jurassic marine sedimentary strata, with the most severe changes recorded by the Early Toarcian (~183 Ma) strata. The Early Toarcian characterized by a global warming event (McArthur et al., 2000; Bailey et al., 2003; Suan et al., 2008; Dera et al., 2009, 2011; Fernandez et al., 2021) was accompanied by elevated continental chemical weathering, bringing a large amount of bio-essential nutrients into the oceans (Cohen et al., 2004; Raucsik and Varga, 2008; Hermoso and Pellenard, 2014; Brazier et al., 2015; Montero-Serrano et al., 2015; Fu et al., 2016; Percival et al., 2016; Them et al., 2017; Krencker et al., 2020). The subsequent elevation of marine primary productivity facilitated the organic carbon production in surface waters, causing increased consumption of ocean oxygen and eventually leading to expanded ocean deoxygenation (e.g., Röhl et al., 2001; Jenkyns, 2010). This Early Toarcian deoxygenation event is commonly used to refer to a time interval during which the world's deep oceans were anoxic/euxinic (Toarcian Oceanic Anoxic Event (T-OAE); e.g., Jenkyns and Clayton, 1986; Jenkyns, 1988; Pearce et al., 2008; Gröcke et al., 2011; Thibault et al., 2018). The dubbed global deep ocean anoxia/euxinia during the Early Toarcian was suggested by widespread distribution of organic carbon-rich sedimentary rocks (Figure 1.1), especially by the occurrence of organic-rich black shales deposited in pelagic depositional settings of palaeo-Pacific (Panthalassic) Ocean (Jenkyns, 1988; Gröcke et al., 2011; Ikeda and Hori, 2014; Ikeda et al., 2018). However, a growing body of evidence has put forward that the global deep ocean anoxia was unacceptable, and instead, proposed that the contemporaneous marine anoxia was only limited to epicontinental marginal basins which were appreciably isolated from the open ocean (McArthur et al., 2008; Dickson et al., 2017; Fantasia et al., 2018; Ruvalcaba Baroni et al., 2018; McArthur, 2019; Remírez and Algeo, 2019).

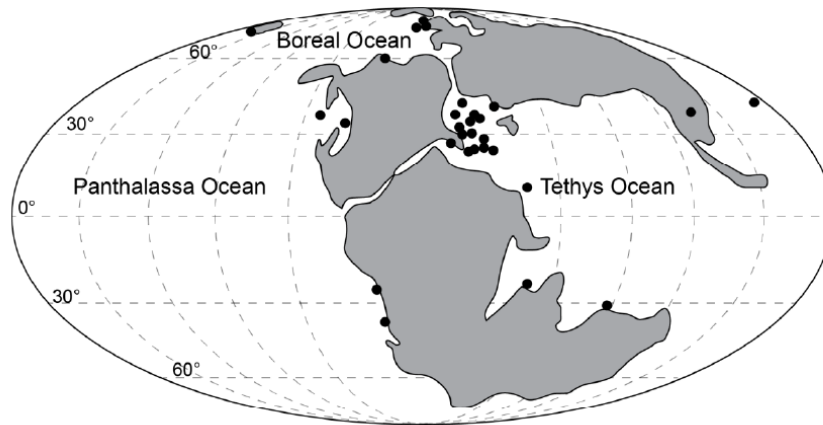


Figure 1.1. Global distribution of the organic-rich deposits (black dots) during the Early Toarcian (modified after Jenkyns et al., 2002).

The extensive burial of organic carbon preferentially removes the isotopically light carbon from seawater and enriches the residual in ^{13}C , the Early Toarcian organic-rich sedimentary successions therefore have recorded an overarching long-term positive carbon isotope excursion (CIE) (Jenkyns et al., 2002). However, the positive CIE was interrupted by a globally synchronous $\sim 3\text{--}7\text{‰}$ negative CIE which was recorded by terrestrial fossil woods (e.g., Hesselbo et al., 2007), land plant lipids (Ruebsam et al., 2020; Xu et al., 2017), marine carbonates and organic matter (e.g., Hesselbo et al., 2000; Röhl et al., 2001; Caruthers et al., 2011; Han et al., 2018; Xu et al., 2018; Wang et al., 2020). This negative isotopic interruption is due to the injection of massive amounts of ^{12}C -enriched CO_2 into the contemporaneous atmosphere-ocean system following the emplacement of the Karoo-Ferrar large igneous province (LIP) (e.g., Pálffy and Smith, 2000; Svensen et al., 2007, 2012; Moulin et al., 2011; Percival et al., 2015; Ivanov et al., 2017; van Acken et al., 2019; Greber et al., 2020) and/or large-scale release of thermogenic/biogenic ^{12}C -enriched CH_4 (e.g., Hesselbo et al., 2000; Kemp et al., 2005; van de Schootbrugge et al., 2013a; Xu et al., 2017; Ruebsam et al., 2019). The negative Toarcian CIE (T-CIE) therefore has been increasingly used as a stratigraphic marker for identifying the dubbed T-OAE interval (e.g., Jenkyns, 2010; Newton et al., 2011; Fu et al., 2016).

Considering that carbon isotope expressions in sedimentary rocks are easily disturbed by local-scale carbon processes (e.g., Jiang et al., 2012), a comprehensive understanding of the features of the negative T-CIEs may to some extent be hindered when correlating the T-OAE intervals worldwide. To exemplify how local carbon cycles influences the expression of T-CIEs, this study investigated the nature of the carbon isotopes for both inorganic and organic reservoirs of the T-CIE sedimentary section

from Dotternhausen quarry, southwestern (SW) Germany. Furthermore, to elucidate the controversy between global ocean anoxia or anoxia in restricted regions, this study reconstructed the nitrogen (N) biogeochemical cycle for the Dotternhausen T-CIE section, given the size of N-involved ecosystem is accompanied by distinct N isotope effects (e.g., Sigman et al., 2009a; Ader et al., 2016; Stüeken et al., 2016; Sigman and Fripiat, 2019).

The long-lasting marine oxygen deficit on epicontinental shelves across the T-CIE interval was accompanied by extensive burial fluxes of metal sulfide and organic matter (e.g., Sælen et al., 2000; Röhl et al., 2001; Frimmel, et al., 2004; Gill et al., 2011; Berner et al., 2013) which are major hosts for zinc (Zn), a sulfide-forming and bio-essential element (John et al., 2007; Little et al., 2016; Vance et al., 2016; Hu et al., 2018; Isson et al., 2018; Sweere et al., 2020). The removal of Zn from seawater to organic-rich marine sediments relates to two main fluxes: organically bound metals and metal sulfides (e.g., sphalerite, wurtzite). Uptake of cellular living organisms generally represents the main export mechanism of Zn to the sediment, where it may be buried as part of organic material or fixed as metal sulfides (Little et al., 2015; Weber et al., 2018). This is particularly true for the Mesozoic OAEs during which high rate of primary productivity accelerated the assimilation of Zn into biomass and then the sinking of Zn into the underlying oxygen-depleted sediments. The resultant organic-rich sedimentary rocks thus contain high amounts of Zn (Montero-Serrano et al., 2015; Sweere et al., 2020; Wang et al., 2020). Recently, organic-rich sedimentary rocks depositing during the Cenomanian-Turonian (Late Cretaceous, ~94 Ma) OAE 2 were used to reconstruct the coevally oceanic Zn-cycle processes (Sweere et al., 2020). In their study, the authors proposed that the disturbance of micronutrient Zn cycling was controlled by fluctuating ocean redox states within the OAE 2 (Sweere et al., 2020). However, in the course of the widespread deposition of T-CIE organic-rich sediments, how oceanic Zn geochemical cycling proceeded in response to the coeval marine anoxia so far remains unexplored. Furthermore, as a traditional redox proxy of tracing seawater chemistry, whether molybdenum (Mo) cycling was tight to that of Zn during the Early Toarcian marine anoxia has not yet been investigated. To constrain marine Zn cycling and further compare it to Mo cycling, two T-CIE sedimentary successions from the Dotternhausen quarry, southwest Germany and the Yorkshire coast, northeastern England, (Figure 1.2) were used in this study.

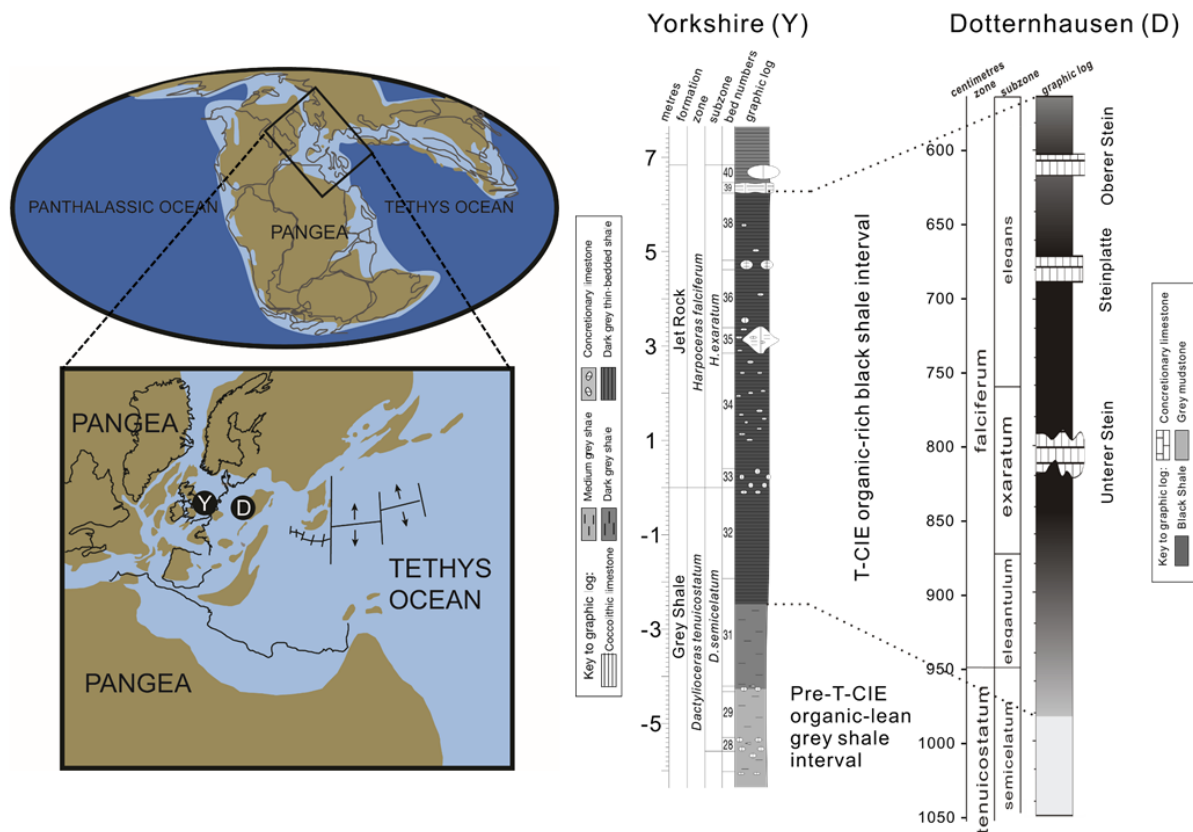


Figure 1.2. Left panel: Paleogeographic maps for the Early Jurassic (Toarcian) and the North European and Northwestern Tethyan regions specifically, after Gill et al. (2011) and Percival et al. (2016). Locations of this studied sample sites are noted as black circles: Yorkshire (Y), England and Dotternhausen (D), Germany. Right panel: Lithologic facies distribution of the Yorkshire (Y) and Dotternhausen (D) sections deposited before and during the T-CIE (modified after Röhl et al., 2001; Pearce et al., 2008).

1.2. Geological setting and materials

The Earth's entire landmass, supercontinent Pangea, during the Early Jurassic suffered a large-scale tectonic plate reorganization. Rifting phases led to the formation of two large continental landmasses: Laurasia and Gondwana (Golonka and Ford, 2000; Palfy and Smith, 2000; Golonka, 2007). The intensive rifting activity was accompanied by an increase in LIP emplacement such as the Karroo-Ferrar LIP which occurred in the southern Gondwana at ~183 Ma (Encarnación et al., 1996; Duncan et al., 1997; Jourdan et al., 2008; Burgess et al., 2015; Moulin et al., 2017; Ait-Itto et al., 2018). The two large continental landmasses were surrounded by epicontinental shallow shelf-seas, which were parts of the Tethys, the Panthalassa and the Arctic Oceans at that time (Figure 1.2; e.g., Wignall and Hallam, 1991). Such shallow shelf-seas widely developed on the northern European epicontinental shelf between 10° and 50° on the northern hemisphere which deepened towards the southeastern part of the

contemporaneous Tethys Ocean (Ziegler, 1988; Bassoulet et al., 1993; Jenkyns, 2010). The northern European epicontinental shelf in the northwestern Tethys was connected to the Arctic Ocean through the Viking Corridor during the Early Jurassic (Prauss and Riegel, 1989; Surlyk, 1991; Bjerrum et al., 2001; Bjerrum and Surlyk, 2001; Scott and Turton, 2001; Dera et al., 2015), and was heavily split into several basins or sub-basins (e.g., Cleveland Basin, Northern and Southern German Basin, Paris Basin) (Ziegler, 1988; Bassoulet et al., 1993). The studied T-CIE sedimentary sections from the Dotternhausen quarry and the Yorkshire coast were deposited in the Southern German Basin and the Cleveland Basin, respectively.

Dotternhausen quarry

The Dotternhausen quarry (48°13'32.60"N, 8°46'29.76"E) is geographically situated in the present-day southwestern (SW) Germany. The Early Toarcian deposits of the Dotternhausen quarry were accumulated in the South German Basin, at the southern margin of European epicontinental shelf, which bridged the northwest Tethys Ocean and the Boreal Sea during the Early Jurassic (Ziegler, 1988). This quarry exhibits the well-studied, and laterally widespread, Lower Toarcian Posidonia Shales, which are world-famous for their exceptionally well-preserved fossils and their high organic matter content (up to 16 wt.% total organic carbon (TOC)) (e.g., Brumsack et al., 1991; Röhl et al., 2001; Schmid- Röhl et al., 2002; Bour et al., 2007; Berner et al., 2013; Ruebsam et al., 2014; Montero-Serrano et al., 2015; Song et al., 2017; Fantasia et al., 2018; Galasso et al., 2021). The sedimentary rocks in the quarry are exceptionally well preserved and thus provide an ideal stratigraphic sequence to investigate the T-CIE interval and allow comparison with other negative CIE records (Röhl et al., 2001).

The sedimentary rocks of the Dotternhausen quarry have been litho- and bio-stratigraphically well characterized, mainly including three ammonite zones (*tenuicostatum*, *falciferum*, and *bifrons*) and some subzones (*elegantulum*, *exaratum*, *elegans*, and *falciferum*) (cf. Röhl et al., 2001; Schmid- Röhl et al., 2002), though the transition between the *tenuicostatum* and *falciferum* zones remains not precisely constrained due to a lack of standard fossils and/or to the existing stratigraphic gap in the Pliensbachian-Toarcian boundary interval (Kuhn and Etter, 1994). Furthermore, the sedimentary rocks of the Dotternhausen quarry have been investigated and subdivided into three contrasting lithofacies units in ascending order: bioturbated

mudstones (1,180–980 cm), laminated oil shales (980–550 cm), and bituminous mudstones (550–0 cm), respectively, in terms of the amounts of organic matter and the types of fabric (cf. Röhl et al., 2001). This study only shows the sedimentary strata from 1,050 to 560 cm (Figure 1.2), which includes the T-CIE (Röhl et al., 2001; Wang et al., 2020). The laminated oil shale unit is largely limited to the uppermost part of *tenuicostatum* zone and the lower and middle parts of the *falciferum* zone (Figure 1.2), is marked by a complete lack of benthic fauna, and exhibits a distinct micro-lamination. The laminated oil shale unit is separated by three calcite-rich beds in different thickness, Unterer Stein, Steinplatte, and Oberer Stein from the bottom up (Frimmel et al., 2004) (Figures 1.2). The thickest one, Unterer Stein (20–30 cm) in the *exaratum* subzone (Figures 1.2), can serve as an efficient stratigraphic marker across Germany, Switzerland, and France within the Lower Toarcian Posidonia Shales in European epicontinental basins/shelves (Kuhn and Etter, 1994; van de Schootbrugge et al., 2005). An increasing body of evidence indicates that the Unterer Stein is an early diagenetic carbonate precipitate associated with organic matter remineralization enhanced by bacterial sulfate reduction within the sediment (Röhl et al., 2001; Röhl and Schmid-Röhl, 2005; Wang et al., 2020). Moreover, the carbonate fraction in the laminated oil shale facies in the Dotternhausen quarry was primarily derived from the solid remains of calcareous phytoplankton, including coccolithophorids and schizosphaerelle (Röhl et al., 2001), which is in contrast to the Unterer Stein bed comprising only few fecal pellets (cf. Frimmel et al., 2004). More detailed geological and paleontological descriptions of the Dotternhausen quarry can be found in previous publications (cf. Röhl et al., 2001; Röhl and Schmid-Röhl, 2005).

Yorkshire coast

The Yorkshire coast is geographically located in present-day northeastern England. The Early Toarcian deposits of the Yorkshire coast were accumulated in the Cleveland Basin, which was situated within the transcontinental Laurasian Seaway extending from ~30 to 60 °N (Bjerrum et al., 2001). The Yorkshire coast primarily includes three sites: Saltwick Bay (54°29'N, 0°35'W), Port Mulgrave (54°32'N, 0°46'W) and Hawsker Bottoms (54°27'N, 0°31'W), all of which exhibit the Whitby Mudstone Formation depositing during the Early Toarcian (Howarth, 1955, 1962, 1973). These Early Toarcian deposits of the Yorkshire coast are predominantly organic-rich mudrocks that are stratigraphically equivalent to similar organic-rich deposits throughout the Central

and Western Europe (e.g., the 'Posidonia Shale' from the Northern and Southern Germany Basin, and the 'Schistes Carton' from the Paris Basin, France) (Jenkyns, 1985, 1988; Farrimond et al., 1989; Hollander et al., 1991; Schmid-Röhl et al., 1999; Röhl et al., 2001; Röhl and Schmid-Röhl, 2005).

The Early Toarcian organic-rich mudrocks (Whitby Mudstone Formation) of the Yorkshire coast are subdivided into three litho-stratigraphic members from the bottom up: Grey Shale Member (-12–0 m), Mulgrave Shale Member (0–29 m), and Alum Shale Member (29–50 m) (Powell, 2010; Ghadeer and Macquaker, 2012; French et al., 2014; Figure 1.2). These Members of the Whitby Mudstone Formation have been bio-stratigraphically well characterized, mainly including three ammonite zones (*D. tenuicostatum*, *H. falciferum*, and *H. bifrons*) and some ammonite subzones (*D. tenuicostatum*, *D. semicelatum*, *Cl. exaratum*, and *H. falciferum*; Figure 1.2). The Grey Shale Member, Mulgrave Shale Member, and Alum Shale Member stratigraphically correspond to the *D. tenuicostatum*, *H. falciferum*, and *H. bifrons* zones, respectively (Howarth, 1955; Powell, 2010). The Grey Shale Member consists of bioturbated, silty mudstones with beds of calcareous siderite concretions. These mudstones have thin sharp-based beds, wave ripple, and starved ripple laminations (Wignall et al., 2005). Grain size and bioturbation intensity decrease toward the top of the unit, and sediment color darkens. In the Grey Shale Member there are three pyrite-rich shales, the lowest of which is the Sulfur Band of Chowns (1968). It is 15 cm in thickness, and its base marks the traditional base of the *D. tenuicostatum* Zone and the base of the Toarcian (Howarth, 1973; McArthur et al., 2008; McArthur, 2019). The other two stratigraphically higher sulfur-rich 'bands' are approximately 20 cm thick and have bases at 1.2 m and 5.0 m above the base of the Toarcian (Howarth, 1973; McArthur et al., 2008; McArthur, 2019). In the Mulgrave Shale Member the lithology dominated by bituminous black shales constitutes the Jet Rock (0–6.3 m) which contains an abundance of highly-altered wood (Jenkyns and Clayton, 1977; Hesselbo et al., 2007; Cohen et al., 2004; Kemp et al., 2005; French et al., 2014). The Jet Rock Member consists of dark, organic matter-rich, fissile mudstones with abundant ammonites and horizons of calcareous nodules. The boundary between the Grey Shale Member and Mulgrave Shale Member of the Whitby Mudstone Formation likely represents an increase in water depth in the basin. The well-studied negative T-CIE was recorded in the uppermost part of the Grey Shale Member (*D. semicelatum* subzone) and the Jet Rock Member (*Cl. exaratum*

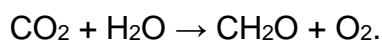
subzone) (Figure 1.2). The Alum Shale Member comprises a gray silty mudstone with several siderite concretions.

1.3. The behavior of stable isotope systems in marine environments

1.3.1. Carbon isotope systematics

Carbon, a bio-essential element for life, plays a critical role in biological and geochemical cycling. It has two stable isotopes ^{12}C and ^{13}C with natural abundances of 98.9 % and 1.1 % (Nier, 1950). Carbon isotope signatures are typically reported as $\delta^{13}\text{C}$ (the per mil (‰) difference in $^{13}\text{C}/^{12}\text{C}$ of a sample relative to the Vienna PeeDee belemnite standard (VPDB)) (Craig, 1957). In the modern ocean system dissolved inorganic carbon (DIC) containing > 99 % HCO_3^- and CO_3^{2-} is the largest carbon reservoir at circumneutral conditions (pH = 5.5–7.4) (Zeebe and Wolf-Gladrow, 2001). Carbon isotope exchange between the DIC and the atmosphere is generally accompanied by a positive isotope fractionation of ~9 ‰ under equilibrium conditions (Emrich and Vogel, 1970; Vogel et al., 1970; Mook et al., 1974). DIC is able to be consumed by calcium ions (Ca^{2+}) to form calcium carbonate (CaCO_3) via $\text{Ca}^{2+} + 2\text{HCO}_3^- \leftrightarrow \text{CaCO}_3 + \text{CO}_2 + \text{H}_2\text{O}$ and $\text{Ca}^{2+} + \text{CO}_3^{2-} \leftrightarrow \text{CaCO}_3$.

During these processes carbon isotope exchange between the DIC and CaCO_3 has a negative isotope fractionation of ~0.9 ‰ in equilibrium systems at a temperature of 20 °C (e.g. Rubinson and Clayton, 1969; Emrich and Vogel, 1970). The other important carbon reservoir in the ocean is dissolved organic carbon (DOC), which is produced by marine primary productivity through uptake of CO_2 :



In contrast to the inorganic carbon system that is typically controlled by isotope equilibrium exchange reactions, the DOC production is a kinetic fractionation process. Light carbon isotopes are always preferentially assimilated by marine producers, and thus the produced organic carbon typically carries ^{13}C -depleted signatures (Hayes et al., 1989). Newly produced organic carbon acting as electron donors plays an important role in the process of other major biogeochemical cycling involving iron, manganese, nitrogen and sulfur (e.g. Froelich et al., 1979; Berner, 1989). This causes that ~99.9 % of organic carbon is recycled back to inorganic carbon, and can largely represent the short-term carbon cycle (minutes to 10³ years) occurring on Earth's surface (Broecker and Peng, 1982; Des Marais, 1997; Berner, 1999). Apart from the

photosynthesized organic carbon in the ocean, the DOC can also derive from the land through hydrological cycling and riverine runoff. The isotope signatures of the terrestrially-sourced organic carbon highly varies depending on the plant types (e.g., O’Leary, 1981; Cerling et al., 1993; Meyers, 1994; Tipple and Pagani, 2007; Kohn, 2010).

In the ocean system on the seafloor the most important sedimentary reservoirs are carbonate carbon (60,000,000 Gt) and organic carbon (14,000,000 Gt), the burial of which significantly influences the carbon cycle in the atmosphere- ocean system on a time scale of 103 to 108 years (e.g., Garrels and Perry, 1974; Walker, 1977; Berner, 1989, 1998; Derry et al., 1992). The carbon isotope mass balance related to this long-term global carbon cycle is constrained by

$$\delta^{13}\text{C}_{\text{input}} = f_{\text{carb}} \times \delta^{13}\text{C}_{\text{carb}} + f_{\text{org}} \times \delta^{13}\text{C}_{\text{org}} \Rightarrow f_{\text{org}} = (\delta^{13}\text{C}_{\text{carb}} - \delta^{13}\text{C}_{\text{input}}) / (\delta^{13}\text{C}_{\text{carb}} - \delta^{13}\text{C}_{\text{org}}),$$

where f_{org} denote the fraction of the global influx of carbon buried as organic carbon (C_{org}). The fraction of buried carbonate carbon (C_{carb}) can therefore be defined as $f_{\text{carb}} = 1 - f_{\text{org}}$. Notably, when the f_{org} increases, $\delta^{13}\text{C}_{\text{carb}}$ and $\delta^{13}\text{C}_{\text{org}}$ values will simultaneously increase to meet the mass balance equation (Wickman, 1956). Examples showing such relationship are the Mesozoic OAEs which are generally defined by a long-term positive excursion in both $\delta^{13}\text{C}_{\text{carb}}$ and $\delta^{13}\text{C}_{\text{org}}$ owing to the significant organic carbon burial onto the coeval seafloor (e.g., Jenkyns, 2010).

1.3.2. Nitrogen isotope systematics

Nitrogen is one of the major nutrients that is essential to all life on Earth, and has two stable isotopes ^{14}N and ^{15}N with natural abundances of 99.6 % and 0.4 %, respectively. Nitrogen isotope signatures are reported as $\delta^{15}\text{N}$ (the per mil (‰) difference in $^{15}\text{N}/^{14}\text{N}$ relative to air- N_2 standard). The distribution of dissolved nutrients in the present-day ocean is captured by the concept of Redfield Ratio (16N:1P) which denotes the average stoichiometric ratio of dissolved N and P and reflect the metabolic requirements of plankton communities (Redfield, 1934). Changes in marine N/P values in the pre-industrial ocean are often linked to be N loss arising from dissimilatory nitrate reduction (denitrification) and/or anaerobic ammonium oxidation (anammox: ammonium oxidation coupled to nitrite reduction) (e.g., Sigman and Casciotti, 2001; Brandes et al., 2007; Canfield et al., 2010). These two processes are the principal sinks for biologically available N in marine environments (e.g. Gruber and Sarmiento, 1997; Kuypers et al., 2005) and occur in oxygen-depleted settings in the water column or

sediments (e.g., Gruber, 2008; Sigman and Fripiat, 2019). Water-column denitrification and/or anammox preferentially removes ^{14}N to the atmosphere as the form of N_2 and/or N_2O , having the potential to enrich the $\delta^{15}\text{N}$ of the residual dissolved N oxyanion pool (e.g., Mariotti et al., 1981; Barford et al., 1999). However, this scenario is based on the fact that the process of quantitative water-column denitrification and/or anammox should be non-quantitative; if not, quantitative water-column denitrification and/or anammox will be accompanied by no net isotope effect (e.g., Ader et al., 2016; Stüeken et al., 2016; Ossa Ossa et al., 2018). Further, biological N processes driven by sedimentary denitrification and/or anammox is generally complete, erasing the associated isotope effect on the $\delta^{15}\text{N}$ of overlying water-column N pool (e.g., Nielsen, 1992; Middelburg et al., 1996; Sigman et al., 2003; Dähnke and Thamdrup, 2013).

The bioavailable N source in marine ecosystems is mainly contributed from biological N_2 fixation (diazotrophy; reduction of N_2 to NH_4^+) which only happens when nutrient N concentrations is much lower than nutrient P (i.e., $\text{N/P} \ll \text{Redfield Ratio}$) (Tyrrell, 1999; Grasby et al., 2020). A common average $\delta^{15}\text{N}$ of ~ 1 ‰ has been suggested for the fixed N input to the ocean from biological N_2 fixation (Sigman et al., 2009b; Sigman and Fripiat, 2018). Although culture experiments have reported light $\delta^{15}\text{N}$ values of down to -7 ‰ from biological N_2 fixation (Zhang et al., 2014), it is rare in natural marine ecosystems (Stüeken et al., 2016). The newly fixed dissolved NH_4^+ in the surface water is often quantitatively oxidized by nitrifying bacteria to NO_3^- , which leaves no net isotope fractionation between the conversion of NH_4^+ to NO_3^- . Other inputs of fixed N to marine environments include terrestrial runoff and atmospheric deposition, the N isotope compositions of which are poorly constrained (Sigman and Fripiat, 2019).

1.3.3. Molybdenum isotope systematics

Molybdenum is a trace element with the concentration of ~ 1.5 $\mu\text{g/g}$ in the upper continental crust (UCC; McLennan, 2001). It has seven stable isotopes: ^{92}Mo , ^{94}Mo , ^{95}Mo , ^{96}Mo , ^{97}Mo , ^{98}Mo , and ^{100}Mo with the natural abundances of 14.65 %, 9.19 %, 15.87 %, 16.67 %, 9.58 %, 24.29 %, and 9.74 %, respectively (de Laeter et al., 2003). Molybdenum isotope signatures are reported in the σ -notation relative to the NIST3134 standard (Goldberg et al., 2013), which was set to 0.25 ‰ following a procedure of Nägler et al. (2014):

$$\delta^{98}\text{Mo} = 1.0025 \times ((^{98}\text{Mo}/^{95}\text{Mo})_{\text{sample}}/({}^{98}\text{Mo}/^{95}\text{Mo})_{\text{NIST3134}} - 1)$$

where δ is expressed in ‰ by multiplication with a factor of 1000. Molybdenum homogeneously exists in the oxygenated modern ocean as the form of molybdate (MoO_4^{2-}) oxyanion with a concentration of ~105 nM and a modern oceanic residence time of ~440–800 ka (Morris, 1975; Collier, 1985; Emerson and Husted, 1991; Colodner et al., 1995; Morford and Emerson, 1999; Barling et al., 2001; Miller et al., 2011; Greber et al., 2015). The isotopic composition of Mo delivered to the oceans has been estimated as ~0.55 ‰ (King and Pett-Ridge, 2018; Neely et al., 2018). The removal fluxes of Mo from the oceans varies as a function of water mass redox conditions. In the modern, predominantly oxic, ocean, the major sink for Mo is Fe-Mn oxides, mainly crusts and nodules in pelagic sediments. This output process preferentially exports light Mo isotopes, yielding a light $\delta^{98}\text{Mo}$ signal of -0.7 ‰ for the adsorbed fractions, and simultaneously enriching the residual seawater Mo reservoir to a heavy $\delta^{98}\text{Mo}$ value of +2.3 ‰ (Siebert et al., 2001, 2003; Barling and Anbar, 2004; Tossell, 2005; McManus et al., 2006; Goldberg et al., 2009; Naegler et al., 2014;). In euxinic (sulfidic and anoxic) water column settings, aqueous H_2S can effectively break the Mo=O bond, transforming MoO_4^{2-} to thiomolybdates ($\text{MoO}_{4-x}\text{S}_x^{2-}$, $x = 1-4$) (Helz et al., 1996). Under these conditions, Mo scavenging into the euxinic sediment is at a high rate which can be 100- to 1000-fold greater than that in oxic settings (Scott and Lyons, 2012). In the presence of aqueous H_2S concentration of < 11 μM in the water column, the transformed $\text{MoO}_{4-x}\text{S}_x^{2-}$ species are adsorbed onto organic matter or form Fe sulfides in the sediment (Helz et al., 1996; McManus et al., 2002; Tribovillard et al., 2006; Naegler et al., 2011). As the aqueous H_2S concentration is above 11 μM , MoO_4^{2-} is effectively converted to tetrathiomolybdate (MoS_4^{2-}) which is then nearly quantitatively scavenged into the underlying euxinic sediment (e.g., black shales), yielding a sediment Mo isotope signal equal to that of the coeval seawater (Helz et al., 1996; Erickson and Helz, 2000; Barling et al., 2001; Siebert et al., 2003; Arnold et al., 2004).

1.3.4. Zinc isotope systematics

Zinc is a trace element with the concentration of ~71 $\mu\text{g/g}$ in the upper continental crust (UCC: McLennan, 2001) and has five stable isotopes: ^{64}Zn , ^{66}Zn , ^{67}Zn , ^{68}Zn and ^{70}Zn with the natural abundances of 49.2 %, 27.7 %, 4.0 %, 18.5 %, and 0.6 %, respectively.

respectively (Rosman, 1972; de Laeter et al., 2003). Sample Zn isotope compositions are measured as the ‰-differences of their $^{66}\text{Zn}/^{64}\text{Zn}$ isotope abundance ratios relative to that of the isotopically certified reference material IRMM-3702 in δ -values. The measured data are then recalculated to the ‘JMC-Lyon’ standard solution which has Zn isotope compositions of 0.29‰ relative to the IRMM-3702 (Moeller et al., 2012):

$$\delta^{66}\text{Zn} = 1.0029 \times ((^{66}\text{Zn}/^{64}\text{Zn})_{\text{sample}} / (^{66}\text{Zn}/^{64}\text{Zn})_{\text{IRMM-3702}} - 1)$$

where δ is expressed in ‰ by multiplication with a factor of 1000. Zinc is fundamental for many life processes, and is characteristic of a nutrient-type distribution profile with the concentration of near zero in the surface ocean due to its high biologic demand (e.g., Chester, 1993; Wyatt et al., 2014). Zn has a short present-day oceanic residence time of ~11,000 yr (Little et al., 2014), which leads to the homogeneous Zn isotope signal of the global deep ocean ($\delta^{66}\text{Zn} = \sim 0.5 \text{ ‰} \pm 0.14 \text{ ‰}$; 2 standard deviations; Conway and John, 2014). The $\delta^{66}\text{Zn}$ value of $\sim +0.5 \text{ ‰}$ for the deep ocean is isotopically heavier than those of the bulk silicate Earth ($\sim +0.27 \text{ ‰}$; Vance et al., 2016) and the Zn sources to the ocean including rivers, aerosol dust, hydrothermal fluids, and benthic inputs, all $\leq 0.3 \text{ ‰}$ (Chen et al., 2013; Little et al., 2014, 2016; Vance et al., 2016 and references therein). By contrast, modern surface-ocean $\delta^{66}\text{Zn}$ values showing a high degree of spatial variability (-1.1 to $+0.9 \text{ ‰}$; Conway and John, 2014) are generally lighter than that in the deep ocean by $\sim 0.5 \text{ ‰}$. The large variation in the surface-ocean Zn isotope signals is complex, but has been linked to be biological uptake, scavenging of isotopically heavy Zn, and water-mass lateral or vertical advections (e.g., Conway and John, 2014).

The main sinks of Zn from the oceans consists of oxic sediments (e.g., Fe-Mn oxyhydroxides, carbonates) and organic-rich continental-margin sediments (e.g., Pichat et al., 2003; Little et al., 2014a, b, 2016). The former with $\delta^{66}\text{Zn}$ values of $\sim +0.9 \text{ ‰}$ are isotopically heavier than those of inputs and deep-ocean seawater (e.g., Conway and John, 2014; Little et al., 2014a, b, Vance et al., 2016). The latter depositing in modern ocean oxygen minimum zones (OMZs) are so far the only reported removal flux of light Zn isotopes from the oceans (Little et al., 2016). The light $\delta^{66}\text{Zn}$ values ($\sim 0.0 \text{ ‰}$) observed for these oxygen-deficient sediments may be as a consequence of non-quantitative Zn removal in sulfides, or owing to scavenging of heavy Zn isotopes just below the surface ocean, leading to light Zn isotope signals in the photic zone in which organic matter is yielded (Little et al., 2016; Vance et al., 2016;

John et al., 2017; Sweere et al., 2018). Furthermore, sediments underlying the restricted, euxinic deep waters (e.g., in Black Sea and Cariaco Basin) also occupy a small fraction of the total Zn sink. They exhibit average $\delta^{66}\text{Zn}$ values of $\sim+0.5$ ‰ which is identical to that of the deep-ocean seawater due to near-quantitative removal of Zn under the condition of the presence of aqueous H_2S in the water column (Vance et al., 2016; Isson et al., 2018; Sweere et al., 2020).

2. Objectives and Expected Outcomes

To understand the Early Toarcian climate warming and seawater chemistry variations, a number of studies ranging from sedimentology (e.g., Howarth, 1955, 1962, 1973; Röhl et al., 2001; Frimmel et al., 2003), paleontology (e.g., Riegraf, 1985; van de Schootbrugge et al., 2005, 2019; Fraguas et al., 2012; van de Schootbrugge and Gollner, 2013b; Correia et al., 2017; Martindale et al., 2017) and geochemistry (e.g., Jenkyns, 1985; Jenkyns and Clayton, 1986; Hesselbo et al., 2000; Kemp et al., 2005; Pearce et al., 2008; Percival et al., 2016; Houben et al., 2021) have been performed on the contemporaneous sedimentary sections deposited worldwide. However, it remains several major questions that are unsolved: 1) whether local-scale carbon cycles had the potential to influence the global carbon event, 2) what the ocean redox structure was, and 3) how the bio-essential element Zn proceeded across the T-CIE interval. This study is built on the use of combined stratigraphically high-resolution geochemical analyses of C, N and Zn isotope compositions for the T-CIE sedimentary sections from Dotternhausen quarry and/or Yorkshire coast.

The major objectives of this study are:

- (1) Exemplifying the existence of local-scale carbon cycles and emphasizing their influence on the expression of the typical T-CIE;
- (2) Clarifying the coeval ocean redox landscape: global deep-ocean anoxia or anoxia only in marginal basins;
- (3) Exhibiting the response of Zn biogeochemical cycling to marine anoxia across the T-CIE interval.

The expected outcomes of this study are:

- (1) Local-scale carbon cycles existed widely, and the resultantly allochthonous carbon process may have disturbed the traditional T-CIE curves

- (2) Seawater anoxia occurred in marginal marine basins, and the term global deep-ocean anoxia probably still needs to be investigated.
- (3) Zinc output into underlying oxygen-depleted marine sediments may increase through combining with organic matter and/or sulfides in water column or pore waters.

3. Results and Discussion

3.1. Results

3.1.1. Element concentrations and carbon, nitrogen and molybdenum isotopes for Dotternhausen samples

3.1.1.1. Element concentrations

The concentrations of major element oxides and trace element of the measured samples from Dotternhausen section are reported in Table 1 (Appendix A; Wang et al., 2020). Aluminum oxide (Al_2O_3) in these Dotternhausen samples has a relatively low abundance (mean = 9.43 wt.%) (see Table 1 in Appendix A; Wang et al., 2020) compared to the upper continental crust (UCC: 15.4 wt.%) (McLennan, 2001). Except the Unterer Stein carbonate bed with high manganese (Mn) concentration (up to ~0.2 wt.%), Mn concentrations for the Dotternhausen T-CIE samples are lower than that of the UCC (Figure 3.1; see Table 1 in Appendix A; Wang et al., 2020). The abundances of immobile trace elements thorium (Th), zirconium (Zr), and scandium (Sc) have a range of 5.1–11.4 $\mu\text{g/g}$, 64.7–184.3 $\mu\text{g/g}$, and 9.4–21.3 $\mu\text{g/g}$, respectively (see Table 1 in Appendix A; Wang et al., 2020). Relative to the UCC (Th: 10.7 $\mu\text{g/g}$, Zr: 190 $\mu\text{g/g}$, and Sc: 13.6 $\mu\text{g/g}$) (McLennan, 2001), the studied samples display low contents of Th (mean = 9.3 $\mu\text{g/g}$) and Zr (mean = 123.2 $\mu\text{g/g}$; see Table 1 in Appendix A; Wang et al., 2020), whereas the mean concentration of Sc (16.4 $\mu\text{g/g}$) approaches that of the UCC (McLennan, 2001). The Th/Sc and Zr/Sc ratios ranging from 0.38 to 0.67 and 4.65 to 9.33, respectively, show no large variations (Figure 3.2). The total rare earth element concentrations (ΣREEs) vary from 141.9 to 273.8 $\mu\text{g/g}$, with an average of 210.1 $\mu\text{g/g}$ (see Table 1 in Appendix A; Wang et al., 2020) which is higher than that of the UCC (168.1 $\mu\text{g/g}$) (McLennan, 2001). Yttrium (Y) and holmium (Ho) geochemical twins due to their similar radius and charge generally have chondritic Y/Ho values of ~28 in clastic sedimentary rocks (see Albut et al., 2018 and references therein). The studied samples

have mildly fluctuating Y/Ho ratios ranging from 25.1 to 31.1 with a mean of 26.8 (Figure 3.2) which is slightly lower than the chondritic value of ~28. Redox-sensitive elements Mo, uranium (U), and vanadium (V)) range from 0.93 to 43.8 $\mu\text{g/g}$, 2.7 to 19.1 $\mu\text{g/g}$ and 99.2 to 463.4 $\mu\text{g/g}$, respectively (Figure 3.1; see Table 1 in Appendix A; Wang et al., 2020). In general, the enrichment or depletion pattern of trace element concentrations with respect to the reference material is critical to reconstruct paleoenvironmental conditions (Tribouillard et al., 2006). In order to trace the authigenic fraction of elements, normalization to an index of the detrital component, normally Al, is necessary (Francois, 1988). The Al concentration of the UCC used for this study is from McLennan (2001). The enrichments of Mo, U, and V are shown in Figure 3.3. The gray bioturbated mudstones depositing before the T-CIE almost do not display enrichments in Mo, U, and V, whereas these elements are obviously enriched in the laminated oil shale facies corresponding to the T-CIE (Figure 3.3).

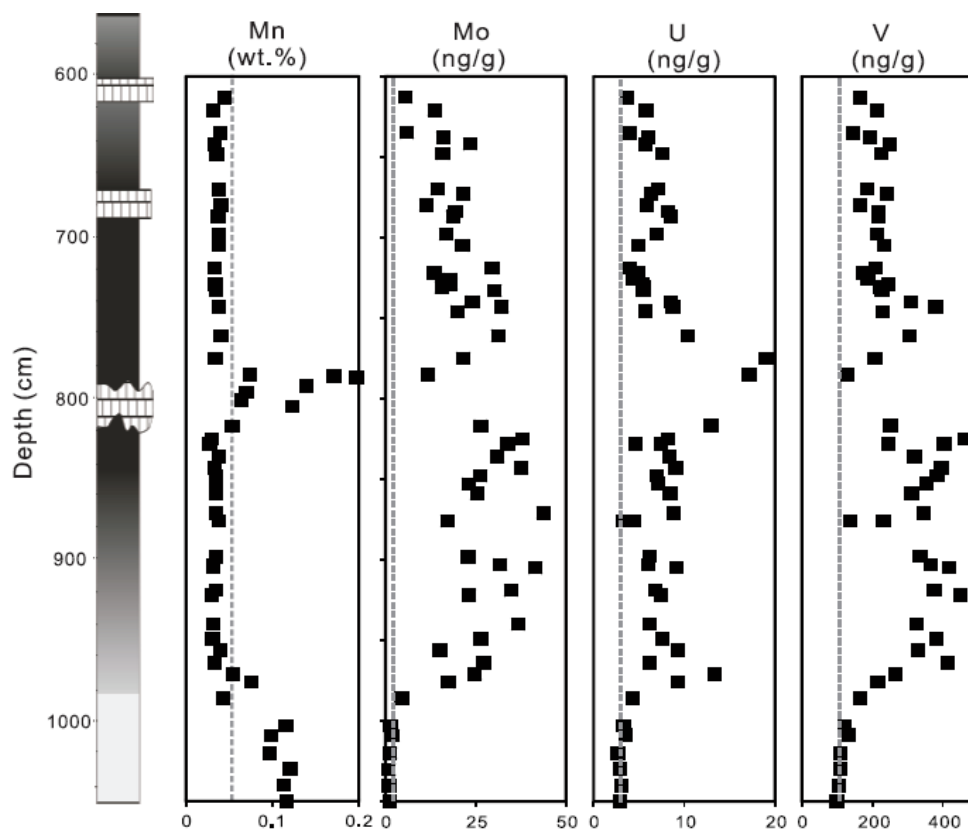


Figure 3.1. Stratigraphic profiles of Mn, Mo, U and V concentrations in the Dotternhausen section. Dashed lines denote the according reference values of upper continental crust (UCC: McLennan, 2001).

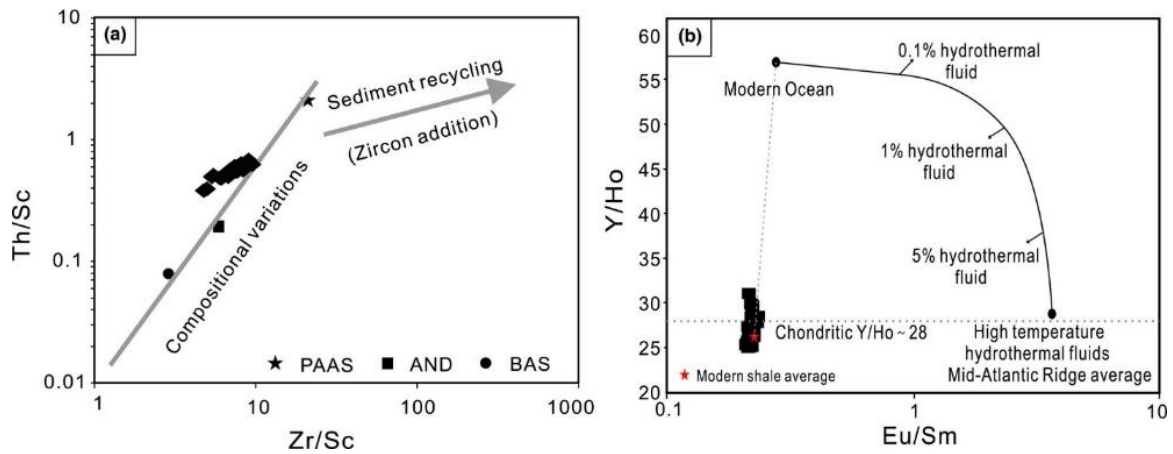


Figure 3.2. (a) Th/Sc vs. Zr/Sc diagram (McLennan et al., 1993). AND, andesite; BAS, basalt; PAAS, post-Archean Australian shale; (b) Y/Ho vs. Eu/Sm diagram (modified from Albut et al., 2018 and references therein).

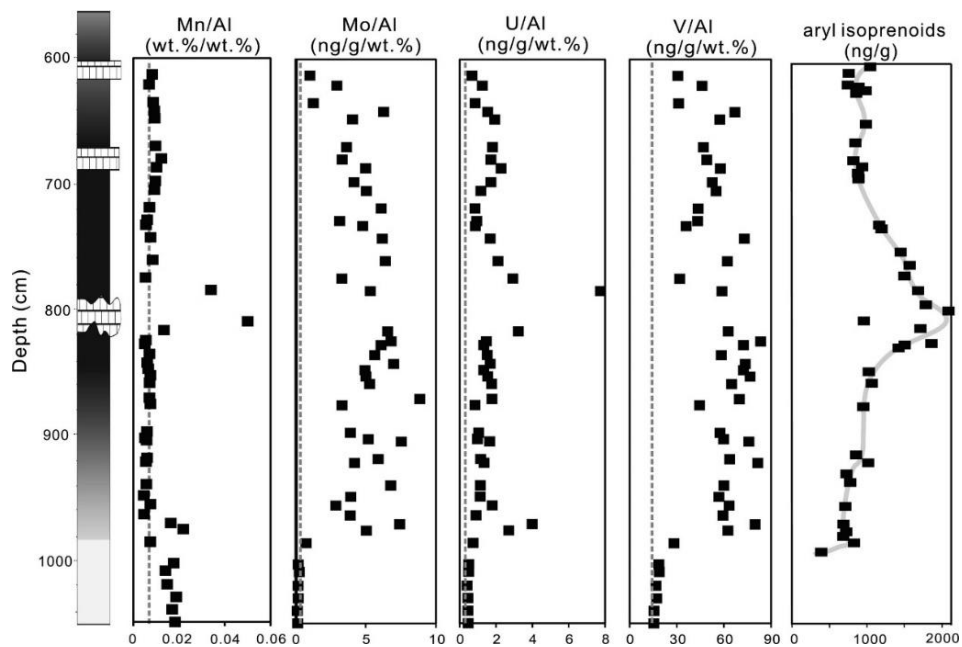


Figure 3.3. Stratigraphic profiles of Mn, Mo, U and V enrichments in the Dotternhausen section. Stratigraphic distribution of aryl isoprenoid (GSB biomarker) abundance is from Schwark and Frimmel (2004). Dashed lines denote the according reference values of upper continental crust (UCC: McLennan, 2001).

The total organic carbon (TOC) contents are reported in Table 2 (Appendix A; Wang et al., 2020) and are plotted in Figures 3.4. Carbonate concentrations are reported in Table 2 (Appendix A; Wang et al., 2020). The gray bioturbated mudstone samples have lower TOC contents < 5 wt.% than laminated oil shales with consistently TOC contents > 5 wt.% (Figure 3.4; see Table 2 in Appendix A; Wang et al., 2020). Unterer Stein shows high carbonate contents with an average of 92 wt.%, the rest of this studied samples exhibit a variation between 3 to 88 wt.%.

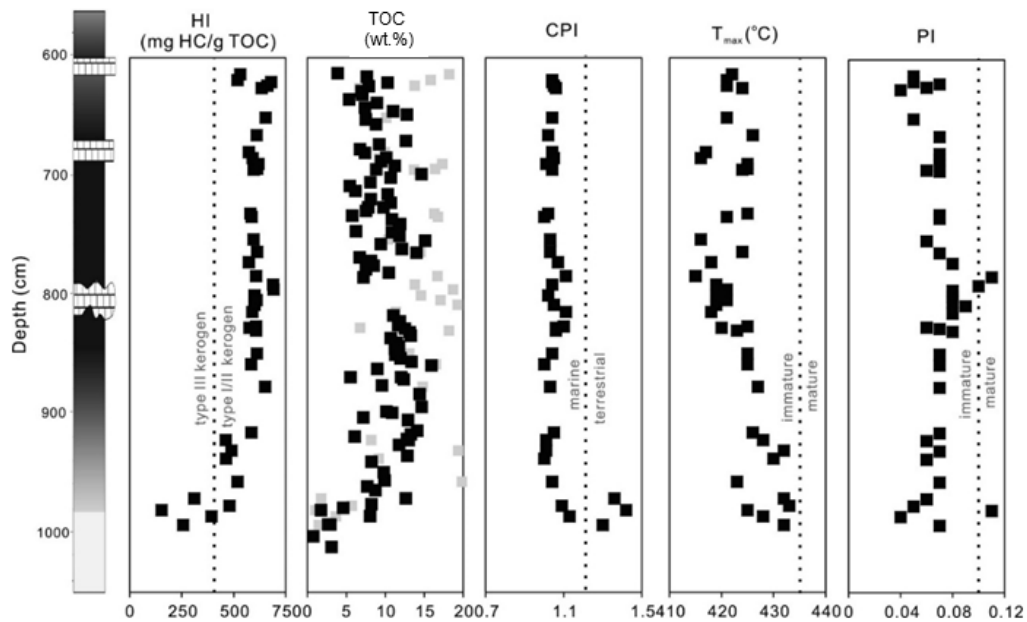


Figure 3.4. Rock-Eval pyrolysis data of the Dotternhausen section. The HI, CPI, T_{max} , PI, and TOC of gray rectangles are from Frimmel et al. (2004).

3.1.1.2. Carbon and oxygen isotope compositions

Bulk carbon and oxygen isotope compositions ($\delta^{13}C$ and $\delta^{18}O$) analyzed in the Isotope Geochemical Laboratory, University of Tuebingen, are given in Table 2 (Appendix A; Wang et al., 2020) and are plotted in Figures 3.5. According to the distribution of organic-rich sediments in the Dotternhausen section, this study places the onset of the T-CIE to a depth of 980 cm in our profile. Four data points at depths between 1,012 cm and 986 cm reveal constant $\delta^{13}C_{carb}$ and $\delta^{13}C_{org}$ values prior to the T-CIE (Figure 3.5; see Table 2 in Appendix A; Wang et al., 2020). The negative $\delta^{13}C_{carb}$ and $\delta^{13}C_{org}$ excursions ranging from 0 to -12 ‰ and -28 to -32 ‰, respectively, are exhibited between depths of 986 cm and 613 cm (Figure 3.5; see Table 2 in Appendix A; Wang et al., 2020). Two-step opposing small-scale excursions of $\delta^{13}C_{carb}$ and $\delta^{13}C_{org}$ records from 876 to 761 cm are obviously observed (Figure 3.5). The $\delta^{13}C_{carb}$ values in the first and smaller scale (from 876 to 825 cm) has a negative excursion, which corresponds to a slightly positive excursion in $\delta^{13}C_{org}$ values. By contrast, the second step (from 825 to 761 cm) has larger magnitude excursions in both $\delta^{13}C_{carb}$ and $\delta^{13}C_{org}$ values (Figure 3.5). The $\Delta^{13}C$ ($\delta^{13}C_{carb} - \delta^{13}C_{org}$) is relatively constant in the lower part (interval 1 from 981 to 883 cm) and upper part (interval 3 from 757 to 613 cm), whereas it drops according to the two-step opposing small-scale excursions (interval 2 from 876 to 761 cm; Figure 3.5). The $\delta^{18}O$ values of carbonates range from

-7 to -4 ‰, and the heaviest values are preserved in the diagenetically lenticular limestone bed of Unterer Stein (Figure 3.5).

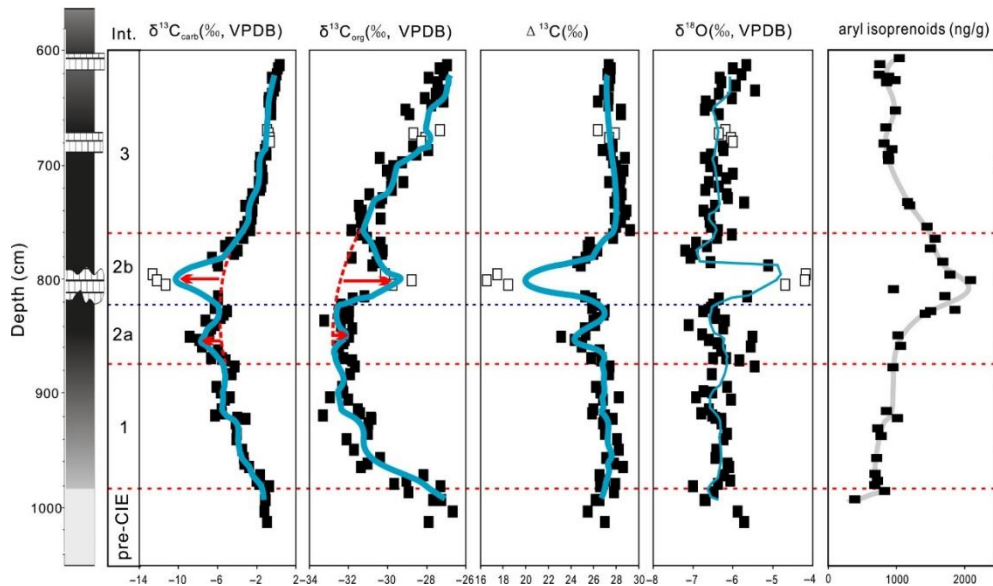


Figure 3.5. Stratigraphic profiles of $\delta^{13}\text{C}_{\text{carb}}$, $\delta^{13}\text{C}_{\text{org}}$, $\Delta^{13}\text{C}$ ($\Delta^{13}\text{C} = \delta^{13}\text{C}_{\text{carb}} - \delta^{13}\text{C}_{\text{org}}$) and $\delta^{18}\text{O}$ in the Dotternhausen section. Stratigraphic distributions of aryl isoprenoid (GSB biomarker) abundance are from Schwark and Frimmel (2004). The red dashed arcs denote the theoretic T-CIE curves without suffering local-scale carbon-cycle perturbations. The blue lines represent the 5-point moving average of the isotopic data. Int.: interval. White rectangles particularly represent the isotopic data from limestone beds.

Carbon isotope compositions of total organic matter and kerogen ($\delta^{13}\text{C}_{\text{org}}$ and $\delta^{13}\text{C}_{\text{ker}}$) analyzed in the laboratory of the Institute of Earth Surface Dynamics (IDYST), University of Lausanne, are given in Table 1 (Appendix B; Wang et al., 2021). The $\delta^{13}\text{C}_{\text{org}}$ and $\delta^{13}\text{C}_{\text{ker}}$ for both pre-T-CIE (from the depth of 1040 to 986 cm) and T-CIE (from the depth of 964 to 621 cm) samples are comparable (see Table 1 in Appendix B; Wang et al., 2021). However, the values of $\delta^{13}\text{C}_{\text{org}}$ and $\delta^{13}\text{C}_{\text{ker}}$ for the T-CIE samples are generally lower than those of the pre-T-CIE samples (see Table 1 in Appendix B; Wang et al., 2021).

3.1.1.3. Nitrogen isotope composition

Total and kerogen nitrogen concentrations (TN_{bulk} and N_{ker}), and nitrogen isotope compositions of bulk rock and separate kerogen ($\delta^{15}\text{N}_{\text{bulk}}$ and $\delta^{15}\text{N}_{\text{ker}}$) for the Dotternhausen samples are given in Table 1 (Appendix B; Wang et al., 2021). Samples before the T-CIE have relatively low TN_{bulk} and N_{ker} values ranging from 0.06 to 0.08 wt.% (mean = 0.08 wt.%) and 0.28 to 0.35 wt.% (mean = 0.32 wt.%), respectively. The TN_{bulk} and N_{ker} for the T-CIE samples display higher values which are in the range of

0.14 to 0.53 wt.% (mean = 0.32 wt.%) and 0.43 to 1.34 wt.% (mean = 1.07 wt.%), respectively. The $\delta^{15}\text{N}_{\text{bulk}}$ values for the pre-T-CIE samples are in the range between 1.9 and 2.4 ‰, while the T-CIE samples display a distinct range between 0.8 and 5.7 ‰. However, the samples deposited before and during the T-CIE show generally comparable average values which are 2.1 ‰ and 2.3 ‰, respectively. The $\delta^{15}\text{N}_{\text{ker}}$ values for the pre-T-CIE and T-CIE samples exhibit more consistent ranges from 1.1 to 2.2 ‰ (mean = 1.8 ‰) and 1.6 to 2.0 ‰ (mean = 1.7 ‰), respectively.

3.1.1.4. Molybdenum isotope composition

The Mo isotope composition ($\delta^{98}\text{Mo}$) for the Dotternhausen samples are given in Table 1 (Appendix C). Its pre-T-CIE samples (from the depth of 1003 to 986 cm) have higher $\delta^{98}\text{Mo}$ values ranging from 0.99 to 1.46 ‰ with the average of 1.23 ± 0.66 ‰ (2 s.d., $n = 2$) than those of the T-CIE samples (from the depth of 976 to 613 cm) which are in the range between 0.46 and 1.11 ‰ (mean = 0.84 ± 0.32 ‰; $n = 37$) (see Table 1 in Appendix C). To correct for possible terrigenous-sourced Mo, the isotope composition of the authigenic Mo fraction ($\delta^{98}\text{Mo}_{\text{auth}}$) was calculated using $\text{Mo}_{\text{detrital}} = 1.5 \mu\text{g/g}$, $\text{Al}_{\text{detrital}} = 8.04 \%$, and $\delta^{98}\text{Mo}_{\text{detrital}} = +0.4 \%$ as the parameters for the UCC endmember (McLennan, 2001; Dahl et al., 2011) by the following equations:

$$f_{\text{detrital}} = (\text{Mo}_{\text{detrital}}/\text{Al}_{\text{detrital}}) \times \text{Al}_{\text{sample}}/\text{Mo}_{\text{sample}}$$

$$\delta^{98}\text{Mo}_{\text{auth}} = (\delta^{98}\text{Mo} - f_{\text{detrital}} \times \delta^{98}\text{Mo}_{\text{detrital}})/(1 - f_{\text{detrital}}).$$

The calculated $\delta^{98}\text{Mo}_{\text{auth}}$ values are close to the $\delta^{98}\text{Mo}$ values ($\delta^{98}\text{Mo}_{\text{auth}} = 1.105 \times \delta^{98}\text{Mo} + 0.0621$; $R^2 = 0.97$; $n = 38$, $p(a) < 0.001$), which may result from the terrigenous Mo comprises only a small fraction of total Mo in most samples. The $\delta^{98}\text{Mo}_{\text{auth}}$ values for T-CIE samples range from +0.47 to +1.27 ‰ (Figure 3.6; see Table 1 in Appendix C) with an average of +0.87 ‰, which is clearly lower than the modern global seawater value of +2.34 ‰ (e.g., Siebert et al., 2003).

3.1.2. Element concentrations for Yorkshire samples

3.1.2.1. Element concentrations

The concentrations of selected major element oxides and trace element of the measured samples from Yorkshire section are reported in Table 1 (Appendix C). The detrital indicator element Al in all the Yorkshire samples has a relatively high

abundance (mean = 9.14 wt.%) (see Table 1 in Appendix C) compared to the UCC (8.04 wt.%: McLennan, 2001). Notably, the pre-T-CIE gray bioturbated shale samples (from the depth of -12.07 to -3 m) have higher Al concentrations with the average of 10.89 wt.% than those of the T-CIE laminated black shale samples (from the depth of -1.71 to 6.15 m) (mean = 8.84 wt.%). The concentrations of redox-sensitive elements Mo, U, and V between the Yorkshire pre-T-CIE and T-CIE samples are obviously different. Mo, U, and V concentrations for the pre-T-CIE samples range from 0.7 to 1.5 µg/g (mean = 0.9 µg/g), 3.1 to 3.8 µg/g (mean = 3.5 µg/g) and 134.9 to 158.7 µg/g (mean = 148.0 µg/g), respectively (see Table 1 in Appendix C), which are on the whole comparable to those of the UCC (Mo: 1.5 µg/g, U: 2.8 µg/g, V: 107 µg/g). By contrast, these element concentrations for the T-CIE samples ranging from 4.2 to 35.9 µg/g (mean = 8.4 µg/g), 4.7 to 17.2 µg/g (mean = 7.2 µg/g), and 150.3 to 299.2 µg/g (mean = 194.8 µg/g), respectively (see Table 1 in Appendix C), are higher than those of the pre-T-CIE samples and the UCC. The concentrations of bio-essential elements copper (Cu), nickel (Ni) and phosphorus (P) between the Yorkshire pre-T-CIE and T-CIE samples are also obviously different. Cu, Ni and P concentrations for the pre-T-CIE samples range from 29.4 to 38.8 µg/g (mean = 35.7 µg/g), 64.2 to 75.4 µg/g (mean = 75.6 µg/g) and 0.027 to 0.061 wt.% (mean = 0.036 wt.%), respectively (see Table 1 in Appendix C). Of which the Cu and Ni concentrations are higher than those of the UCC (Cu: 25 µg/g, Ni: 44 µg/g), while the P concentration is lower than that of the UCC (P: 0.07 wt.%). For the T-CIE samples, Cu, Ni and P concentrations are in the range between 41.4 and 151.7 µg/g (mean = 83.6 µg/g), 75.8 and 203.9 µg/g (mean = 99.4 µg/g) and 0.031 and 0.284 wt.% (mean = 0.097 wt.%), respectively (see Table 1 in Appendix C), which are significantly higher than those of the pre-T-CIE samples and the UCC. The concentration of another bio-limiting element Zn for the Yorkshire pre-T-CIE and T-CIE samples does not show an obvious difference. For the pre-T-CIE samples, Zn concentration ranges from 77.5 to 121.9 µg/g (mean = 102.9 µg/g), whereas the T-CIE samples have the Zn concentration of 77.4 to 224.8 µg/g (mean = 128.0 µg/g) (see Table 1 in Appendix C). Both mean values are obviously higher than that of the UCC (71 µg/g).

3.1.3. Zinc isotope compositions for Yorkshire and Dotternhausen samples

The Yorkshire pre-T-CIE samples show $\delta^{66}\text{Zn}_{\text{bulk}}$ values varying from +0.18 to +0.23 ‰ with an average of $+0.19 \pm 0.04$ ‰ (2 s.d., n = 7), whereas the Dotternhausen

pre-T-CIE samples have relatively heavy $\delta^{66}\text{Zn}_{\text{bulk}}$ values that are in the range of +0.29 to +0.38 ‰ averaging $+0.35 \pm 0.06$ ‰ (2 s.d., $n = 7$) (Figure 3.6; see Table 1 in Appendix C). The pre-T-CIE $\delta^{66}\text{Zn}_{\text{bulk}}$ values for both sedimentary sections are, however, comparable to that of the lithogenic average ($\sim 0.27 \pm 0.07$ ‰; Little et al., 2016 and references therein). Across the T-CIE interval, an overall positive excursion of $\delta^{66}\text{Zn}_{\text{bulk}}$ is observed for both Yorkshire and Dotternhausen samples which range from 0.29 to 0.55 ‰ (mean = $+0.41 \pm 0.12$ ‰; 2 s.d., $n = 41$) and from 0.32 to 0.66 ‰ (mean = $+0.52 \pm 0.17$ ‰; 2 s.d., $n = 39$), respectively (Figure 3.6; see Table 1 in Appendix C). A prominent negative $\delta^{66}\text{Zn}_{\text{bulk}}$ excursion in both Yorkshire and Dotternhausen T-CIE strata is observed in Figure 3.6. This negative shift towards the similar minimum value of ~ 0.3 ‰ at the depth of ~ 1.0 m and ~ 820 cm in the Yorkshire and Dotternhausen sections, respectively (Figure 3.6; see Table 1 in Appendix C). However, the negative $\delta^{66}\text{Zn}_{\text{bulk}}$ excursion of the Yorkshire and Dotternhausen sections is exhibited on different lithological facies: organic-rich black shales and a diagenetic limestone bed (Unterer Stein) (cf. Figure 3.6; Röhl et al., 2001).

Assuming the sedimentation rates for the Yorkshire and Dotternhausen T-CIE strata are respectively constant, they can be calculated by the equation:

$$\text{sedimentation rates} = \text{distance/duration (D)}$$

where the distance denotes the thickness of T-CIE strata expressed in Yorkshire and Dotternhausen sedimentary sections, and the duration (D) denotes the temporal interval of T-CIE which ranges from ~ 120 to $\sim 1,200$ kyr (Suan et al., 2008; Ogg and Hinnov, 2012). The thickness of the Yorkshire and Dotternhausen T-CIE strata are ~ 8.8 m (from ~ 2.5 to 6.3 m) and ~ 360 cm (from ~ 980 to 620 cm), respectively (Figures 1.2 and 3.6; Röhl et al., 2001; Pearce et al., 2008; French et al., 2014). After entering the T-CIE interval, the temporal appearance of the negative shift in $\delta^{66}\text{Zn}_{\text{bulk}}$ values at the depth of ~ 1.0 m and ~ 820 cm in Yorkshire and Dotternhausen sections can be simply determined. It respectively took the geologic time of $\sim 0.40 \times D$ and $\sim 0.44 \times D$ to arrive at the negative $\delta^{66}\text{Zn}_{\text{bulk}}$ shift observed in Yorkshire and Dotternhausen sections. Therefore, this drop of $\delta^{66}\text{Zn}_{\text{bulk}}$ values found in these two sedimentary sections occurred nearly concurrently after the onset of the T-CIE.

The analytical methods for all geochemical data mentioned above are given in Appendix D.

Yorkshire

Dotternhausen

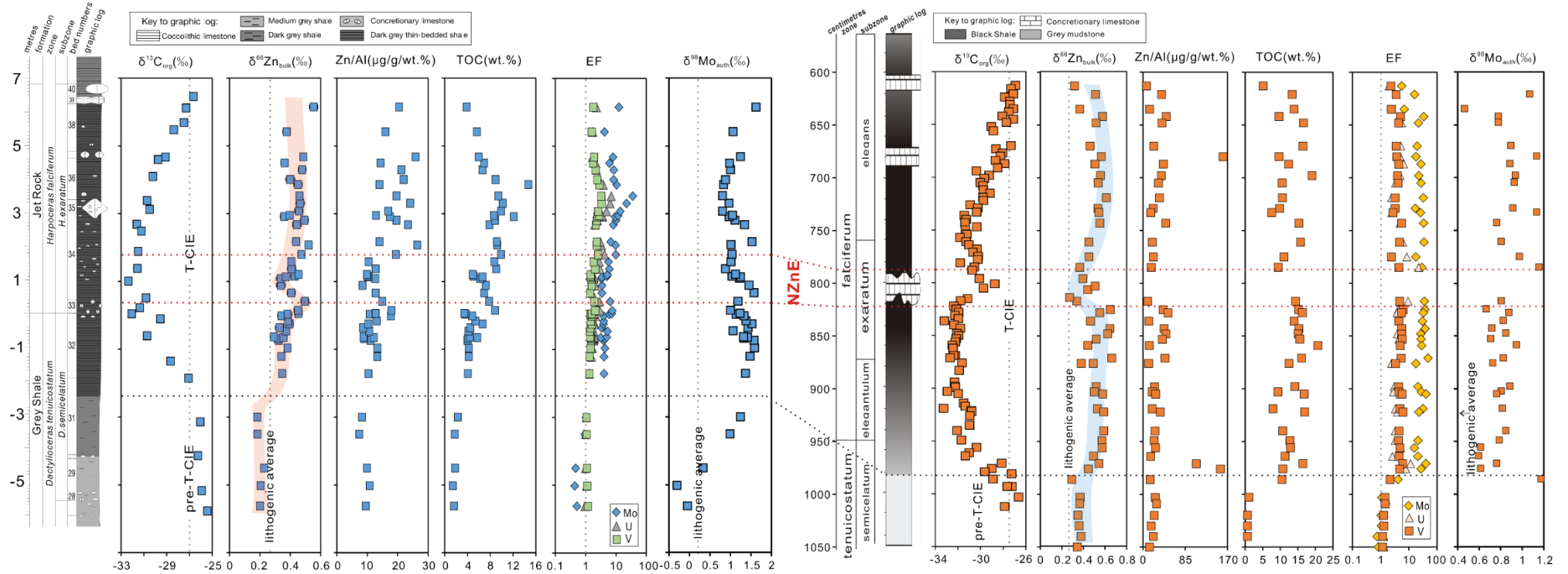


Figure 3.6. Chemostratigraphic $\delta^{13}\text{C}_{\text{org}}$, $\delta^{66}\text{Zn}_{\text{bulk}}$, Zn/Al, TOC content, enrichment factors (EFs) of Mo-U-V elements, and $\delta^{98}\text{Mo}_{\text{auth}}$ for the Yorkshire and Dotternhausen sedimentary sections throughout the pre-T-CIE and T-CIE intervals. The interval bracketed by two dashed red lines denotes the negative bulk Zn isotope excursion (NZnE). The $\delta^{13}\text{C}_{\text{org}}$, TOC and $\delta^{98}\text{Mo}_{\text{auth}}$ data for the Yorkshire samples are from Pearce et al. (2008).

3.2. Discussion

3.2.1. Evidence for local carbon cycles superimposed on the T-CIE

3.2.1.1. Negligible effects of terrigenous-sourced organic carbon, thermal maturity, and hydrothermal fluids on $\delta^{13}\text{C}_{\text{org}}$ across the T-CIE

Given terrestrial and marine organic matters commonly exhibit distinct $\delta^{13}\text{C}$ signatures, terrestrial-sourced organic carbon has the potential to influence the $\delta^{13}\text{C}_{\text{org}}$ record of marine sediments deposited across the T-CIE (Suan et al., 2015). Indeed, decomposed organic material from land plants can be easily transported into the Early Toarcian continental shelf seas due to accelerated hydrological cycle (Izumi et al., 2018) in relation to intensive continental chemical weathering (e.g., Cohen et al., 2004; Percival et al., 2016). The discrimination between marine and terrestrial organic matter can be performed by hydrogen index (HI) (e.g., Peters et al., 2005; Dembicki, 2009). In general, a HI value higher than 400 mg hydrocarbon (HC)/g TOC is indicative of the preservation of oil-prone marine organic matter (types I and II kerogen) dominated by algae and bacteria (Röhl et al., 2001). Characterizing the kerogen types by HI may be not straightforward, given high thermal volatilization can considerably contribute to lower this index (Dembicki, 2009; de Kock et al., 2017). However, the Dotternhausen black shale and limestone beds exhibiting relatively invariable HI values of ~580 mg HC/g TOC and high TOC contents of ~13 wt.% (Figure 3.4) imply that the organic matter was well preserved and of predominantly marine origin—here, bolstered by the oil shale character of the studied section (Röhl et al., 2001). Further, the Dotternhausen black shale sediments having relatively low carbon preference index (CPI) value of ~1 (Figure 3.4) attest to low contribution from terrestrial-derived organic matter (generally $\text{CPI} > 1.2$; Ruebsam et al., 2018).

The Dotternhausen black shale $\delta^{13}\text{C}_{\text{org}}$ signals can also be disturbed by recycled sediments from organic matter-rich catchment areas. In general, recycled organic matter is characteristic of high thermal maturity which can significantly alter the primarily preserved $\delta^{13}\text{C}_{\text{org}}$ values. To evaluate whether recycled organic matter exists in the Dotternhausen black shales, we here refer to molecular maturity indicators Rock-Eval T_{max} (°C) and production index (PI) from previous studies (cf. Frimmel, 2003; Frimmel et al., 2004). The persistently low T_{max} values (mean = 427 °C) together with the high HI values (Figure 6) imply that the organic matter in the Dotternhausen black shales is neither overmature nor inert. This indicates the lack of significant

contamination from recycled sediments on these Dotternhausen black shales. The possibility of sedimentary recycling can also be evaluated by inorganic proxies. For instance, recycled sediments would display a substantial increase in Zr/Sc along with a much smaller magnitude increase in Th/Sc (McLennan et al., 1993). In the crossplot of Zr/Sc versus Th/Sc (McLennan et al., 1993), though the Dotternhausen black shale samples show a slight deviation from the compositional variation trend indicative of single cycling from parent rock material, all their Zr/Sc ratios (< 10) (Figure 3.2a) are low and comparable to that of pristine provenance rocks. This pattern indirectly reveals the minimal influence from polycyclic reworking of sedimentary rocks. In addition, hydrothermal fluid carrying hydrocarbon can in part change organic-rich sedimentary rock $\delta^{13}\text{C}_{\text{org}}$ values (Pinti et al., 2009; Jiang et al., 2012). This possibility can be tested using a crossplot between sedimentary Y/Ho and Eu/Sm (Figure 3.2b; cf. Albut et al., 2018 and references therein). Yttrium is less effectively scavenged from seawater than the trivalent REE Ho, leading to high residual Y/Ho ratios in the oceans. The Y/Ho ratios of Dotternhausen black shale samples largely fall chondritic line (Y/Ho = ~28) and are similar to the modern shale average (Figure 3.2b; Albut et al., 2018 and references therein). High-temperature hydrothermal fluids are also marked by the chondritic Y/Ho ratio, but have higher Eu/Sm ratio than oceanic or continental crust due to the higher solubility of reduced divalent Eu compared to trivalent Sm. The Dotternhausen black shales having Eu/Sm ratios between 0.21 and 0.23 are in the range of the modern shale average, but are an order of magnitude lower than typical high-temperature hydrothermal fluids at mid-ocean ridges (Figure 3.2b). These observations indicate the minimal alteration from hydrothermal activity on the Dotternhausen black shale facies. In summary, the Dotternhausen black shale sample $\delta^{13}\text{C}_{\text{org}}$ values were not prominently affected by terrigenous-derived organic matter, contaminated by sedimentary recycling, and altered by hydrothermal activity.

3.2.1.2. Marine redox condition record in the Dotternhausen succession during the T-CIE

The T-CIE was marked by high-rate organic carbon production occurring in the proximal continental shelf areas of the northwestern part of Tethys margin (e.g., Frimmel et al., 2004; Schwark and Frimmel, 2004; French et al., 2014). The accelerated production of organic carbon was related to high marine productivity rate (e.g., Jenkyns, 2010; Röhl et al., 2001) arising from excessive nutrient input from

enhanced continental weathering (e.g., Cohen et al., 2004; Percival et al., 2016). Subsequently, the yielded organic matter suffered aerobic degradation during which seawater molecular oxygen was massively consumed (Röhl et al., 2001). Furthermore, the coeval strong water-column stratification and hydrological restriction have prevented efficient ventilation between bottom water and the outside open ocean, promoting the formation of oxygen-depleted benthic seawaters in the northwestern Tethys shelf-sea settings (e.g., Röhl et al., 2001; McArthur et al., 2008; Dera and Donnadieu, 2012; Hermoso et al., 2013; Ruvalcaba Baroni et al., 2018). Further, the existence of aryl isoprenoids (Figure 3.5), biomarkers for GSB (cf. Schwark and Frimmel, 2004) in the Dotternhausen black shale facies implies the coeval euxinic depositional conditions with aqueous hydrogen sulfide (H_2S) in the seawater. Such seawater redox structure is also supported by the strong authigenic enrichment of redox-sensitive elements Mo, U and V (Figure 3.3). For the Dotternhausen section, the aryl isoprenoid concentration shows a gradual increasing trend in its lower part, followed by a decreasing trend in its upper part (Figure 3.3). The GSB, which are anoxygenic autotrophs, are able to oxidize H_2S to sulfate (SO_4^{2-}) (e.g., Riccardi et al., 2007). GSB bloom will strengthen the assimilative consumption of H_2S (Hurse et al., 2008), thus lowering its concentration in the bottom anoxic/euxinic water mass and deepening the seawater sulfidic oxygen minimum zone (chemocline). Alternatively, free oxygen produced by oxygenic photosynthesizers can also oxidize H_2S under high Eh conditions and thus change the depth of the seawater chemocline. However, this possibility contradicts the fact that GSB prosperity occurred at c. 800 cm in the Dotternhausen section (Figure 3.5), considering GSB cannot thrive in oxic marine environments. To conclude, if the chemocline is defined here as a mid-depth thick water mass in which GSB progressively thrive (e.g., marked by the gradual increase in aryl isoprenoid concentration), the Dotternhausen T-CIE sediments are deposited in redox-stratified environments without a significant change in the depth of the upper limit of this chemocline (Figure 3.7). In contrast, strengthened aqueous H_2S consumption from the bottom euxinic water mass during GSB bloom (shown by maximum concentrations of aryl isoprenoid) likely deepened the lower limit of the chemocline down to or near the water-sediment interface (Figure 3.7b). This was in favor of higher fluxes of electron acceptors such as SO_4^{2-} and probably a small amount of manganese (Mn) oxyhydroxides (Figures 3.1 and 3.3) to the sediment, and thus fueled higher rate of dissimilatory reduction of SO_4^{2-} and Mn-oxyhydroxides. This

process promoted organic carbon remineralization and led to the formation of the diagenetic Unterer Stein carbonate bed.

3.2.1.3. Evidence for second-order perturbations of the Toarcian carbon cycle

Decoupled $\delta^{13}\text{C}_{\text{carb}}-\delta^{13}\text{C}_{\text{org}}$ superimposed on the T-CIE in Dotternhausen, Germany

In Earth's history carbon-cycle fluctuations such as the Mesozoic CIEs (Kuypers et al., 1999; Hesselbo et al., 2000; Kemp et al., 2005) and Neoproterozoic Snowball Earth events (Och and Shields-Zhou, 2012; Sahoo et al., 2012) were commonly accompanied by changes in sedimentary $\delta^{13}\text{C}_{\text{carb}}$ and $\delta^{13}\text{C}_{\text{org}}$ records. In general, a common means to distinguish whether one carbon-cycle event is global- or local-scale is the evaluation of the nature of the concurrently preserved sedimentary $\delta^{13}\text{C}_{\text{carb}}$ and $\delta^{13}\text{C}_{\text{org}}$ signals (Knoll et al., 1986). Unpaired $\delta^{13}\text{C}_{\text{carb}}-\delta^{13}\text{C}_{\text{org}}$ is often related to the presence of second-order local-scale carbon-cycle perturbations (e.g., Jiang et al., 2012; Meyer et al., 2013); paired $\delta^{13}\text{C}_{\text{carb}}-\delta^{13}\text{C}_{\text{org}}$ is commonly attributed to global-scale carbon cycles (e.g., Ader et al., 2009; Li et al., 2018). The Early Toarcian was marked by a global-scale addition of isotopically light carbon (CH_4 and/or CO_2) into the coeval atmosphere-ocean system, leading to wide-distributed negative CIEs recorded in the sediments of northwestern Tethys (e.g., Hesselbo et al., 2000, 2007; Svensen et al., 2007), eastern Tethys (Fu et al., 2016), southwestern Tethys (Ruebsam et al., 2020), southeastern Tethys (Newton et al., 2011; Han et al., 2018), northwestern Panthalassa (Izumi et al., 2018), and northeastern Panthalassa (Caruthers et al., 2011). If the widespread T-CIE was a global carbon-cycle event, it is expected to be accompanied by a constant $\Delta^{13}\text{C}_{\text{carb-org}}$ between DIC and DOC reservoirs. In this study, both $\delta^{13}\text{C}_{\text{carb}}$ and $\delta^{13}\text{C}_{\text{org}}$ of the Dotternhausen section show pronounced negative CIEs (Figure 3.5). Obviously $\delta^{13}\text{C}_{\text{carb}}-\delta^{13}\text{C}_{\text{org}}$ covariations have been exhibited in the lower (interval 1: 981–883 cm) and upper (interval 3: 757–613 cm) *falciferum* zone (Figures 3.8a and c) of the T-CIE interval. Intervals 1 and 3 display relatively constant $\Delta^{13}\text{C}_{\text{carb-org}}$ values of $\sim 27\text{‰}$ and $\sim 28\text{‰}$, respectively (Figures 3.5 and 3.8a), which most likely reflect global-scale carbon-cycle perturbations during the Early Toarcian. However, a prominent two-step $\delta^{13}\text{C}_{\text{carb}}-\delta^{13}\text{C}_{\text{org}}$ decoupling signature, along with two different magnitudes of decreases in $\Delta^{13}\text{C}_{\text{carb-org}}$ values, is observed around the climax of the CIE (interval 2a and 2b; Figures 3.5 and 3.8a), pointing to a local-scale carbon-cycle disturbance. The

first step in interval 2a is of smaller magnitude compared to the much larger second step in interval 2b (Figures 3.5 and 3.8a).

Possible mechanism(s) for the local-scale $\delta^{13}\text{C}_{\text{carb}}-\delta^{13}\text{C}_{\text{org}}$ decoupling

Interval 2a

The negative $\Delta^{13}\text{C}_{\text{carb-org}}$ excursion is more influenced by the variation of $\delta^{13}\text{C}_{\text{carb}}$ compared to $\delta^{13}\text{C}_{\text{org}}$ values (Figure 3.5). However, the black shale carbonate components in the interval 2a consist of biogenic calcites related to calcareous phytoplankton (Frimmel et al., 2004) and disseminated authigenic grains. The contribution of carbonate carbon from organic matter remineralization (C_{org}) and seawater inorganic carbon (C_{sw}) can be roughly estimated using the following equation (cf. Heimann et al., 2010; Konhauser et al., 2017):

$$[\text{DIC}]_{\text{total}} \times \delta^{13}\text{C}_{\text{total}} = [\text{DIC}]_{\text{org}} \times \delta^{13}\text{C}_{\text{org}} + [\text{DIC}]_{\text{sw}} \times \delta^{13}\text{C}_{\text{sw}}$$

where the $[\text{DIC}]_{\text{total}}$, $[\text{DIC}]_{\text{org}}$, and $[\text{DIC}]_{\text{sw}}$ represent total inorganic carbon, inorganic carbon derived from remineralized organic matter, and inorganic carbon from seawater, respectively; $\delta^{13}\text{C}_{\text{total}}$ and $\delta^{13}\text{C}_{\text{sw}}$ represent the $\delta^{13}\text{C}$ of total carbonate ($\delta^{13}\text{C}_{\text{carb}}$) and seawater, respectively. Assuming the Phanerozoic $\delta^{13}\text{C}_{\text{sw}}$ is near-zero (Shields and Veizer, 2002 and references therein), the calculated $[\text{DIC}]_{\text{org}}$ ($([\text{DIC}]_{\text{total}} \times \delta^{13}\text{C}_{\text{total}})/\delta^{13}\text{C}_{\text{org}}$) varies from 13 and 28 % $[\text{DIC}]_{\text{total}}$ (mean = 20 % $[\text{DIC}]_{\text{total}}$) (see Table 2 in Appendix A; Wang et al., 2020), while $[\text{DIC}]_{\text{sw}}$ has an average of 80 % $[\text{DIC}]_{\text{total}}$. This estimate can be translated by the cross-plot of $\delta^{13}\text{C}_{\text{carb}}$ versus $\delta^{18}\text{O}$ (Figure 3.9b; Konhauser et al., 2017; Ossa Ossa et al., 2018). The interval 2a samples display $\delta^{13}\text{C}_{\text{carb}}$ values between -8.8 and -4.2 ‰ and almost all of them plot above the line of $\text{C}_{\text{org}}:\text{C}_{\text{sw}} = 1:3$ (Figure 3.9b). These observations demonstrate carbonate carbon of samples in interval 2a is contributed by $[\text{DIC}]_{\text{sw}}$ (~80 %) and remineralized organic matter (~20 %) (Figure 3.9b). Organic matter remineralization through anaerobic or microaerophilic microbial processes requires electron acceptors (e.g., Heimann et al., 2010; Konhauser et al., 2017 and references therein), which here are SO_4^{2-} and possible Mn-oxyhydroxides (see section 3.2.1.2). Carbonates produced by these processes typically have lighter $\delta^{13}\text{C}_{\text{carb}}$ values compared to that of the surrounding $[\text{DIC}]_{\text{sw}}$.

Notably, the negative $\delta^{13}\text{C}_{\text{carb}}$ shift in interval 2a is concurrent with a very minor positive $\delta^{13}\text{C}_{\text{org}}$ shift (Figure 3.5). The small positive excursion in $\delta^{13}\text{C}_{\text{org}}$ can be explained by an increase in the contribution of ^{13}C -enriched GSB biomass through primary productivity (van Breugel et al., 2006; Takahashi et al., 2010). However,

considering the increase in $\delta^{13}\text{C}_{\text{org}}$ is small, it does not have a considerable influence on the negative $\Delta^{13}\text{C}_{\text{carb-org}}$ excursion in interval 2a, though this interval is representative of the initial stage of the GSB bloom. In this regard, the precipitation of carbonate components of the interval 2a black shales was in equilibrium with seawater isotope composition, but was also assisted by a small contribution of ^{12}C -enriched carbon source produced through organic matter remineralization (Figure 3.7a). This small contribution of ^{12}C likely interprets the small magnitude of the negative $\Delta^{13}\text{C}_{\text{carb-org}}$ excursion recorded in this interval.

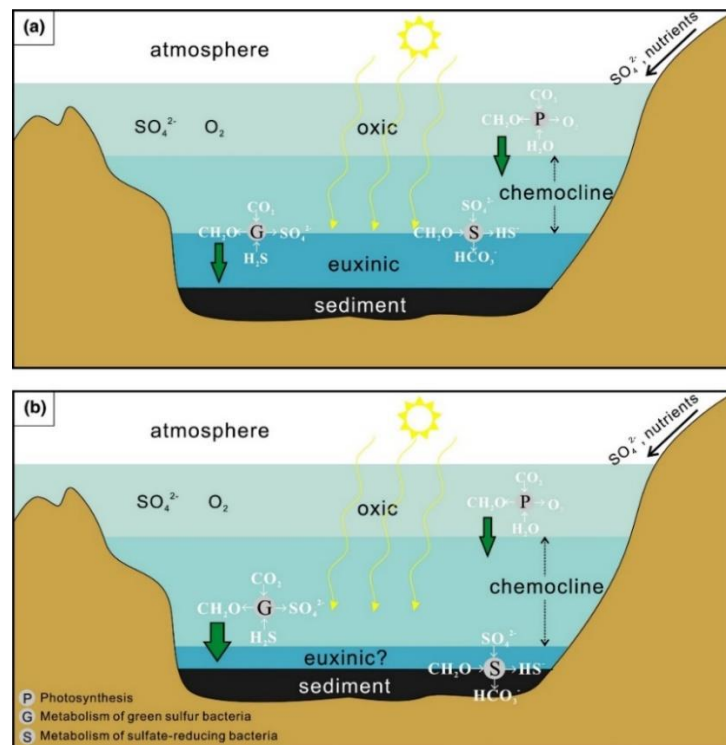


Figure 3.7. Schematic representation of the Toarcian CIE northwestern Tethys seawater column during the gradual increase of GSB activity and associated $\delta^{13}\text{C}_{\text{carb}}-\delta^{13}\text{C}_{\text{org}}$ decoupling. (a) Interval 2a: the initial stage of GSB bloom. (b) Interval 2b: the height of GSB bloom along with microbial sulfate reduction. The light, medium, and dark blue colors represent oxic, sulfidic oxygen minimum zone, and euxinic conditions, respectively, in the water column.

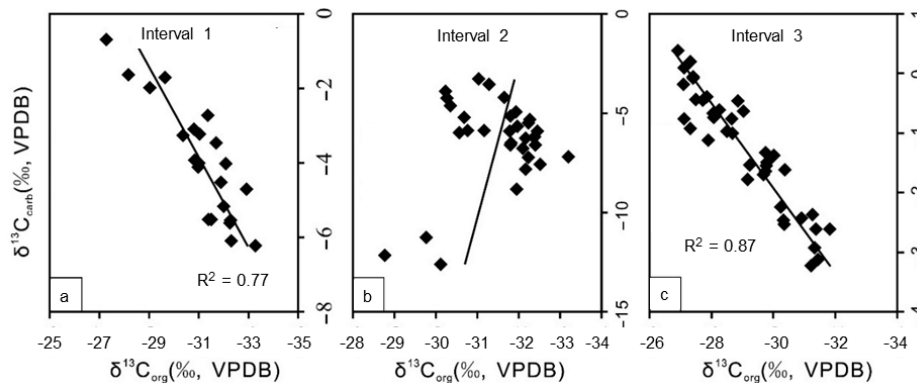


Figure 3.8. Cross-plots of $\delta^{13}\text{C}_{\text{carb}}-\delta^{13}\text{C}_{\text{org}}$ in different intervals of the Dotterhausen carbon isotopic profiles.

Interval 2b

In this interval, the negative $\Delta^{13}\text{C}_{\text{carb-org}}$ excursion is concurrently accompanied by a shift towards higher $\delta^{13}\text{C}_{\text{org}}$ and lower $\delta^{13}\text{C}_{\text{carb}}$ values (Figure 3.5). Diagenesis on organic-rich sediments has a minimal impact on their $\delta^{13}\text{C}_{\text{org}}$ values (e.g., Watanabe et al., 1997; Jiang et al., 2012), it thus cannot explain the positive $\delta^{13}\text{C}_{\text{org}}$ shift shown in interval 2b (see section 3.2.1.1). This increased $\delta^{13}\text{C}_{\text{org}}$ signal rather represents a primary C isotope composition imparted by the dominant productive marine biota. Given the GSB biomass is ^{13}C -enriched (see interval 2a), the maximum of GSB activity across the interval 2b indicated by the highest concentration of aryl isoprenoid generated more ^{13}C -enriched biomass (Figure 3.5). This process is tied to the positive $\delta^{13}\text{C}_{\text{org}}$ excursion. The $\delta^{13}\text{C}_{\text{carb}}-\delta^{13}\text{C}_{\text{org}}$ decoupling in interval 2b can thus be partly explained by the climax of GSB metabolism.

Importantly, the interval 2b contains a change in lithofacies from carbonate-bearing laminated black shales in its lowermost part to the diagenetic Unterer Stein carbonate layer upward and then back to carbonate-bearing laminated black shales (Figure 3.5). The low $\delta^{13}\text{C}_{\text{carb}}$ values of the Unterer Stein layer may primarily result from diagenetic carbonate precipitation through microbial sulfate reduction (MSR) as well as a small contribution of dissimilatory Mn-oxyhydroxides reduction (see section 3.2.1.2). Such diagenetic carbonates having low $\delta^{13}\text{C}_{\text{carb}}$ values may facilitate the negative $\Delta^{13}\text{C}_{\text{carb-org}}$ excursion in this interval (cf. Heimann et al., 2010; Konhauser et al., 2017). However, the cross-plot of $\delta^{13}\text{C}_{\text{carb}}$ versus $\delta^{18}\text{O}$ shows the limestone bed samples fall between $\text{C}_{\text{org}}:\text{C}_{\text{sw}} = 1:1$ and $\text{C}_{\text{org}}:\text{C}_{\text{sw}} = 1:2$ lines (Figure 3.9b), and the calculated $[\text{DIC}]_{\text{org}}$ changes between 38 and 42 % $[\text{DIC}]_{\text{total}}$ (41 % $[\text{DIC}]_{\text{total}}$ on average; see Table 2 in Appendix A; Wang et al., 2020). This demonstrates that a greater amount of carbonate carbon in the Unterer Stein samples were derived from organic matter remineralization, compared to those in interval 2a, although the $[\text{DIC}]_{\text{sw}}$ still served as a major carbon contributor for the Unterer Stein carbonate bed. By contrast, the black shale samples of the lowermost and upper parts of interval 2b are plotted above the $\text{C}_{\text{org}}:\text{C}_{\text{sw}} = 1:3$ line (Figure 3.9b); furthermore, the calculated $[\text{DIC}]_{\text{org}}$ with the average of 17 % $[\text{DIC}]_{\text{total}}$ indicates their carbonate carbon components were mainly derived from $[\text{DIC}]_{\text{sw}}$. It follows that the sediment pore waters or diagenetic environments where the precipitation of the diagenetic Unterer Stein bed was still in equilibrium with seawater. However, carbonate grains in the black shales in interval 2b could have precipitated either in the water column or in sediments. Therefore, the $\delta^{13}\text{C}_{\text{carb}}-\delta^{13}\text{C}_{\text{org}}$ decoupling

in the interval 2b largely resulted from a GSB bloom and was further exaggerated by authigenic carbonate (Unterer Stein) precipitation arising from organic matter remineralization (see section 3.2.1.2; Figure 3.7b).

To summarize, the coeval decreases in $\delta^{13}\text{C}_{\text{carb}}$ and increases in $\delta^{13}\text{C}_{\text{org}}$ values that lead to the two-step $\Delta^{13}\text{C}_{\text{carb-org}}$ decoupling in interval 2, reflect a joint effect of elevated GSB and sulfate-reducing bacteria (SRB) activities (Figure 3.7). The GSB bloom resulted in high consumption of H_2S from the ambient euxinic bottom water and likely depended the chemocline near to the water-sediment interface. This allowed higher SO_4^{2-} flux to the anoxic sediment pore waters and ultimately led to authigenic carbonate precipitation assisted by higher rates of SRB-induced organic matter remineralization. In contrast, the following coeval increase in $\delta^{13}\text{C}_{\text{carb}}$ and decrease in $\delta^{13}\text{C}_{\text{org}}$ values, which ended this two-step $\Delta^{13}\text{C}_{\text{carb-org}}$ decoupling in the upper part of interval 2b, were mainly caused by a decline of GSB activity as a consequence of exhausted H_2S availability in the water column. However, interval 2b represents the peak of the GSB bloom and explains the larger $\Delta^{13}\text{C}_{\text{carb-org}}$ decoupling in this interval compared to the lower 2a. Interestingly, this GSB bloom in interval 2 might have consumed enough H_2S in the T-OAE water column to re-establish environmental conditions favorable for increased expansion of aerobic metabolisms, that is, oxygenic photosynthesis, and ultimately trigger the progressive recovery to the end of the T-CIE shown in the overlying interval 3 (Figure 3.5).

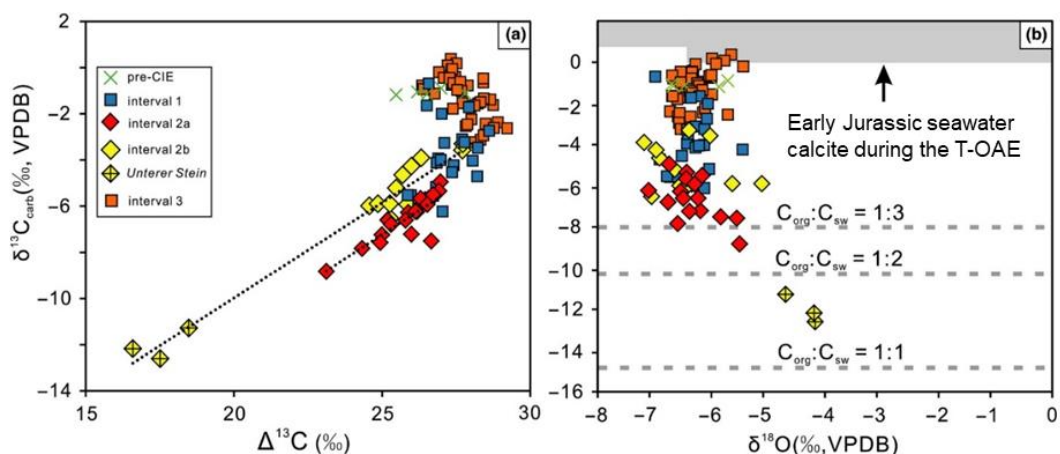


Figure 3.9. Cross-plots of $\delta^{13}\text{C}_{\text{carb}}$ vs $\Delta^{13}\text{C}$ (a) and $\delta^{13}\text{C}_{\text{carb}}$ vs $\delta^{18}\text{O}$ (b) for different sedimentary intervals in the Dotterhausen. (a) The interval 2a (black shales) and 2b (Unterer Stein and black shales) show strong correlations between $\delta^{13}\text{C}_{\text{carb}}$ and $\Delta^{13}\text{C}$. (b) A model showing the carbonate carbon contribution between organic matter oxidation (C_{org}) and seawater inorganic carbon (C_{sw}) (cf. Heimann et al., 2010; Konhauser et al., 2017). The isotope composition of Early Jurassic seawater calcites during the T-OAE interval were estimated from the belemnites ($\delta^{13}\text{C}_{\text{bel}}$: ~ 0 to $+2$ ‰ and $\delta^{18}\text{O}_{\text{bel}}$: ~ -6 to 0 ‰; Ullmann et al., 2014) and platform limestone ($\delta^{13}\text{C}_{\text{limestone}}$: $\sim +1$ to $+2$ ‰ and $\delta^{18}\text{O}_{\text{limestone}}$: ~ -8 to -5 ‰; Han et al., 2018).

3.2.1.4. Implication for ecosystem structure on local-scale carbon-cycle perturbation

Marine sedimentary co-varying $\delta^{13}\text{C}_{\text{carb}}-\delta^{13}\text{C}_{\text{org}}$ is commonly related to primary (photosynthetic) production and insignificant post-depositional alteration (cf. Jiang et al., 2012). Here, it has been shown that a rapid carbon-cycle perturbation induced by intense GSB activity is able to decouple the primary $\delta^{13}\text{C}_{\text{carb}}$ and $\delta^{13}\text{C}_{\text{org}}$ signals. In Earth's history, the dramatic rise in GSB activity occurred not only in T-OAE epicontinental seas (Sælen et al., 2000; Röhl et al., 2001; Pancost et al., 2004; Schwark and Frimmel, 2004; van Breugel et al., 2006; Xu et al., 2018), but also in plenty of ancient marine realms during the end-Ordovician, end-Devonian, end-Permian and end-Triassic mass extinctions forced by increased seawater H_2S (e.g., Joachimski et al., 2001; Riccardi et al., 2007; Richoz et al., 2012). These mass extinctions accompanied by decoupled $\delta^{13}\text{C}_{\text{carb}}-\delta^{13}\text{C}_{\text{org}}$ signals broadly corresponds to elevated GSB activities (van de Schootbrugge and Gollner, 2013b and references therein), hinting the role of GSB in disturbing the coeval carbon cycles. Therefore, to comprehensively understand factors for decoupling sedimentary $\delta^{13}\text{C}_{\text{carb}}$ and $\delta^{13}\text{C}_{\text{org}}$, carbon-cycle turnover resulting from an abrupt GSB proliferation may play a crucial role and should be further considered.

3.2.1.5. Tethys-wide but locally variable second-order perturbations of the Toarcian carbon cycle

In theory, $\delta^{13}\text{C}_{\text{carb}}-\delta^{13}\text{C}_{\text{org}}$ coupling is expected in all existing T-CIE sedimentary sections owing to the global-scale Early Toarcian carbon event. In contrast to this expectation, $\delta^{13}\text{C}_{\text{carb}}-\delta^{13}\text{C}_{\text{org}}$ decoupling (yellow areas in Figure 3.10a and yellow squares in Figure 3.10b) is also observed in other T-CIE sections Bilong Co (eastern Tethys: Fu et al., 2016), Sancerre (northwestern Tethys: Hermoso et al., 2012), and Nianduo (southeastern Tethys: Han et al., 2018). The observations imply the pervasive existence of second-order carbon-cycle perturbations in oxygen-depleted (anoxic/euxinic) restricted and unrestricted depositional settings throughout the Tethyan margin during the T-CIE. Both, the Bilong Co and Sancerre sections, show $\delta^{13}\text{C}_{\text{carb}}-\delta^{13}\text{C}_{\text{org}}$ coupling below and above the decoupling interval (blue and orange areas in Figure 3.10a; blue and orange squares in Figure 3.10b), which is similar to that of the Dotternhausen section. In contrast, such coupled $\delta^{13}\text{C}_{\text{carb}}-\delta^{13}\text{C}_{\text{org}}$ intervals

(Figure 3.10c) are not shown in the Nianduo CIE profile, hinting persistent local-scale carbon cycles throughout the entire T-CIE interval.

Notably, the $\delta^{13}\text{C}_{\text{carb}}$ profiles of these T-CIE sections are obviously different from one another, and so are the $\delta^{13}\text{C}_{\text{org}}$ profiles (Figures 3.5 and 3.10). Intriguingly, $\delta^{13}\text{C}_{\text{carb}}$ and $\delta^{13}\text{C}_{\text{org}}$ decoupling of these T-CIE sections also behave very differently (Figures 3.5 and 3.10), even Dotternhausen and Sancerre T-CIE sections were deposited in adjacent sites (NW-Tethys). Specifically, $\delta^{13}\text{C}_{\text{org}}$ in the decoupled part of the Sancerre section (NW-Tethys) is relatively constant, while $\delta^{13}\text{C}_{\text{carb}}$ shows obvious decreasing and then increasing trends (Figure 3.10). In the decoupled part of the Dotternhausen section (NW-Tethys), $\delta^{13}\text{C}_{\text{org}}$ shows a positive excursion, whereas the coincident $\delta^{13}\text{C}_{\text{carb}}$ displays a negative excursion (Figure 3.5). This stratigraphic carbon isotopic difference for the two T-CIE sections may be associated with their restricted depositional conditions (McArthur et al., 2008; Ruvalcaba Baroni et al., 2018; McArthur, 2019). However, further detailed work beyond the scope of this study is required to unravel $\delta^{13}\text{C}_{\text{carb}}-\delta^{13}\text{C}_{\text{org}}$ decoupling patterns, if present, in T-CIE sections.

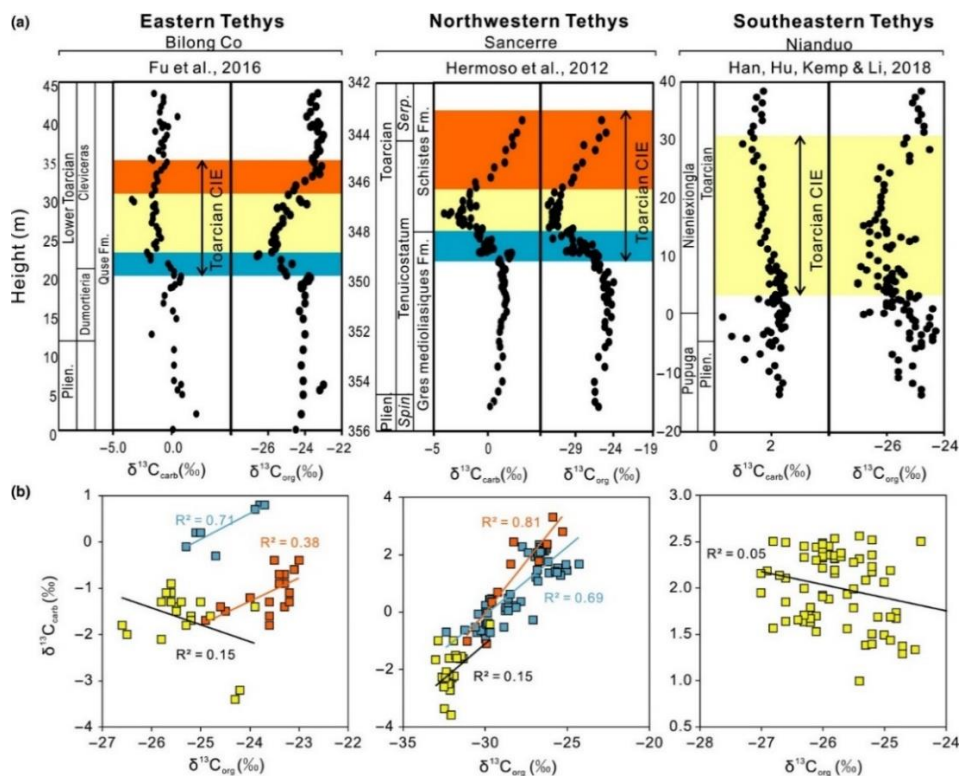


Figure 3.10. $\delta^{13}\text{C}_{\text{carb}}-\delta^{13}\text{C}_{\text{org}}$ decoupling signals (yellow areas in panel a and yellow squares in panel b) from geographically distinct localities (Bilong Co in eastern Tethys, Fu et al., 2016; Sancerre in northwestern Tethys, Hermoso et al., 2012; Nianduo in southeastern Tethys, Han et al., 2018) are identified across the Toarcian CIE shown in panel a. Blue and orange colors in both panel a and b standing for the observed coupled $\delta^{13}\text{C}_{\text{carb}}-\delta^{13}\text{C}_{\text{org}}$ signals across the Toarcian CIE are comparable to the marked interval 1 and 3 in the studied Dotternhausen section. Fm., formation; Plien., Pliensbachian; Serp., Serpentinum; Spin., Spinatum.

3.2.2. Restricted oxygen-deficient basins on the northern European epicontinental shelf across the T-CIE

3.2.2.1. Evaluation of primary N isotopic signals

Organic matter from land plants through continental weathering may be an additional N source and thus impact sedimentary N isotope composition. Organic-lean grey shales in the studied Dotternhausen section from the depth of 1050 to 980 cm (Figure 1.2) were deposited before the T-CIE interval. These grey shale samples contain high amounts of land plant-derived organic matter, which is inferred from the low HI values (< 400 mg hydrocarbon (HC)/g TOC) and high oxygen index (OI) values (up to 100 mg CO_2 /g TOC) (cf. Röhl et al., 2001; Frimmel et al., 2004; Wang et al., 2020). By contrast, the T-CIE organic-rich black shales from the depth of 986 to 600 cm in this section (Figure 1.2) were of primarily marine origin (Röhl et al., 2001; Frimmel et al., 2004; Wang et al., 2020) and thus can be used to reconstruct marine N biogeochemical cycling during the T-CIE.

The $\delta^{15}\text{N}$ of sedimentary rocks is a robust proxy to dictate the primary biomass signal of living organisms if it is, in substance, not altered by allochthonous inorganic N, diagenesis, metamorphism or metasomatism (e.g., Ader et al., 2006; Stüeken et al., 2016). Nitrogen in sedimentary rocks mainly exists in organic- and clay-bound forms (mainly as ammonium (NH_4^+)). A high fraction of inorganic N (NH_4^+) has the potential to substantially influence organic-bound $\delta^{15}\text{N}$, which is especially true of organic-lean sediments (e.g., Schubert and Calvert, 2001). The Dotternhausen T-CIE samples having high TOC content (15.6 wt.% on average) (see Tables 2 and 3 in Appendix A and B, respectively; Wang et al., 2020, 2021) demonstrate the minimal alteration on the primary $\delta^{15}\text{N}$ by inorganic N. In the cross-plot of TOC versus TN_{bulk} ($R^2 = 0.43$; $p = 0.00$; Figure 3.11a) for the Dotternhausen T-CIE samples, the positive correlation indicates that most N was sourced from marine organic matter. Further, the absence of correlation between TN_{bulk} and detrital indicator Al concentration (Figure 3.11b) implies the negligible N contribution from detrital input.

The release of NH_4^+ arising from organic matter remineralization in diagenetic environments can in part affect the $\delta^{15}\text{N}_{\text{bulk}}$ values. For example, oxic diagenetic processes are able to cause an obvious increase in $\delta^{15}\text{N}_{\text{bulk}}$ values by ~ 4 ‰, while anoxic diagenesis is often accompanied by a negligible isotopic fractionation of < 1 ‰ (Altabet et al., 1999; Ader et al., 2006; Stüeken et al., 2016). In this study, early diagenetic alteration on the $\delta^{15}\text{N}_{\text{bulk}}$ values of the Dotternhausen T-CIE samples can

be discounted. This is because these samples are enriched in TOC, prone to anoxic diagenesis, and were deposited in redox-stratified settings with oxic surface and euxinic bottom waters (Röhl et al., 2001; Schwark and Frimmel, 2004; Wang et al., 2020) which further impeded oxic diagenesis. This inference is also evidenced by the lack of negative correlations of $\delta^{15}\text{N}_{\text{bulk}}$ versus TOC and $\delta^{13}\text{C}_{\text{org}}$ versus TOC (Figures 3.11c and d) which are often expected following early diagenetic alteration processes (e.g., Wang et al., 2018).

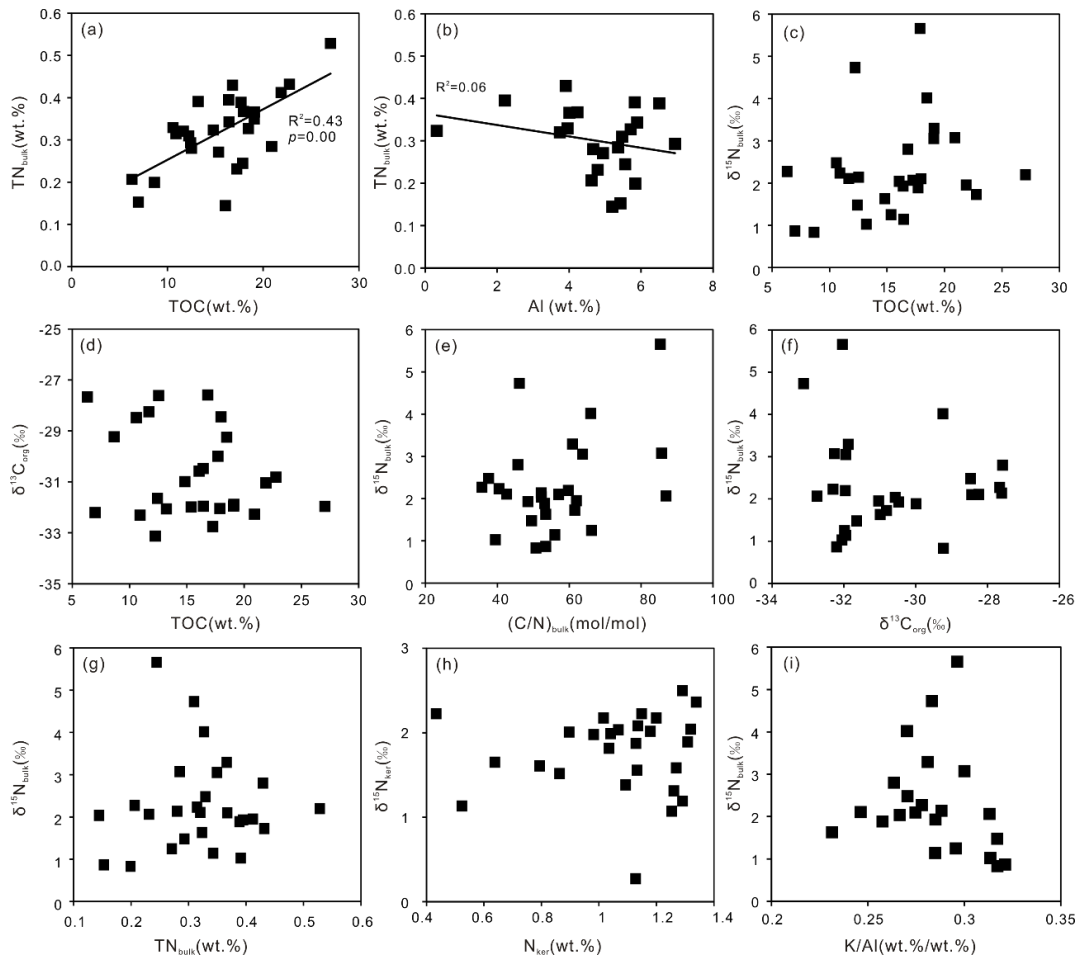


Figure 3.11. Cross-plots of geochemical data for the Dotternhausen T-CIE samples. Data show: (a) TN_{bulk} vs. TOC, (b) TN_{bulk} vs. Al, (c) $\delta^{15}\text{N}_{\text{bulk}}$ vs. TOC, (d) $\delta^{13}\text{C}_{\text{org}}$ vs. TOC, (e) $\delta^{15}\text{N}_{\text{bulk}}$ vs. $(\text{C}/\text{N})_{\text{bulk}}$, (f) $\delta^{15}\text{N}_{\text{bulk}}$ vs. $\delta^{13}\text{C}_{\text{org}}$, (g) $\delta^{15}\text{N}_{\text{bulk}}$ vs. TN_{bulk} , (h) $\delta^{15}\text{N}_{\text{ker}}$ vs. N_{ker} , and (i) $\delta^{15}\text{N}_{\text{bulk}}$ vs. K/Al . The data of Al and K concentrations are from Wang et al. (2020). R^2 represents the coefficient of the determination of the covariation.

Thermal devolatilization of organic matter owing to processes of burial diagenesis and metamorphism tends to preferentially release organic-bound ^{14}N , resulting in an increase in $\delta^{15}\text{N}_{\text{bulk}}$ by 1 to 2 ‰ for greenschist facies, 3 to 4 ‰ for lower amphibolite facies, and up to 6 to 12 ‰ for upper amphibolite facies (e.g., Ader et al., 2006). However, for the Dotternhausen T-CIE samples, it has been constrained that their organic matter was well preserved and did not obviously suffer thermal volatilization

(Wang et al., 2020), implying a negligible rise in their $\delta^{15}\text{N}_{\text{bulk}}$ values. On the other hand, thermal volatilization causing preferential release of ^{14}N is typically accompanied by positive covariations of $\delta^{15}\text{N}_{\text{bulk}}$ versus $(\text{C}/\text{N})_{\text{bulk}}$ and $\delta^{15}\text{N}_{\text{bulk}}$ versus $\delta^{13}\text{C}_{\text{org}}$, and negative covariations of $\delta^{15}\text{N}_{\text{bulk}}$ versus TN_{bulk} and $\delta^{15}\text{N}_{\text{ker}}$ versus N_{ker} (Ader et al., 2006, 2016; Kipp et al., 2018; Mettam et al., 2019). No such covariations (Figures 3.11e, f, g and h) again demonstrate the negligible alteration from systematic burial diagenetic or metamorphic processes on the primary N isotope signals of the Dotternhausen T-CIE samples. Furthermore, organic-bound NH_4^+ can be substituted by externally fluid-sourced potassium ions (K^+) due to equal charge and similar sizes through metasomatism, and thus primary $\delta^{15}\text{N}_{\text{bulk}}$ records can be altered (Ader et al., 2016; Stüeken et al., 2016). However, the scarcity of a correlation between $\delta^{15}\text{N}_{\text{bulk}}$ and K/Al (Figure 3.11i) excludes this possibility.

Additionally, $\delta^{15}\text{N}_{\text{ker}}$ can be used to calibrate and evaluate the preservation extent of the primarily deposited N isotope signal imparted by the originally sinking biomass (e.g., Ader et al., 2016; Stüeken et al., 2016, 2017; Kipp et al., 2018). Most of the Dotternhausen T-CIE samples exhibits an overall minimal offset between $\delta^{15}\text{N}_{\text{bulk}}$ and $\delta^{15}\text{N}_{\text{ker}}$ ($\Delta^{15}\text{N}_{\text{bulk-ker}} = \delta^{15}\text{N}_{\text{bulk}} - \delta^{15}\text{N}_{\text{ker}}$, $0.2 \pm 0.8 \text{ ‰}$; average ± 1 standard deviation), excluding three samples (DH-836, DH-825 and DH-729) with high $\delta^{15}\text{N}_{\text{bulk}}$ values (up to $+5.7 \text{ ‰}$), where the offset is up to $+4.1 \text{ ‰}$ (Figure 3.12; see Table 1 in Appendix B; Wang et al., 2021). The primary N isotope signals of these three samples were likely affected by locally small-scale post-depositional modifications (Ader et al., 2016; Stüeken et al., 2017; Kipp et al., 2018) and will thus be excluded for further discussion. By contrast, the Dotternhausen samples with minimal $\delta^{15}\text{N}_{\text{bulk}}-\delta^{15}\text{N}_{\text{ker}}$ offset mostly likely have preserved their primary N isotope signals.

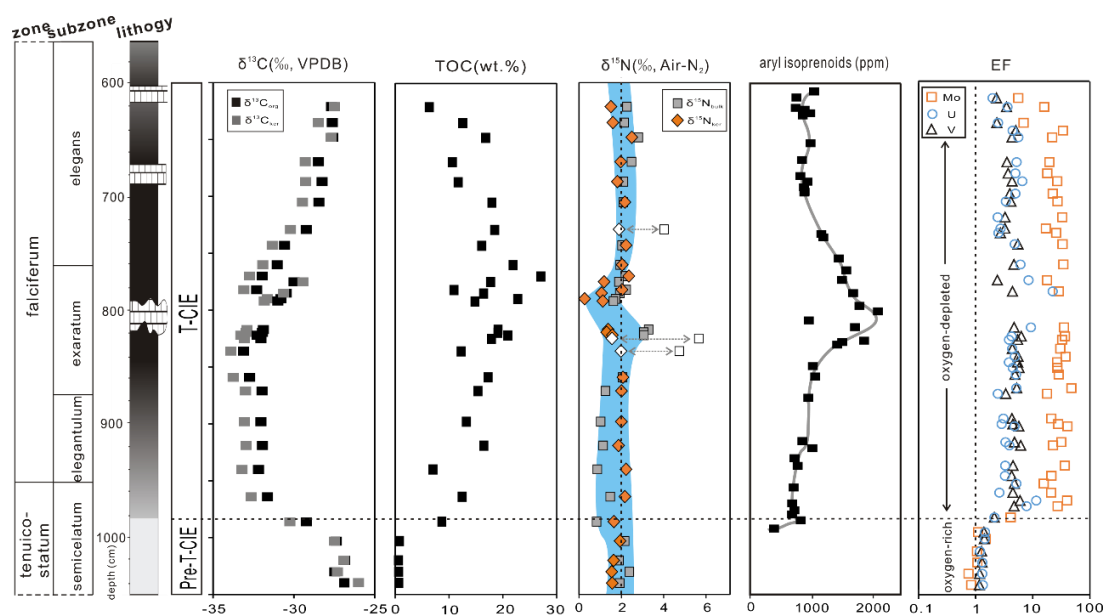


Figure 3.12. Chemostratigraphic $\delta^{13}\text{C}$, total organic carbon (TOC) content, $\delta^{15}\text{N}$, aryl isoprenoid content and enrichment factors (EFs) of Mo, V and U for Dotternhausen sedimentary section. Reliable N isotope values for the Dotternhausen samples are denoted in the $\delta^{15}\text{N}$ panel using a blue shading. The white diamonds and squares in the $\delta^{15}\text{N}$ panel denote the excluded samples that have large offsets between $\delta^{15}\text{N}_{\text{bulk}}$ and $\delta^{15}\text{N}_{\text{ker}}$ (see section 3.2.2.1 for detailed discussion). The data of aryl isoprenoid content are from Schwark and Frimmel (2004). The Mo, V, U and AI concentration data are from Wang et al. (2020). The EF is calculated relative to upper continental crust (UCC; McLennan, 2001) using the equation of $[(\text{element}/\text{Al})_{\text{sample}}/(\text{element}/\text{Al})_{\text{UCC}}]$.

3.2.2.2. Marine N biogeochemical cycling during the Dotternhausen T-CIE

Well preserved primary N isotope compositions of sedimentary organic matter can act as an effective indicator for reconstructing the input (e.g., diazotrophy, an atmospheric N_2 fixation metabolism using metal-based nitrogenase enzymes) and output (e.g., denitrification and/or anammox) fluxes of bioavailable N in marine environments. Diazotrophy through Mo-based nitrogenase is the most representative form of N_2 fixation in natural environments (Tyrrell, 1999; Stüeken et al., 2016). In Mo-limited marine settings, V- or iron (Fe)-based nitrogenase can alternatively be used by N_2 fixation. Culture experiments have shown that the expression of N_2 fixation through Mo- versus alternative-based nitrogenase can be discriminated by the produced biomass N isotope compositions (Bauersachs et al., 2009; Zhang et al., 2014). In these experiments, biomass related to the Mo-based diazotrophy has $\delta^{15}\text{N}$ values between -4 and $+2$ ‰, whereas biomass associated with alternative nitrogenase yields $\delta^{15}\text{N}$ values as low as -7 ‰. In the modern ocean, aerobic N cycle is dominated by largely quantitative nitrification and partial denitrification and/or anammox in OMZs. This process preferentially releases isotopically light N, leaving the remaining deep ocean

NO_3^- pool higher $\delta^{15}\text{N}$ with an average of $\sim +5\text{‰}$ (e.g., Tesdal et al., 2013; Sigman and Fripiat, 2019). Biomass preserves this signature in marine sediments. Therefore, in ancient sedimentary rocks, $\delta^{15}\text{N}$ values ranging between -4 and $+2\text{‰}$ can be attributed to the dominant operation of Mo-based diazotrophy, whereas higher $\delta^{15}\text{N}$ of $> +3\text{‰}$ indicates water-column partial denitrification and/or anammox (e.g., Garvin et al., 2009; Stüeken et al., 2016; Gilleaudeau et al., 2020).

In the Dotternhausen section, the initiation of the T-CIE coincides with the onset of the authigenic enrichment of redox-sensitive elements Mo, V and U (expressed by enrichment factors (EFs); Figure 3.12). These elements are more soluble and less particle-reactive under oxygen-rich seawater states, which tends not to express authigenic enrichment in the oxic sediments; on the other hand, these elements are less soluble and more particle-reactive under oxygen-depleted seawater conditions, which can result in substantially authigenic accumulation of sedimentary Mo, V and U (Algeo and Maynard, 2004; Tribouillard et al., 2006). The obvious authigenic enrichment of the Mo, V and U for the Dotternhausen T-CIE samples is thus indicative of the development of euxinic bottom-water conditions at that time. Furthermore, an obvious correlation between the height of the T-CIE curve and aryl isoprenoid concentration (see Figure 3.12; Wang et al., 2020) implies the peak of the T-CIE corresponds to the highest level of euxinic water column conditions. Evidence for the marine anoxia during the T-CIE was traditionally described to reflect the T-OAE (e.g., Pearce et al., 2008; Thibault et al., 2018).

For the Dotternhausen shale samples, both $\delta^{13}\text{C}$ for TOC and separated kerogen (expressed by $\delta^{13}\text{C}_{\text{org}}$ and $\delta^{13}\text{C}_{\text{ker}}$) exhibit comparable negative excursion, reaching minima of -33.1‰ and -33.4‰ , respectively (Figure 3.12; see Table 1 in Appendix B; Wang et al., 2021). Their $\delta^{15}\text{N}$ values are primarily in the range between $+0.3$ and $+2.5\text{‰}$ (average ± 1 standard deviation; $\delta^{15}\text{N}_{\text{bulk}} = +2.0 \pm 0.6\text{‰}$ and $\delta^{15}\text{N}_{\text{ker}} = +1.8 \pm 0.5\text{‰}$) (Figure 3.12; see Table 1 in Appendix B; Wang et al., 2021). Across the T-CIE, the bottom-water euxinia led to the occurrence of water-column denitrification and/or anammox at the redoxcline (Figure 3.13). However, the reliable $\delta^{15}\text{N}$ values ranging from $+0.3$ to $+2.5\text{‰}$ observed in the uppermost *tenuicostatum* and lower *falciferum* zones (Figure 3.12) do not reflect the isotope effect of water-column partial denitrification and/or anammox (typically $> +3\text{‰}$; cf. Garvin et al., 2009; Stüeken et al., 2016; Gilleaudeau et al., 2020). By contrast, such a N isotope signal is consistent with Mo-based diazotrophy occurring under N-limited conditions. The severe shortage

of bioavailable N in the coeval depositional environment resulted from quantitative denitrification and/or anammox by which no isotopic effect was imparted. The other possibility is similar to the modern Black Sea in which although anoxic bottom waters may have contained high abundance of dissolved N, the very weak exchange between bottom- and surface-waters likely caused N scarcity for organisms in surface waters. Cyanobacteria thus enhanced the N_2 fixation rate to compensate this famine bioavailable N, here characteristic of the absence of any large isotopic change. Notably, in the middle of the *exaratum* subzone of the Dotternhausen section, there is a small negative $\delta^{15}N$ excursion to ~ 0 ‰ (Figure 3.12). This N isotopic depletion corresponds to the highest level of bottom-water euxinia (Schwark and Frimmel, 2004; Wang et al., 2020) and may thus be caused by elevated Mo-based N_2 fixation capturing more atmospheric N_2 (~ 0 ‰) (Figure 3.13). Given this small negative excursion in $\delta^{15}N$ coincides with highest aryl isoprenoid abundance, it may thus be, alternatively, tied to enhanced contribution of ^{14}N -enriched GSB biomass (Fogel and Cifuentes, 1993; Schwark and Frimmel, 2004) (Figures 3.12 and 3.13). Nevertheless, bioavailable N famine occurring in surface waters was as a consequence of N loss to the atmosphere (through quantitative denitrification and/or anammox) and/or the lack of bottom- and surface-water exchange across the Dotternhausen T-CIE interval. In this view, atmospheric N_2 was substantially fixed through Mo-based diazotrophs to keep pace with this seawater N scarcity.

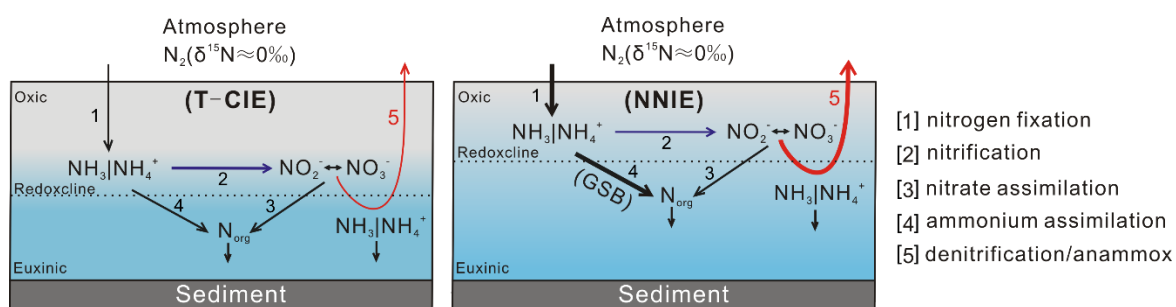


Figure 3.13. Schematic sketch showing N biogeochemical cycling in the Dotternhausen depositional setting across the T-CIE interval. During the maximum anoxia at the height of T-CIE (NNIE), thicker black arrows in [1] and [4] indicate enhanced nitrogen fixation and ammonium assimilation, respectively, while thicker red arrow in [5] denotes quantitative denitrification and/or anammox. NNIE: negative nitrogen isotope excursion (see Figure 3.12). GSB: green sulfur bacteria.

3.2.2.3. Can the northern European epicontinental shelf settings be invoked to validate an evolved oceanic anoxic event during the T-CIE?

Sedimentary sections deposited during the T-CIE on the northern European epicontinental shelf are generally characteristic of high TOC concentration (e.g., Jenkyns, 2010). In addition to modern hydrographically restricted environments (e.g., Black Sea), organic-rich sediments are also distributed in upwelling (unrestricted)-induced OMZ settings (Little et al., 2016) in which water-column partial denitrification and/or anammox exists (Lam and Kuypers, 2011). By contrast, the Dotternhausen T-CIE organic-rich black shales were deposited in settings with water-column quantitative denitrification and/or anammox (see section 3.2.2.2). This finding convincingly demonstrates that during the T-CIE interval the Dotternhausen organic-rich black shales were deposited in a restricted regime with minimal bottom- and surface-water exchange. Such nature of water-mass restriction heavily prevented bottom waters or open ocean from supplying bioavailable N and thus extremely limited NO_3^- inventory existed in surface waters. The minor amount of NO_3^- was ultimately quantitatively consumed when the water column became extensively euxinic throughout the T-CIE (Schwark and Frimmel, 2004). The reduced N species of NH_4^+ acquired via N_2 fixation therewith succeeded NO_3^- as the main bioavailable N form. In NH_4^+ -replete environments, NH_4^+ assimilation by organisms is generally accompanied by a large isotope fractionation (-27 to -4 ‰), followed by the formation of low biomass $\delta^{15}\text{N}$ values (e.g., Higgins et al., 2012; Stüeken et al., 2016). However, this possibility is apparently conflicting with the Dotternhausen T-CIE $\delta^{15}\text{N}$ values ($+0.3$ to $+2.5$ ‰) (Figure 3.12). It further implies that the ecosystem assimilating this newly fixed N was too small to outbalance the $\delta^{15}\text{N}$ values of the preserved biomass due to a restricted depositional setting. An analog having such restricted environments is the Black Sea across the Holocene during which N_2 fixation occurred prevalently and the produced biomass exhibited $\delta^{15}\text{N}$ values of ~ 0 to $+2$ ‰ stimulated by bioavailable N deficit (Tyrrell, 1999; Fulton et al., 2012). Such scenario can also be found in Archean and mid-Proterozoic marine environments (cf. Stüeken et al., 2016; Ossa Ossa et al., 2019).

In this study, $\delta^{15}\text{N}_{\text{bulk}}$ data were compiled from multiple T-CIE sections including Rietheim (Switzerland), Réka Valley (Hungary), Yorkshire (UK), Winterborne Kingston (UK) and Mochras (UK) deposited on the northern European epicontinental shelf and are in the range between -4 and $+2$ ‰ (Figure 3.14). However, a pelagic T-CIE section

from Dogna (Italy) shows a slightly larger $\delta^{15}\text{N}_{\text{bulk}}$ variation (-3 to $+4$ ‰) (Figure 3.14). The deposition of the Dogna T-CIE section was related to be unstable redox conditions (Dickson et al., 2017). Nevertheless, $\delta^{15}\text{N}$ values up to $+4$ ‰ from this Dogna T-CIE section is possibly associated with NO_3^- assimilation or water-column partial denitrification and/or anammox in OMZs elsewhere in a likely oxygenated Tethyan Sea (see review from Ader et al., 2016). Notably, the $\delta^{15}\text{N}$ values of other T-CIE sections from the shallow shelf settings fall in the range of Mo-based N_2 fixation. This N_2 -fixation record is in contrast to the existence of water-column partial denitrification and/or anammox in unrestricted settings ($\delta^{15}\text{N}$ values typically $> +3$ ‰; e.g., Garvin et al., 2009; Ader et al., 2016; Stüeken et al., 2016; Gilleaudeau et al., 2020), but is in line with redox-controlled N biogeochemical cycle in restricted environments.

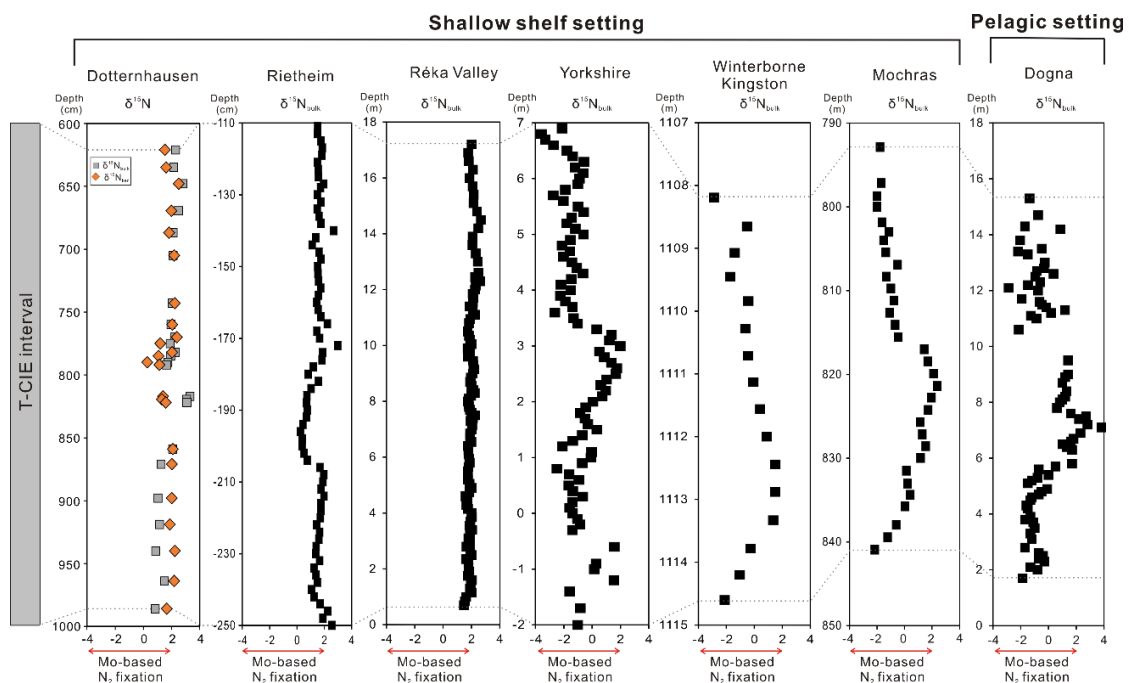


Figure 3.14. Comparison of $\delta^{15}\text{N}$ records among multiple T-CIE sections. The $\delta^{15}\text{N}_{\text{bulk}}$ data of Rietheim (Switzerland) and Réka Valley (Hungary) sections are from Montero-Serrano et al. (2015) and Ruebsam et al. (2018), respectively. The $\delta^{15}\text{N}_{\text{bulk}}$ data of Yorkshire (represented by Hawsker Bottom; UK), Winterborne Kingston (UK), Mochras (UK) and Dogna (Italy) sections are from Jenkyns et al. (2001).

To confirm the scenario of water-mass restriction for the northern European epicontinental shelf during the T-CIE, organic-rich sediment Mo/TOC mass ratio from this shelf setting was used here. This indicator is based on the observation that the slope of the Mo vs. TOC regression line is low at ~ 4.5 $\mu\text{g/g/wt.}\%$ (Figure 3.15a) for modern Black Sea organic-rich sediments deposited under severely restricted conditions with very slow water-mass renewal rates (Algeo and Lyons, 2006). The low slope value of the Mo vs. TOC regression line is attributed to basin-scale aqueous Mo

drawdown along with limited resupply. When hydrographic restriction decreases, the increased open ocean water-mass renewal replenishes Mo and thus will result in a high slope value in organic-rich marine sediments. Slopes in Mo vs. TOC space for T-CIE sections are very variable (0.4-1.1 $\mu\text{g/g/wt.}\%$), and are lower than ~ 4.5 $\mu\text{g/g/wt.}\%$, indicating that their depositional settings during the T-CIE were even more restricted than those of the modern Black Sea (Figure 3.15a). Given dissolved Mo drawdown is very fast when abundant aqueous H_2S is present (Algeo and Maynard, 2004; Reinhard et al., 2013), the persistently high authigenic enrichment of Mo throughout the entire Dotternhausen T-CIE section (Figure 3.12) implies limited but permanent Mo feeding from a larger oxic Mo reservoir, i.e., open ocean (Algeo and Lyons, 2006). The absence of evidence for quantitative Mo drawdown in pelagic Tethyan black shales from the Dogna section demonstrates that Mo likely remained dissolved in coeval oxic seawater, and their light $\delta^{98}\text{Mo}$ values (Dickson et al., 2017) further support that the water column, at least at the site of deposition, was not anoxic and sulfidic (euxinic) during the T-CIE. This may explain why the Dogna section did not record the N isotopic effect of water-column denitrification and/or anammox at the site of the deposition, though the water-column of deposition was neither euxinic nor sulfidic oxygen-depleted (OMZ).

In addition, it has been proposed that a cross-plot of cadmium (Cd)/Mo versus manganese*cobalt (Mn*Co) for modern high-TOC marine sediments can be used to evaluate water-mass restriction conditions (Figure 3.15b; cf. Sweere et al., 2016, 2020). In upwelling (unrestricted) regions, organic-rich sediments are generally characteristic of high Cd/Mo ratios (> 0.1) due to high Cd uptake in organic matter relative to Mo (Conway and John, 2015). In restricted settings, though seawater oxygen depletion is favourable for Cd and Mo deposition, relatively low-rate marine productivity is not conducive to organic-driven Cd output, eventually leading to low sedimentary Cd/Mo ratios (< 0.1) (Sweere et al., 2016 and references therein). Rivers and/or surface seawaters are significantly enriched in Co and Mn abundances compared to open-ocean sub-surface waters which feed upwelling systems. In this regard, restricted marine settings typically display high Co and Mn concentrations (Sweere et al., 2016 and references therein). The distinct geochemical behaviours of Co and Mn ultimately lead to high CoxMn values (> 0.4 $\mu\text{g/g*wt.}\%$) for organic-rich sediments in restricted depositional environments, while low CoxMn values (< 0.4 $\mu\text{g/g*wt.}\%$) for the counterpart from upwelling (unrestricted) settings. A CoxMn versus

Cd/Mo cross-plot shows the representative Dotternhausen and Yorkshire T-CIE section samples fall in the restricted area (Figure 3.15b). This observation further implies hydrographically restricted water-mass conditions for the northern European epicontinental shelf seas during the T-CIE.

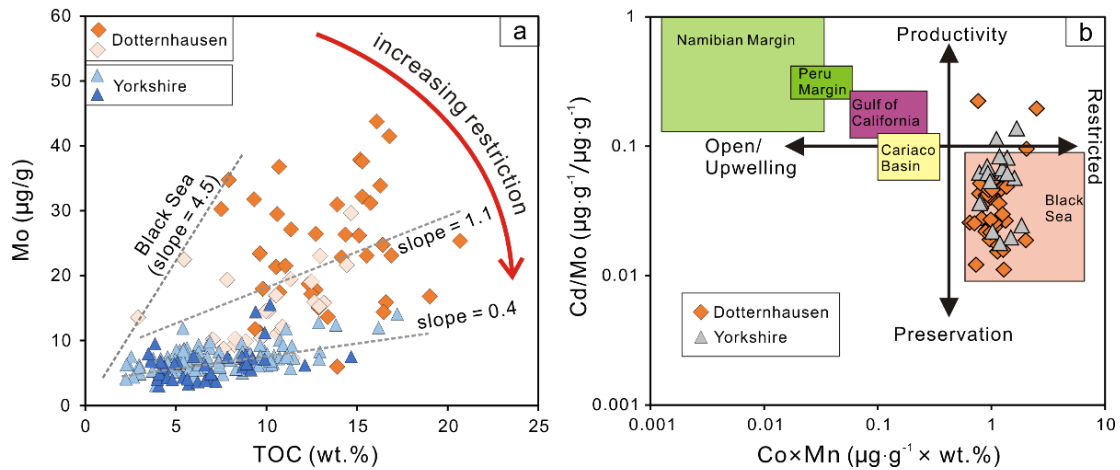


Figure 3.15. Cross-plots of Mo vs. TOC contents (a) and Cd/Mo vs. Co x Mn (b) for Dotternhausen and Yorkshire T-CIE organic-rich samples. a: The lower the slope the more depleted is the aqueous Mo reservoir due to hydrographically restricted water-mass circulation in coeval depositional settings (Algeo and Lyons, 2006). b: the values of Cd/Mo and Co x Mn for modern organic-rich sediments from distinct depositional settings follow Sweere et al. (2016). Heavy and light blue triangles in a denoting the Yorkshire sample data are from Pearce et al. (2008) and Thibault et al. (2018), respectively. Grey triangles in b denoting the Yorkshire sample data are from McArthur (2019). Heavy orange diamonds in a and b, and light ones in a denoting Dotternhausen sample date are from Wang et al. (2020) and Dickson et al. (2017), respectively.

Collectively, the combination of N isotope and elemental concentration data for T-CIE sedimentary sections provides important insights into the Early Jurassic ocean redox structure. Though these data point out that the deoxygenated marine conditions commonly identified in several T-CIE localities on the northern European epicontinental shelf do not reflect the coeval Tethyan ocean redox structure, are rather indicative of the development of oxygen-deficient basins. However, validating the existence of global deep-ocean anoxia during the T-CIE interval needs reliable redox investigations (e.g., through redox-sensitive trace elements and Fe speciation) for deep open-ocean sedimentary sections.

3.2.3. Zinc geochemical cycling response to the Early Jurassic (Toarcian) marine anoxia

3.2.3.1 Local marine redox and productivity controls on $\delta^{66}\text{Zn}_{\text{bulk}}$ during the T-CIE?

Sedimentary $\delta^{66}\text{Zn}$ records are dominated by burial pathways which are commonly impacted by seawater redox conditions and marine productivity (e.g., John et al., 2007; Kunzmann et al., 2013; John and Conway, 2014; Little et al., 2016; Isson et al., 2018; Sweere et al., 2018, 2020; Köbberich and Vance, 2019). Temporarily more reducing conditions could have led to a smaller isotopic offset between seawater and sediments, compared to sediments deposited under less reducing conditions, as observed in the present-day continental-margin sediments (Little et al., 2016). The modern ocean sediments deposited in anoxic to mildly sulfidic environments that exhibit higher $\delta^{66}\text{Zn}$ values than sediments from suboxic to anoxic conditions (cf. Little et al., 2016). It has been proposed that marine productivity by living organisms preferentially assimilates light Zn isotopes which are then exported onto the seafloor by the produced biomass, enriching the residual seawater Zn in heavy isotopes (e.g., Kunzmann et al., 2013; Isson et al., 2018). To explore whether these two mechanisms may have controlled the $\delta^{66}\text{Zn}_{\text{bulk}}$ values of the Yorkshire and Dotternhausen organic-rich black shales, enrichment factors (EFs) of redox-sensitive elements Mo, U and V (e.g., Algeo and Maynard, 2004; Algeo and Tribovillard, 2009; Tribovillard et al., 2012) and bio-essential nutrient elements Cu, Ni, and P (e.g., Tyrrell, 1999; Schenau et al., 2005; Tribovillard et al., 2006) are employed here. If sedimentary $\delta^{66}\text{Zn}_{\text{bulk}}$ records are dominated by local marine redox states or marine productivity, a correlation between the $\delta^{66}\text{Zn}_{\text{bulk}}$ values and the EFs of redox-sensitive elements or bio-essential nutrient elements is expected. However, our data show no such correlations of $\delta^{66}\text{Zn}_{\text{bulk}}$ versus Mo_{EF} , U_{EF} and V_{EF} (Figure 3.16), which indicates negligible local seawater redox control on the $\delta^{66}\text{Zn}_{\text{bulk}}$ patterns of both Yorkshire and Dotternhausen T-CIE samples. Further, the absence of systematic covariations of $\delta^{66}\text{Zn}_{\text{bulk}}$ versus Cu_{EF} , Ni_{EF} and P_{EF} (Figure 3.16) implies a minimal export productivity control on the two T-CIE sections' $\delta^{66}\text{Zn}_{\text{bulk}}$. These observations demonstrate that the perturbations of $\delta^{66}\text{Zn}_{\text{bulk}}$ values across the T-CIE interval are not simply controlled by the coeval basinal-scale marine redox or productivity conditions. Instead, the stratigraphic $\delta^{66}\text{Zn}_{\text{bulk}}$ patterns of the Yorkshire and Dotternhausen T-CIE sedimentary sections are more likely to be related to global deep-ocean Zn reservoir composition (see section 3.2.3.4). The positive $\delta^{66}\text{Zn}_{\text{bulk}}$ excursion

for the T-CIE organic-rich black shale samples compared to the pre-T-CIE organic-lean grey shale samples may be caused by a joint control between expanded marine anoxia and/or elevated marine productivity which at the global scale accelerated the removal of light Zn isotopes onto the seafloor and enriched the seawater in ^{66}Zn .

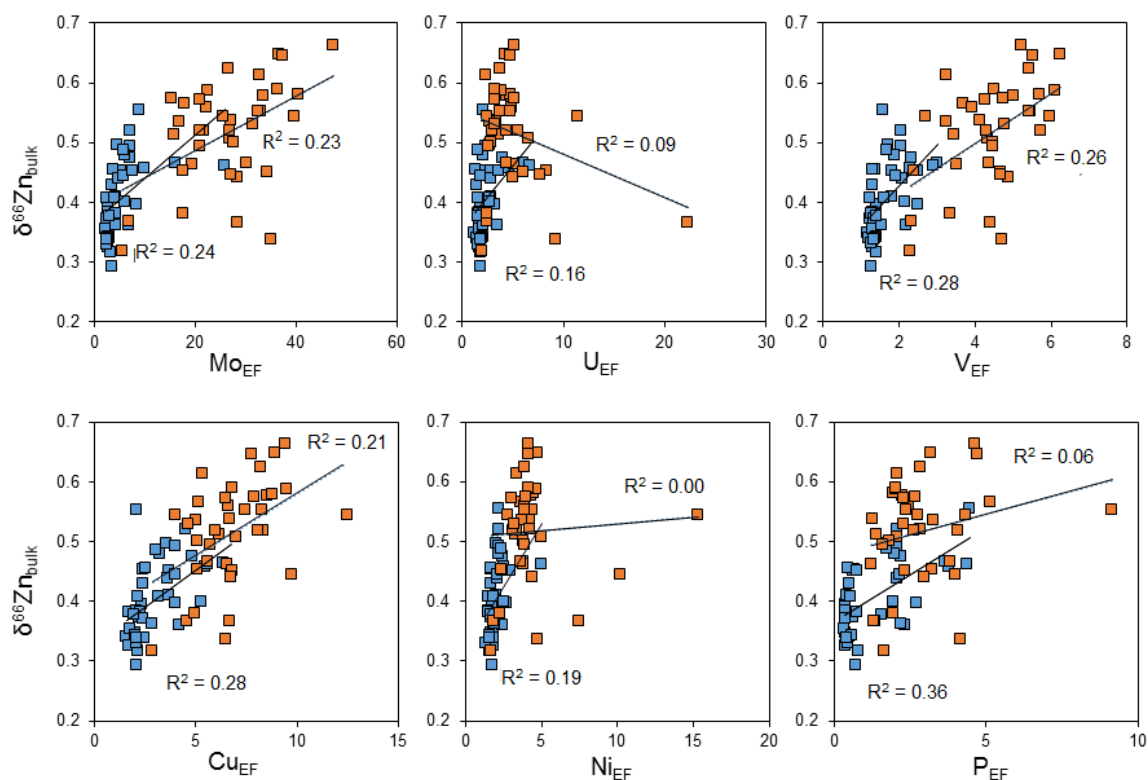


Figure 3.16. Cross-plots between $\delta^{66}\text{Zn}_{\text{bulk}}$ and enrichment factors (EFs) of redox-sensitive elements Mo, U and V, and bio-essential nutrient elements Cu, Ni and P for the Yorkshire (blue rectangles) and Dotternhausen (orange squares) T-CIE organic-rich black shale samples. The EF is calculated relative to upper continental crust (UCC; McLennan, 2001) using the equation of $[(\text{element}/\text{Al})_{\text{sample}}/(\text{element}/\text{Al})_{\text{UCC}}]$. R^2 represents the coefficient of the determination of the covariation.

3.2.3.2. Determination of the authigenic Zn isotope compositions for T-CIE organic-rich black shales

Considering the possible contamination from terrigenous-sourced Zn, obtaining authigenic Zn isotope composition (expressed by $\delta^{66}\text{Zn}_{\text{auth}}$) through lithogenic correction appears requisite. However, Zn enrichment in marine sediments is difficult to spot, which is unlike Mo. This is because the Zn abundance of the detrital background can be on the order of 10–100 $\mu\text{g}/\text{g}$, compared to approximately 1 $\mu\text{g}/\text{g}$ for Mo (McLennan, 2001; Rudnick and Gao, 2003), which may give rise to a large bias on the original $\delta^{66}\text{Zn}$ signal of the sediment authigenic component (cf. Vance et al., 2016). It follows that calculating $\delta^{66}\text{Zn}_{\text{auth}}$ values on a sample by sample basis using the

traditional Zn–aluminum (Al) systematics (cf. Little et al., 2016) for the Yorkshire and Dotternhausen T-CIE organic-rich black shales seems irrational. To address this issue, this study alternatively used a cross-plot between $\delta^{66}\text{Zn}_{\text{bulk}}$ and Al/Zn (Figure 3.17a; Vance et al., 2016). At Al/Zn = 0 on this cross-plot, the concentration of detrital indicator Al is set to be zero, meaning no detrital Zn contribution on the sediment authigenic Zn component (cf. Vance et al., 2016). Thus, $\delta^{66}\text{Zn}_{\text{auth}}$ records can be roughly represented by the intercept on y (here, $\delta^{66}\text{Zn}_{\text{bulk}}$)-axis (Figure 3.17a; cf. Vance et al., 2016). In this study, for organic-rich black shale samples of the Yorkshire and Dotternhausen T-CIE sections, the intercepts on y-axis are +0.54 ‰ and +0.63 ‰, respectively (Figure 3.17a), which stand for the two sections' $\delta^{66}\text{Zn}_{\text{auth}}$ estimates.

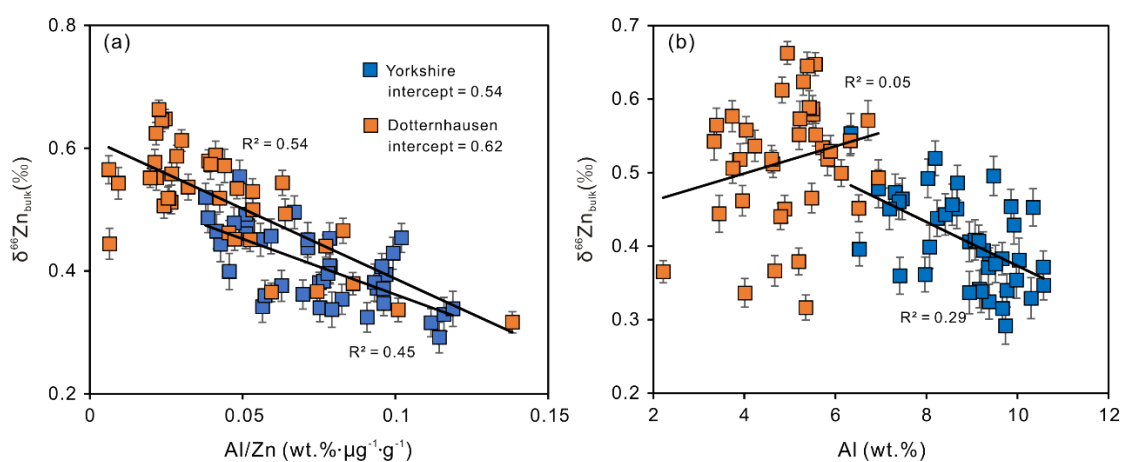


Figure 3.17. Cross-plots of (a) $\delta^{66}\text{Zn}_{\text{bulk}}$ versus Al/Zn and (b) $\delta^{66}\text{Zn}_{\text{bulk}}$ versus Al for Yorkshire and Dotternhausen T-CIE organic-rich black shale samples. In a, the intercepts at Al/Zn = 0 of correlation trends provide the $\delta^{66}\text{Zn}_{\text{auth}}$ estimates. R^2 represents the coefficient of the determination of the covariation.

3.2.3.3. The modern-like Zn geochemical cycling in the Early Toarcian ocean

In the modern ocean, surface-water $\delta^{66}\text{Zn}$ is spatially heterogeneous and is generally lower than that of the deep waters whose $\delta^{66}\text{Zn}$ is nearly homogeneous with an average of $+0.50 \pm 0.14$ ‰ (2 s.d.; Conway and John, 2014, 2015; Isson et al., 2018). However, the response of $\delta^{66}\text{Zn}_{\text{auth}}$ for organic-rich sediments deposited in hydrographically open versus restricted marine environments to the homogeneous oceanic Zn inventory behaves discrepantly (Figure 3.18; Little et al., 2016; Vance et al., 2016; Isson et al., 2018). Organic-rich sediments of the modern continental-margin OMZ sites represent the only known sink for isotopically light Zn (Little et al., 2016). Their $\delta^{66}\text{Zn}_{\text{auth}}$ values are generally lighter than in the deep ocean by ~ 0.5 ‰ (Little et al., 2016). By contrast, organic-rich sediments accumulating underneath euxinic deep waters (i.e., in modern Black Sea and Cariaco Basin) favored by the hydrographic

water-mass restriction feature heavy Zn isotope records (Figure 3.18; Vance et al., 2016; Isson et al., 2018). Their $\delta^{66}\text{Zn}_{\text{auth}}$ values of $\sim+0.5$ to $+0.6$ ‰ are within uncertainty identical to that of the average deep-ocean composition. This observation is because in both Black Sea and Cariaco Basin sulfidic bottom waters the dissolved Zn fed from the outside open ocean 1) has the deficient concentration compared to hydrogen sulfide (H_2S), and 2) suffers near-quantitative removal through precipitation of highly stable Zn sulfide (ZnS) complex (Algeo and Tribouillard, 2009; Vance et al., 2016; Isson et al., 2018; Sweere et al., 2020). Therefore, in euxinic depositional settings, where Zn drawdown is (near-) quantitative, underlying organic-rich sedimentary $\delta^{66}\text{Zn}$ is expected to mirror the original isotope composition of the Zn source in deep seawater (analogous to Mo) (cf. Vance et al., 2016).

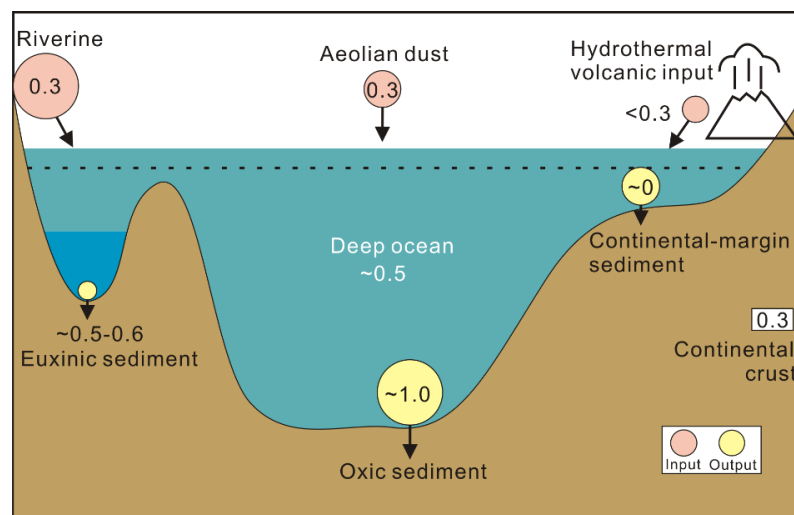


Figure 3.18. A sketch showing Zn inputs and outputs in the modern ocean (modified after Sweere et al., 2018). The associated Zn isotope systems are based on data from Conway and John (2014, 2015), Little et al. (2014b, 2016), Vance et al. (2016) and Isson et al. (2018). The size of circles stands for the relative Zn flux sizes, and numbers are their Zn isotope compositions in per mil (‰).

In this study, the Yorkshire and Dotternhausen T-CIE organic-rich black shales contain high TOC abundance of > 4 wt.% (Röhl et al., 2001; Pearce et al., 2008; Wang et al., 2020). Though their deposition was claimed to be in response to global ocean anoxia (Pearce et al., 2008; Thibault et al., 2018), a growing body of geochemical evidence has shown that they were in fact deposited in mutually separate, restricted environments (McArthur et al., 2008; Dickson et al., 2017; McArthur, 2019; Remírez and Algeo, 2020; Wang et al., 2021). Furthermore, the Yorkshire and Dotternhausen T-CIE organic-rich black shales display persistently high abundances of authigenic redox-sensitive elements (i.e., Mo, U and V; Figure 3.6) and GSB biomarker (Frimmel et al., 2004; Schwark and Frimmel, 2004; French et al., 2014). This indicates that

oxygen-depleted benthic water mass containing aqueous H_2S has diffused into the photic zone in both the Cleveland Basin (Yorkshire coast) and the Southern German Basin (Dotternhausen quarry) during the T-CIE interval. Taken together, these T-CIE organic-rich sedimentary rocks accumulated under redox-stratified seawater conditions which splits the water column into thin oxic surface and thick euxinic bottom. Such restriction and redox nature for the Early Toarcian Cleveland Basin and Southern German Basin are visibly comparable to those of the modern analogs (i.e., Black Sea and Cariaco Basin). It follows that the $\delta^{66}\text{Zn}_{\text{auth}}$ records for the T-CIE euxinic organic-rich black shales from the Yorkshire coast of Cleveland Basin and the Dotternhausen quarry of Southern German Basin can reflect the coeval local deep seawater Zn isotope signal. Given the persistent existence of the authigenic Zn enrichment for the organic-rich sediments in both sedimentary sections through the entire T-CIE interval (Figure 3.6), Zn replenishment into their depositional environments has to be dependent on water-mass renewal from a large Zn reservoir, i.e., open ocean. The contemporaneous local deep seawater Zn isotope signal (reflected by $\delta^{66}\text{Zn}_{\text{auth}}$) can thus stand for the global average deep-ocean composition. Here, the $\delta^{66}\text{Zn}_{\text{auth}}$ estimates for the T-CIE black shale samples of Yorkshire (+0.54 ‰) and Dotternhausen (+0.63 ‰) sections (Figure 3.17a) are indiscernible from that of the modern global deep water ($\delta^{66}\text{Zn}$: $+0.50 \pm 0.14$ ‰; Conway and John, 2014, 2015; Isson et al., 2018). This finding therefore indicates that the Zn biogeochemical cycling in the Early Toarcian ocean during the T-CIE interval has overall reached the present-day level. By contrast, the Cenomanian-Turonian OAE 2 interval exhibiting very fluctuating global deep-ocean Zn isotope signals (~ -0.09 to $+0.85$ ‰ with a mean of ~ -0.33 ‰) due to ocean redox perturbations (Sweere et al., 2020) significantly differ from that of the modern ocean ($\delta^{66}\text{Zn}$: $+0.50 \pm 0.14$ ‰; Conway and John, 2014, 2015; Isson et al., 2018). The difference in global deep-ocean $\delta^{66}\text{Zn}$ between the T-OAE (~ 183 Ma) and the OAE 2 (~ 94 Ma) further imparts a non-linear evolutionary trend for ocean Zn cycling over geologic time.

3.2.3.4. A short-lived ocean oxygenation recorded by a negative Zn isotope excursion?

Zinc itself is not redox-sensitive, but its dissolved species are easily complexed by aqueous H_2S in sulfidic pore waters or seawater. The Zn- H_2S complex preferentially incorporates light Zn isotope, enriching the ambient microenvironments in residual

^{66}Zn , when removal is non-quantitative (Little et al., 2016; Vance et al., 2016; Sweere et al., 2020). This process widely exists in the modern continental-margin OMZ settings in which the formation of authigenic Zn sulfide in the underlying organic-rich sediments is suggested to be the driver of the present-day heavy isotope composition of deep seawater (cf. Little et al., 2016). On the other hand, Zn also has an affinity for oxic sediments (i.e., iron–manganese (Fe–Mn) (oxyhydr)oxides, carbonates) which carry Zn isotope composition of 0.4–0.5 ‰ higher than that of average deep ocean (Figure 3.18; Pichat et al., 2003; Little et al., 2014a, b). The nearly homogeneous Zn isotope composition of the modern deep ocean is in fact set by Zn balance between input and output fluxes to and from the ocean (cf. Conway and John, 2014; Sweere et al., 2020). However, the steady-state global ocean Zn cycle may be unbalanced if there is an alteration of the input and output fluxes in concert with global environmental perturbations. A significant increase in Zn input flux into the ocean system from allochthonous Zn sources such as riverine discharge, hydrothermal fluids, eolian dust, all ≤ 0.3 ‰ (Figure 3.18; Little et al., 2016; Lemaitre et al., 2020), can in part decrease the deep-ocean Zn isotope composition (cf. Sweere et al., 2018), and vice versa. Further, a substantial change in the proportion of Zn removal into the continental-margin OMZ organic-rich sediments and the oxic sediments that constitute the main Zn outputs in the modern ocean can also alter the deep-ocean $\delta^{66}\text{Zn}$ (cf. Sweere et al., 2018, 2020). Specifically, a relative increase in the removal flux of Zn from seawater into continental-margin organic-rich sediments compared to Zn burial in oxic sediments would cause a shift toward higher $\delta^{66}\text{Zn}$ values of the global ocean and vice versa.

To understand the possible existence of remarkable variations in deep-ocean $\delta^{66}\text{Zn}$ throughout the T-CIE interval, lithogenic-corrected $\delta^{66}\text{Zn}_{\text{auth}}$ of the studied Yorkshire and Dotternhauen T-CIE sedimentary rocks are theoretically required (see section 3.2.3.3). Considering the possible existence of a significant bias on calculated $\delta^{66}\text{Zn}_{\text{auth}}$ values (see section 3.2.3.3), this study alternatively employed a cross-plot between $\delta^{66}\text{Zn}_{\text{bulk}}$ and Al to evaluate the detrital contribution on the primary authigenic Zn isotope signals. A lack of any marked covariation between $\delta^{66}\text{Zn}_{\text{bulk}}$ and Al (Figure 3.17b) indicates that the $\delta^{66}\text{Zn}_{\text{bulk}}$ values for the two T-CIE sections are actually controlled by the authigenic sedimentary Zn suffering negligible influence from detrital input. For the diagenetic limestone samples from the Dotternhausen section, their $\delta^{66}\text{Zn}_{\text{bulk}}$ directly represents their $\delta^{66}\text{Zn}_{\text{auth}}$ signals due to their low Al concentrations

(Wang et al., 2020). However, these diagenetic limestone $\delta^{66}\text{Zn}_{\text{bulk}}$ values can only be representative of the local-scale Zn cycling in the South German Basin rather than that of the global-scale deep ocean. Collectively, deep-ocean Zn-cycle perturbation trends, if present, can thus be reflected by organic-rich black shale $\delta^{66}\text{Zn}_{\text{bulk}}$ records, though its exact Zn isotope signature may not be mirrored.

The synchronous negative $\delta^{66}\text{Zn}_{\text{bulk}}$ excursion (see section 3.2.3.3) observed in the Yorkshire and Dotternhausen T-CIE stratigraphic profiles corresponds to distinct lithological facies that are black shales and a diagenetic limestone bed (Unterer Stein), respectively (Figure 3.6). The observed negative $\delta^{66}\text{Zn}_{\text{bulk}}$ shift in organic-rich black shales of the Yorkshire section represents an oceanic Zn-cycle event. It is unlikely that the $\delta^{66}\text{Zn}_{\text{bulk}}$ drop results from an increasing input flux from allochthonous isotopically light Zn sources into the contemporaneous ocean. This is because there is no significant increase in the Zn/Al values during this short negative Zn isotope excursion interval (Figure 3.6). Instead, the negative shift in $\delta^{66}\text{Zn}_{\text{bulk}}$ is most likely to be caused by one ocean oxygenation event which leads to a global decrease in the proportion of Zn removal into organic-rich continental-margin sediments relative to oxic sediments. Given the two sections' negative $\delta^{66}\text{Zn}_{\text{bulk}}$ excursion occurred concurrently, this ocean oxygenation may in part accelerate the delivery of electron acceptor (e.g., sulfate) onto sediment-seawater interface occurring in the South German Basin. This process may thus favor the formation of the diagenetic limestone bed (Unterer Stein) observed in Dotternhausen section (Figure 3.6). Its negative $\delta^{66}\text{Zn}_{\text{bulk}}$ shift may thus be related to the coeval decreased deep-ocean $\delta^{66}\text{Zn}$ or the basinal-scale released light Zn isotopes from organic matter remineralization during diagenesis, or both.

Short-lived ocean oxygenation events during the T-CIE interval have also been documented by ichnological records which have pointed out that episodic oxygen fluctuations indeed developed in basinal bottom waters of the Tethys Ocean and Panthalassa Ocean (Izumi et al., 2012; Fernández-Martínez et al., 2021; Rodríguez-Tovar, 2021). Nonetheless, the current uncertainty in the interpretation of the transient negative $\delta^{66}\text{Zn}_{\text{bulk}}$ excursion may be further improved by (i) providing detailed ichnological records for the Yorkshire and Dotternhausen T-CIE sedimentary sections, to better constrain short-term oxygen fluctuations; (ii) analyzing Zn isotope data for T-CIE sedimentary rocks from other sites, to complementarily constrain the coeval deep-ocean seawater $\delta^{66}\text{Zn}$ more accurately.

3.2.3.5. Zinc has a higher potential to track redox-driven ocean chemistry variation than Mo

Mo isotope composition of euxinic organic-rich sediments is a widely used proxy to record global ocean isotope signature in Earth's history (e.g., Dickson et al., 2012; Cheng et al., 2016; Goldberg et al., 2016; Kendall et al., 2017). However, caution should be exercised when using euxinic organic-rich sediment Mo isotopes to reconstruct the coeval seawater $\delta^{98}\text{Mo}$. At a certain aqueous H_2S concentration of $> 11 \mu\text{M}$, almost all dissolved molybdate anion (MoO_4^{2-}) is converted to tetrathiomolybdate (MoS_4^{2-}) and quantitatively scavenged into the underlying sediment, yielding sediment $\delta^{98}\text{Mo}$ equal to that of the seawater source (Algeo and Lyons, 2006; Helz et al., 2011). When aqueous H_2S is below this threshold, incomplete transformation of MoO_4^{2-} to MoS_4^{2-} followed by non-quantitative Mo removal leads to a significant isotope fractionation from the ambient seawater and then the fractionated Mo isotope is recorded by the sediment (Poulson et al., 2006; Neubert et al., 2008). These two scenarios are well represented by the modern hydrographically restricted Black Sea and Cariaco Basin, respectively, in which the Mo supply to their sulfidic bottom water is mainly derived from the open ocean. Black Sea euxinic sediments carry the averaged global ocean $\delta^{98}\text{Mo}$ of $+2.34 \text{‰}$ due to the high H_2S abundance of $> 11 \mu\text{M}$ in its bottom water (Erickson and Helz, 2000; Barling et al., 2001; Neubert et al., 2008). By contrast, $\delta^{98}\text{Mo}$ for euxinic sediments from Cariaco Basin is much lighter (mostly between 1 and 2 ‰) owing to its low water column H_2S concentration (Helz et al., 1996; Arnold et al., 2004; Brüske et al., 2020). In addition to redox control, the lighter $\delta^{98}\text{Mo}$ for Cariaco Basin euxinic sediments may also arise from a local Fe–Mn (oxyhydr)oxides particulate shuttle which adsorbs and delivers a large fraction of light Mo isotopes to the sediment (cf. Scholz et al., 2017). Any paleo-approach attempting to identify a trigger for a shift to lighter Mo isotope values in organic-rich sediments needs assess if particulate Mo delivery with Fe–Mn (oxyhydr)oxides can be ruled out. Otherwise, Mo isotope fractionation associated with this shuttle may disturb the determination of seawater redox variations. In this study, the incomparable Mo isotope in terms of authigenic values and stratigraphic trends for the Yorkshire and Dotternhausen T-CIE organic-rich sedimentary rocks (Figure 3.6) cannot simultaneously reflect the coeval global ocean seawater chemical composition and variation. Instead, these Mo isotopic discrepancies are indicative of the existence of isotopic offset from the contemporaneous seawater, at least for one of the two sites.

This Mo isotopic offset between seawater and sediments can be related to low concentration of water-column H_2S ($< 11 \mu\text{M}$) and/or the operation of a local Fe–Mn (oxyhydr)oxide shuttle. Though the aqueous H_2S concentration is difficult to determine in the coeval depositional settings, the indeed presence of a local Fe–Mn (oxyhydr)oxide shuttle (Figure 3.19; Algeo and Tribovillard, 2009) disallows the $\delta^{98}\text{Mo}$ interpretation to be a result of a global driver.

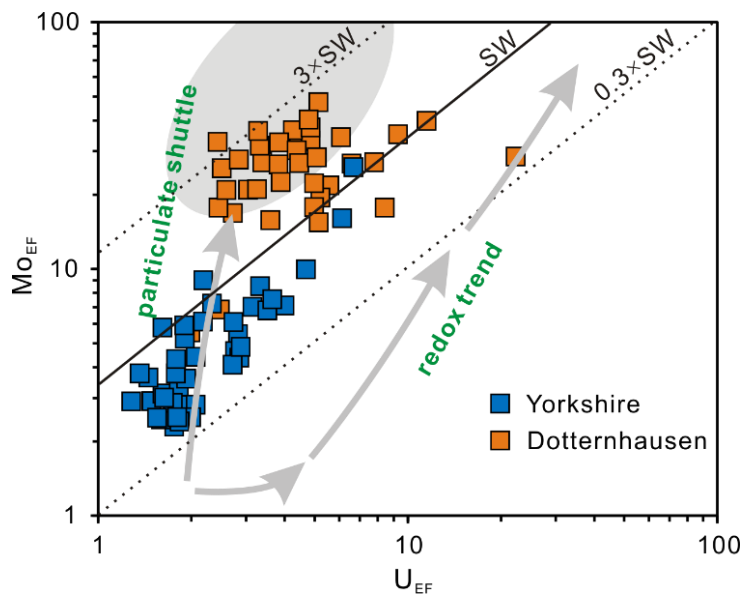


Figure 3.19. Cross-plot of Mo_{EF} versus U_{EF} for the Yorkshire and Dotternhausen organic-rich black shale samples. The seawater lines show Mo/U molar ratio equal to the seawater value (SW) and to multiples thereof ($3 \times \text{SW}$, $0.3 \times \text{SW}$). The pattern of Mo and U EFs is compared to the model behaviours proposed by Algeo and Tribovillard (2009). The Yorkshire and Dotternhausen samples obviously display evidence for the operation of an active particulate shuttle.

Authigenic Zn isotope for organic-rich sediments also has the capability of recording the global ocean isotope composition, if a fixed isotopic offset from seawater during Zn removal can be determined (Vance et al., 2016; Sweere et al., 2020). Lacking a net Zn isotope fractionation from seawater is expected in most sulfidic environments in which near-quantitative precipitation of dissolved Zn always occurs. This is in marked contrast to Mo since near-quantitative Zn removal only requires excess concentrations of aqueous H_2S relative to Zn (Yan et al., 2018; Sweere et al., 2020) instead of the H_2S abundance of $> 11 \mu\text{M}$. Furthermore, a local Fe–Mn (oxyhydr)oxide particulate shuttle, if present, does not significantly influence the Zn isotope composition of the authigenic components in the sediment, though preferentially adsorbed heavy Zn isotopes by this shuttle may be transported onto the seafloor. This is likely because most of dissolved Zn has been preferentially combined by aqueous H_2S , leaving insignificant Zn available for the adsorption onto Fe–Mn (oxyhydr)oxide particulates. The phenomenon is well

expressed by the modern Cariaco Basin whose Zn supply mainly derives from the open ocean (i.e., Atlantic) deep waters (Isson et al., 2018). Near-quantitative Zn sequestration occurring in the Cariaco Basin renders the authigenic $\delta^{66}\text{Zn}$ of the underlying euxinic sediments capture the present-day deep ocean signature (Isson et al., 2018), regardless of the active operation of a Fe–Mn (oxyhydr)oxide shuttle (Algeo and Tribovillard, 2009). The scenario is further exhibited by this studied Early Toarcian Yorkshire and Dotternhausen organic-rich sedimentary rocks. They deposited in separate persistently euxinic environments and suffered distinct influence of local Fe–Mn (oxyhydr)oxide shuttling during the T-CIE interval (Figure 3.19; McArthur et al., 2008; Dickson et al., 2017; McArthur, 2019; Wang et al., 2020), but still display comparable authigenic Zn isotope records and stratigraphic Zn isotope trends (Figure 3.6). The observations imply that near-quantitative Zn removal with minimal isotopic effects between seawater and sediments easily occurs under excessive H_2S conditions.

Frequent redox perturbations in the ocean happen in Earth's history, which is characteristic of significantly changes in seawater Mo and Zn isotope compositions (e.g., Kendall et al., 2017; Sweere et al., 2018, 2020). Expanded oceanic anoxia leads to a secular decrease in isotope composition of Mo but increase in isotope composition of Zn in seawater and vice versa (e.g., Kendall et al., 2017; Sweere et al., 2018, 2020). Such oceanic redox variations are to date abundantly investigated by the use of authigenic Mo isotope records of organic-rich sedimentary rocks (e.g., Dickson et al., 2012; Cheng et al., 2016; Goldberg et al., 2016). Notably, if this redox-sensitive element removal from seawater into the sediment is non-quantitative owing to $< 11 \mu\text{M}$ H_2S concentration and/or is partly accelerated by an active operation of Fe–Mn (oxyhydr)oxide shuttle, the possibly resultant isotope fractionations may complicate the reliable explanation of the sediment authigenic Mo isotope compositions. In this instance, authigenic Zn isotope for such organic-rich sedimentary rocks may take this opportunity serving as an alternative proxy to trace the contemporaneous oceanic redox changes.

4. References

- Ader, M., Cartigny, P., Boudou, J.P., Oh, J.H., Petit, E. and Javoy, M., 2006. Nitrogen isotopic evolution of carbonaceous matter during metamorphism: Methodology and preliminary results. *Chemical Geology*, 232(3-4), pp.152-169.
- Ader, M., Macouin, M., Trindade, R.I.F., Hadrien, M., Yang, Z.Y., Sun, Z.M. and Besse, J., 2009. A multilayered water column in the Ediacaran Yangtze platform? Insights from carbonate and organic matter paired $\delta^{13}\text{C}$. *Earth and Planetary Science Letters*, 288(1-2), pp.213-227.
- Ader, M., Thomazo, C., Sansjofre, P., Busigny, V., Papineau, D., Laffont, R., Cartigny, P. and Halverson, G.P., 2016. Interpretation of the nitrogen isotopic composition of Precambrian sedimentary rocks: Assumptions and perspectives. *Chemical Geology*, 429, pp.93-110.
- Albut, G., Babechuk, M.G., Kleinhanns, I.C., Bengler, M., Beukes, N.J., Steinhilber, B., Smith, A.J., Kruger, S.J. and Schoenberg, R., 2018. Modern rather than Mesoarchaeon oxidative weathering responsible for the heavy stable Cr isotopic signatures of the 2.95 Ga old Ijzermijn iron formation (South Africa). *Geochimica et Cosmochimica Acta*, 228, pp.157-189.
- Algeo, T.J. and Lyons, T.W., 2006. Mo–total organic carbon covariation in modern anoxic marine environments: Implications for analysis of paleoredox and paleohydrographic conditions. *Paleoceanography*, 21(1). <https://doi.org/10.1029/2004PA001112>.
- Algeo, T.J. and Maynard, J.B., 2004. Trace-element behavior and redox facies in core shales of Upper Pennsylvanian Kansas-type cyclothems. *Chemical Geology*, 206(3-4), pp.289-318.
- Algeo, T.J. and Tribouillard, N., 2009. Environmental analysis of paleoceanographic systems based on molybdenum–uranium covariation. *Chemical Geology*, 268(3-4), pp.211-225.
- Altabet, M.A., Pilska, C., Thunell, R., Pride, C., Sigman, D., Chavez, F. and Francois, R., 1999. The nitrogen isotope biogeochemistry of sinking particles from the margin of the Eastern North Pacific. *Deep Sea Research Part I: Oceanographic Research Papers*, 46(4), pp.655-679.
- Arnold, G.L., Anbar, A.D., Barling, J. and Lyons, T.W., 2004. Molybdenum isotope evidence for widespread anoxia in mid-Proterozoic oceans. *Science*, 304(5667), pp.87-90.
- Bailey, T.R., Rosenthal, Y., McArthur, J.M., Van de Schootbrugge, B. and Thirlwall, M.F., 2003. Paleocyanographic changes of the Late Pliensbachian–Early Toarcian interval: a possible link to the genesis of an Oceanic Anoxic Event. *Earth and Planetary Science Letters*, 212(3-4), pp.307-320.
- Barford, C.C., Montoya, J.P., Altabet, M.A. and Mitchell, R., 1999. Steady-state nitrogen isotope effects of N_2 and N_2O production in *Paracoccus denitrificans*. *Applied and Environmental Microbiology*, 65(3), pp.989-994.

- Barling, J. and Anbar, A.D., 2004. Molybdenum isotope fractionation during adsorption by manganese oxides. *Earth and Planetary Science Letters*, 217(3-4), pp.315-329.
- Barling, J., Arnold, G.L. and Anbar, A.D., 2001. Natural mass-dependent variations in the isotopic composition of molybdenum. *Earth and Planetary Science Letters*, 193(3-4), pp.447-457.
- Bauersachs, T., Schouten, S., Compaoré, J., Wollenzien, U., Stal, L.J. and Sinninghe Damsteé, J.S., 2009. Nitrogen isotopic fractionation associated with growth on dinitrogen gas and nitrate by cyanobacteria. *Limnology and Oceanography*, 54(4), pp.1403-1411.
- Berner, R.A., 1989. Biogeochemical cycles of carbon and sulfur and their effect on atmospheric oxygen over Phanerozoic time. *Global and Planetary Change*, 1(1-2), pp.97-122.
- Berner, R.A., 1998. The carbon cycle and carbon dioxide over Phanerozoic time: the role of land plants. *Philosophical Transactions of the Royal Society of London. Series B: Biological Sciences*, 353(1365), pp.75-82.
- Berner, R.A., 1999. A new look at the long-term carbon cycle. *GSA Today*, 9(11), pp.1-6.
- Berner, Z.A., Puchelt, H., Noeltner, T. and Kramar, U.T.Z., 2013. Pyrite geochemistry in the Toarcian Posidonia Shale of south-west Germany: Evidence for contrasting trace-element patterns of diagenetic and syngenetic pyrites. *Sedimentology*, 60(2), pp.548-573.
- Bjerrum, C.J., Surlyk, F., Callomon, J.H. and Slingerland, R.L., 2001. Numerical paleoceanographic study of the Early Jurassic transcontinental Laurasian Seaway. *Paleoceanography*, 16(4), pp.390-404.
- Brandes, J.A. and Devol, A.H., 1997. Isotopic fractionation of oxygen and nitrogen in coastal marine sediments. *Geochimica et Cosmochimica Acta*, 61(9), pp.1793-1801.
- Brandes, J.A., Devol, A.H. and Deutsch, C., 2007. New developments in the marine nitrogen cycle. *Chemical Reviews*, 107(2), pp.577-589.
- Brazier, J.M., Suan, G., Tacail, T., Simon, L., Martin, J.E., Mattioli, E. and Balter, V., 2015. Calcium isotope evidence for dramatic increase of continental weathering during the Toarcian oceanic anoxic event (Early Jurassic). *Earth and Planetary Science Letters*, 411, pp.164-176.
- Broecker, W.S. and Peng, T.H., 1986. Carbon cycle: 1985 glacial to interglacial changes in the operation of the global carbon cycle. *Radiocarbon*, 28(2A), pp.309-327.
- Brüske, A., Weyer, S., Zhao, M.Y., Planavsky, N.J., Wegwerth, A., Neubert, N., Dellwig, O., Lau, K.V. and Lyons, T.W., 2020. Correlated molybdenum and uranium isotope signatures in modern anoxic sediments: implications for their use as paleo-redox proxy. *Geochimica et Cosmochimica Acta*, 270, pp.449-474.
- Canfield, D.E., Glazer, A.N. and Falkowski, P.G., 2010. The evolution and future of Earth's nitrogen cycle. *Science*, 330(6001), pp.192-196.

- Caruthers, A.H., Gröcke, D.R. and Smith, P.L., 2011. The significance of an Early Jurassic (Toarcian) carbon-isotope excursion in Haida Gwaii (Queen Charlotte Islands), British Columbia, Canada. *Earth and Planetary Science Letters*, 307(1-2), pp.19-26.
- Cerling, T.E., Wang, Y. and Quade, J., 1993. Expansion of C4 ecosystems as an indicator of global ecological change in the late Miocene. *Nature*, 361(6410), pp.344-345.
- Chen, H., Savage, P.S., Teng, F.Z., Helz, R.T. and Moynier, F., 2013. Zinc isotope fractionation during magmatic differentiation and the isotopic composition of the bulk Earth. *Earth and Planetary Science Letters*, 369, pp.34-42.
- Chen, X., Sageman, B.B., Yao, H., Liu, S.A., Han, K., Zou, Y. and Wang, C., 2021. Zinc isotope evidence for paleoenvironmental changes during Cretaceous Oceanic Anoxic Event 2. *Geology*, 49(4), pp.412-416.
- Cheng, M., Li, C., Zhou, L., Algeo, T.J., Zhang, F., Romaniello, S., Jin, C.S., Lei, L.D., Feng, L.J. and Jiang, S.Y., 2016. Marine Mo biogeochemistry in the context of dynamically euxinic mid-depth waters: a case study of the lower Cambrian Niutitang shales, South China. *Geochimica et Cosmochimica Acta*, 183, pp.79-93.
- Chester, R., 1993. *Marine Geochemistry*, Chapman & Hall, London (1993), p. 698
- Cohen, A.S., Coe, A.L., Harding, S.M. and Schwark, L., 2004. Osmium isotope evidence for the regulation of atmospheric CO₂ by continental weathering. *Geology*, 32(2), pp.157-160.
- Collier, R.W., 1985. Molybdenum in the Northeast Pacific Ocean. *Limnology and Oceanography*, 30(6), pp.1351-1354.
- Colodner, D., Edmond, J. and Boyle, E., 1995. Rhenium in the Black Sea: comparison with molybdenum and uranium. *Earth and Planetary Science Letters*, 131(1-2), pp.1-15.
- Conway, T.M. and John, S.G., 2014. The biogeochemical cycling of zinc and zinc isotopes in the North Atlantic Ocean. *Global Biogeochemical Cycles*, 28(10), pp.1111-1128.
- Conway, T.M. and John, S.G., 2015. The cycling of iron, zinc and cadmium in the North East Pacific Ocean—Insights from stable isotopes. *Geochimica et Cosmochimica Acta*, 164, pp.262-283.
- Correia, V.F., Riding, J.B., Duarte, L.V., Fernandes, P. and Pereira, Z., 2017. The palynological response to the Toarcian Oceanic Anoxic Event (Early Jurassic) at Peniche, Lusitanian Basin, western Portugal. *Marine Micropaleontology*, 137, pp.46-63.
- Craig, H., 1957. Isotopic standards for carbon and oxygen and correction factors for mass-spectrometric analysis of carbon dioxide. *Geochimica et Cosmochimica Acta*, 12(1-2), pp.133-149.
- Dähnke, K. and Thamdrup, B., 2013. Nitrogen isotope dynamics and fractionation during sedimentary denitrification in Boknis Eck, Baltic Sea. *Biogeosciences*, 10(5), pp.3079-3088.

- De Kock, M.O., Beukes, N.J., Adeniyi, E.O., Cole, D., Gotz, A.E., Geel, C. and Ossa, F.G., 2017. Deflating the shale gas potential of South Africa's Main Karoo basin. *South African Journal of Science*, 113(9-10), pp.1-12.
- De Laeter, J.R., Böhlke, J.K., De Bièvre, P., Hidaka, H., Peiser, H.S., Rosman, K.J.R. and Taylor, P.D.P., 2003. Atomic weights of the elements: Review 2000 (IUPAC Technical Report). *Pure and Applied Chemistry*, 75(6), pp.683-800.
- Dembicki Jr, H., 2009. Three common source rock evaluation errors made by geologists during prospect or play appraisals. *AAPG Bulletin*, 93(3), pp.341-356.
- Dera, G., Brigaud, B., Monna, F., Laffont, R., Pucéat, E., Deconinck, J.F., Pellenard, P., Joachimski, M.M. and Durllet, C., 2011. Climatic ups and downs in a disturbed Jurassic world. *Geology*, 39(3), pp.215-218.
- Dera, G. and Donnadieu, Y., 2012. Modeling evidences for global warming, Arctic seawater freshening, and sluggish oceanic circulation during the Early Toarcian anoxic event. *Paleoceanography*, 27(2). <https://doi.org/10.1029/2012PA002283>.
- Dera, G., Neige, P., Dommergues, J.L. and Brayard, A., 2011. Ammonite paleobiogeography during the Pliensbachian–Toarcian crisis (Early Jurassic) reflecting paleoclimate, eustasy, and extinctions. *Global and Planetary Change*, 78(3-4), pp.92-105.
- Dera, G., Pucéat, E., Pellenard, P., Neige, P., Delsate, D., Joachimski, M.M., Reisberg, L. and Martinez, M., 2009. Water mass exchange and variations in seawater temperature in the NW Tethys during the Early Jurassic: evidence from neodymium and oxygen isotopes of fish teeth and belemnites. *Earth and Planetary Science Letters*, 286(1-2), pp.198-207.
- Derry, L.A., Kaufman, A.J. and Jacobsen, S.B., 1992. Sedimentary cycling and environmental change in the Late Proterozoic: evidence from stable and radiogenic isotopes. *Geochimica et Cosmochimica Acta*, 56(3), pp.1317-1329.
- Des Marais, D.J., 1997. Long-term evolution of the biogeochemical carbon cycle. *Reviews in Mineralogy and Geochemistry*, 35, pp.429-448.
- Dickson, A.J., Cohen, A.S. and Coe, A.L., 2012. Seawater oxygenation during the Paleocene-Eocene thermal maximum. *Geology*, 40(7), pp.639-642.
- Dickson, A.J., Gill, B.C., Ruhl, M., Jenkyns, H.C., Porcelli, D., Idiz, E., Lyons, T.W. and van den Boorn, S.H., 2017. Molybdenum-isotope chemostratigraphy and paleoceanography of the Toarcian Oceanic Anoxic Event (Early Jurassic). *Paleoceanography*, 32(8), pp.813-829.
- Ellwood, M.J. and Van den Berg, C.M., 2000. Zinc speciation in the northeastern Atlantic Ocean. *Marine Chemistry*, 68(4), pp.295-306.
- Emerson, S.R. and Huested, S.S., 1991. Ocean anoxia and the concentrations of molybdenum and vanadium in seawater. *Marine Chemistry*, 34(3-4), pp.177-196.

- Emrich, K., Ehhalt, D.H. and Vogel, J.C., 1970. Carbon isotope fractionation during the precipitation of calcium carbonate. *Earth and Planetary Science Letters*, 8(5), pp.363-371.
- Erickson, B.E. and Helz, G.R., 2000. Molybdenum (VI) speciation in sulfidic waters: stability and lability of thiomolybdates. *Geochimica et Cosmochimica Acta*, 64(7), pp.1149-1158.
- Fantasia, A., Föllmi, K.B., Adatte, T., Spangenberg, J.E. and Mattioli, E., 2019. Expression of the Toarcian Oceanic Anoxic Event: new insights from a Swiss transect. *Sedimentology*, 66(1), pp.262-284.
- Fernández-Martínez, J., Rodríguez-Tovar, F.J., Piñuela, L., Martínez-Ruiz, F. and García-Ramos, J.C., 2021. Bottom-and pore-water oxygenation during the early Toarcian Oceanic Anoxic Event (T-OAE) in the Asturian Basin (N Spain): Ichnological information to improve facies analysis. *Sedimentary Geology*, p.105909. <https://doi.org/10.1016/j.sedgeo.2021.105909>.
- Fernandez, A., Korte, C., Ullmann, C.V., Looser, N., Wohlwend, S. and Bernasconi, S.M., 2021. Reconstructing the magnitude of Early Toarcian (Jurassic) warming using the reordered clumped isotope compositions of belemnites. *Geochimica et Cosmochimica Acta*, 293, pp.308-327.
- Fogel, M.L. and Cifuentes, L.A., 1993. Isotope fractionation during primary production. In *Organic Geochemistry* (pp. 73-98). Springer, Boston, MA.
- Fraguas, Á., Comas-Rengifo, M.J., Gómez, J.J. and Goy, A., 2012. The calcareous nanofossil crisis in Northern Spain (Asturias province) linked to the Early Toarcian warming-driven mass extinction. *Marine Micropaleontology*, 94, pp.58-71.
- Francois, R., 1988. A study on the regulation of the concentrations of some trace metals (Rb, Sr, Zn, Pb, Cu, V, Cr, Ni, Mn and Mo) in Saanich Inlet sediments, British Columbia, Canada. *Marine Geology*, 83(1-4), pp.285-308.
- Frimmel, A., 2003. Hochau. ösende Untersuchungen von Biomarkern an epikontinentalen Schwarzschiefern des Unteren Toarciums (Posidonienschiefer, Lias ϵ) von SW-Deutschland. Retrieved from <https://publikationen.uni-tuebingen.de/xmlui/handle/10900/48450>.
- Frimmel, A., Oschmann, W. and Schwark, L., 2004. Chemostratigraphy of the Posidonia Black Shale, SW Germany: I. Influence of sea-level variation on organic facies evolution. *Chemical Geology*, 206(3-4), pp.199-230.
- Froelich, P., Klinkhammer, G.P., Bender, M.L., Luedtke, N.A., Heath, G.R., Cullen, D., Dauphin, P., Hammond, D., Hartman, B. and Maynard, V., 1979. Early oxidation of organic matter in pelagic sediments of the eastern equatorial Atlantic: suboxic diagenesis. *Geochimica et Cosmochimica Acta*, 43(7), pp.1075-1090.

- Fu, X., Wang, J., Feng, X., Wang, D., Chen, W., Song, C. and Zeng, S., 2016. Early Jurassic carbon-isotope excursion in the Qiangtang Basin (Tibet), the eastern Tethys: Implications for the Toarcian Oceanic anoxic event. *Chemical Geology*, 442, pp.62-72.
- Fu, X., Wang, J., Zeng, S., Feng, X., Wang, D. and Song, C., 2017. Continental weathering and palaeoclimatic changes through the onset of the Early Toarcian oceanic anoxic event in the Qiangtang Basin, eastern Tethys. *Palaeogeography, Palaeoclimatology, Palaeoecology*, 487, pp.241-250.
- Fujii, T., Moynier, F., Pons, M.L. and Albarède, F., 2011. The origin of Zn isotope fractionation in sulfides. *Geochimica et Cosmochimica Acta*, 75(23), 7632-7643.
- Fulton, J.M., Arthur, M.A. and Freeman, K.H., 2012. Black Sea nitrogen cycling and the preservation of phytoplankton $\delta^{15}\text{N}$ signals during the Holocene. *Global Biogeochemical Cycles*, 26(2). <https://doi.org/10.1029/2011GB004196>.
- Garrels, R.M. and Perry, E.A., 1974. Cycling of carbon, sulfur, and oxygen through geologic time. *The Sea*, 5, pp.303-336.
- Garvin, J., Buick, R., Anbar, A.D., Arnold, G.L. and Kaufman, A.J., 2009. Isotopic evidence for an aerobic nitrogen cycle in the latest Archean. *Science*, 323(5917), pp.1045-1048.
- Gill, B.C., Lyons, T.W. and Jenkyns, H.C., 2011. A global perturbation to the sulfur cycle during the Toarcian Oceanic Anoxic Event. *Earth and Planetary Science Letters*, 312(3-4), pp.484-496.
- Gilleaudeau, G.J., Sahoo, S.K., Ostrander, C.M., Owens, J.D., Poulton, S.W., Lyons, T.W. and Anbar, A.D., 2020. Molybdenum isotope and trace metal signals in an iron-rich Mesoproterozoic ocean: A snapshot from the Vindhyan Basin, India. *Precambrian Research*, 343, p.105718.
- Goldberg, T., Archer, C., Vance, D. and Poulton, S.W., 2009. Mo isotope fractionation during adsorption to Fe (oxyhydr) oxides. *Geochimica et Cosmochimica Acta*, 73(21), pp.6502-6516.
- Goldberg, T., Poulton, S.W., Wagner, T., Kolonic, S.F. and Rehkämper, M., 2016. Molybdenum drawdown during cretaceous oceanic anoxic event 2. *Earth and Planetary Science Letters*, 440, pp.81-91.
- Grasby, S.E., Knies, J., Beauchamp, B., Bond, D.P., Wignall, P. and Sun, Y., 2020. Global warming leads to Early Triassic nutrient stress across northern Pangea. *GSA Bulletin*, 132(5-6), pp.943-954.
- Greber, N.D., Davies, J.H., Gaynor, S.P., Jourdan, F., Bertrand, H. and Schaltegger, U., 2020. New high precision U-Pb ages and Hf isotope data from the Karoo large igneous province; implications for pulsed magmatism and early Toarcian environmental perturbations. *Results in Geochemistry*, 1, p.100005. <https://doi.org/10.1016/j.ringeo.2020.100005>.

- Greber, N.D., Mäder, U. and Nägler, T.F., 2015. Experimental dissolution of molybdenum-sulphides at low oxygen concentrations: A first-order approximation of late Archean atmospheric conditions. *Earth and Space Science*, 2(5), pp.173-180.
- Gröcke, D.R., Hori, R.S., Trabucho-Alexandre, J., Kemp, D.B. and Schwark, L., 2011. An open ocean record of the Toarcian oceanic anoxic event. *Solid Earth*, 2(2), pp.245-257.
- Gruber, N., 2008. The marine nitrogen cycle: overview and challenges. *Nitrogen in the Marine Environment*, 2, pp.1-50.
- Gruber, N. and Sarmiento, J.L., 1997. Global patterns of marine nitrogen fixation and denitrification. *Global Biogeochemical Cycles*, 11(2), pp.235-266.
- Han, Z., Hu, X., Kemp, D.B. and Li, J., 2018. Carbonate-platform response to the Toarcian Oceanic Anoxic Event in the southern hemisphere: Implications for climatic change and biotic platform demise. *Earth and Planetary Science Letters*, 489, pp.59-71.
- Hayes, J.M., Popp, B.N., Takigiku, R. and Johnson, M.W., 1989. An isotopic study of biogeochemical relationships between carbonates and organic carbon in the Greenhorn Formation. *Geochimica et Cosmochimica Acta*, 53(11), pp.2961-2972.
- Heimann, A., Johnson, C.M., Beard, B.L., Valley, J.W., Roden, E.E., Spicuzza, M.J. and Beukes, N.J., 2010. Fe, C, and O isotope compositions of banded iron formation carbonates demonstrate a major role for dissimilatory iron reduction in ~2.5 Ga marine environments. *Earth and Planetary Science Letters*, 294(1-2), pp.8-18.
- Helz, G.R., Bura-Nakić, E., Mikac, N. and Ciglencčki, I., 2011. New model for molybdenum behavior in euxinic waters. *Chemical Geology*, 284(3-4), pp.323-332.
- Helz, G.R., Miller, C.V., Charnock, J.M., Mosselmans, J.F.W., Pattrick, R.A.D., Garner, C.D. and Vaughan, D.J., 1996. Mechanism of molybdenum removal from the sea and its concentration in black shales: EXAFS evidence. *Geochimica et Cosmochimica Acta*, 60(19), pp.3631-3642.
- Hermoso, M., Minoletti, F. and Pellenard, P., 2013. Black shale deposition during Toarcian super-greenhouse driven by sea level. *Climate of the Past*, 9(6), pp.2703-2712.
- Hermoso, M., Minoletti, F., Rickaby, R.E., Hesselbo, S.P., Baudin, F. and Jenkyns, H.C., 2012. Dynamics of a stepped carbon-isotope excursion: Ultra high-resolution study of Early Toarcian environmental change. *Earth and Planetary Science Letters*, 319, pp.45-54.
- Hermoso, M. and Pellenard, P., 2014. Continental weathering and climatic changes inferred from clay mineralogy and paired carbon isotopes across the early to middle Toarcian in the Paris Basin. *Palaeogeography, Palaeoclimatology, Palaeoecology*, 399, pp.385-393.
- Hesselbo, S.P., Gröcke, D.R., Jenkyns, H.C., Bjerrum, C.J., Farrimond, P., Bell, H.S.M. and Green, O.R., 2000. Massive dissociation of gas hydrate during a Jurassic oceanic anoxic event. *Nature*, 406(6794), pp.392-395.

- Hesselbo, S.P., Jenkyns, H.C., Duarte, L.V. and Oliveira, L.C., 2007. Carbon-isotope record of the Early Jurassic (Toarcian) Oceanic Anoxic Event from fossil wood and marine carbonate (Lusitanian Basin, Portugal). *Earth and Planetary Science Letters*, 253(3-4), pp.455-470.
- Higgins, M.B., Robinson, R.S., Husson, J.M., Carter, S.J. and Pearson, A., 2012. Dominant eukaryotic export production during ocean anoxic events reflects the importance of recycled NH_4^+ . *Proceedings of the National Academy of Sciences*, 109(7), pp.2269-2274.
- Houben, A.J., Goldberg, T. and Slomp, C.P., 2021. Biogeochemical evolution and organic carbon deposition on the Northwestern European Shelf during the Toarcian Ocean Anoxic Event. *Palaeogeography, Palaeoclimatology, Palaeoecology*, 565, p.110191. <https://doi.org/10.1016/j.palaeo.2020.110191>.
- Howarth, M.K., 1955. Domes of the Yorkshire coast. *Proc. Yorkshire Geol. Soc.*, 30, 147–175.
- Howarth, M.K., 1962. The jet rock series and the alum shale series of the Yorkshire coast. *Proc. Yorkshire Geol. Soc.*, 33, 381–422.
- Howarth, M.K., 1973. The stratigraphy and ammonite fauna of the upper Liassic Grey Shales of the Yorkshire coast. *Bull. Br. Mus. Nat. Hist. Geol.*, 24, 235–277.
- Hu, S.Y., Evans, K., Rempel, K., Guagliardo, P., Kilburn, M., Craw, D., Grice, K. and Dick, J., 2018. Sequestration of Zn into mixed pyrite-zinc sulfide framboids: A key to Zn cycling in the ocean?. *Geochimica et Cosmochimica Acta*, 241, pp.95-107.
- Hurse, T.J., Kappler, U. and Keller, J., 2008. Using Anoxygenic Photosynthetic Bacteria for the Removal of Sulfide from Wastewater. In: Hell R., Dahl C., Knaff D., Leustek T. (eds) Sulfur Metabolism in Phototrophic Organisms. *Advances in Photosynthesis and Respiration*, vol 27. Springer, Dordrecht. https://doi.org/10.1007/978-1-4020-6863-8_22.
- Ikeda, M. and Hori, R.S., 2014. Effects of Karoo–Ferrar volcanism and astronomical cycles on the Toarcian oceanic anoxic events (Early Jurassic). *Palaeogeography, Palaeoclimatology, Palaeoecology*, 410, pp.134-142.
- Ikeda, M., Hori, R.S., Ikehara, M., Miyashita, R., Chino, M. and Yamada, K., 2018. Carbon cycle dynamics linked with Karoo-Ferrar volcanism and astronomical cycles during Pliensbachian-Toarcian (Early Jurassic). *Global and Planetary Change*, 170, pp.163-171.
- Isson, T.T., Love, G.D., Dupont, C.L., Reinhard, C.T., Zumberge, A.J., Asael, D., Gueguen, B., McCrow, J., Gill, B.C., Owens, J. and Rainbird, R.H., 2018. Tracking the rise of eukaryotes to ecological dominance with zinc isotopes. *Geobiology*, 16(4), pp.341-352.
- Ivanov, A.V., Meffre, S., Thompson, J., Corfu, F., Kamenetsky, V.S., Kamenetsky, M.B. and Demoulova, E.I., 2017. Timing and genesis of the Karoo-Ferrar large igneous province: New high precision U-Pb data for Tasmania confirm short duration of the major magmatic pulse. *Chemical Geology*, 455, pp.32-43.

- Izumi, K., Kemp, D.B., Itamiya, S. and Inui, M., 2018. Sedimentary evidence for enhanced hydrological cycling in response to rapid carbon release during the early Toarcian oceanic anoxic event. *Earth and Planetary Science Letters*, 481, pp.162-170.
- Izumi, K., Miyaji, T. and Tanabe, K., 2012. Early Toarcian (Early Jurassic) oceanic anoxic event recorded in the shelf deposits in the northwestern Panthalassa: Evidence from the Nishinakayama Formation in the Toyora area, west Japan. *Palaeogeography, Palaeoclimatology, Palaeoecology*, 315, pp.100-108.
- Jarvis, I., Lignum, J.S., Gröcke, D.R., Jenkyns, H.C. and Pearce, M.A., 2011. Black shale deposition, atmospheric CO₂ drawdown, and cooling during the Cenomanian-Turonian Oceanic Anoxic Event. *Paleoceanography*, 26(3). <https://doi.org/10.1029/2010PA002081>.
- Jenkyns, H.C., 1985. The Early Toarcian and Cenomanian-Turonian anoxic events in Europe: comparisons and contrasts. *Geologische Rundschau*, 74(3), pp.505-518.
- Jenkyns, H.C., 1988. The early Toarcian (Jurassic) anoxic event; stratigraphic, sedimentary and geochemical evidence. *American Journal of Science*, 288(2), pp.101-151.
- Jenkyns, H.C., 2010. Geochemistry of oceanic anoxic events. *Geochemistry, Geophysics, Geosystems*, 11(3). <https://doi.org/10.1029/2009GC002788>.
- Jenkyns, H.C. and Clayton, C.J., 1986. Black shales and carbon isotopes in pelagic sediments from the Tethyan Lower Jurassic. *Sedimentology*, 33(1), pp.87-106.
- Jenkyns, H.C., Dickson, A.J., Ruhl, M. and Van den Boorn, S.H., 2017. Basalt-seawater interaction, the Plenus Cold Event, enhanced weathering and geochemical change: deconstructing Oceanic Anoxic Event 2 (Cenomanian–Turonian, Late Cretaceous). *Sedimentology*, 64(1), pp.16-43.
- Jenkyns, H.C., Jones, C.E., Gröcke, D.R., Hesselbo, S.P. and Parkinson, D.N., 2002. Chemostratigraphy of the Jurassic System: applications, limitations and implications for palaeoceanography. *Journal of the Geological Society*, 159(4), pp.351-378.
- Jiang, G., Wang, X., Shi, X., Xiao, S., Zhang, S. and Dong, J., 2012. The origin of decoupled carbonate and organic carbon isotope signatures in the early Cambrian (ca. 542–520 Ma) Yangtze platform. *Earth and Planetary Science Letters*, 317, pp.96-110.
- Joachimski, M.M., Ostertag-Henning, C., Pancost, R.D., Strauss, H., Freeman, K.H., Littke, R., Damste, J.S.S. and Racki, G., 2001. Water column anoxia, enhanced productivity and concomitant changes in $\delta^{13}\text{C}$ and $\delta^{34}\text{S}$ across the Frasnian–Famennian boundary (Kowala—Holy Cross Mountains/Poland). *Chemical Geology*, 175(1-2), pp.109-131.
- John, S.G. and Conway, T.M., 2014. A role for scavenging in the marine biogeochemical cycling of zinc and zinc isotopes. *Earth and Planetary Science Letters*, 394, pp.159-167.
- John, S.G., Geis, R.W., Saito, M.A. and Boyle, E.A., 2007. Zinc isotope fractionation during high-affinity and low-affinity zinc transport by the marine diatom *Thalassiosira oceanica*. *Limnology and Oceanography*, 52(6), pp.2710-2714.

- John, S.G., Kunzmann, M., Townsend, E.J. and Rosenberg, A.D., 2017. Zinc and cadmium stable isotopes in the geological record: A case study from the post-snowball Earth Nuccaleena cap dolostone. *Palaeogeography, Palaeoclimatology, Palaeoecology*, 466, pp.202-208.
- Kemp, D.B., Coe, A.L., Cohen, A.S. and Schwark, L., 2005. Astronomical pacing of methane release in the Early Jurassic period. *Nature*, 437(7057), pp.396-399.
- Kendall, B., Dahl, T.W. and Anbar, A.D., 2017. The stable isotope geochemistry of molybdenum. *Reviews in Mineralogy and Geochemistry*, 82(1), pp.683-732.
- King, E.K., Perakis, S.S. and Pett-Ridge, J.C., 2018. Molybdenum isotope fractionation during adsorption to organic matter. *Geochimica et Cosmochimica Acta*, 222, pp.584-598.
- Kipp, M.A., Stüeken, E.E., Yun, M., Bekker, A. and Buick, R., 2018. Pervasive aerobic nitrogen cycling in the surface ocean across the Paleoproterozoic Era. *Earth and Planetary Science Letters*, 500, pp.117-126.
- Krencker, F.N., Fantasia, A., Danisch, J., Martindale, R., Kabiri, L., El Ouali, M. and Bodin, S., 2020. Two-phased collapse of the shallow-water carbonate factory during the late Pliensbachian–Toarcian driven by changing climate and enhanced continental weathering in the Northwestern Gondwana Margin. *Earth-Science Reviews*, p.103254. <https://doi.org/10.1016/j.earscirev.2020.103254>.
- Knoll, A.H., Hayes, J.M., Kaufman, A.J., Swett, K. and Lambert, I.B., 1986. Secular variation in carbon isotope ratios from Upper Proterozoic successions of Svalbard and East Greenland. *Nature*, 321(6073), pp.832-838.
- Kohn, M.J., 2010. Carbon isotope compositions of terrestrial C₃ plants as indicators of (paleo) ecology and (paleo) climate. *Proceedings of the National Academy of Sciences*, 107(46), pp.19691-19695.
- Konhauser, K.O., Planavsky, N.J., Hardisty, D.S., Robbins, L.J., Warchola, T.J., Haugaard, R., Lalonde, S.V., Partin, C.A., Oonk, P.B.H., Tsikos, H. and Lyons, T.W., 2017. Iron formations: A global record of Neoproterozoic to Palaeoproterozoic environmental history. *Earth-Science Reviews*, 172, pp.140-177.
- Kuypers, M.M., Lavik, G., Woebken, D., Schmid, M., Fuchs, B.M., Amann, R., Jørgensen, B.B. and Jetten, M.S., 2005. Massive nitrogen loss from the Benguela upwelling system through anaerobic ammonium oxidation. *Proceedings of the National Academy of Sciences*, 102(18), pp.6478-6483.
- Kuypers, M.M., Pancost, R.D. and Damste, J.S.S., 1999. A large and abrupt fall in atmospheric CO₂ concentration during Cretaceous times. *Nature*, 399(6734), pp.342-345.
- Lam, P. and Kuypers, M.M., 2011. Microbial nitrogen cycling processes in oxygen minimum zones. *Annual Review of Marine Science*, 3, pp.317-345.

- Lemaitre, N., de Souza, G.F., Archer, C., Wang, R.M., Planquette, H., Sarthou, G. and Vance, D., 2020. Pervasive sources of isotopically light zinc in the North Atlantic Ocean. *Earth and Planetary Science Letters*, 539, p.116216. <https://doi.org/10.1016/j.epsl.2020.116216>.
- Li, D., Zhang, X., Hu, D., Chen, X., Huang, W., Zhang, X., Li, M., Qin, L., Peng, S. and Shen, Y., 2018. Evidence of a large $\delta^{13}\text{C}_{\text{carb}}$ and $\delta^{13}\text{C}_{\text{org}}$ depth gradient for deep-water anoxia during the late Cambrian SPICE event. *Geology*, 46(7), pp.631-634.
- Little, S.H., Sherman, D.M., Vance, D. and Hein, J.R., 2014a. Molecular controls on Cu and Zn isotopic fractionation in Fe–Mn crusts. *Earth and Planetary Science Letters*, 396, pp.213-222.
- Little, S.H., Vance, D., Lyons, T.W. and McManus, J., 2015. Controls on trace metal authigenic enrichment in reducing sediments: insights from modern oxygen-deficient settings. *American Journal of Science*, 315(2), pp.77-119.
- Little, S.H., Vance, D., McManus, J. and Severmann, S., 2016. Key role of continental margin sediments in the oceanic mass balance of Zn and Zn isotopes. *Geology*, 44(3), pp.207-210.
- Little, S.H., Vance, D., Walker-Brown, C. and Landing, W.M., 2014b. The oceanic mass balance of copper and zinc isotopes, investigated by analysis of their inputs, and outputs to ferromanganese oxide sediments. *Geochimica et Cosmochimica Acta*, 125, pp.673-693.
- Mariotti, A., Germon, J.C., Hubert, P., Kaiser, P., Letolle, R., Tardieux, A. and Tardieux, P., 1981. Experimental determination of nitrogen kinetic isotope fractionation: some principles; illustration for the denitrification and nitrification processes. *Plant and Soil*, 62(3), pp.413-430.
- Martindale, R.C., Them, T.R., Gill, B.C., Marroquín, S.M. and Knoll, A.H., 2017. A new Early Jurassic (ca. 183 Ma) fossil Lagerstätte from Ya Ha Tinda, Alberta, Canada. *Geology*, 45(3), pp.255-258.
- McArthur, J.M., 2019. Early Toarcian black shales: A response to an oceanic anoxic event or anoxia in marginal basins?. *Chemical Geology*, 522, pp.71-83.
- McArthur, J.M., Algeo, T.J., Van de Schootbrugge, B., Li, Q. and Howarth, R.J., 2008. Basinal restriction, black shales, Re-Os dating, and the Early Toarcian (Jurassic) oceanic anoxic event. *Paleoceanography*, 23(4). <https://doi.org/10.1029/2008PA001607>.
- McArthur, J.M., Donovan, D.T., Thirlwall, M.F., Fouke, B.W. and Matthey, D., 2000. Strontium isotope profile of the early Toarcian (Jurassic) oceanic anoxic event, the duration of ammonite biozones, and belemnite palaeotemperatures. *Earth and Planetary Science Letters*, 179(2), pp.269-285.

- McLennan, S.M., 2001. Relationships between the trace element composition of sedimentary rocks and upper continental crust. *Geochemistry, Geophysics, Geosystems*, 2(4). <https://doi.org/10.1029/2000GC000109>.
- McLennan, S.M., Hemming, S., McDaniel, D.K. and Hanson, G.N., 1993. Geochemical approaches to sedimentation, provenance, and tectonics. *Special Papers-Geological Society of America*, pp.21-21. <https://doi.org/10.1130/SPE284-p21>.
- McManus, J., Berelson, W.M., Severmann, S., Poulson, R.L., Hammond, D.E., Klinkhammer, G.P. and Holm, C., 2006. Molybdenum and uranium geochemistry in continental margin sediments: paleoproxy potential. *Geochimica et Cosmochimica Acta*, 70(18), pp.4643-4662.
- McManus, J., Nägler, T.F., Siebert, C., Wheat, C.G. and Hammond, D.E., 2002. Oceanic molybdenum isotope fractionation: Diagenesis and hydrothermal ridge-flank alteration. *Geochemistry, Geophysics, Geosystems*, 3(12), pp.1-9.
- Mettam, C., Zerkle, A.L., Claire, M.W., Prave, A.R., Poulton, S.W. and Junium, C.K., 2019. Anaerobic nitrogen cycling on a Neoarchaeon ocean margin. *Earth and Planetary Science Letters*, 527, p.115800. <https://doi.org/10.1016/j.epsl.2019.115800>.
- Meyers, P.A., 1994. Preservation of elemental and isotopic source identification of sedimentary organic matter. *Chemical Geology*, 114(3-4), pp.289-302.
- Meyer, K.M., Yu, M., Lehrmann, D., van de Schootbrugge, B. and Payne, J.L., 2013. Constraints on Early Triassic carbon cycle dynamics from paired organic and inorganic carbon isotope records. *Earth and Planetary Science Letters*, 361, pp.429-435.
- Middelburg, J.J., Soetaert, K., Herman, P.M. and Heip, C.H., 1996. Denitrification in marine sediments: A model study. *Global Biogeochemical Cycles*, 10(4), pp.661-673.
- Miller, C.A., Peucker-Ehrenbrink, B., Walker, B.D. and Marcantonio, F., 2011. Re-assessing the surface cycling of molybdenum and rhenium. *Geochimica et Cosmochimica Acta*, 75(22), pp.7146-7179.
- Moldowan, J.M., Peters, K.E. and Walters, C.C., 2005. *The Biomarker Guide: Biomarkers and Isotopes in Petroleum Systems and Earth History*. Cambridge University Press.
- Montero-Serrano, J.C., Föllmi, K.B., Adatte, T., Spangenberg, J.E., Tribovillard, N., Fantasia, A. and Suan, G., 2015. Continental weathering and redox conditions during the early Toarcian Oceanic Anoxic Event in the northwestern Tethys: Insight from the Posidonia Shale section in the Swiss Jura Mountains. *Palaeogeography, Palaeoclimatology, Palaeoecology*, 429, pp.83-99.
- Mook, W.G., Bommerson, J.C. and Staverman, W.H., 1974. Carbon isotope fractionation between dissolved bicarbonate and gaseous carbon dioxide. *Earth and Planetary Science Letters*, 22(2), pp.169-176.

- Morford, J.L., Emerson, S.R., Breckel, E.J. and Kim, S.H., 2005. Diagenesis of oxyanions (V, U, Re, and Mo) in pore waters and sediments from a continental margin. *Geochimica et Cosmochimica Acta*, 69(21), pp.5021-5032.
- Morris, A.W., 1975. Dissolved molybdenum and vanadium in the northeast Atlantic Ocean. *Deep Sea Research and Oceanographic Abstracts*, 22(1), pp.49-54.
- Moulin, M., Fluteau, F., Courtillot, V., Marsh, J., Delpech, G., Quidelleur, X., Gérard, M. and Jay, A.E., 2011. An attempt to constrain the age, duration, and eruptive history of the Karoo flood basalt: Naude's Nek section (South Africa). *Journal of Geophysical Research: Solid Earth*, 116(B7). <https://doi.org/10.1029/2011JB008210>.
- Nägler, T.F., Anbar, A.D., Archer, C., Goldberg, T., Gordon, G.W., Greber, N.D., Siebert, C., Sohrin, Y. and Vance, D., 2014. Proposal for an international molybdenum isotope measurement standard and data representation. *Geostandards and Geoanalytical Research*, 38(2), pp.149-151.
- Nägler, T.F., Neubert, N., Böttcher, M.E., Dellwig, O. and Schnetger, B., 2011. Molybdenum isotope fractionation in pelagic euxinia: Evidence from the modern Black and Baltic Seas. *Chemical Geology*, 289(1-2), pp.1-11.
- Neely, R.A., Gislason, S.R., Ólafsson, M., McCoy-West, A.J., Pearce, C.R. and Burton, K.W., 2018. Molybdenum isotope behaviour in groundwaters and terrestrial hydrothermal systems, Iceland. *Earth and Planetary Science Letters*, 486, pp.108-118.
- Neubert, N., Nägler, T.F. and Böttcher, M.E., 2008. Sulfidity controls molybdenum isotope fractionation into euxinic sediments: Evidence from the modern Black Sea. *Geology*, 36(10), pp.775-778.
- Newton, R.J., Reeves, E.P., Kafousia, N., Wignall, P.B., Bottrell, S.H. and Sha, J.G., 2011. Low marine sulfate concentrations and the isolation of the European epicontinental sea during the Early Jurassic. *Geology*, 39(1), pp.7-10.
- Nielsen, L.P., 1992. Denitrification in sediment determined from nitrogen isotope pairing. *FEMS Microbiology Letters*, 86(4), pp.357-362.
- Nier, A.O., 1950. A redetermination of the relative abundances of the isotopes of carbon, nitrogen, oxygen, argon, and potassium. *Physical Review*, 77(6), pp.789-793.
- Och, L.M. and Shields-Zhou, G.A., 2012. The Neoproterozoic oxygenation event: environmental perturbations and biogeochemical cycling. *Earth-Science Reviews*, 110(1-4), pp.26-57.
- Ogg, J.G. and Hinnov, L.A., 2012. Jurassic (Chapter 26). In: Gradstein, F.M., Ogg, J.G., Schmitz, M., Ogg, G. (eds.), *The Geologic Time Scale 2012*, Elsevier, Amsterdam, pp.731-791.
- O'Leary, M.H., 1981. Carbon isotope fractionation in plants. *Phytochemistry*, 20(4), pp.553-567.

- Ossa Ossa F., Hofmann, A., Wille, M., Spangenberg, J.E., Bekker, A., Poulton, S.W., Eickmann, B. and Schoenberg, R., 2018. Aerobic iron and manganese cycling in a redox-stratified Mesoproterozoic epicontinental sea. *Earth and Planetary Science Letters*, 500, pp.28-40.
- Pancost, R.D., Crawford, N., Magness, S., Turner, A., Jenkyns, H.C. and Maxwell, J.R., 2004. Further evidence for the development of photic-zone euxinic conditions during Mesozoic oceanic anoxic events. *Journal of the Geological Society*, 161(3), pp.353-364.
- Pálffy, J. and Smith, P.L., 2000. Synchrony between Early Jurassic extinction, oceanic anoxic event, and the Karoo-Ferrar flood basalt volcanism. *Geology*, 28(8), pp.747-750.
- Pearce, C.R., Cohen, A.S., Coe, A.L. and Burton, K.W., 2008. Molybdenum isotope evidence for global ocean anoxia coupled with perturbations to the carbon cycle during the Early Jurassic. *Geology*, 36(3), pp.231-234.
- Percival, L.M., Cohen, A.S., Davies, M.K., Dickson, A.J., Hesselbo, S.P., Jenkyns, H.C., Leng, M.J., Mather, T.A., Storm, M.S. and Xu, W., 2016. Osmium isotope evidence for two pulses of increased continental weathering linked to Early Jurassic volcanism and climate change. *Geology*, 44(9), pp.759-762.
- Percival, L.M.E., Witt, M.L.I., Mather, T.A., Hermoso, M., Jenkyns, H.C., Hesselbo, S.P., Al-Suwaidi, A.H., Storm, M.S., Xu, W. and Ruhl, M., 2015. Globally enhanced mercury deposition during the end-Pliensbachian extinction and Toarcian OAE: A link to the Karoo–Ferrar Large Igneous Province. *Earth and Planetary Science Letters*, 428, pp.267-280.
- Pichat, S., Douchet, C. and Albarède, F., 2003. Zinc isotope variations in deep-sea carbonates from the eastern equatorial Pacific over the last 175 ka. *Earth and Planetary Science Letters*, 210(1-2), pp.167-178.
- Poulson, R.L., Siebert, C., McManus, J. and Berelson, W.M., 2006. Authigenic molybdenum isotope signatures in marine sediments. *Geology*, 34(8), pp.617-620.
- Raucsik, B. and Varga, A., 2008. Climato-environmental controls on clay mineralogy of the Hettangian–Bajocian successions of the Mecsek Mountains, Hungary: an evidence for extreme continental weathering during the early Toarcian oceanic anoxic event. *Palaeogeography, Palaeoclimatology, Palaeoecology*, 265(1-2), pp.1-13.
- Redfield, A.C., 1934. On the proportions of organic derivatives in sea water and their relation to the composition of plankton (pp. 176-192). Liverpool: University Press of Liverpool.
- Reinhard, C.T., Planavsky, N.J., Robbins, L.J., Partin, C.A., Gill, B.C., Lalonde, S.V., Bekker, A., Konhauser, K.O. and Lyons, T.W., 2013. Proterozoic ocean redox and biogeochemical stasis. *Proceedings of the National Academy of Sciences*, 110(14), pp.5357-5362.
- Remírez, M.N. and Algeo, T.J., 2020. Carbon-cycle changes during the Toarcian (Early Jurassic) and implications for regional versus global drivers of the Toarcian oceanic anoxic

event. *Earth-Science Reviews*, p.103283.
<https://doi.org/10.1016/j.earscirev.2020.103283>.

- Riccardi, A., Kump, L.R., Arthur, M.A. and D'Hondt, S., 2007. Carbon isotopic evidence for chemocline upward excursions during the end-Permian event. *Palaeogeography, Palaeoclimatology, Palaeoecology*, 248(1-2), pp.73-81.
- Richoz, S., van De Schootbrugge, B., Pross, J., Püttmann, W., Quan, T.M., Lindström, S., Heunisch, C., Fiebig, J., Maquil, R., Schouten, S. and Hauzenberger, C.A., 2012. Hydrogen sulphide poisoning of shallow seas following the end-Triassic extinction. *Nature Geoscience*, 5(9), pp.662-667.
- Riegraf, W., 1985. Mikrofauna, Biostratigraphie und Fazies im Unteren Toarcium Südwestdeutschlands und Vergleich mit benachbarten Gebieten.
- Rodríguez-Tovar, F.J., 2021. Ichnology of the Toarcian Oceanic Anoxic Event: An underestimated tool to assess palaeoenvironmental interpretations. *Earth-Science Reviews*, p.103579. <https://doi.org/10.1016/j.earscirev.2021.103579>.
- Rosales, I., Quesada, S. and Robles, S., 2004. Paleotemperature variations of Early Jurassic seawater recorded in geochemical trends of belemnites from the Basque–Cantabrian basin, northern Spain. *Palaeogeography, Palaeoclimatology, Palaeoecology*, 203(3-4), pp.253-275.
- Rosman, K.J.R., 1972. A survey of the isotopic and elemental abundance of zinc. *Geochimica et Cosmochimica Acta*, 36(7), pp.801-819.
- Röhl, H.J., Schmid-Röhl, A., Oschmann, W., Frimmel, A. and Schwark, L., 2001. The Posidonia Shale (Lower Toarcian) of SW-Germany: an oxygen-depleted ecosystem controlled by sea level and palaeoclimate. *Palaeogeography, Palaeoclimatology, Palaeoecology*, 165(1-2), pp.27-52.
- Rubinson, M. and Clayton, R.N., 1969. Carbon-13 fractionation between aragonite and calcite. *Geochimica et Cosmochimica Acta*, 33(8), pp.997-1002.
- Rudnick, R.L., Gao, S., Holland, H.D. and Turekian, K.K., 2003. Composition of the continental crust. *The Crust*, 3, pp.1-64.
- Ruebsam, W., Mayer, B. and Schwark, L., 2019. Cryosphere carbon dynamics control early Toarcian global warming and sea level evolution. *Global and Planetary Change*, 172, pp.440-453.
- Ruebsam, W., Müller, T., Kovács, J., Pálffy, J. and Schwark, L., 2018. Environmental response to the early Toarcian carbon cycle and climate perturbations in the northeastern part of the West Tethys shelf. *Gondwana Research*, 59, pp.144-158.
- Ruebsam, W., Reolid, M. and Schwark, L., 2020. $\delta^{13}\text{C}$ of terrestrial vegetation records Toarcian CO_2 and climate gradients. *Scientific reports*, 10(1), pp.1-8.

- Ruvalcaba Baroni, I., Pohl, A., van Helmond, N.A., Papadomanolaki, N.M., Coe, A.L., Cohen, A.S., van de Schootbrugge, B., Donnadieu, Y. and Slomp, C.P., 2018. Ocean circulation in the Toarcian (Early Jurassic): A key control on deoxygenation and carbon burial on the European shelf. *Paleoceanography and Paleoclimatology*, 33(9), pp.994-1012.
- Sahoo, S.K., Planavsky, N.J., Kendall, B., Wang, X., Shi, X., Scott, C., Anbar, A.D., Lyons, T.W. and Jiang, G., 2012. Ocean oxygenation in the wake of the Marinoan glaciation. *Nature*, 489(7417), pp.546-549.
- Sælen, G., Tyson, R.V., Telnæs, N. and Talbot, M.R., 2000. Contrasting watermass conditions during deposition of the Whitby Mudstone (Lower Jurassic) and Kimmeridge Clay (Upper Jurassic) formations, UK. *Palaeogeography, Palaeoclimatology, Palaeoecology*, 163(3-4), pp.163-196.
- Scholz, F., Siebert, C., Dale, A.W. and Frank, M., 2017. Intense molybdenum accumulation in sediments underneath a nitrogenous water column and implications for the reconstruction of paleo-redox conditions based on molybdenum isotopes. *Geochimica et Cosmochimica Acta*, 213, pp.400-417.
- Schwark, L. and Frimmel, A., 2004. Chemostratigraphy of the Posidonia Black Shale, SW-Germany: II. Assessment of extent and persistence of photic-zone anoxia using aryl isoprenoid distributions. *Chemical Geology*, 206(3-4), pp.231-248.
- Scott, C. and Lyons, T.W., 2012. Contrasting molybdenum cycling and isotopic properties in euxinic versus non-euxinic sediments and sedimentary rocks: Refining the paleoproxies. *Chemical Geology*, 324, pp.19-27.
- Scott, R.A. and Turton, M.A., 2001. Mesozoic tectonic events in the North Atlantic and Arctic: stratigraphic response in an adjacent rift-flank basin (Sverdrup Basin, Arctic Canada). *Polarforschung*, 69, pp.73-83.
- Shields, G. and Veizer, J., 2002. Precambrian marine carbonate isotope database: Version 1.1. *Geochemistry, Geophysics, Geosystems*, 3(6). <https://doi.org/10.1029/2001GC000266>.
- Siebert, C., Nägler, T.F. and Kramers, J.D., 2001. Determination of molybdenum isotope fractionation by double-spike multicollector inductively coupled plasma mass spectrometry. *Geochemistry, Geophysics, Geosystems*, 2(7). <https://doi.org/10.1029/2000GC000124>.
- Siebert, C., Nägler, T.F., von Blanckenburg, F. and Kramers, J.D., 2003. Molybdenum isotope records as a potential new proxy for paleoceanography. *Earth and Planetary Science Letters*, 211(1-2), pp.159-171.
- Sigman, D.M., Casciotti, K.L., Andreani, M., Barford, C., Galanter, M.B.J.K. and Böhlke, J.K., 2001. A bacterial method for the nitrogen isotopic analysis of nitrate in seawater and freshwater. *Analytical Chemistry*, 73(17), pp.4145-4153.

- Sigman, D.M., Karsh, K.L. and Casciotti, K.L., 2009a. Nitrogen isotopes in the ocean. In *Encyclopedia of Ocean Sciences* (eds J Steele, S Thorpe and K Turekian), pp. 40–54. Amsterdam: Elsevier.
- Sigman, D.M., DiFiore, P.J., Hain, M.P., Deutsch, C., Wang, Y., Karl, D.M., Knapp, A.N., Lehmann, M.F. and Pantoja, S., 2009b. The dual isotopes of deep nitrate as a constraint on the cycle and budget of oceanic fixed nitrogen. *Deep Sea Research Part I: Oceanographic Research Papers*, 56(9), pp.1419-1439.
- Sigman, D.M. and Fripiat, F., 2019. Nitrogen isotopes in the ocean. *Encyclopedia of Ocean Sciences*, 1, pp.263-278.
- Sigman, D.M., Robinson, R., Knapp, A.N., Van Geen, A., McCorkle, D.C., Brandes, J.A. and Thunell, R.C., 2003. Distinguishing between water column and sedimentary denitrification in the Santa Barbara Basin using the stable isotopes of nitrate. *Geochemistry, Geophysics, Geosystems*, 4(5). <https://doi.org/10.1029/2002GC000384>.
- Stüeken, E.E., Kipp, M.A., Koehler, M.C. and Buick, R., 2016. The evolution of Earth's biogeochemical nitrogen cycle. *Earth-Science Reviews*, 160, pp.220-239.
- Stüeken, E.E., Zalomis, J., Meixnerová, J. and Buick, R., 2017. Differential metamorphic effects on nitrogen isotopes in kerogen extracts and bulk rocks. *Geochimica et Cosmochimica Acta*, 217, pp.80-94.
- Suan, G., Pittet, B., Bour, I., Mattioli, E., Duarte, L.V. and Mailliot, S., 2008. Duration of the Early Toarcian carbon isotope excursion deduced from spectral analysis: consequence for its possible causes. *Earth and Planetary Science Letters*, 267(3-4), pp.666-679.
- Suan, G., van De Schootbrugge, B., Adatte, T., Fiebig, J. and Oschmann, W., 2015. Calibrating the magnitude of the Toarcian carbon cycle perturbation. *Paleoceanography*, 30(5), pp.495-509.
- Svensen, H., Corfu, F., Polteau, S., Hammer, Ø. and Planke, S., 2012. Rapid magma emplacement in the Karoo large igneous province. *Earth and Planetary Science Letters*, 325, pp.1-9.
- Svensen, H., Planke, S., Chevallier, L., Malthe-Sørensen, A., Corfu, F. and Jamtveit, B., 2007. Hydrothermal venting of greenhouse gases triggering Early Jurassic global warming. *Earth and Planetary Science Letters*, 256(3-4), pp.554-566.
- Sweere, T.C., Dickson, A.J., Jenkyns, H.C., Porcelli, D., Elrick, M., van den Boorn, S.H. and Henderson, G.M., 2018. Isotopic evidence for changes in the zinc cycle during Oceanic Anoxic Event 2 (Late Cretaceous). *Geology*, 46(5), pp.463-466.
- Sweere, T.C., Dickson, A.J., Jenkyns, H.C., Porcelli, D. and Henderson, G.M., 2020. Zinc-and cadmium-isotope evidence for redox-driven perturbations to global micronutrient cycles during Oceanic Anoxic Event 2 (Late Cretaceous). *Earth and Planetary Science Letters*, 546, p.116427.

- Sweere, T., van den Boorn, S., Dickson, A.J. and Reichart, G.J., 2016. Definition of new trace-metal proxies for the controls on organic matter enrichment in marine sediments based on Mn, Co, Mo and Cd concentrations. *Chemical Geology*, 441, pp.235-245.
- Tesdal, J.E., Galbraith, E.D. and Kienast, M., 2013. Nitrogen isotopes in bulk marine sediment: linking seafloor observations with subseafloor records. *Biogeosciences*, 10(1), pp.101-118.
- Them, T.R., Gill, B.C., Selby, D., Gröcke, D.R., Friedman, R.M. and Owens, J.D., 2017. Evidence for rapid weathering response to climatic warming during the Toarcian Oceanic Anoxic Event. *Scientific Reports*, 7(1), pp.1-10.
- Thibault, N., Ruhl, M., Ullmann, C.V., Korte, C., Kemp, D.B., Gröcke, D.R. and Hesselbo, S.P., 2018. The wider context of the Lower Jurassic Toarcian oceanic anoxic event in Yorkshire coastal outcrops, UK. *Proceedings of the Geologists' Association*, 129(3), pp.372-391.
- Tipple, B.J. and Pagani, M., 2007. The early origins of terrestrial C4 photosynthesis. *Annu. Rev. Earth Planet. Sci.*, 35, pp.435-461.
- Tossell, J.A., 2005. Calculating the partitioning of the isotopes of Mo between oxidic and sulfidic species in aqueous solution. *Geochimica et Cosmochimica Acta*, 69(12), pp.2981-2993.
- Tribovillard, N., Algeo, T.J., Lyons, T. and Riboulleau, A., 2006. Trace metals as paleoredox and paleoproductivity proxies: an update. *Chemical Geology*, 232(1-2), pp.12-32.
- Tyrrell, T., 1999. The relative influences of nitrogen and phosphorus on oceanic primary production. *Nature*, 400(6744), pp.525-531.
- Ullmann, C.V., Thibault, N., Ruhl, M., Hesselbo, S.P. and Korte, C., 2014. Effect of a Jurassic oceanic anoxic event on belemnite ecology and evolution. *Proceedings of the National Academy of Sciences*, 111(28), pp.10073-10076.
- van Breugel, Y., Baas, M., Schouten, S., Mattioli, E. and Sinninghe Damsté, J.S., 2006. Isorenieratane record in black shales from the Paris Basin, France: Constraints on recycling of respired CO₂ as a mechanism for negative carbon isotope shifts during the Toarcian oceanic anoxic event. *Paleoceanography*, 21(4). <https://doi.org/10.1029/2006PA001305>.
- van de Schootbrugge, B., Bachan, A., Suan, G., Richoz, S. and Payne, J.L., 2013a. Microbes, mud and methane: cause and consequence of recurrent Early Jurassic anoxia following the end-Triassic mass extinction. *Palaeontology*, 56(4), pp.685-709.
- van de Schootbrugge, B., Bailey, T.R., Rosenthal, Y., Katz, M.E., Wright, J.D., Miller, K.G., Feist-Burkhardt, S. and Falkowski, P.G., 2005. Early Jurassic climate change and the radiation of organic-walled phytoplankton in the Tethys Ocean. *Paleobiology*, 31(1), pp.73-97.

- van de Schootbrugge, B. and Gollner, S., 2013b. Altered primary production during mass-extinction events. *The Paleontological Society Papers*, 19, 87-114.
- Vance, D., Little, S.H., Archer, C., Cameron, V., Andersen, M.B., Rijkenberg, M.J. and Lyons, T.W., 2016. The oceanic budgets of nickel and zinc isotopes: the importance of sulfidic environments as illustrated by the Black Sea. *Philosophical Transactions of the Royal Society A: Mathematical, Physical and Engineering Sciences*, 374(2081), p.20150294.
- Vogel, J.C., Grootes, P.M. and Mook, W.G., 1970. Isotopic fractionation between gaseous and dissolved carbon dioxide. *Zeitschrift für Physik A Hadrons and Nuclei*, 230(3), pp.225-238.
- Walker, A.J. and Ho, L.C., 1977. Carbon translocation in the tomato: effects of fruit temperature on carbon metabolism and the rate of translocation. *Annals of Botany*, 41(4), pp.825-832.
- Wang, D., Ling, H.F., Struck, U., Zhu, X.K., Zhu, M., He, T., Yang, B., Gamper, A. and Shields, G.A., 2018. Coupling of ocean redox and animal evolution during the Ediacaran-Cambrian transition. *Nature Communications*, 9(1), pp.1-8.
- Wang, Y., Ossa Ossa, F., Spangenberg, J.E., Wille, M. and Schoenberg, R., 2021. Restricted oxygen-deficient basins on the northern European epicontinental shelf across the Toarcian carbon isotope excursion interval. *Paleoceanography and Paleoclimatology*, 36(6). <https://doi.org/10.1029/2020PA004207>.
- Wang, Y., Ossa Ossa, F., Wille, M., Schurr, S., Saussele, M.E., Schmid-Röhl, A. and Schoenberg, R., 2020. Evidence for local carbon-cycle perturbations superimposed on the Toarcian carbon isotope excursion. *Geobiology*, 18(6), pp.682-709.
- Watanabe, Y., Naraoka, H., Wronkiewicz, D.J., Condie, K.C. and Ohmoto, H., 1997. Carbon, nitrogen, and sulfur geochemistry of Archean and Proterozoic shales from the Kaapvaal Craton, South Africa. *Geochimica et Cosmochimica Acta*, 61(16), pp.3441-3459.
- Weber, T., John, S., Tagliabue, A. and DeVries, T., 2018. Biological uptake and reversible scavenging of zinc in the global ocean. *Science*, 361(6397), pp.72-76.
- Wickman, F.E., 1956. The cycle of carbon and the stable carbon isotopes. *Geochimica et Cosmochimica Acta*, 9(3), pp.136-153.
- Wignall, P.B. and Hallam, A., 1991. Biofacies, stratigraphic distribution and depositional models of British onshore Jurassic black shales. *Geological Society, London, Special Publications*, 58(1), pp.291-309.
- Wyatt, N.J., Milne, A., Woodward, E.M.S., Rees, A.P., Browning, T.J., Bouman, H.A., Worsfold, P.J. and Lohan, M.C., 2014. Biogeochemical cycling of dissolved zinc along the GEOTRACES South Atlantic transect GA10 at 40 S. *Global Biogeochemical Cycles*, 28(1), pp.44-56.
- Xu, W., Ruhl, M., Jenkyns, H.C., Hesselbo, S.P., Riding, J.B., Selby, D., Naafs, B.D.A., Weijers, J.W., Pancost, R.D., Tegelaar, E.W. and Idiz, E.F., 2017. Carbon sequestration

in an expanded lake system during the Toarcian oceanic anoxic event. *Nature Geoscience*, 10(2), pp.129-134.

Xu, W., Ruhl, M., Jenkyns, H.C., Leng, M.J., Huggett, J.M., Minisini, D., Ullmann, C.V., Riding, J.B., Weijers, J.W., Storm, M.S. and Percival, L.M., 2018. Evolution of the Toarcian (Early Jurassic) carbon-cycle and global climatic controls on local sedimentary processes (Cardigan Bay Basin, UK). *Earth and Planetary Science Letters*, 484, pp.396-411.

Yan, B., Zhu, X., He, X. and Tang, S., 2019. Zn isotopic evolution in early Ediacaran ocean: A global signature. *Precambrian Research*, 320, pp.472-483.

Zeebe, R.E. and Wolf-Gladrow, D., 2001. CO₂ in seawater: equilibrium, kinetics, isotopes. Elsevier Oceanography Series (No. 65), pp.1-360.

Zhang, X., Sigman, D.M., Morel, F.M. and Kraepiel, A.M., 2014. Nitrogen isotope fractionation by alternative nitrogenases and past ocean anoxia. *Proceedings of the National Academy of Sciences*, 111(13), pp.4782-4787.

APPENDIX

Appendix A

Wang et al. (2020). Evidence for local carbon-cycle perturbations superimposed on the Toarcian carbon isotope excursion. *Geobiology*, 18(6), pp.682-709.

Appendix B

Wang et al. (2021). Restricted oxygen-deficient basins on the northern European epicontinental shelf across the Toarcian carbon isotope excursion interval. *Paleoceanography and Paleoclimatology*, 36(6).
<https://doi.org/10.1029/2020PA004207>.


Appendix C

Wang et al. (ready for submission) Zinc geochemical cycling response to the Early Jurassic (Toarcian: ~183 Ma) marine anoxia and its paleoenvironmental significance.

Appendix D

Analytical methods

Evidence for local carbon-cycle perturbations superimposed on the Toarcian carbon isotope excursion

Yunfeng Wang¹  | Frantz Ossa Ossa^{1,2} | Martin Wille³ | Simon Schurr⁴ | Mario-Erich Saussele¹ | Annette Schmid-Röhl⁵ | Ronny Schoenberg^{1,2}

¹Department of Geosciences, University of Tuebingen, Tuebingen, Germany

²Department of Geology, University of Johannesburg, Johannesburg, South Africa

³Institute of Geological Sciences, University of Bern, Bern, Switzerland

⁴Institute of Geology and Paleontology, University of Muenster, Muenster, Germany

⁵Fossil Museum and Werkforum, Holcim (Süddeutschland) GmbH, Dotternhausen, Germany

Correspondence

Yunfeng Wang, Department of Geosciences, University of Tuebingen, Schnarrenbergstrasse 94-96, 72076 Tuebingen, Germany.
Emails: yunfeng.wang@uni-tuebingen.de; w727801127@hotmail.com

Funding information

China Scholarship Council.

Abstract

A Jurassic negative carbon isotope excursion (CIE), co-evolved with Toarcian Oceanic Anoxic Event (OAE) at ~183 Ma, is suggested to be linked to a global carbon-cycle perturbation and is well documented for Toarcian terrestrial fossil woods and marine sediments around the globe. A theoretically coupled $\delta^{13}\text{C}_{\text{carb}}-\delta^{13}\text{C}_{\text{org}}$ pattern due to such dubbed global carbon-cycle event from the negative CIE in Dotternhausen Toarcian stratigraphic profile (southwest Germany) is unexpectedly disturbed by two-step $\delta^{13}\text{C}_{\text{carb}}-\delta^{13}\text{C}_{\text{org}}$ decoupling in which the last step, upper in the stratigraphic order, is of higher magnitude. However, the trigger(s) for these sudden decoupling disturbances are still poorly constrained. Here, connecting new carbon and oxygen isotope data with documentary lipid biomarkers shows that the global carbon cycle during the Toarcian OAE was disturbed by enhanced green sulfur bacteria (GSB) metabolisms and early diagenesis at local scales. The first step $\delta^{13}\text{C}_{\text{carb}}-\delta^{13}\text{C}_{\text{org}}$ decoupling was induced in the initial stage of the GSB bloom. The second step of much larger $\delta^{13}\text{C}_{\text{carb}}-\delta^{13}\text{C}_{\text{org}}$ decoupling arising from a GSB prosperity was, however, exaggerated by early diagenesis through the respiration of sulfate-reducing bacteria (SRB). Paleo-geographically distinct localities of the Tethys region show contrasting decoupled $\delta^{13}\text{C}_{\text{carb}}-\delta^{13}\text{C}_{\text{org}}$ patterns, which implies that the second-order carbon-cycle perturbations have pervasively and independently impacted the global carbon event during the Toarcian OAE.

KEYWORDS

carbon isotope excursion, green sulfur bacteria, local carbon cycling, Toarcian, $\delta^{13}\text{C}_{\text{carb}}-\delta^{13}\text{C}_{\text{org}}$ decoupling

1 | INTRODUCTION

Sudden and large-magnitude changes in global carbon-cycle perturbations along with carbon isotope excursions (CIEs) seem to be recurrent phenomena during greenhouse periods in Earth's history

(Jenkyns, 2010). One of the considerably negative CIEs in Earth's history occurred during the Early Jurassic, near-contemporaneously with the Toarcian Oceanic Anoxic Event (OAE at ~183 Ma; Jenkyns, 1988). The Toarcian OAE was a time of severe environmental change that was linked to elevated continental weathering rates (Cohen,

[Correction added on 15 September 2020, after first online publication: The order of Figures 4, 5 and 6 has been swapped.]

This is an open access article under the terms of the Creative Commons Attribution License, which permits use, distribution and reproduction in any medium, provided the original work is properly cited.

© 2020 The Authors. *Geobiology* published by John Wiley & Sons Ltd

Coe, Harding, & Schwark, 2004; Percival et al., 2016; Them et al., 2017), marine mass extinctions (Danise, Twitchett, & Little, 2015; Little & Benton, 1995; Wignall et al., 2006), biocalcification crises (Han, Hu, Kemp, & Li, 2018; Trecalli et al., 2012), widespread anoxia (Pearce, Cohen, Coe, & Burton, 2008), and considerable accumulation of organic-rich sediments (Baudin, Herbin, & Vandenbroucke, 1990; Jenkyns, 1988). This event is generally accompanied by a globally synchronous ~3–7‰ negative CIE, expressed in terrestrial fossil wood (e.g., Hesselbo, Jenkyns, Duarte, & Oliveira, 2007), land plant lipids (Ruebsam, Reolid, & Schwark, 2020; Xu et al., 2017), marine carbonates, and organic matters (e.g., Caruthers, Gröcke, & Smith, 2011; Hesselbo et al., 2000; Xu et al., 2018), interrupting a longer term positive excursion (Jenkyns et al., 2002) attributed to the global increase in organic carbon burial (Jenkyns, 2010). It has been constrained that the observed early Toarcian carbon-cycle perturbation to the global-scale exogenic carbon cycle was probably linked to the injection of massive amounts of CO₂ into the atmosphere-ocean system following the emplacement of the Karoo-Ferrar large igneous province (e.g., Svensen et al., 2007) and/or large-scale release of thermogenic/biogenic methane (e.g., Hesselbo et al., 2000; Kemp, Coe, Cohen, & Schwark, 2005). However, so far, the most negative $\delta^{13}\text{C}_{\text{org}}$ values down to -33‰ during these Toarcian CIEs (e.g., Hesselbo et al., 2000; Kemp, Coe, Cohen, & Schwark, 2005) are not compelling for the typical light carbon isotope compositions of <-35‰ for heterotrophic-derived biomass involving methane as the main carbon source (e.g., Hinrichs, 2002; Raghoebarsing et al., 2006). Nevertheless, considering the confirmed global perturbation of the carbon cycle during the Toarcian OAE and the subsequent equilibration between the dissolved inorganic carbon (DIC) and dissolved organic carbon (DOC) reservoirs, a co-variation between $\delta^{13}\text{C}_{\text{carb}}$ and $\delta^{13}\text{C}_{\text{org}}$ would be expected (Knoll, Hayes, Kaufman, Swett, & Lambert, 1986). However, a number of studies have observed unpaired curves between $\delta^{13}\text{C}_{\text{carb}}$ and $\delta^{13}\text{C}_{\text{org}}$ records in Toarcian OAE stratigraphic profiles (Fu et al., 2016; Han, Hu, Kemp, & Li, 2018; Hermoso et al., 2012; Röhl, Schmid-Röhl, Oschmann, Frimmel, & Schwark, 2001), indicating that second-order carbon cycles might have played a significant role during the Toarcian OAE. In general, unmatched $\delta^{13}\text{C}_{\text{carb}}$ and $\delta^{13}\text{C}_{\text{org}}$ records can be diagnostic for post-depositional diagenetic alteration, hydrocarbon contamination, DOC contribution, terrestrial contamination (Jiang et al., 2012; Maloof et al., 2010), or metabolisms by Chlorobiaceae, such as green sulfur bacteria (GSB), which are anoxygenic phototrophs that are able to oxidize hydrogen sulfide (H₂S) to sulfate (SO₄²⁻) at low light availability (Riccardi, Kump, Arthur, & D'Hondt, 2007). However, how and to what extent second-order carbon cycling is responsible for the observed Toarcian OAE $\delta^{13}\text{C}_{\text{carb}}$ - $\delta^{13}\text{C}_{\text{org}}$ decoupling remain poorly constrained. Therefore, little attention has been attributed to carbon-cycle perturbations at a local scale. As such, a more comprehensive understanding of the features of the Toarcian negative CIEs might be, in part, hindered when correlating the Toarcian OAE chemostratigraphy worldwide.

This study re-investigates the nature of the Toarcian CIE for both the DIC and DOC reservoirs at the Toarcian OAE sedimentary section of Dotternhausen, Germany, which is characterized

by well-preserved organic-rich sediments (Röhl, Schmid-Röhl, Oschmann, Frimmel, & Schwark, 2001). Thus, these sediments provide an especially valuable archive for tracking coeval carbon-cycle processes and evolution of the contemporaneous biosphere (Schwark & Frimmel, 2004). To do so, new outcrop and drillcore samples from the Dotternhausen section were sampled at a high-stratigraphic resolution for integrated analyses of bulk $\delta^{13}\text{C}_{\text{carb}}$, $\delta^{13}\text{C}_{\text{org}}$, $\delta^{18}\text{O}_{\text{carb}}$, total organic carbon on a carbonate-free base (TOC_{cf}), carbonate concentration, and major- and trace-elemental contents. Additionally, we compiled and compared the previously published $\delta^{13}\text{C}_{\text{carb}}$ - $\delta^{13}\text{C}_{\text{org}}$ records from geographically different Toarcian OAE localities (Bilong Co section in eastern Tethys, Fu et al., 2016; Sancerre section in northwestern Tethys, Hermoso et al., 2012; and Nianduo section in southeastern Tethys, Han, Hu, Kemp, & Li, 2018), in order to investigate whether second-order carbon-cycle processes may have superimposed the Toarcian OAE $\delta^{13}\text{C}_{\text{carb}}$ and $\delta^{13}\text{C}_{\text{org}}$ records on a global scale.

2 | GEOLOGICAL BACKGROUND

During the Jurassic, most of present-day Europe was located on a broad and shallow continental shelf that deepened toward the south-east Tethys Ocean (Jenkyns, 2010) (Figure 1a). The coeval shallow shelf was marked by several sub-basins within which the water-mass circulation was hydrographically restricted (McArthur et al., 2008; Röhl, Schmid-Röhl, Oschmann, Frimmel, & Schwark, 2001). Moreover, global warming linked to the massive carbon emissions (Cohen, Coe, Harding, & Schwark, 2004; Hesselbo et al., 2000; Kemp, Coe, Cohen, & Schwark, 2005; Ruebsam, Münzberger, & Schwark, 2014; Ruebsam, Mayer, & Schwark, 2019) as well as tectonic activities (e.g., breakup of the Pangaea Supercontinent) may jointly have been responsible for a major marine transgression and deoxygenation during the early Jurassic (Toarcian), at least in the vastly extending shallow marine areas developed by the opening Tethys Ocean. These prominent changes in paleoceanic conditions and paleoclimate were likely responsible for the widespread deposition of organic-rich sediments during that time (e.g., Baudin, Herbin, & Vandenbroucke, 1990).

The Toarcian OAE Dotternhausen sedimentary section (48°13'32.60"N, 8°46'29.76"E), geographically situated in southwestern Germany, represents a mid-paleo-latitude basin, at the southern margins of European epicontinental seaways, which bridged the northwest Tethys Ocean and the Boreal Sea during the Early Jurassic (Ziegler, 1988) (Figure 1b,c). This section exhibits the well-studied, and laterally widespread, Lower Toarcian Posidonia Shales, which are world-famous for their exceptionally well-preserved fossils and their high organic matter content (up to 16 wt.% TOC) (Bour, Mattioli, & Pittet, 2007; Fantasia, Föllmi, Adatte, Spangenberg, & Montero-Serrano, 2018; Montero-Serrano et al., 2015; Ruebsam, Münzberger, & Schwark, 2014; Song, Littke, & Weniger, 2017). The sedimentary rocks are exceptionally well preserved and thus provide an ideal stratigraphic sequence to investigate the Toarcian OAE and compare it with the worldwide negative

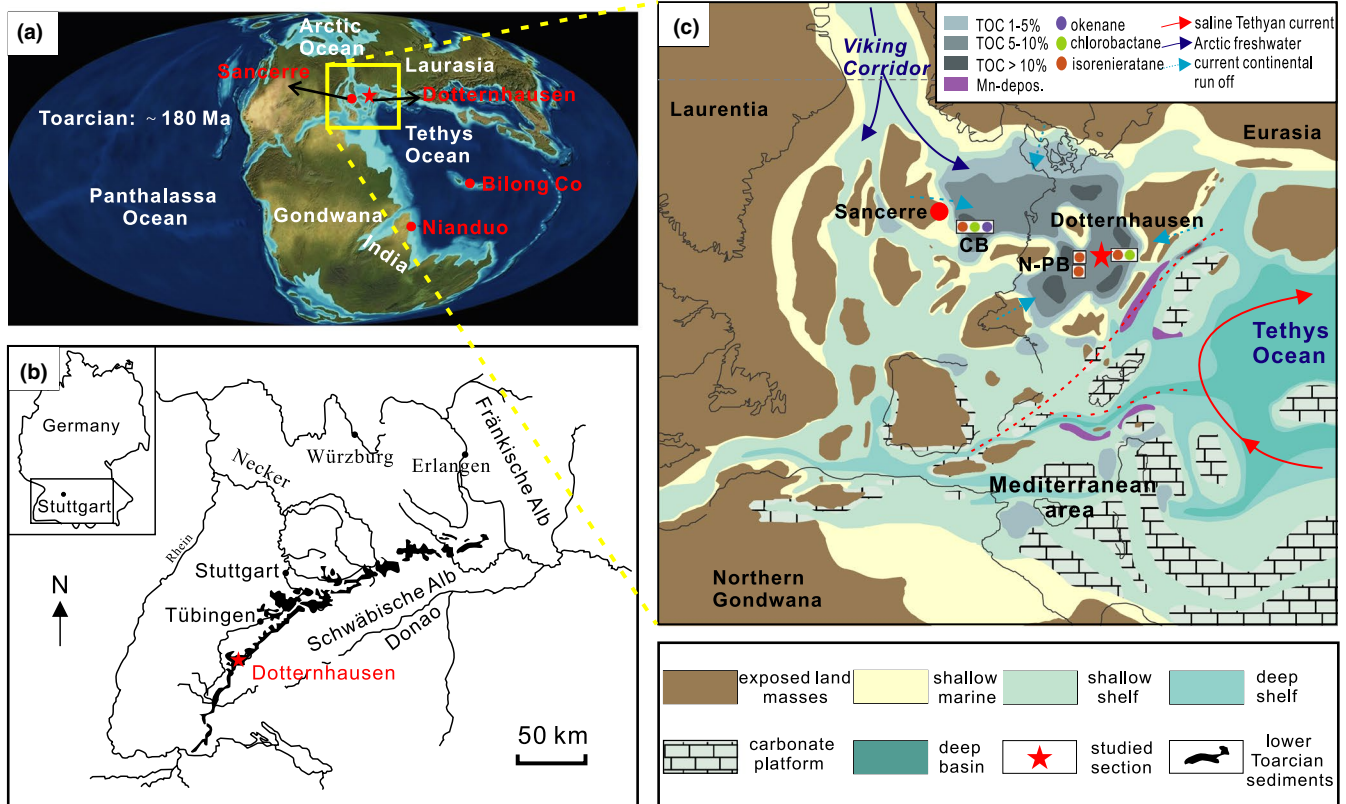


FIGURE 1 (a) Global paleogeography of the early Toarcian showing northwestern Tethys shelf seas (adapted from Ron Blakey, <http://jan.ucc.nau.edu/~rcb7/>); (b) present location of the studied Dotternhausen quarry (modified after Röhl, Schmid-Röhl, Oschmann, Frimmel, & Schwark, 2001); (c) paleogeography of the northwestern Tethys shelf area, an epicontinental shelf sea that opened toward the Tethys in the southeast (modified after Ruebsam, Münzberger, & Schwark, 2014). During early Toarcian, contrasting paleogeographic settings were probably linked to the influence of different current systems (Bjerrum, Surlyk, Callomon, & Slingerland, 2001; Mattioli, Pittet, Suan, & Mailliot, 2008). Total organic carbon (TOC) and biomarker data in Dotternhausen (red star), Cleveland Basin (CB), and northern Paris Basin (N-PB) are from Schouten, van Kaam-Peters, Rijpstra, Schoell, & Damsté (2000), French et al. (2014) and van Breugel, Baas, Schouten, Mattioli, & Sinninghe Damsté (2006), respectively. The geographically distant localities of Bilong Co, Nianduo and Sancerre (red dots) were compared in this study

CIE records (Röhl, Schmid-Röhl, Oschmann, Frimmel, & Schwark, 2001). The Dotternhausen sedimentary section has been litho- and bio-stratigraphically well characterized, mainly including three ammonite zones (*tenuicostatum*, *falciferum*, and *bifrons*) and some subzones (*elegantulum*, *exaratum*, *elegans*, and *falciferum*; Figure 2), though the transition between the *tenuicostatum* and *falciferum* zones remains not precisely constrained due to a lack of standard fossils and/or to the existing stratigraphic gap in the Pliensbachian-Toarcian boundary interval (Kuhn & Etter, 1994). Furthermore, the whole section has been investigated and subdivided into three contrasting lithofacies units in ascending order: bioturbated mudstones (1,180–980 cm), laminated oil shales (980–550 cm), and bituminous mudstones (550–0 cm), respectively, in terms of the amounts of organic matter and the types of fabric (cf. Röhl, Schmid-Röhl, Oschmann, Frimmel, & Schwark, 2001). This study only shows the sedimentary strata from 1,180 to 560 cm (Figure 2), which include the Toarcian negative CIE. The laminated oil shale unit is largely limited to the uppermost part of *tenuicostatum* zone and the lower and middle parts of the *falciferum* zone (Figure 2), is marked by a complete lack of benthic fauna, and exhibits a distinct micro-lamination.

The laminated oil shale unit is separated by three calcite-rich beds in different thickness, Unterer Stein, Steinplatte, and Oberer Stein from the bottom up (Frimmel, Oschmann, & Schwark, 2004) (Figures 2 and 3a). The thickest one, Unterer Stein (20–30 cm) in the *exaratum* subzone (Figures 2 and 3b), can serve as an efficient stratigraphic marker across Germany, Switzerland, and France within the Lower Toarcian Posidonia Shales in European epicontinental basins/shelves (Kuhn & Etter, 1994; van de Schootbrugge et al., 2005). An increasing body of evidence indicates that the Unterer Stein is an early diagenetic precipitate associated with organic matter remineralization enhanced by bacterial sulfate reduction within the sediment (Röhl and Schmid-Röhl, 2005; Röhl, Schmid-Röhl, Oschmann, Frimmel, & Schwark, 2001). Moreover, the carbonate fraction in the laminated oil shale facies in the Dotternhausen section was primarily derived from the hard parts of calcareous phytoplankton, including coccolithophorids and schizosphaerelle (Röhl, Schmid-Röhl, Oschmann, Frimmel, & Schwark, 2001), which is in contrast to the Unterer Stein bed which comprises only few fecal pellets (figure 5 of Frimmel, Oschmann, & Schwark, 2004). More detailed geological and paleontological descriptions of the Dotternhausen section can

FIGURE 2 Facies distribution and lamination types of the Dotternhausen section during Toarcian OAE (modified after Röhl, Schmid-Röhl, Oschmann, Frimmel, & Schwark, 2001)

Dotternhausen Section

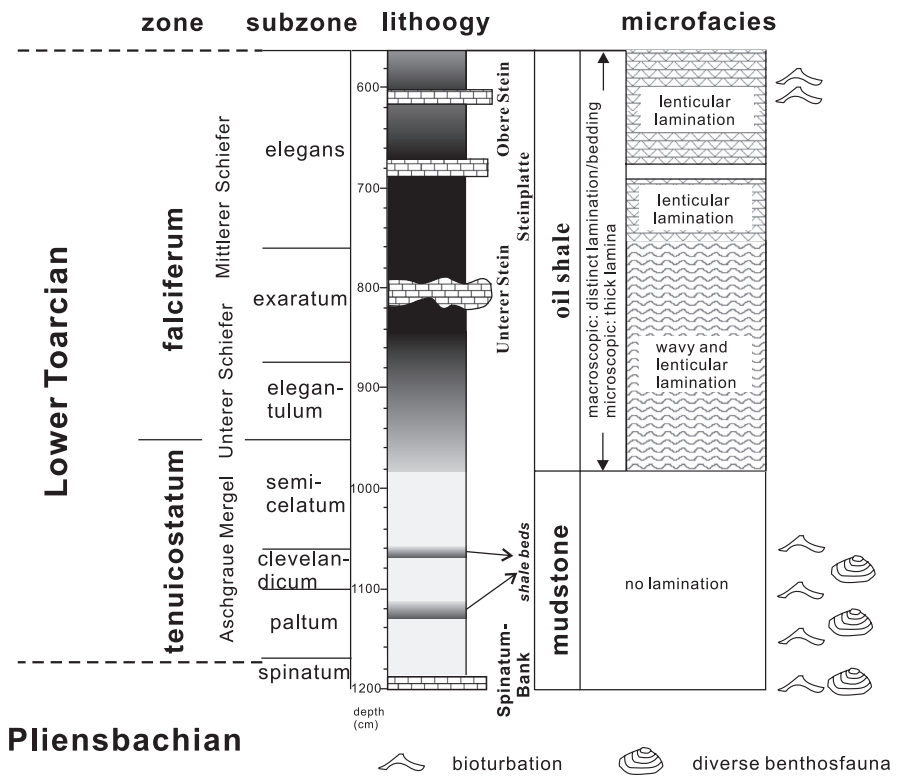
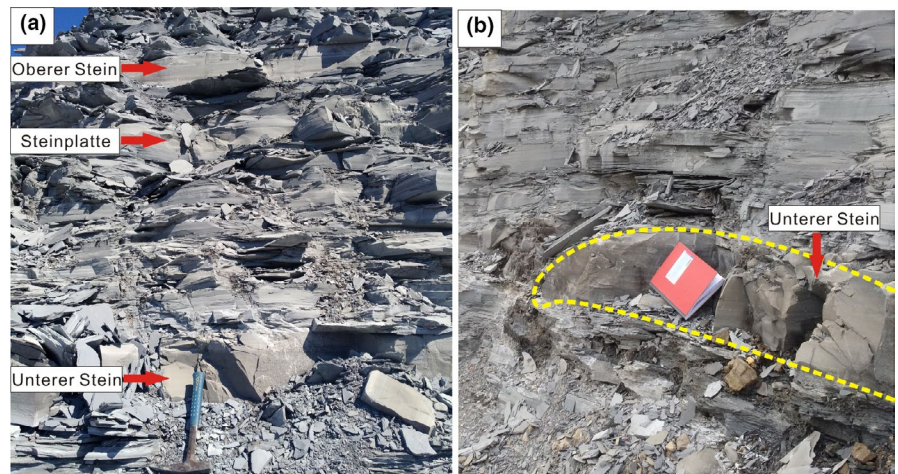


FIGURE 3 Photographs of the Dotternhausen sedimentary section. (a) Dotternhausen Toarcian CIE black shale facies intercalated by three limestone beds (Unterer Stein, Steinplatte and Oberer Stein). (b) Diagenetic Unterer Stein carbonate bed with the thickness of 20–30 cm



be found in previous publications (cf. Röhl and Schmid-Röhl, 2005; Röhl, Schmid-Röhl, Oschmann, Frimmel, & Schwark, 2001).

3 | MATERIALS AND METHODS

Samples of this study include gray mudstones, black shales, and diagenetic limestones taken from the stratigraphic section of the Dotternhausen profile (Figure 2) between depths of 610 m (upper *falciferum elegans*, starting with the limestone unit “Oberer Stein”) and 1,010 m (upper *tenuicostatum semicelatum*) at a high resolution with an average spacing of 3.5 cm. Notably, outcrop samples were

taken on a freshly quarried surface avoiding the long-term influence from surface weathering and contamination by vegetation. Powders from outcrop and drillcore samples were prepared using a diamond-mounted driller and dried at 60°C for further analyses.

3.1 | Elemental analyses

3.1.1 | Major elements analyses

100 mg sample powders were mixed with 500 mg of Merck Spectromelt® A12 and were heated to 1,050°C for 30 min using

Oxiflux system to prepare homogeneous glass beads. These beads were then dissolved in polypropylene bottles using 100 g of 2% HNO_3 to a dilution factor of $\sim 1,000$ and then were diluted with 2% HNO_3 to obtain a final dilution factor of 1:150,000 for major element concentration measurement. Loss on ignition (LOI) was determined on a separate ~ 100 mg sample aliquot by the weight loss after 60 min of heating in a furnace at $1,050^\circ\text{C}$. Analyses were carried out on a Thermo Fisher Scientific iCap-Qc quadrupole inductively coupled plasma mass spectrometer (Q-ICP-MS) using a similar experimental design as described in detail below for the trace element determinations (Section 3.1.2.). Calibration for sample unknowns used the powder reference materials W-2a (United States Geological Survey; USGS) prepared as above and using the major element values reported in Govindaraju & Roelandts (1989). Secondary quality control standards were also prepared from the international reference materials (QS-1, OU-6, SCo-1, and AGV-2), and the precision range of major elements relative to the recommended values from GeoReM. Data are reported as elemental concentrations expressed in weight percent (wt.%), and generally, uncertainties for major elements are better than 1 wt.% (1σ).

3.1.2 | Trace elements analyses

~ 200 mg of dried powder materials was weighted and ashed in a furnace at 500°C for 15 hr to oxidize organic matter. These ashed sample powders were re-weighed immediately upon cooling to determine the loss of weight during the ashing process. ~ 25 mg of ashed powders was weighed and digested in a 4 ml (4:1) HF- HNO_3 volumetric mixture on hot plates at 120°C for 2 days. Following digestion, the dissolved sample mixtures were evaporated, and the residues were reacted with 2 ml 6 M HCl at 120°C for 24 hr to dissolve potential fluorides. Upon drying the samples, they were taken up in 1 ml 14.5 M HNO_3 , heated to 120°C for 1 hr and dried again to volatilize excess fluorine and chlorine. This last step was repeated to ensure full conversion of the samples to nitric form. The samples were then taken up in 1 ml 5 M HNO_3 and gravimetrically diluted to ~ 30 ml 2% HNO_3 stock solutions with a nominal dilution factor of $\sim 1,000$. Powders of rock reference materials used for calibration and quality control were also digested using this procedure. For analyses, all stock solutions were then further diluted with 2% HNO_3 to a nominal, gravimetric dilution factor of $\sim 10,000$. This 2% HNO_3 , as an internal standard during ICP-MS analysis, contains a mixed spike of ^6Li (~ 3 ng/g), In (~ 1 ng/g), Re (~ 1 ng/g), and Bi (~ 1 ng/g). All samples were measured using a Thermo Fisher Scientific iCap-Qc ICP-MS coupled to an ESI SC-2 DX autosampler with an ESI Fast uptake system equipped with a 4 ml sample loop. All sample liquids were introduced from the loop using the iCap-Q peristaltic pump (at 30–35 rpm) and aspirated with a PFA nebulizer into a Peltier-cooled cyclonic spray chamber. The nebulizer and cool gas flow rates were typically ~ 1 and 14 L/min, respectively, and the interface was configured with Ni sampler cone, with a Cu core and Ni skimmer cone with a high-matrix insert.

The analytical procedure was analogous to that described in previous studies (Albut et al., 2018; Babechuk, Widdowson, Murphy, & Kamber, 2015; Kamber, Webb, & Gallagher, 2014). Oxide/hydroxide interference rates of Ba on Eu, Nd on the MREE to HREE (Gd, Tb, Dy, Er), Zr, on Ag, and the isobaric overlap of ^{160}Dy on ^{160}Gd were quantified ahead of each experiment. Remaining interference “rates” were determined according to a previous quantification scaled to the daily Nd oxide on Gd production rate (Aries et al., 2007; Ulrich, Kamber, Woodhead, & Spencer, 2010). A daily measurement of the $^6\text{Li}/^7\text{Li}$ ratio in unspiked USGS standard AGV-2 was also applied to determine a correction factor for the contribution of natural ^6Li in sample unknowns. Experimental sequences contained measurements of the internal standard-bearing carrier acid, procedural blanks, rock calibration (W-2a), and quality control standard (OU-6, QS-1, BCR-2, BHVO-2, BIR-1, and IF-G), sample unknowns, and a final batch of standards. Repeated measurement of a monitor solution (mixture of dissolved rock standards) was made every 5–7 samples for external drift correction remaining after internal standard spike correction. Following the introduction of each sample liquid into the ICP-MS, the sample uptake probe and tubing were rinsed with 5% HNO_3 . Additional washing with acid blank bracketed monitor samples or was placed between samples known or expected to have contrasting matrices or analyte abundance. In the course of experiments, analyte isotopes were measured in the iCap-Q STD mode, typically with five repeats of 25–30 sweeps at 3 channels (0.1 amu spacing) and analyte dwell times ranging from 10–30 ms. Mean analyte intensities were corrected offline for blank, isobaric interferences, and signal drift. Corrected intensities were calibrated using the average response of repeated measurements (5–8) of the USGS reference material W-2a at different dilution factors ($\sim 10,000$, $\sim 20,000$, and $\sim 40,000$), which was prepared from at least three separate powder digestions. The calibration lines that show tighter ranges were constructed using the laboratory's preferred analyte concentrations for the W-2a standard. The overall intermediate method precision and accuracy are monitored using the repeated measurements of reference materials (OU-6, QS-1, BCR-2, BHVO-2, BIR-1, and IF-G), representing a range in analyte concentrations and sample matrices. The method precision, estimated from the 1 r.s.d of the mean, is better than 3% for most elements.

3.2 | TOC_{cf} and carbonate content analyses

To avoid biases related to carbonate (CaCO_3) dilution, this study reports carbon-free total organic carbon contents (TOC_{cf}). Powdered mudstone and shale samples had thus to be decarbonized in 15-ml centrifuge tubes by drop-wise addition of 16% HCl at room temperature to remove all inorganic carbon. The residual samples were then centrifuged for 10 min at 246 g, decanted and again mixed with approximately 10 ml Milli-Q H_2O . This procedure was repeated 7–10 times until the samples were neutralized. Upon complete drying of the samples, between 5 and 70 mg of decalcified samples were weighed into tin-capsules. TOC_{cf} concentrations

were performed with a VARIO EL Elemental Analyzer at Center for Applied Geosciences, University of Tuebingen, Germany. Acetanilide standard (C_8H_9NO , 71.9% Carbon, 10.36% Nitrogen) was analyzed at the beginning, middle, and end of each sample set. All the measured TOC_{cf} contents were reported as a weight percent (wt.%) of the total fraction, and the external reproducibility is better than 1 wt.% (1σ). Decalcifying procedures refer to organic carbon isotopic analysis (see below).

For the carbonate content measurement, the treatment procedures for the studied samples are described below for $\delta^{13}C_{carb}$ (Section 3.3). An almost perfect linear correlation ($R^2 = .9917$) between samples weight (for samples between 10 and 150 mg $CaCO_3$) and the 2nd peak area on the Finnigan MAT 252 gas source mass spectrometer (for further details see Spötl & Vennemann, 2003) allows for the calculation of the carbonate content in each specific sample. These calculated carbonate contents were then divided by total sample weights and multiplied with 100 to obtain the carbonate contents of the bulk samples in %.

3.3 | Bulk isotopic analyses

Carbonate fractions of the selected samples were measured for their $\delta^{13}C_{carb}$ and $\delta^{18}O$ compositions using a Finnigan MAT 252 gas source mass spectrometer combined with a Thermo-Finnigan Gasbench II/CTC Combi-Pal autosampler at the Isotope Geochemistry Laboratory, University of Tuebingen. Both devices are connected using the continuous flow technique with a He stream as carrier gas. ~50 mg gray mudstone and shale powders, and ~5 mg diagenetic limestone powders were loaded into 10-ml glass vials, sealed with a rubber septum. The vials were then placed in an aluminum tray and heated to 90°C. 20 drops of 99% phosphoric acid were added into the vials, after purging them with pure He gas. After 90 min' reaction time, the released CO_2 was transferred to the mass spectrometer using a He carrier gas via a GC gas column to separate other components. The collected CO_2 was analyzed relative to international reference materials (NBS18, $\delta^{13}C_{carb} = -5\text{‰}$, $\delta^{18}O = -22.96\text{‰}$ and NBS19, $\delta^{13}C_{carb} = 1.95\text{‰}$, $\delta^{18}O = -2.20\text{‰}$) and an internal laboratory tank gas standard, which was calibrated against the in-house Laaser marble reference material. All measured values are given in per mille (‰) notation relative to the Vienna PeeDee belemnite standard reference material (VPDB) for $\delta^{13}C$ and VPDB for $\delta^{18}O$. The repeatability and intermediate precision of the analyses were monitored by replicate measurements of the laboratory standard Laaser marble and the NBS18 and NBS19. All analyzed results have a reproducibility of $\pm 0.1\text{‰}$ (1σ) for both $\delta^{13}C_{carb}$ and $\delta^{18}O$.

Analyses of $\delta^{13}C_{org}$ were conducted on an Elemental Analyzer NC2500 connected to a Thermo Quest Delta Plus XL mass spectrometer in continuous flow online-mode at the Isotope Geochemistry Laboratory, University of Tuebingen. ~100 mg of sample powders was decalcified in 15-ml centrifuge tubes by drop-wise addition of 16% HCl to remove all inorganic carbon (TIC). Decalcified samples containing

0.05 mg carbon were weighed in tin capsules and combusted at 1,050°C in an oxidation tube and at 650°C in a reduction tube, before they were cooled in a watertrap and transferred through a GC gas column into the mass spectrometer. Sample organic carbon was measured relative to an internal acetanilide standard which is calibrated against an in-house (e.g., Laaser marble) and international reference material (USGS24, $\delta^{13}C_{org} = -16.00\text{‰}$). $\delta^{13}C_{org}$ results have an external reproducibility of $\pm 0.1\text{‰}$ (1σ) for shale and $\pm 0.2\text{‰}$ (1σ) for limestones.

4 | RESULTS

4.1 | Element geochemistry

The concentrations of major element oxides and trace element data of the measured samples from Dotternhausen are reported in Table 1. Aluminum oxide (Al_2O_3) in these Dotternhausen samples has a relatively low abundance (mean = 9.43 wt.%) (Table 1) compared to the upper continental crust (UCC: 15.4 wt.%) (McLennan, 2001). Except the Unterer Stein carbonate bed where manganese (Mn) concentration approaches 0.2 wt.%, the Dotternhausen Toarcian OAE profile remains relatively lower than that of the UCC (Table 1; Figure S1). The abundances of immobile trace elements thorium (Th), zirconium (Zr), and scandium (Sc) have a range of 5.1–11.4 $\mu\text{g/g}$, 64.7–184.3 $\mu\text{g/g}$, and 9.4–21.3 $\mu\text{g/g}$, respectively (Table 1). Relative to the UCC (Th: 10.7 $\mu\text{g/g}$, Zr: 190 $\mu\text{g/g}$, and Sc: 13.6 $\mu\text{g/g}$) (McLennan, 2001), the studied samples display low contents of Th (mean = 9.3 $\mu\text{g/g}$) and Zr (mean = 123.2 $\mu\text{g/g}$; Table 1), whereas the mean concentration of Sc (16.4 $\mu\text{g/g}$) approaches that of the UCC (McLennan, 2001). The Th/Sc and Zr/Sc ratios ranging from 0.38 to 0.67 and 4.65 to 9.33, respectively, show no large variations (Figure 4). The total rare earth element concentrations (ΣREEs) vary from 141.9 to 273.8 $\mu\text{g/g}$, with an average of 210.1 $\mu\text{g/g}$ (Table 1) which is higher than that of the UCC (168.1 $\mu\text{g/g}$) (McLennan, 2001). Yttrium (Y) and holmium (Ho) geochemical twins due to their similar radius and charge generally have chondritic Y/Ho values of ~28 in clastic sedimentary rocks (see Albut et al., 2018 and references therein). The studied samples have mildly fluctuating Y/Ho ratios ranging from 25.1 to 31.1 with a mean of 26.8 (Figure 4) which is slightly lower than the chondritic value of ~28. Redox-sensitive elements (molybdenum (Mo), uranium (U), and vanadium (V)) range from 0.93 to 43.8 $\mu\text{g/g}$, 2.7 to 19.1 $\mu\text{g/g}$ and 99.2 to 463.4 $\mu\text{g/g}$, respectively (Table 1; Figure S1). In general, the enrichment or depletion pattern of trace element concentrations with respect to the reference material is critical to reconstruct paleoenvironmental conditions (Tribouillard, Algeo, Lyons, & Riboulleau, 2006). In order to trace the authigenic fraction of elements, normalization to an index of the detrital component, normally Al, is necessary (Francois, 1988). The Al concentration of the UCC used for this study is from McLennan (2001). The enrichments of Mo, U, and V are shown in Figure 5. The gray bioturbated mudstones almost do not display enrichments in Mo, U, and V, whereas these elements are obviously enriched in the laminated oil shale facies corresponding to the Toarcian OAE and associated CIE (Figure 5).

TABLE 1 ICP-MS data for Dotternhausen samples

Depth (cm)	613	621	635	638	642	648	656	670	673	680	684	687	698	705
Major [wt.%]														
SiO ₂	33.31	28.52	29.20	25.12	23.44	25.12	25.97	24.60	24.60	21.37	23.60	23.60	26.49	26.35
TiO ₂	0.54	0.49	0.47	0.41	0.40	0.41	0.43	0.41	0.41	0.31	0.39	0.39	0.41	0.42
Al ₂ O ₃	10.10	8.75	8.82	7.38	7.05	7.38	7.79	7.48	7.48	6.40	7.07	7.07	7.63	7.99
Fe ₂ O ₃	3.82	6.91	3.82	3.63	4.23	3.63	4.63	3.97	3.97	3.29	3.75	3.75	4.44	3.95
MnO	0.06	0.04	0.05	0.05	0.04	0.05	0.04	0.05	0.05	0.05	0.05	0.05	0.05	0.05
MgO	2.05	1.45	2.07	1.17	1.19	1.17	1.12	1.63	1.63	1.45	1.22	1.22	1.30	1.53
CaO	20.89	18.21	21.89	24.12	24.38	24.12	22.91	21.92	21.92	28.48	25.02	25.02	23.73	23.44
Na ₂ O	0.30	0.27	0.26	0.23	0.21	0.23	0.23	0.23	0.23	0.17	0.20	0.20	0.22	0.23
K ₂ O	1.92	1.55	1.62	1.24	1.22	1.24	1.22	1.29	1.29	1.07	1.11	1.11	1.18	1.40
P ₂ O ₅	0.08	0.06	0.06	0.14	0.07	0.14	0.03	0.04	0.04	0.15	0.07	0.07	0.09	0.05
LOI	26.22	33.37	29.42	34.39	35.39	34.39	35.21	35.27	35.27	33.44	34.70	34.70	34.44	33.70
Total sum	99.3	99.6	97.7	97.9	97.6	97.9	99.6	96.9	96.9	96.2	97.2	97.2	100.0	99.1
Trace [µg/g]														
Li	33.0	37.9	31.7	31.7	38.8	31.7	30.7	34.2	40.7	27.3	34.7	32.5	30.4	37.0
Be	2.4	2.6	2.2	2.0	2.5	2.0	1.9	2.3	2.7	1.9	2.3	2.1	2.0	2.5
Sc	15.0	15.3	14.8	14.3	15.0	13.4	12.2	14.2	15.8	12.6	14.9	14.9	14.3	15.7
V	164.1	213.3	145.9	194.3	250.2	224.3	226.2	185.9	242.2	166.3	218.0	215.9	212.3	232.6
Cr	80.8	93.7	77.7	80.6	90.5	72.0	71.8	75.2	96.2	58.4	80.9	73.1	70.6	95.7
Co	14.5	30.9	20.4	39.6	39.6	21.8	32.6	28.3	34.7	18.8	28.1	26.4	30.5	27.9
Ni	50.5	85.1	48.1	94.9	88.2	73.2	84.1	83.2	96.5	67.4	111.6	102.6	86.7	99.8
Cu	48.0	89.3	66.7	96.2	99.4	101.2	96.2	80.8	99.3	54.4	91.6	81.6	83.4	88.3
Zn	39.2	163.7	61.2	184.9	165.9	143.9	120.9	84.0	148.7	510.3	144.8	147.0	142.8	126.1
Ga	14.4	17.8	13.6	15.1	17.7	15.4	14.7	15.9	20.0	12.5	16.2	15.3	15.0	16.7
As	19.1	36.4	25.2	28.5	60.3	17.9	19.2	21.7	25.6	15.2	21.4	18.8	19.9	18.7
Rb	95.3	103.3	86.6	83.8	102.1	79.1	79.6	88.4	109.5	70.2	90.2	82.7	78.4	95.8
Sr	3,623.8	2,670.8	2,002.9	2,407.0	1,481.4	2,065.0	2,201.2	2,242.0	2,164.2	4,350.7	2,361.2	1,667.4	1,072.5	809.1
Y	21.9	25.0	24.0	25.4	24.3	36.2	21.6	24.8	27.7	25.1	28.5	33.5	37.8	30.7
Zr	101.2	115.5	87.1	99.5	125.8	105.7	102.1	103.3	135.7	75.8	109.1	102.9	103.2	113.9
Nb	12.4	14.1	10.8	11.9	14.8	12.6	11.5	12.0	16.2	9.2	13.2	12.1	11.9	14.0
Mo	5.5	13.6	6.0	16.0	23.4	15.9	20.1	14.4	21.6	11.3	19.4	18.7	16.8	21.4
Cd	0.1	0.6	0.2	0.7	0.6	0.7	0.6	0.3	0.5	2.5	0.7	0.7	0.6	0.5
Sn	2.3	2.8	2.1	2.3	2.8	2.3	2.3	2.3	3.0	1.9	2.4	2.2	2.2	2.6

(Continues)

TABLE 1 (Continued)

Depth (cm)	613	621	635	638	642	648	656	670	673	680	684	687	698	705
Sb	1.6	2.1	1.4	2.0	2.5	1.9	1.8	1.8	2.2	1.1	1.9	1.7	1.6	1.9
Cs	5.5	6.0	5.0	5.0	6.0	4.6	4.7	5.2	6.4	4.1	5.3	4.8	4.6	5.6
Ba	271.4	526.1	254.1	273.7	293.5	269.4	234.4	278.7	329.2	223.6	260.7	300.3	239.4	260.6
La	31.8	36.6	29.2	34.7	39.7	35.6	31.3	31.3	40.4	26.4	36.2	35.9	37.4	39.7
Ce	60.6	71.3	56.5	66.6	75.2	74.3	57.6	61.7	80.3	55.2	74.1	78.3	81.9	80.7
Pr	7.0	8.5	6.9	8.0	8.7	9.9	6.7	7.2	9.3	6.7	8.7	9.7	10.4	9.3
Nd	25.9	31.6	26.1	29.7	31.0	41.7	24.4	27.2	35.1	25.9	32.9	38.5	42.4	35.4
Sm	4.9	6.1	5.1	5.6	5.5	8.8	4.6	5.2	6.7	5.2	6.4	7.9	9.0	7.0
Eu	1.0	1.3	1.1	1.2	1.2	1.9	1.0	1.1	1.4	1.2	1.4	1.7	2.0	1.5
Tb	0.7	0.8	0.7	0.8	0.8	1.2	0.6	0.8	0.9	0.8	0.9	1.1	1.3	1.0
Gd	4.4	5.4	4.7	5.2	5.0	8.8	4.2	4.9	6.1	5.2	6.1	7.7	8.8	6.5
Dy	4.0	4.8	4.5	4.8	4.6	6.9	3.9	4.5	5.3	4.6	5.4	6.5	7.2	5.8
Ho	0.8	1.0	0.9	1.0	1.0	1.3	0.8	0.9	1.1	1.0	1.1	1.3	1.4	1.2
Er	2.4	2.7	2.6	2.8	2.8	3.4	2.4	2.6	3.0	2.6	3.0	3.4	3.7	3.2
Tm	0.4	0.4	0.4	0.4	0.4	0.5	0.3	0.4	0.5	0.4	0.5	0.5	0.5	0.5
Yb	2.3	2.7	2.6	2.7	2.7	2.9	2.3	2.5	2.9	2.4	2.9	3.0	3.2	3.0
Lu	0.3	0.4	0.4	0.4	0.4	0.4	0.3	0.4	0.4	0.4	0.4	0.4	0.5	0.4
Hf	2.5	3.0	2.3	2.4	3.2	2.6	2.6	2.5	3.4	2.0	2.7	2.6	2.5	2.9
Ta	0.8	0.9	0.7	0.8	1.0	0.8	0.8	0.8	1.1	0.6	0.8	0.8	0.8	0.9
W	1.0	1.0	0.8	0.9	1.2	0.9	0.9	1.1	1.2	0.7	0.9	0.9	0.9	1.1
Tl	0.9	3.9	1.1	4.0	4.6	2.6	5.6	2.9	4.1	2.0	3.1	2.9	2.6	3.0
Pb	15.9	17.9	13.7	19.0	20.2	17.0	17.0	16.5	21.6	12.1	17.1	15.6	15.7	17.8
Th	8.3	9.2	7.1	8.0	9.5	8.1	8.1	8.1	10.1	6.0	8.4	8.0	8.2	9.4
U	3.7	5.8	4.0	6.0	5.8	7.6	4.9	7.2	6.3	5.9	8.2	8.6	7.0	5.0

Depth (cm)	719	722	726	729	733	740	743	761	775	785	786	787	792	796	801	805	810
Major [wt.%]																	
SiO ₂	31.33			36.27	39.90		32.64	31.41	40.10	16.31	5.34	5.12	1.96	1.26	0.79	0.95	4.10
TiO ₂	0.51			0.61	0.65		0.54	0.51	0.70	0.25	0.06	0.05	0.04	0.03	0.02	0.02	0.04
Al ₂ O ₃	9.12			10.79	11.95		9.83	9.23	12.30	4.18	1.09	0.80	0.61	0.43	0.29	0.36	0.98
Fe ₂ O ₃	5.64			6.95	5.48		5.67	5.82	6.37	2.15	3.05	2.98	1.71	0.67	0.58	0.98	3.40
MnO	0.04			0.04	0.04		0.05	0.05	0.04	0.10	0.21	0.26	0.18	0.09	0.08	0.16	0.26

(Continues)

TABLE 1 (Continued)

Depth (cm)	719	722	726	729	733	740	743	761	775	785	786	787	792	796	801	805	810
MgO	1.55			2.15	2.28		1.60	2.07	2.11	1.04	0.62	0.66	0.67	0.67	0.70	0.63	0.67
CaO	18.07			13.94	11.13		15.97	17.20	10.94	36.61	47.53	49.53	51.94	52.68	54.05	52.96	48.97
Na ₂ O	0.27			0.30	0.32		0.28	0.26	0.43	0.14	0.04	0.05	0.06	0.02	0.02	0.02	0.03
K ₂ O	1.53			1.86	2.21		1.67	1.68	2.02	0.76	0.14	0.22	0.09	0.05	0.02	0.03	0.11
P ₂ O ₅	0.09			0.16	0.15		0.42	0.10	0.19	0.03	0.03	0.00	0.03	0.02	0.01	0.01	0.03
LOI	29.71			27.21	27.85		31.81	31.03	26.15	37.93	36.37	39.28	40.88	42.29	42.80	41.54	36.30
Total sum	97.9			100.3	102.0		100.5	99.3	101.4	99.5	96.85	98.94	98.16	98.21	99.36	97.66	94.89
Trace [$\mu\text{g/g}$]																	
Li	28.7	24.7	29.1	38.2	37.3	38.4	44.5	41.8	29.1	19.2							
Be	2.0	1.7	2.1	2.6	2.7	2.7	3.0	3.1	2.3	1.6							
Sc	12.7	12.7	12.6	16.0	15.7	15.5	16.3	18.1	13.0	9.4							
V	210.5	173.0	187.1	221.3	227.8	309.8	379.4	303.8	207.7	130.1							
Cr	92.3	62.7	65.2	119.1	206.5	87.4	113.7	102.6	67.4	45.9							
Co	28.9	26.0	26.4	30.2	26.7	21.1	24.2	31.4	21.8	17.5							
Ni	90.5	89.2	71.1	117.0	129.5	96.5	116.4	126.9	122.4	66.2							
Cu	80.8	91.8	75.5	90.0	79.0	98.6	121.3	103.7	103.0	46.0							
Zn	151.7	162.7	159.4	114.1	97.5	127.6	225.7	90.5	66.8	36.7							
Ga	13.9	12.3	14.5	18.4	17.6	18.4	21.5	21.9	14.6	9.8							
As	86.0	15.5	31.9	23.1	76.8	18.3	22.6	27.8	18.6	12.2							
Rb	75.3	60.8	78.4	103.8	103.6	99.0	115.5	115.2	78.9	51.3							
Sr	2,422.6	3,328.7	2,578.4	816.9	643.1	739.4	564.7	611.7	547.7	542.6							
Y	31.2	30.9	30.3	33.8	32.7	44.3	44.5	35.1	61.7	34.0							
Zr	101.2	83.9	97.0	130.7	121.4	125.1	144.4	155.6	103.0	64.7							
Nb	11.8	9.7	11.2	15.9	14.8	15.0	17.7	19.5	12.9	8.2							
Mo	29.5	13.5	17.8	15.6	30.3	24.1	32.2	31.2	21.5	11.8							
Cd	0.6	0.7	0.7	0.4	0.4	0.8	1.5	0.8	0.5	0.2							
Sn	2.1	1.8	2.1	2.8	2.7	2.7	3.2	3.2	2.1	1.4							
Sb	2.2	1.3	1.6	1.9	2.3	1.7	2.3	2.1	1.5	1.8							
Cs	4.3	3.5	4.3	6.0	5.8	5.7	6.6	6.5	4.4	2.9							
Ba	228.8	212.1	222.3	275.2	260.2	385.6	325.9	335.6	240.1	152.5							
La	33.4	29.0	31.6	41.7	38.2	43.1	47.3	44.0	43.5	27.8							

(Continues)

TABLE 1 (Continued)

Depth (cm)	719	722	726	729	733	740	743	761	775	785	786	787	792	796	801	805	810
Ce	68.5	60.0	66.6	82.7	78.1	89.3	94.5	84.1	105.3	57.5							
Pr	8.3	7.3	8.1	9.6	9.2	10.8	11.3	9.5	13.7	7.0							
Nd	32.4	27.9	32.1	36.1	35.2	42.2	43.2	35.1	56.7	27.6							
Sm	6.5	5.5	6.5	7.0	7.0	8.5	8.6	6.8	12.1	5.6							
Eu	1.4	1.3	1.4	1.5	1.5	1.9	1.9	1.4	2.7	1.2							
Tb	0.9	0.9	1.0	1.0	1.0	1.3	1.3	1.0	1.8	0.9							
Gd	6.3	5.7	6.4	6.7	6.6	8.4	8.5	6.3	12.4	5.8							
Dy	5.6	5.3	5.5	6.1	5.9	7.5	7.5	5.9	10.4	5.3							
Ho	1.1	1.1	1.1	1.3	1.2	1.5	1.6	1.3	2.1	1.1							
Er	3.1	3.1	3.0	3.5	3.4	4.2	4.3	3.7	5.3	3.0							
Tm	0.5	0.5	0.4	0.5	0.5	0.6	0.6	0.6	0.7	0.4							
Yb	2.8	2.8	2.7	3.3	3.1	3.7	3.9	3.6	3.8	2.5							
Lu	0.4	0.4	0.4	0.5	0.5	0.5	0.6	0.5	0.5	0.4							
Hf	2.5	2.0	2.4	3.2	3.1	3.1	3.6	3.9	2.5	1.6							
Ta	0.8	0.6	0.7	1.0	1.0	1.0	1.1	1.3	0.8	0.5							
W	0.9	0.8	1.1	1.2	1.4	1.1	1.3	1.4	1.0	0.7							
Tl	2.4	1.8	2.5	2.0	2.1	2.0	2.9	3.4	2.0	1.4							
Pb	14.6	13.0	15.4	19.0	18.2	18.3	22.2	23.1	16.6	9.5							
Th	7.6	6.2	7.3	9.8	9.5	9.7	11.0	10.9	8.1	5.1							
U	4.1	4.9	4.3	5.4	5.5	8.5	8.8	10.3	19.1	17.2							
Depth (cm)	817	822	825	828	836	843	848	853	859	871	876	898	903	905	919	922	
Major [wt.%]																	
SiO ₂	25.04	35.19	36.19	34.51	35.74	34.89	34.63	30.54	31.08	33.02	32.78	36.66	39.05	35.29	37.46	33.91	
TiO ₂	0.43	0.59	0.61	0.60	0.60	0.59	0.57	0.50	0.53	0.55	0.55	0.60	0.72	0.60	0.66	0.57	
Al ₂ O ₃	7.57	10.13	10.50	10.51	10.35	10.16	10.00	8.68	9.06	9.34	9.81	11.01	11.58	10.41	11.13	10.39	
Fe ₂ O ₃	3.74	5.74	5.90	12.01	6.29	5.17	6.43	5.58	5.49	5.01	5.81	6.79	10.85	5.81	7.63	6.21	
MnO	0.07	0.04	0.04	0.04	0.05	0.04	0.04	0.04	0.04	0.05	0.05	0.04	0.04	0.04	0.05	0.04	
MgO	1.67	1.67	1.66	1.86	1.70	1.65	1.62	1.58	1.60	1.61	2.06	2.03	1.75	1.89	2.00	1.71	
CaO	22.79	13.13	12.04	6.91	13.47	14.08	13.15	16.81	14.20	16.15	15.54	11.50	7.93	11.43	10.88	12.11	
Na ₂ O	0.22	0.33	0.36	0.32	0.33	0.34	0.32	0.28	0.29	0.30	0.30	0.35	0.36	0.34	0.32	0.32	
K ₂ O	1.36	1.94	1.98	2.13	1.87	1.87	1.90	1.70	1.81	1.76	2.04	2.20	2.10	1.99	2.02	2.00	

(Continues)

TABLE 1 (Continued)

Depth (cm)	817	822	825	828	836	843	848	853	859	871	876	898	903	905	919	922
P ₂ O ₅	0.15	0.17	0.15	0.12	0.18	0.22	0.13	0.11	0.12	0.20	0.09	0.13	0.10	0.09	0.12	0.10
LOI	34.54	32.86	31.22	31.08	29.42	31.21	32.96	35.11	32.28	25.50	30.09	29.80	25.77	31.76	31.02	32.95
Total sum	97.6	101.8	100.7	100.1	100.0	100.2	101.8	100.9	96.5	93.5	99.1	101.1	100.3	99.6	103.3	100.3
Trace [$\mu\text{g/g}$]																
Li	64.9		44.3	46.2	42.2	52.8	42.5	38.0	42.1	39.1	39.4	45.1	45.2	46.5	43.3	46.7
Be	2.2		2.9	3.2	2.7	2.6	2.8	2.6	3.0	2.5	2.8	3.1	2.7	3.1	2.7	3.0
Sc	13.6		19.0	19.8	18.7	17.8	17.2	16.2	18.4	18.2	17.0	18.7	17.9	20.3	18.0	20.7
V	251.2		463.4	403.3	319.6	395.5	383.5	352.5	311.7	345.1	231.4	335.4	366.2	418.0	375.2	448.6
Cr	72.0		102.7	118.2	90.8	92.9	94.1	83.8	99.7	90.1	89.7	99.5	103.5	110.1	96.0	118.2
Co	23.9		31.2	44.9	29.5	24.3	35.4	25.7	32.7	28.7	25.3	28.4	31.3	28.4	23.5	40.1
Ni	105.6		145.3	120.6	109.4	122.1	113.5	106.6	116.2	112.8	65.1	101.5	127.7	136.5	105.1	141.1
Cu	81.4		154.9	143.7	95.6	129.9	135.6	116.1	100.4	145.7	80.3	108.6	97.0	151.0	84.9	162.0
Zn	41.1		209.8	258.1	65.1	209.2	225.3	166.2	62.1	201.4	59.1	129.4	110.8	134.6	106.9	179.8
Ga	15.5		22.7	24.1	19.3	20.7	21.2	18.7	21.2	20.1	17.8	21.8	19.9	22.0	19.9	22.4
As	16.3		23.9	57.6	26.6	20.3	47.2	23.2	24.4	20.3	33.9	29.1	59.4	23.1	34.1	27.4
Rb	79.9		116.7	129.5	106.2	105.8	112.9	99.4	113.2	100.5	108.0	122.5	114.0	119.9	112.0	119.2
Sr	571.4		709.7	562.7	1,066.9	798.8	674.7	698.2	729.7	898.5	999.2	1,042.4	910.4	800.9	409.9	639.4
Y	38.0		45.0	37.2	52.8	54.8	40.0	39.1	44.4	53.5	31.1	37.9	35.8	42.4	37.3	41.5
Zr	102.6		156.5	166.1	153.5	143.8	145.4	129.3	148.6	132.7	122.2	147.5	167.1	165.3	149.5	156.6
Nb	13.5		19.0	20.1	18.6	17.5	17.7	15.0	18.0	16.1	15.3	17.6	21.6	19.4	19.1	18.3
Mo	26.3		37.9	33.9	31.0	37.6	26.2	23.1	25.4	43.8	17.2	22.9	31.8	41.5	34.8	23.1
Cd	0.3		1.6	1.0	0.5	1.9	1.3	1.0	0.4	2.3	0.4	0.6	1.4	1.8	1.2	1.1
Sn	2.2		3.5	3.1	3.0	3.2	3.2	2.7	3.0	3.1	2.6	3.2	3.0	3.4	3.2	3.4
Sb	1.7		3.1	3.4	3.0	2.9	3.5	2.4	3.0	2.3	2.8	2.5	3.6	3.4	3.4	2.9
Cs	4.5		6.7	7.3	6.0	6.0	6.5	5.6	6.4	5.7	6.1	6.8	6.4	6.6	6.2	6.9
Ba	241.3		296.3	294.9	283.0	276.0	282.0	254.9	298.3	287.1	261.7	296.9	288.4	297.8	249.5	289.8
La	37.1		48.3	43.9	51.5	49.2	43.8	38.6	44.5	46.6	34.4	44.0	44.2	46.8	42.6	45.4
Ce	72.6		99.5	92.8	110.3	106.6	89.0	82.7	96.1	102.7	70.2	93.4	85.6	96.2	85.9	96.7
Pr	8.4		11.4	10.4	13.1	13.1	10.1	9.4	11.1	12.8	8.0	10.5	9.9	11.2	9.9	11.3
Nd	32.4		43.0	38.7	51.5	52.3	37.9	36.0	43.1	51.5	29.4	39.7	36.7	42.0	36.9	42.8
Sm	6.5		8.5	7.6	10.5	10.7	7.4	7.2	8.7	10.7	5.7	7.9	6.9	8.3	7.2	8.6
Eu	1.4		1.9	1.6	2.3	2.4	1.6	1.6	1.9	2.4	1.2	1.7	1.5	1.8	1.6	1.9

(Continues)

TABLE 1 (Continued)

Depth (cm)	817	822	825	828	836	843	848	853	859	871	876	898	903	905	919	922
Tb	1.0	1.1	1.3	1.1	1.6	1.6	1.1	1.1	1.3	1.6	0.9	1.2	1.0	1.3	1.1	1.3
Gd	6.5	7.2	8.4	7.2	10.4	10.8	7.2	7.2	8.5	10.8	5.3	7.5	6.5	8.0	6.8	8.4
Dy	6.0	6.8	7.8	6.8	9.3	9.5	6.9	6.8	7.8	9.4	5.4	6.9	6.3	7.6	6.5	7.8
Ho	1.3	1.4	1.6	1.4	1.9	2.0	1.5	1.4	1.6	1.9	1.2	1.5	1.4	1.6	1.4	1.6
Er	3.6	4.2	4.6	4.2	5.2	5.2	4.2	4.1	4.5	5.1	3.4	4.1	3.9	4.7	4.0	4.6
Tm	0.5	0.6	0.7	0.6	0.7	0.7	0.6	0.6	0.7	0.7	0.5	0.6	0.6	0.7	0.6	0.7
Yb	3.3	4.1	4.5	4.1	4.7	4.6	4.0	3.9	4.3	4.4	3.4	3.9	3.9	4.6	4.0	4.5
Lu	0.5	0.6	0.7	0.6	0.7	0.7	0.6	0.6	0.6	0.6	0.5	0.6	0.6	0.7	0.6	0.7
Hf	2.6	4.2	3.9	4.2	4.0	3.6	3.7	3.2	3.7	3.3	3.3	3.8	4.4	4.2	4.0	4.0
Ta	0.9	1.3	1.3	1.3	1.2	1.2	1.2	1.0	1.2	1.1	1.0	1.2	1.4	1.3	1.3	1.2
W	5.9	11.9	1.3	11.9	1.6	9.5	1.2	1.1	8.4	7.4	6.5	1.3	1.4	7.6	1.3	6.0
Tl	1.9	5.0	3.5	5.0	3.0	2.9	3.4	2.9	2.8	2.5	2.9	2.9	4.1	4.5	3.0	5.5
Pb	14.9	25.6	25.6	26.0	20.4	22.8	24.4	19.5	20.2	21.1	20.6	21.5	33.3	32.4	22.9	37.4
Th	7.8	11.4	11.4	11.4	11.0	10.5	10.3	9.2	10.7	10.0	9.1	11.1	11.1	11.3	10.4	11.3
U	13.0	8.2	8.2	7.4	8.3	9.1	7.0	7.1	8.5	8.8	4.4	6.2	6.1	9.2	6.8	7.4
Depth (cm)	940	949	956	964	971	976	986	986	1,003	1,009	1,020	1,030	1,040	1,050		
SiO ₂	33.24	41.90	31.73	43.12	19.18	23.36	35.00	37.37	37.37	38.94	36.50	36.40	37.33	36.13		
TiO ₂	0.58	0.72	0.51	0.81	0.30	0.32	0.55	0.62	0.62	0.67	0.64	0.61	0.62	0.61		
Al ₂ O ₃	10.25	12.69	9.86	13.11	6.30	6.51	11.04	12.36	12.36	13.19	12.37	12.13	12.61	12.14		
Fe ₂ O ₃	12.58	6.18	5.15	6.23	3.79	3.73	9.37	3.50	3.50	4.30	4.09	4.15	4.04	3.92		
MnO	0.04	0.04	0.05	0.04	0.07	0.10	0.06	0.15	0.15	0.13	0.13	0.16	0.15	0.15		
MgO	2.07	2.32	1.69	2.39	1.18	1.34	1.76	2.27	2.27	2.33	2.43	2.53	2.59	2.49		
CaO	9.45	7.31	16.79	7.42	26.29	27.27	11.83	18.88	18.88	16.59	18.80	18.85	18.68	18.89		
Na ₂ O	0.34	0.43	0.31	0.45	0.20	0.22	0.38	0.42	0.42	0.45	0.43	0.43	0.43	0.42		
K ₂ O	2.10	2.52	1.91	2.65	1.20	1.25	2.23	2.56	2.23	2.74	2.58	2.54	2.65	2.46		
P ₂ O ₅	0.10	0.13	0.12	0.10	0.13	0.12	0.11	0.13	0.11	0.13	0.11	0.14	0.15	0.16		
LOI	28.97	25.15	31.37	23.82	36.93	30.45	28.19	23.62	28.19	20.58	21.18	21.85	21.50	21.60		
Total sum	99.7	99.4	99.5	100.1	95.6	94.7	100.5	101.9	99.3	100.1	99.3	99.8	100.8	99.0		
Trace [$\mu\text{g/g}$]																
Li	41.7	52.9	43.1	51.7	30.8	27.1	50.6	46.0	46.0	49.7	43.7	43.2	44.4	44.7		
Be	2.8	3.4	2.6	3.3	1.9	1.6	2.8	2.3	2.3	2.7	2.4	2.3	2.3	2.3		

(Continues)

TABLE 1 (Continued)

Depth (cm)	940	949	956	964	971	976	986	1,003	1,009	1,020	1,030	1,040	1,050
Sc	18.5	21.7	20.7	20.5	18.7	15.0	21.3	18.5	19.4	17.8	17.5	17.9	18.0
V	325.3	381.5	330.2	413.2	266.0	215.4	164.7	121.8	132.0	110.4	110.4	103.9	99.2
Cr	97.6	126.1	101.4	127.0	75.8	69.6	109.2	80.8	87.5	76.3	75.6	75.9	76.0
Co	40.1	30.7	34.6	30.8	37.4	33.1	106.9	17.4	23.7	21.2	20.6	19.1	23.7
Ni	123.3	112.9	115.8	149.6	279.7	192.6	224.3	70.8	84.0	74.1	73.6	68.5	70.2
Cu	115.4	136.2	127.9	123.6	129.8	104.8	115.5	35.6	47.8	37.2	35.7	36.0	32.4
Zn	124.5	143.9	123.1	105.8	320.4	476.2	81.7	148.3	192.1	150.7	106.4	140.4	85.9
Ga	19.7	25.3	19.1	23.5	14.6	12.2	20.3	17.4	19.1	17.1	16.6	16.7	16.4
As	85.8	21.0	20.7	22.5	22.8	21.8	67.4	10.0	13.9	11.0	10.5	11.2	9.9
Rb	113.9	140.7	107.0	138.9	70.4	63.3	117.1	108.5	118.2	106.7	106.6	107.2	105.9
Sr	551.5	413.5	833.8	510.1	2,750.1	1,503.5	871.0	1,766.0	1,782.2	1,341.5	1,107.9	1,028.8	1,128.9
Y	34.7	41.0	48.3	32.8	61.1	55.6	34.8	34.3	32.3	27.8	31.9	33.0	35.1
Zr	137.7	172.7	120.9	184.3	87.2	73.2	111.1	98.8	115.3	99.5	95.4	95.2	97.5
Nb	17.7	22.2	14.7	24.5	9.1	8.2	14.4	13.7	14.8	13.7	13.3	13.2	13.1
Mo	36.8	26.5	15.1	27.1	24.8	17.4	4.5	1.3	2.0	1.3	0.9	1.0	1.2
Cd	0.6	1.2	0.7	1.2	2.4	3.4	0.1	0.2	0.3	0.2	0.1	0.2	0.1
Sn	3.1	3.9	3.0	3.9	2.0	2.1	3.5	3.0	3.2	2.8	2.8	2.8	2.7
Sb	3.0	3.6	2.2	3.3	1.9	1.3	3.6	0.8	1.2	1.0	0.8	0.8	0.7
Cs	6.4	7.8	6.3	7.7	4.3	3.7	7.0	6.4	7.1	6.4	6.3	6.4	6.3
Ba	324.0	338.5	280.4	333.3	219.1	187.0	353.4	321.7	354.5	311.5	321.0	319.6	308.9
La	39.0	47.6	46.0	44.2	43.1	34.8	48.0	42.5	47.1	41.7	38.7	38.8	41.2
Ce	85.8	103.3	106.9	88.3	102.6	78.3	96.4	86.2	95.4	84.9	78.6	79.0	84.0
Pr	9.8	12.2	13.3	10.0	14.0	10.8	10.9	10.4	11.2	9.9	9.6	9.9	10.7
Nd	37.3	47.2	54.0	35.0	61.0	48.2	40.3	39.5	40.6	35.4	36.6	38.4	42.1
Sm	7.4	9.6	11.7	6.3	13.7	11.3	7.7	7.7	7.3	6.4	7.5	8.1	8.8
Eu	1.6	2.0	2.5	1.3	3.2	2.6	1.6	1.7	1.6	1.3	1.6	1.7	1.9
Tb	1.1	1.4	1.7	0.9	2.0	1.7	1.1	1.1	1.0	0.9	1.0	1.1	1.2
Gd	7.1	8.9	11.1	5.6	13.9	11.6	7.0	7.2	6.5	5.5	6.8	7.3	8.1
Dy	6.5	7.8	9.4	5.8	11.2	9.8	6.4	6.3	5.9	5.1	5.9	6.2	6.8
Ho	1.4	1.6	1.9	1.3	2.2	2.0	1.3	1.3	1.2	1.1	1.2	1.3	1.3
Er	3.8	4.4	4.9	3.8	5.4	5.0	3.7	3.5	3.4	3.0	3.3	3.4	3.5
Tm	0.6	0.7	0.7	0.6	0.7	0.7	0.6	0.5	0.5	0.5	0.5	0.5	0.5

(Continues)

TABLE 1 (Continued)

Depth (cm)	940	949	956	964	971	976	986	1,003	1,009	1,020	1,030	1,040	1,050
Yb	3.7	4.2	4.3	3.9	4.4	4.0	3.5	3.3	3.3	2.9	3.0	3.1	3.2
Lu	0.5	0.6	0.6	0.6	0.6	0.6	0.5	0.5	0.5	0.4	0.4	0.4	0.5
Hf	3.6	4.5	3.2	4.8	2.1	1.8	3.1	2.8	3.2	2.8	2.7	2.8	2.8
Ta	1.1	1.5	1.0	1.6	0.6	0.5	1.0	0.9	1.0	0.9	0.9	0.9	0.9
W	1.1	7.7	7.2	7.0	4.1	5.1	6.0	1.8	1.8	1.3	1.1	1.0	1.0
Tl	3.8	3.6	3.6	5.8	6.4	5.5	2.0	0.5	0.7	0.6	0.6	0.6	0.6
Pb	71.1	58.8	60.5	79.5	72.2	45.7	73.2	21.0	26.4	22.1	21.2	21.8	21.6
Th	10.0	12.4	9.9	12.8	7.1	5.8	10.4	9.3	10.6	9.7	9.5	9.5	9.6
U	6.2	7.6	9.3	6.3	13.3	9.3	4.3	3.3	3.5	2.7	2.9	3.0	3.0

4.2 | TOC_{cf}, carbonate and isotopic data

The TOC_{cf} contents and bulk stable isotope (carbon and oxygen) data are given in Table 2 and are plotted in Figures 6 and 7. Carbonate concentrations are reported in Table 2. The gray bioturbated mudstone samples have lower TOC_{cf} contents <5 wt.% than laminated oil shales with consistently TOC_{cf} contents >5 wt.% (Table 2, Figure 6). Unterer Stein shows high carbonate contents with an average of 92 wt%, the rest of this studied samples exhibit a variation between 3 to 88 wt%. According to the distribution of organic-rich sediments in the Dotternhausen section, this study places the onset of the Toarcian OAE to a depth of 980 cm in our profile. Four data points at depths between 1,012 cm and 986 cm reveal constant $\delta^{13}\text{C}_{\text{carb}}$ and $\delta^{13}\text{C}_{\text{org}}$ values prior to the Toarcian OAE (Figure 7). The negative $\delta^{13}\text{C}_{\text{carb}}$ and $\delta^{13}\text{C}_{\text{org}}$ excursions ranging from 0 to -12‰ and -28 to -32‰, respectively, are exhibited between depths of 986 cm and 613 cm (Figure 7). Two-step opposing small-scale excursions of $\delta^{13}\text{C}_{\text{carb}}$ and $\delta^{13}\text{C}_{\text{org}}$ records from 876 to 761 cm are obviously observed (Figure 7). The $\delta^{13}\text{C}_{\text{carb}}$ values in the first and smaller scale (from 876 to 825 cm) has a negative excursion, which corresponds to a slightly positive excursion in $\delta^{13}\text{C}_{\text{org}}$ values. By contrast, the second step (from 825 to 761 cm) has larger magnitude excursions in both $\delta^{13}\text{C}_{\text{carb}}$ and $\delta^{13}\text{C}_{\text{org}}$ values (Figure 7). The $\Delta^{13}\text{C}$ ($\delta^{13}\text{C}_{\text{carb}} - \delta^{13}\text{C}_{\text{org}}$) is relatively constant in the lower part (interval 1 from 981 to 883 cm) and upper part (interval 3 from 757 to 613 cm), whereas it drops according to the two-step opposing small-scale excursions (interval 2 from 876 to 761 cm; Figure 7). The $\delta^{18}\text{O}$ values of carbonates range from -7 to -4‰, and the heaviest values are preserved in the diagenetically lenticular limestone bed of Unterer Stein (Figure 7).

5 | DISCUSSION

5.1 | Negligible effects of terrigenous-sourced organic carbon, thermal maturity, and hydrothermal fluids on $\delta^{13}\text{C}_{\text{org}}$ across the Toarcian CIE

Due to the contrasting $\delta^{13}\text{C}$ signatures between terrestrial and marine organic matters, terrestrial-sourced organic carbon can lead to a significant influence on $\delta^{13}\text{C}_{\text{org}}$ record of marine sediments deposited across the Toarcian CIE (Suan et al., 2015). Indeed, decomposed organic material from land plants can be easily washed into shelf-sea settings as a result of an accelerated hydrological cycle (Izumi, Kemp, Itamiya, & Inui, 2018) arising from the intensive chemical weathering (e.g., Cohen, Coe, Harding, & Schwark, 2004; Percival et al., 2016). Hydrogen index (HI) is an efficient indicator that can distinguish between marine and terrestrial organic matter (e.g., Dembicki, 2009; Peters, Walters, & Moldowan, 2005). In general, a HI value higher than 400 mg hydrocarbon (HC)/g TOC indicates the preservation of oil-prone marine organic matter (types I and II kerogen) dominated by algae and bacteria (Röhl, Schmid-Röhl, Oschmann, Frimmel, & Schwark, 2001). Although the use of HI in characterizing the type of

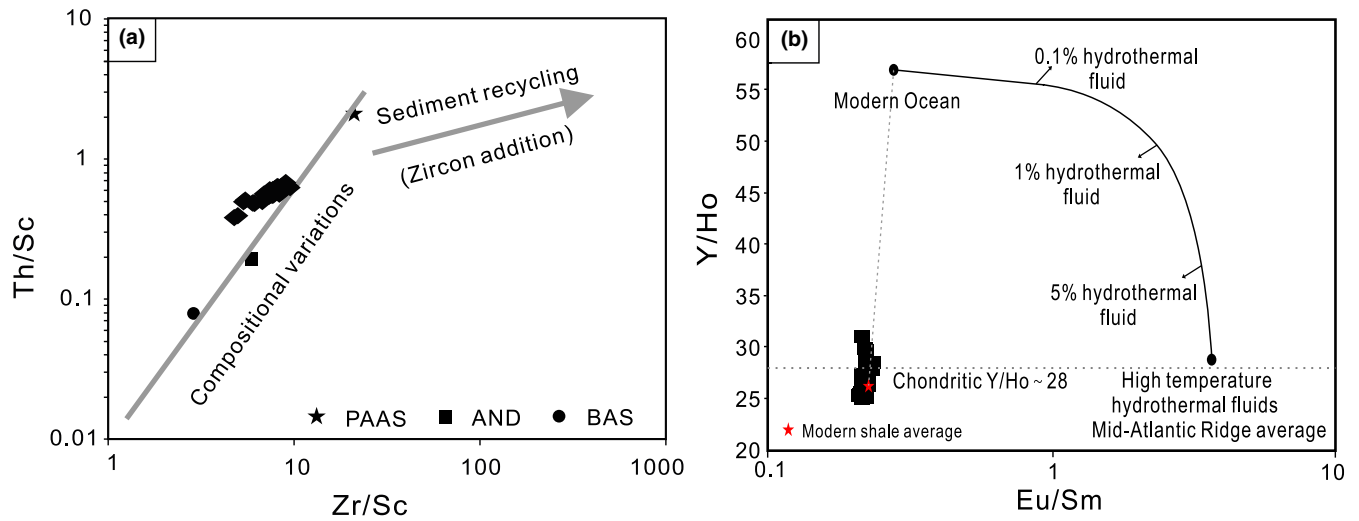


FIGURE 4 (a) Th/Sc vs. Zr/Sc diagram (McLennan, Hemming, McDaniel, & Hanson, 1993). AND, andesite; BAS, basalt; PAAS, post-Archean Australian shale; (b) Y/Ho vs. Eu/Sm diagram (modified from Albut et al., 2018, and references therein)

kerogen is not straightforward, because high thermal volatilization can considerably contribute to lower this index (Dembicki, 2009; de Kock et al., 2017), the Dotternhausen black shale and limestone beds exhibit relatively invariable HI values of ~580 mg HC/g TOC and

high TOC_{cf} contents of ~13 wt.% (Figure 6). This demonstrates that the organic matter was well preserved and of predominantly marine origin—here, bolstered by the oil shale character of the studied section (Röhl, Schmid-Röhl, Oschmann, Frimmel, & Schwark, 2001).

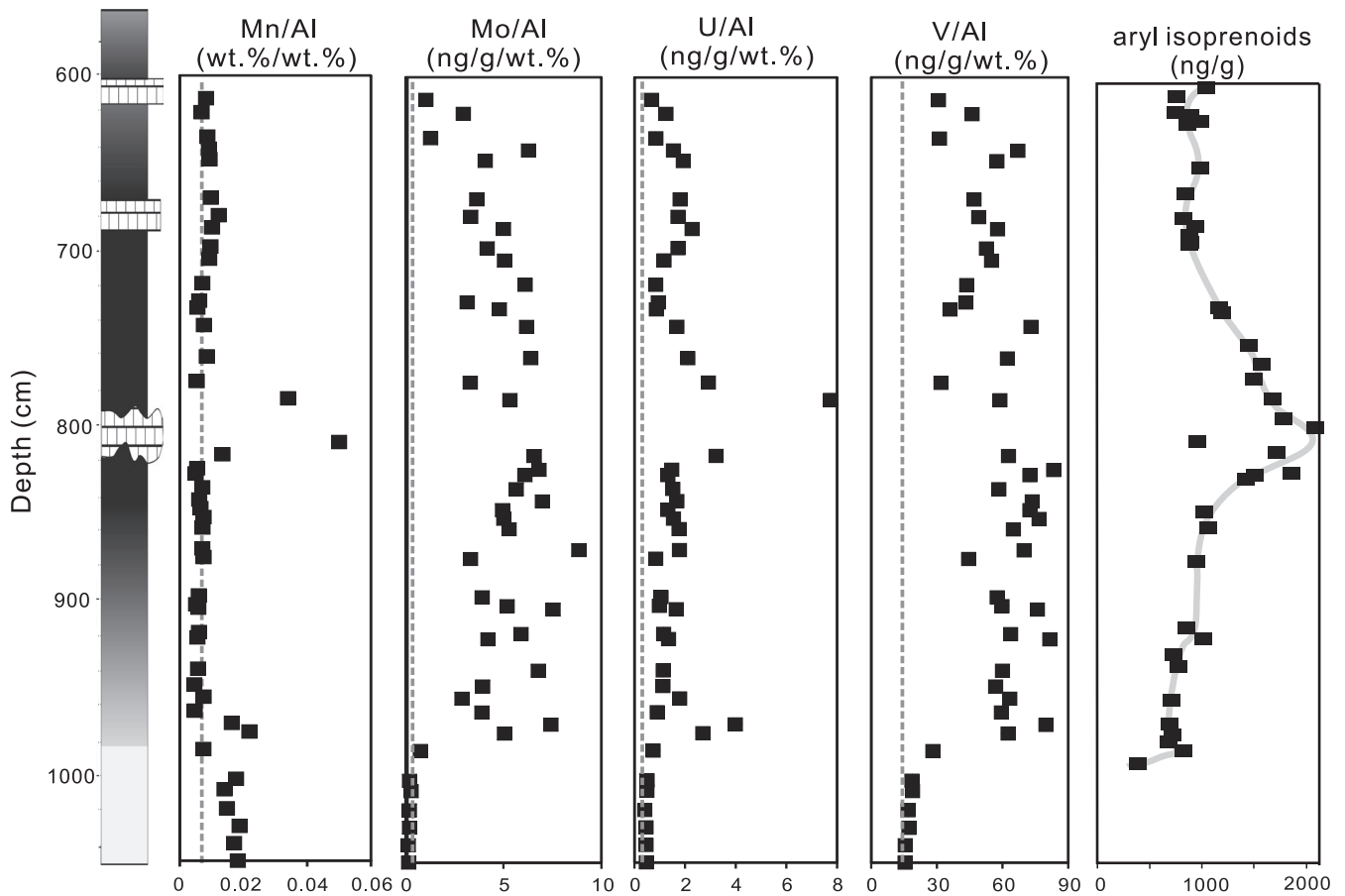


FIGURE 5 Stratigraphic profiles of Mn, Mo, U and V enrichments in the Dotternhausen section. Stratigraphic distribution of aryl isoprenoid (GSB biomarker) abundance is from Schwark & Frimmel (2004). Dashed lines denote the according reference values of upper continental crust (UCC; McLennan, 2001)

TABLE 2 Stable isotope and TOC_{cf} carbonate data for Dotternhausen samples

Depth [cm]	$\delta^{13}\text{C}_{\text{carb}}$ [‰] VPDB	$\delta^{13}\text{C}_{\text{org}}$ [‰] VPDB	$\Delta^{13}\text{C}_{\text{carb-}}$ $\delta^{13}\text{C}_{\text{org}}$ [‰] VPDB	$\delta^{18}\text{O}$ [‰] VPDB	TOC _{cf} [wt.%]	CaCO ₃ [wt.%]	[DIC] _{total} [wt.%]	[DIC] _{org} [wt.%]	[DIC] _{org} / [DIC] _{total} [%]
613	0.38	-26.94	27.32	-5.65	3.9	29.79	3.57	—	—
616	0.19	-27.32	27.51	-5.99	7.6	44.76	5.37	—	—
621	0.09	-27.12	27.21	-5.77	10.3	8.61	1.03	0.00	0
624	-0.4	-27.87	27.47	-6.32	7.9	43.94	5.27	0.08	1
628	-0.08	-27.43	27.35	-6.28	7.0	39.86	4.78	0.01	0
631	-0.06	-27.42	27.37	-5.92	7.0	29.68	3.56	0.01	0
635	-0.19	-27.11	26.92	-5.44	5.4	44.32	5.32	0.04	1
638	-0.44	-27.52	27.08	-6.34	8.9	40.16	4.82	0.08	2
642	-0.74	-28.09	27.35	-6.01	7.4	29.24	3.51	0.09	3
645	-0.77	-27.12	26.35	-6.67	11.0	65.54	7.86	0.22	3
648	-0.45	-27.74	27.28	-6.54	12.8	29.03	3.48	0.06	2
652	-0.64	-29.05	28.41	-6.69	7.5	56.48	6.78	0.15	2
656	-0.47	-28.87	28.41	-6.34	8.8	41.47	4.98	0.08	2
670	-0.93	-27.32	26.39	-6.19	12.7	31.73	3.81	0.13	3
673	-0.77	-28.66	27.89	-6.35	9.2	28.2	3.38	0.09	3
677	-0.67	-28.07	27.4	-6.04	6.8	58.63	7.04	0.17	2
680	-0.62	-28.26	27.64	-6	7.4	56.25	6.75	0.15	2
684	-1.01	-28.69	27.68	-6.25	10.1	37.75	4.53	0.16	4
687	-1.12	-27.9	26.78	-6.22	9.5	42.99	5.16	0.21	4
691	-0.97	-28.51	27.54	-6.54	11.2	32.62	3.91	0.13	3
694	-1.62	-30.37	28.75	-6.69	8.8	49.81	5.98	0.32	5
698	-1.54	-29.25	27.71	-6.48	14.6	3.47	0.42	0.02	5
701	-1.7	-29.68	27.98	-6.56	10.7	42.86	5.14	0.29	6
705	-1.38	-30.03	28.65	-6.38	8.1	31.96	3.84	0.18	5
708	-1.55	-29.79	28.24	-5.99	5.5	24.86	2.98	0.16	5
712	-1.33	-29.76	28.43	-6.16	6.2	48.94	5.87	0.26	4
715	-1.78	-29.17	27.39	-6.6	10.3	43.79	5.25	0.32	6
719	-1.49	-29.8	28.32	-6.34	8.1	36.63	4.40	0.22	5
722	-1.64	-29.76	28.12	-6.68	10.7	53.12	6.37	0.35	6
726	-2.43	-30.92	28.49	-6.15	9.8	36.32	4.36	0.34	8
729	-2.24	-30.25	28.01	-6.11	7.5	36.84	4.42	0.33	7
733	-2.53	-30.35	27.82	-5.71	5.8	29.11	3.49	0.29	8
736	-3.12	-31.44	28.32	-6.44	10.8	87.92	10.55	1.05	10
740	-2.37	-31.28	28.91	-6.73	11.9	24.88	2.99	0.23	8
743	-2.61	-31.38	28.77	-6.59	11.8	24.69	2.96	0.25	8
747	-2.46	-30.34	27.88	-6.56	10.8	36.91	4.43	0.36	8
750	-2.93	-31.34	28.42	-6.57	11.8	25.3	3.04	0.28	9
754	-3.23	-31.22	27.99	-6.54	15.1	32.59	3.91	0.40	10
757	-2.62	-31.83	29.22	-6.37	9.4	25.5	3.06	0.25	8
761	-3.57	-31.28	27.71	-6.02	12.1	29.08	3.49	0.40	11
764	-3.3	-31.03	27.72	-6.39	14.0	25.04	3.00	0.32	11
768	-4.64	-30.33	25.69	-6.91	6.7	52.69	6.32	0.97	15
771	-5.21	-30.68	25.47	-6.64	8.2	54.45	6.53	1.11	17

(Continues)

TABLE 2 (Continued)

Depth [cm]	$\delta^{13}\text{C}_{\text{carb}}$ [‰] VPDB	$\delta^{13}\text{C}_{\text{org}}$ [‰] VPDB	$\Delta^{13}\text{C}_{\text{carb-}}$ org [‰] VPDB	$\delta^{18}\text{O}$ [‰] VPDB	TOC _{cf} [wt.%]	CaCO ₃ [wt.%]	[DIC] _{total} [wt.%]	[DIC] _{org} [wt.%]	[DIC] _{org} / [DIC] _{total} [%]
775	-3.9	-30.22	26.32	-7.18	8.5	42.64	5.12	0.66	13
778	-4.26	-30.25	25.99	-6.97	7.5	50.9	6.11	0.86	14
781	-6.52	-31.8	25.27	-7.05	10.5	33.54	4.02	0.83	21
785	-5.99	-30.56	24.57	-6.55	7.2	67.14	8.06	1.58	20
788	-5.89	-30.75	24.86	-5.11		81.99	9.84	1.88	19
796	-12.6	-30.11	17.51	-4.17		95.05	11.41	4.77	42
801	-12.17	-28.76	16.59	-4.19		87.79	10.53	4.46	42
805	-11.27	-29.75	18.48	-4.69		92.57	11.11	4.21	38
815	-5.89	-31.15	25.26	-5.63		83.4	10.01	1.89	19
817	-5.92	-31.77	25.85	-6.34	11.0	48.61	5.83	1.09	19
822	-6.19	-32.37	26.18	-6.48	11.9	24.48	2.94	0.56	19
825	-6.27	-32.15	25.88	-6.54	11.7	21.27	2.55	0.50	20
828	-4.95	-31.93	26.97	-6.74	12.5	13.37	1.60	0.25	16
831	-5.34	-32.26	26.92	-6.43	13.1	14.81	1.78	0.29	17
834	-5.66	-31.96	26.3	-6.44	13.3	19.04	2.28	0.40	18
836	-7.21	-33.2	25.99	-6.19	10.7	23.95	2.87	0.62	22
840	-6.23	-32.36	26.13	-7.1	11.5	35.83	4.30	0.83	19
843	-6.6	-31.79	25.19	-6.23	11.8	22.18	2.66	0.55	21
848	-6.79	-32.09	25.3	-6.76	11.6	23.16	2.78	0.59	21
850	-8.82	-31.94	23.12	-5.5	11.3	41.24	4.95	1.37	28
853	-7.83	-32.15	24.32	-6.59	12.0	29.84	3.58	0.87	24
856	-7.24	-32.23	24.99	-6.38	13.4	26.44	3.17	0.71	22
859	-7.57	-32.51	24.94	-5.55	15.9	22.47	2.70	0.63	23
862	-5.92	-32.44	26.52	-6.29	9.0	18.97	2.28	0.42	18
869	-5.5	-32.22	26.72	-6.16	5.5	17.01	2.04	0.35	17
869	-6.6	-32.39	25.79	-6.49	12.0	23.58	2.83	0.58	20
871	-5.14	-31.79	26.66	-5.83	12.4	28.36	3.40	0.55	16
876	-4.23	-31.64	27.41	-5.45	9.6	28.61	3.43	0.46	13
883	-4.53	-31.89	27.36	-6.52	14.4	18.91	2.27	0.32	14
894	-6.09	-32.3	26.21	-6.13	14.7	20.83	2.50	0.47	19
898	-5.55	-32.28	26.73	-6.73	10.1	20.81	2.50	0.43	17
899	-5.62	-32.23	26.61	-6.51	10.9	16.18	1.94	0.34	17
903	-4.71	-32.92	28.21	-6.91	7.2	13.99	1.68	0.24	14
905	-5.17	-31.98	26.82	-6.04	12.9	23.07	2.77	0.45	16
914	-5.53	-31.5	25.97	-6.59	14.1	19.69	2.36	0.41	18
917	-5.52	-31.37	25.86	-6.78	13.3	23.59	2.83	0.50	18
919	-6.23	-33.27	27.04	-6.51	6.1	19.31	2.32	0.43	19
921	-3.93	-30.83	26.9	-6.43	12.8	21.22	2.55	0.32	13
922	-3.1	-30.8	27.7	-6.28	13.0	24.4	2.93	0.29	10
926	-4.12	-30.96	26.84	-6.28	11.8	23.23	2.79	0.37	13
935	-4	-30.98	26.98	-6.13	12.8	24.56	2.95	0.38	13
940	-4.03	-32.08	28.05	-6.22	8.2	18.06	2.17	0.27	13
949	-3.47	-31.7	28.23	-6.41	9.8	15.18	1.82	0.20	11

(Continues)

TABLE 2 (Continued)

Depth [cm]	$\delta^{13}\text{C}_{\text{carb}}$ [‰] VPDB	$\delta^{13}\text{C}_{\text{org}}$ [‰] VPDB	$\Delta^{13}\text{C}_{\text{carb-}}_{\text{org}}$ [‰] VPDB	$\delta^{18}\text{O}$ [‰] VPDB	TOC _{cf} [wt.%]	CaCO ₃ [wt.%]	[DIC] _{total} [wt.%]	[DIC] _{org} [wt.%]	[DIC] _{org} / [DIC] _{total} [%]
956	-3.26	-30.36	27.1	-6.43	9.9	34.48	4.14	0.44	11
961	-3.23	-31.01	27.78	-6.12	7.7	18.44	2.21	0.23	10
964	-2.73	-31.34	28.61	-6.08	8.7	14.38	1.73	0.15	9
971	-1.64	-28.15	26.51	-6.21	12.6	51.81	6.22	0.36	6
976	-2	-29.02	27.01	-6.06	8.2	49.93	5.99	0.41	7
979	-1.71	-29.64	27.93	-6.36	4.6	22.09	2.65	0.15	6
981	-0.69	-27.27	26.57	-6.99	1.8	17.65	2.12	0.05	3
986	-1.11	-28.91	27.8	-6.47	8.0	22.78	2.73	0.10	4
993	-1.05	-27.24	26.19	-6.7	2.7	25.43	3.05	0.12	4
993	-1.15	-27.66	26.51	-6.67	3.0	27.82	3.34	0.14	4
1,003	-1.18	-26.65	25.47	-5.87	0.8	35.73	4.29	0.19	4
1,012	-0.89	-27.88	26.99	-5.71	3.1	28.8	3.46	0.11	3

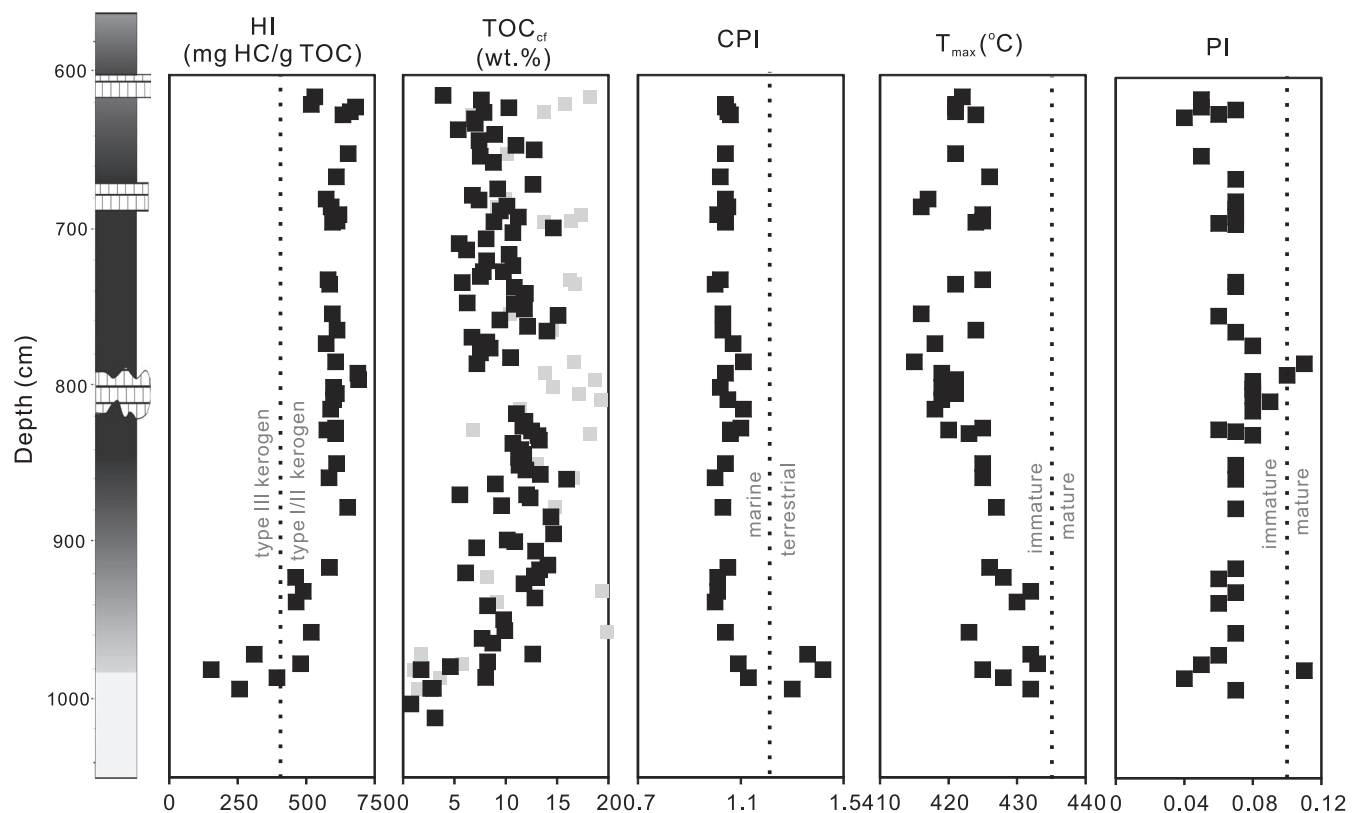


FIGURE 6 Rock-Eval pyrolysis data of the Dotternhausen sedimentary section. The HI, CPI, T_{max} , PI, and TOC_{cf} of gray rectangles are from Frimmel, Oschmann, & Schwark (2004)

The carbon preference index (CPI) with relatively low values of ~1 in the Dotternhausen black shale sediments (Figure 6) further implies low contribution from terrestrial-derived organic matter (CPI >1.2: Ruebsam, Müller, Kovács, Pálffy, & Schwark, 2018).

The $\delta^{13}\text{C}_{\text{org}}$ signals in the Dotternhausen black shales can also be perturbed by recycled sediments from organic matter-rich

catchment areas. Such recycled organic matter is generally marked by high thermal maturity that can alter the primarily preserved organic carbon isotope signals. To assess the possible contamination from recycled organic matters on the Dotternhausen black shales, we here refer to molecular maturity indicators such as Rock-Eval T_{max} (°C) and production index (PI) published in previous studies

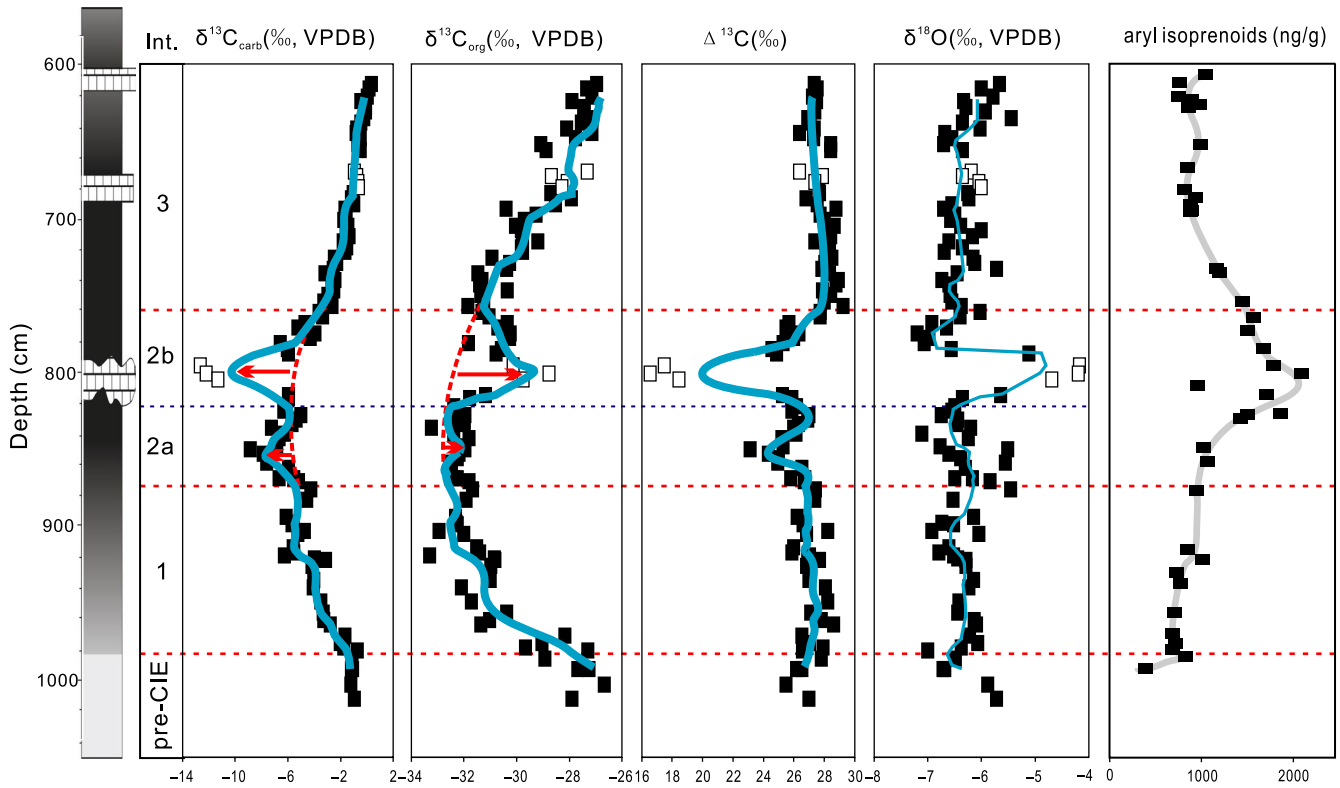


FIGURE 7 Stratigraphic profiles of $\delta^{13}\text{C}_{\text{carb}}$, $\delta^{13}\text{C}_{\text{org}}$, $\Delta^{13}\text{C}$ ($\Delta^{13}\text{C} = \delta^{13}\text{C}_{\text{carb}} - \delta^{13}\text{C}_{\text{org}}$) and $\delta^{18}\text{O}$ in the Dotternhausen section. Stratigraphic distributions of aryl isoprenoid (GSB biomarker) abundance are from Schwark & Frimmel (2004). The red dashed arcs denote the theoretic Toarcian CIE curves without suffering local-scale carbon-cycle perturbations. The blue lines represent the 5-point moving average of the isotopic data. Int.: interval. White rectangles particularly represent the isotopic data from limestone beds

(cf. Frimmel, 2003; Frimmel, Oschmann, & Schwark, 2004). The T_{max} values (mean = 427°C) without any considerable variation (Figure 6) together with high HI demonstrate that the organic matter in Dotternhausen black shale is neither overmature nor inert. This demonstrates the lack of significant contamination with recycled sediments. The possibility of sedimentary recycling can also be traced by inorganic proxies. For instance, recycled sediments would display a substantial increase in Zr/Sc along with a much smaller magnitude increase in Th/Sc (McLennan, Hemming, McDaniel, & Hanson, 1993). A crossplot of Zr/Sc versus Th/Sc was adopted to track possible recycling processes on the studied black shale samples (McLennan, Hemming, McDaniel, & Hanson, 1993). Though the data show a slight deviation from the compositional variation trend indicative for single cycling from parent rock material, all their Zr/Sc ratios (<10) (Figure 4a) are low and comparable to that of pristine provenance rocks, indirectly revealing the minimal influence from polycyclic reworking of sedimentary rocks. In addition, hydrothermal fluid can preferentially liberate ^{12}C and introduce external hydrocarbon into organic-rich sedimentary rocks, which would influence their pristine $\delta^{13}\text{C}_{\text{org}}$ values (Jiang et al., 2012; Pinti, Hashizume, Sugihara, Massault, & Philippot, 2009). The influence of high-temperature fluids on sediments can be tested in a crossplot between Y/Ho and Eu/Sm (Figure 4b; cf. Albut et al., 2018, and references therein). The Dotternhausen black shales exhibit chondritic Y/Ho

ratios (~28) similar to the modern shale average (Albut et al., 2018, and references therein). Yttrium is less effectively scavenged from seawater than the trivalent REE Ho, leading to high residual Y/Ho ratios in the oceans. High-temperature hydrothermal fluids are also characterized by chondritic Y/Ho ratios, but exhibit higher Eu/Sm ratios than oceanic or continental crust due to the higher solubility of reduced divalent Eu compared to trivalent Sm. The Dotternhausen black shales have Eu/Sm ratios of 0.21 and 0.23, which are within the range of the modern shale average, but an order of magnitude lower than typical high-temperature hydrothermal fluids at mid-ocean ridges (Figure 4b). This observation demonstrates negligible alteration by hydrothermal activity on the studied black shale facies. In summary, the $\delta^{13}\text{C}_{\text{org}}$ records of Dotternhausen Toarcian CIE samples were not significantly influenced by terrigenous-derived organic matters, contaminated by recycling of old sediments, and altered by hydrothermal activity.

5.2 | Marine redox condition record in the Dotternhausen succession during the Toarcian CIE

During the Toarcian CIE high rates of organic carbon production occurred in the proximal shelf areas of the northwestern part of Tethys margin (e.g., French et al., 2014; Frimmel, Oschmann, & Schwark,

2004; Schwark & Frimmel, 2004). These were commonly tied to high marine productivity rates (e.g., Jenkyns, 2010; Röhl, Schmid-Röhl, Oschmann, Frimmel, & Schwark, 2001) caused by excessive nutrient input from enhanced continental weathering (e.g., Cohen, Coe, Harding, & Schwark, 2004; Percival et al., 2016). It was proposed that the generated organic matter subsequently suffered aerobic degradation during which the seawater oxygen inventory was massively depleted (Röhl, Schmid-Röhl, Oschmann, Frimmel, & Schwark, 2001). Furthermore, at a high sea-level stand during the Toarcian CIE period (Ruebsam, Mayer, & Schwark, 2019), the strong water-column stratification and hydrological restriction have prevented efficient ventilation between bottom waters and the outside open ocean, which eventually promoted the formation of anoxic benthic seawaters in the northwestern Tethys shelf-sea settings (e.g., Guillaume and Yannick, 2012; Hermoso et al., 2013; McArthur et al., 2008; Ruvalcaba Baroni et al., 2018; Röhl, Schmid-Röhl, Oschmann, Frimmel, & Schwark, 2001). The euxinic depositional condition for the Dotternhausen black shale facies was determined by the existence of aryl isoprenoids (Figure 5), biomarkers for GSB (cf. Schwark & Frimmel, 2004), which implies relatively high aqueous hydrogen sulfide (H_2S) concentration in the seawater. Such a seawater redox structure is further supported by the strong authigenic enrichment of redox-sensitive elements, that is, Mo, U, and V (Figure 5). For the Dotternhausen sedimentary profile, a gradual increase in aryl

isoprenoid concentration is exhibited in its lower part, followed by a decreasing trend in its upper part (Figure 5). The GSB, which are anoxygenic autotrophs, are able to oxidize H_2S to sulfate (SO_4^{2-}) (e.g., Riccardi, Kump, Arthur, & D'Hondt, 2007). A bloom of GSB in the seawater will thus enhance the assimilative consumption of H_2S (Hurse, Kappler, & Keller, 2008), which can, to a certain extent, lower its concentration in the bottom anoxic/euxinic water mass, and thus deepen the seawater sulfidic oxygen minimum zone (chemocline). Alternatively, molecular oxygen generated by oxygenic photosynthesizers can also oxidize H_2S under high Eh conditions and thus change the depth of the seawater chemocline. However, this possibility is in conflict with the fact that GSB bloomed at c. 800 cm in the Dotternhausen profile (Figure 7), since GSB cannot thrive in oxic marine environments. In conclusion, if the chemocline is defined here as a relatively thick mid-depth water mass in which GSB progressively thrive (e.g., marked by the gradual increase in aryl isoprenoid concentration), the depositional environment of the Dotternhausen CIE sediments is considered to be characterized by a redox stratified seawater without a significant variation in the depth of the upper limit of this chemocline (Figure 8). In contrast, enhanced H_2S consumption in the bottom euxinic water mass during the height of GSB activity (maximum concentrations of aryl isoprenoid biomarkers) likely deepened the lower limit of the chemocline down to or near the water-sediment interface (Figure 8b). This favored higher fluxes

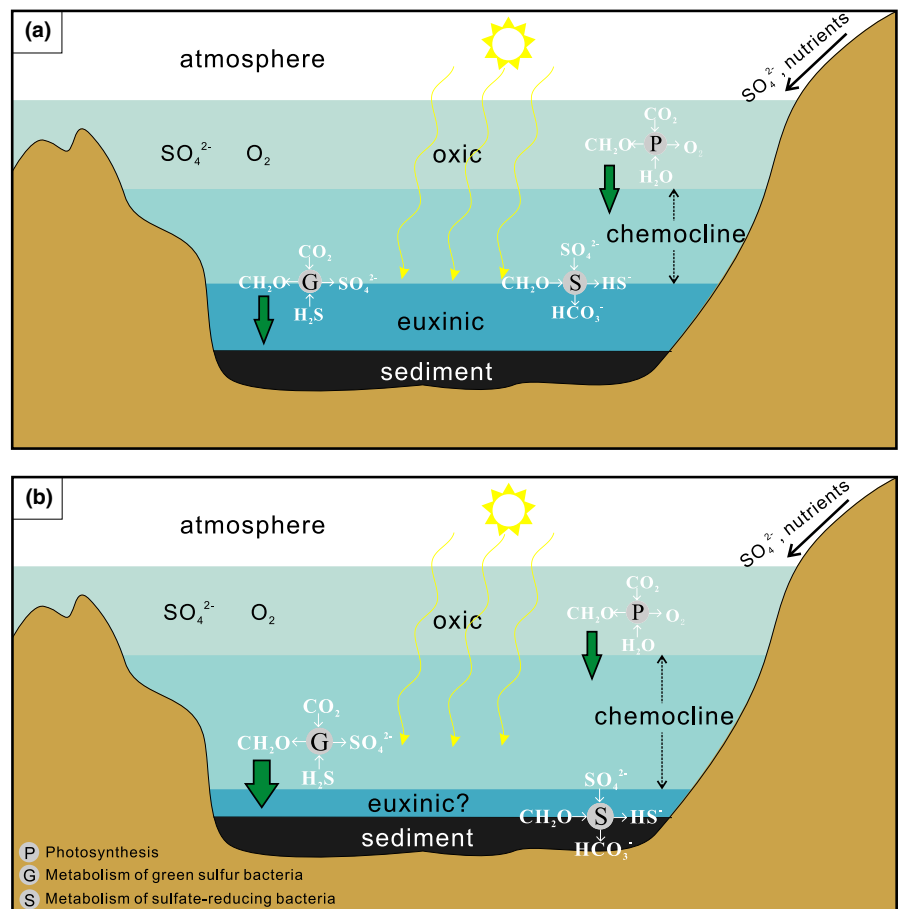


FIGURE 8 Schematic representation of the Toarcian CIE northwestern Tethys seawater column during the gradual increase of GSB activity and associated $\delta^{13}\text{C}_{\text{carb}} - \delta^{13}\text{C}_{\text{org}}$ decoupling. (a) Interval 2a: the initial stage of GSB bloom. (b) Interval 2b: the height of GSB bloom along with microbial sulfate reduction. The light, medium, and dark blue colors represent oxic, sulfidic oxygen minimum zone, and euxinic conditions, respectively, in the water column

of electron acceptors such as SO_4^{2-} and probably a small amount of manganese (Mn) oxyhydroxides (Figure 5 and Figure S1) to the sediment and thus fueled higher rate of dissimilatory reduction of SO_4^{2-} and Mn-oxyhydroxides. This caused an increase of organic carbon remineralization and promoted the formation of the diagenetic Unterer Stein lenticular carbonate bed.

5.3 | Evidence for second-order perturbations of the Toarcian carbon cycle

5.3.1 | Decoupled $\delta^{13}\text{C}_{\text{carb}}$ - $\delta^{13}\text{C}_{\text{org}}$ superimposed on the Toarcian CIE in Dotternhausen, Germany

Carbon-cycle fluctuations in Earth's history such as the Mesozoic CIEs (Hesselbo et al., 2000; Kemp, Coe, Cohen, & Schwark, 2005; Kuypers, Pancost, & Damste, 1999) and Neoproterozoic Snowball Earth events (Och & Shields-Zhou, 2012; Sahoo et al., 2012) were commonly associated with changes in coeval $\delta^{13}\text{C}_{\text{carb}}$ and $\delta^{13}\text{C}_{\text{org}}$ records. Generally, a common approach used to distinguish whether a carbon cycle is global- or local scale is to evaluate the nature of the concurrently preserved $\delta^{13}\text{C}_{\text{carb}}$ and $\delta^{13}\text{C}_{\text{org}}$ signatures in sediments (Knoll, Hayes, Kaufman, Swett, & Lambert, 1986). Unpaired $\delta^{13}\text{C}_{\text{carb}}$ - $\delta^{13}\text{C}_{\text{org}}$ is often suggested to have been impacted by second-order local-scale carbon-cycle perturbations (e.g., Jiang et al., 2012; Meyer et al., 2013); paired $\delta^{13}\text{C}_{\text{carb}}$ - $\delta^{13}\text{C}_{\text{org}}$ is usually attributed to changes in the global carbon cycle (e.g., Ader et al., 2009; Li et al., 2018). It is widely accepted that the global injection of isotopically light carbon (CH_4 and/or CO_2) into the coeval atmosphere-ocean system during the early Toarcian led to widespread negative CIEs recorded in northwestern Tethys (e.g., Hesselbo et al., 2000; Hesselbo, Jenkyns, Duarte, & Oliveira, 2007; Svensen et al., 2007), eastern Tethys (Fu et al., 2016), southwestern Tethys (Ruebsam et al., 2020), south-eastern Tethys (Newton et al., 2011; Han, Hu, Kemp, & Li, 2018), northwestern Panthalassa (Izumi, Kemp, Itamiya, & Inui, 2018), and northeastern Panthalassa (Caruthers, Gröcke, & Smith, 2011). If the widespread Toarcian CIE was thus a global alteration of the carbon cycle, it is expected to be accompanied by a constant $\Delta^{13}\text{C}_{\text{carb-org}}$ between DIC and DOC reservoirs. In this study, negative CIEs are observed in both $\delta^{13}\text{C}_{\text{carb}}$ and $\delta^{13}\text{C}_{\text{org}}$ records from the Dotternhausen section (Figure 7) of the northwestern Tethys (Figure 1). Pronounced $\delta^{13}\text{C}_{\text{carb}}$ - $\delta^{13}\text{C}_{\text{org}}$ covariations have been shown in the lower (interval 1: 981–883 cm) and upper (interval 3: 757–613 cm) *falciferum* zone (Figure 9a,c) of the Toarcian CIE interval. Intervals 1 and 3 display relatively constant $\Delta^{13}\text{C}_{\text{carb-org}}$ values around 27‰ and 28‰, respectively (Figures 7 and 10a), which most likely reflect global-scale carbon-cycle perturbations during the Toarcian. However, a prominent two-step $\delta^{13}\text{C}_{\text{carb}}$ - $\delta^{13}\text{C}_{\text{org}}$ decoupling signature, along with two distinct magnitudes of decreased $\Delta^{13}\text{C}_{\text{carb-org}}$ values, is observed around the climax of the CIE (interval 2a and 2b; Figures 7 and 10a), which points to a local-scale disturbance of the carbon cycle. The first step in interval 2a is of smaller magnitude compared to the much larger second step in interval 2b (Figures 7 and 10a).

5.3.2 | Possible mechanism(s) for the local-scale $\delta^{13}\text{C}_{\text{carb}}$ - $\delta^{13}\text{C}_{\text{org}}$ decoupling

Interval 2a

The negative excursion in $\Delta^{13}\text{C}_{\text{carb-org}}$ is more influenced by the variation in the $\delta^{13}\text{C}_{\text{carb}}$ than $\delta^{13}\text{C}_{\text{org}}$ values (Figure 7). However, carbonates in the black shales of interval 2a represent a combination of biogenic calcites related to calcareous phytoplankton (Frimmel, Oschmann, & Schwark, 2004) and disseminated authigenic grains. A rough estimate of contribution from organic matter remineralization (C_{org}) and seawater inorganic carbon (C_{sw}) in carbonate can be obtained with the following equation (cf. Heimann et al., 2010; Konhauser et al., 2017):

$$[\text{DIC}]_{\text{total}} \times \delta^{13}\text{C}_{\text{total}} = [\text{DIC}]_{\text{org}} \times \delta^{13}\text{C}_{\text{org}} + [\text{DIC}]_{\text{sw}} \times \delta^{13}\text{C}_{\text{sw}}$$

where the $[\text{DIC}]_{\text{total}}$, $[\text{DIC}]_{\text{org}}$, and $[\text{DIC}]_{\text{sw}}$ denote total inorganic carbon, inorganic carbon derived from remineralized organic matter, and inorganic carbon from seawater; $\delta^{13}\text{C}_{\text{total}}$ and $\delta^{13}\text{C}_{\text{sw}}$ denote the $\delta^{13}\text{C}$ of total carbonate ($\delta^{13}\text{C}_{\text{carb}}$) and seawater. Assuming that the $\delta^{13}\text{C}$ values of Phanerozoic $[\text{DIC}]_{\text{sw}}$ is near to zero (Shields & Veizer, 2002 and references therein), $[\text{DIC}]_{\text{org}}$ (equals to $([\text{DIC}]_{\text{total}} \times \delta^{13}\text{C}_{\text{total}}) / \delta^{13}\text{C}_{\text{org}}$) varies between 13% and 28% $[\text{DIC}]_{\text{total}}$ (average of 20%) (Table 2), while $[\text{DIC}]_{\text{sw}}$ has an average of 80%. This estimate can be translated by the $\delta^{13}\text{C}_{\text{carb}}$ versus $\delta^{18}\text{O}$ cross-plots (Figure 10b; Konhauser et al., 2017; Ossa Ossa et al., 2018). The samples of the interval 2a have $\delta^{13}\text{C}_{\text{carb}}$ values between -8.8 and -4.2 ‰ and almost all of them plot above the line of $\text{C}_{\text{org}} : \text{C}_{\text{sw}} = 1:1$ (Figure 10b). This implies that carbon components of these carbonates are contributed by $\sim 80\%$ of DIC and only $\sim 20\%$ of remineralized organic carbon (Figure 10b). The remineralization of organic matter occurs through anaerobic or microaerophilic microbial processes that require electron acceptors (e.g., Heimann et al., 2010; Konhauser et al., 2017 and references therein), which here are sulfate and possibly Mn-oxyhydroxides (see Section 5.2). These processes produce carbonates with lighter $\delta^{13}\text{C}_{\text{carb}}$ values compared to the ambient DIC composition.

It can be noticed that the shift toward negative $\delta^{13}\text{C}_{\text{carb}}$ values in interval 2a is accompanied by a very minor shift of $\delta^{13}\text{C}_{\text{org}}$ toward heavier values (Figure 7). The metabolisms of anoxygenic phototrophs (GSB) yield ^{13}C -enriched biomass through primary productivity (Takahashi, Kaiho, Oba, & Kakegawa, 2010; van Breugel, Baas, Schouten, Mattioli, & Sinninghe Damsté, 2006) and can explain the small increase in $\delta^{13}\text{C}_{\text{org}}$ values observed in interval 2a. However, since this $\delta^{13}\text{C}_{\text{org}}$ increase is minimal, it does not have a major impact on the overall $\Delta^{13}\text{C}_{\text{carb-org}}$ negative excursion—though this interval represents the early stage of the GSB bloom. In view of this, carbonates in the interval 2a precipitated in equilibrium with seawater isotope composition, but were further aided by a small contribution of isotopically lighter carbon generated through microbial-induced organic carbon remineralization (Figure 8a). This small contribution of light carbon isotopes likely explains the smaller magnitude of the $\Delta^{13}\text{C}_{\text{carb-org}}$ negative excursion recorded in this interval.

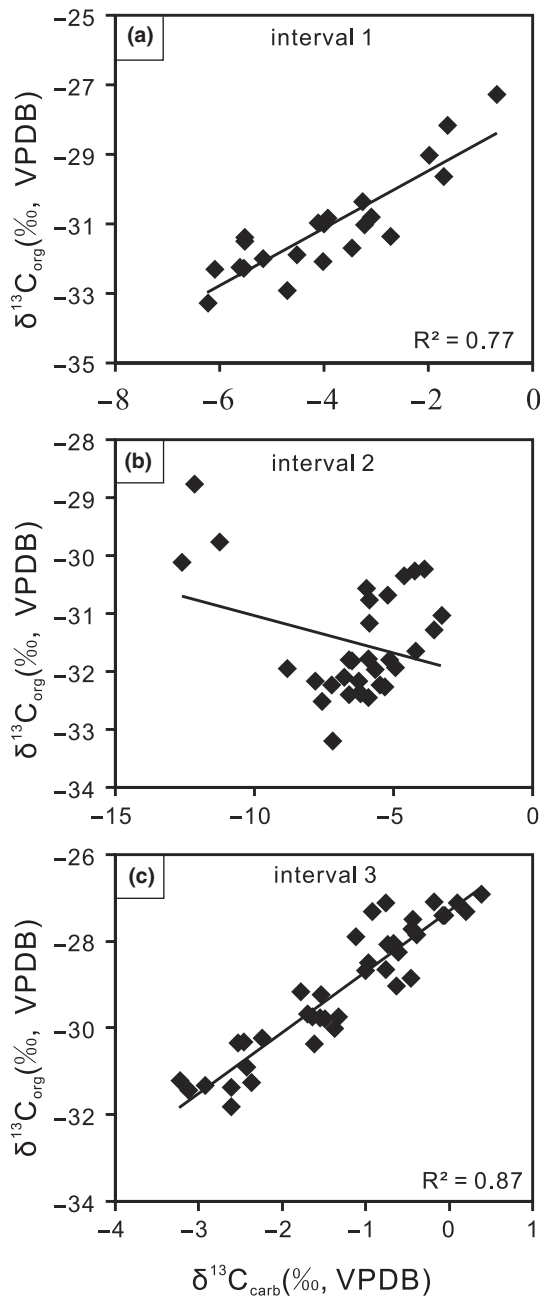


FIGURE 9 Crossplots of $\delta^{13}\text{C}_{\text{carb}}-\delta^{13}\text{C}_{\text{org}}$ in different intervals of the Dotternhausen carbon isotopic profiles

Interval 2b

The negative $\Delta^{13}\text{C}_{\text{carb-orig}}$ excursion in this interval is accompanied by a shift to heavier $\delta^{13}\text{C}_{\text{org}}$ and lighter $\delta^{13}\text{C}_{\text{carb}}$ values (Figure 7). Assuming that diagenesis of organic-rich sediments is widely described to have a minimal effect on $\delta^{13}\text{C}_{\text{org}}$ values (e.g., Jiang et al., 2012; Watanabe et al., 1997), it cannot thus explain the positive shift in $\delta^{13}\text{C}_{\text{org}}$ values recorded in interval 2b (see Section 5.1). This $\delta^{13}\text{C}_{\text{org}}$ record rather reflects a pristine isotope signal imparted by the dominant productive marine biota. As stated above (see interval 2a), the biomass produced by GSB is ^{13}C -enriched. Across interval 2b the height of GSB activity is obviously indicated by the maximum

concentration of aryl isoprenoid biomarkers, which generated more isotopically heavy biomass and the associated $\delta^{13}\text{C}_{\text{org}}$ positive excursion (Figure 7). The $\delta^{13}\text{C}_{\text{carb}}-\delta^{13}\text{C}_{\text{org}}$ decoupling in interval 2b can thus partly be explained by the climax of GSB metabolism.

Importantly, interval 2b includes changes in lithofacies from carbonate-bearing laminated black shales in its lowermost part to the diagenetic Unterer Stein carbonate bed upward and then back to carbonate-bearing laminated black shales (Figure 7). Therefore, the light carbon isotope composition of the Unterer Stein may be dominantly attributed to diagenetic carbonate precipitation through microbial sulfate reduction (MSR) with a minor contribution from dissimilatory Mn-oxyhydroxides reduction (see Section 5.2). Such diagenetic processes produce carbonates with light $\delta^{13}\text{C}_{\text{carb}}$ values, which may enhance the negative $\Delta^{13}\text{C}_{\text{carb-orig}}$ excursion in this interval (cf. Heimann et al., 2010; Konhauser et al., 2017). However, the $\delta^{13}\text{C}_{\text{carb}}$ versus $\delta^{18}\text{O}$ diagram indicates that the limestone bed samples fall between $\text{C}_{\text{org}}:\text{C}_{\text{sw}} = 1:1$ and $\text{C}_{\text{org}}:\text{C}_{\text{sw}} = 1:2$ lines (Figure 10b), and the calculated $[\text{DIC}]_{\text{org}}$ values vary between 38% and 42% $[\text{DIC}]_{\text{total}}$ (41% on average). This implies relatively greater amounts of carbon components derived from organic matter remineralization during diagenesis, compared to those in interval 2a—though the DIC_{sw} was still a major contributor in this carbonate bed. In contrast, samples from the carbonate-bearing laminated black shales (lowermost and upper parts of interval 2b) are exclusively distributed above the $\text{C}_{\text{org}}:\text{C}_{\text{sw}} = 1:3$ line (Figure 10b) with the calculated average $[\text{DIC}]_{\text{org}}$ value of 17%, demonstrating that their carbonate carbon components were mainly sourced from DIC_{sw} . It follows that the sediment pore waters or diagenetic environment in which the lenticular Unterer Stein carbonate bed precipitated was still in equilibrium with seawater. However, carbonate grains in the laminated black shale could have precipitated either in the water column or in sediments. Therefore, the $\delta^{13}\text{C}_{\text{org}}-\delta^{13}\text{C}_{\text{carb}}$ decoupling in interval 2b was largely caused by a GSB bloom and further exaggerated by the remineralization of organic material by MSR through authigenic carbonate precipitation (see Section 5.2; Figure 8b).

In summary, the coeval decreases in $\delta^{13}\text{C}_{\text{carb}}$ and increases in $\delta^{13}\text{C}_{\text{org}}$ values, which contributed to the two-step $\Delta^{13}\text{C}_{\text{carb-orig}}$ decoupling in interval 2, reflect a combined effect of enhanced activity of GSB and sulfate-reducing bacteria (SRB) (Figure 8). The GSB bloom caused high H_2S consumption in the euxinic bottom water and likely expanded the chemocline near to the water-sediment interface. This allowed higher sulfate flux to the anoxic sediment pore waters and ultimately caused carbonate precipitation aided by higher rates of SRB-induced organic carbon remineralization. In contrast, the following coeval increase in $\delta^{13}\text{C}_{\text{carb}}$ and decrease in $\delta^{13}\text{C}_{\text{org}}$ values, which ended this two-step $\Delta^{13}\text{C}_{\text{carb-orig}}$ decoupling in the upper part of interval 2b, were mainly caused by a decline of GSB activity as a consequence of exhausted H_2S availability in the water column. However, interval 2b represents the peak of the GSB bloom and explains the more pronounced $\Delta^{13}\text{C}_{\text{carb-orig}}$ decoupling in this interval compared to the lower 2a. Interestingly, this GSB bloom in interval 2 might have consumed enough H_2S in the Toarcian OAE water column to re-establish environmental conditions favorable for an increased expansion of aerobic metabolisms,

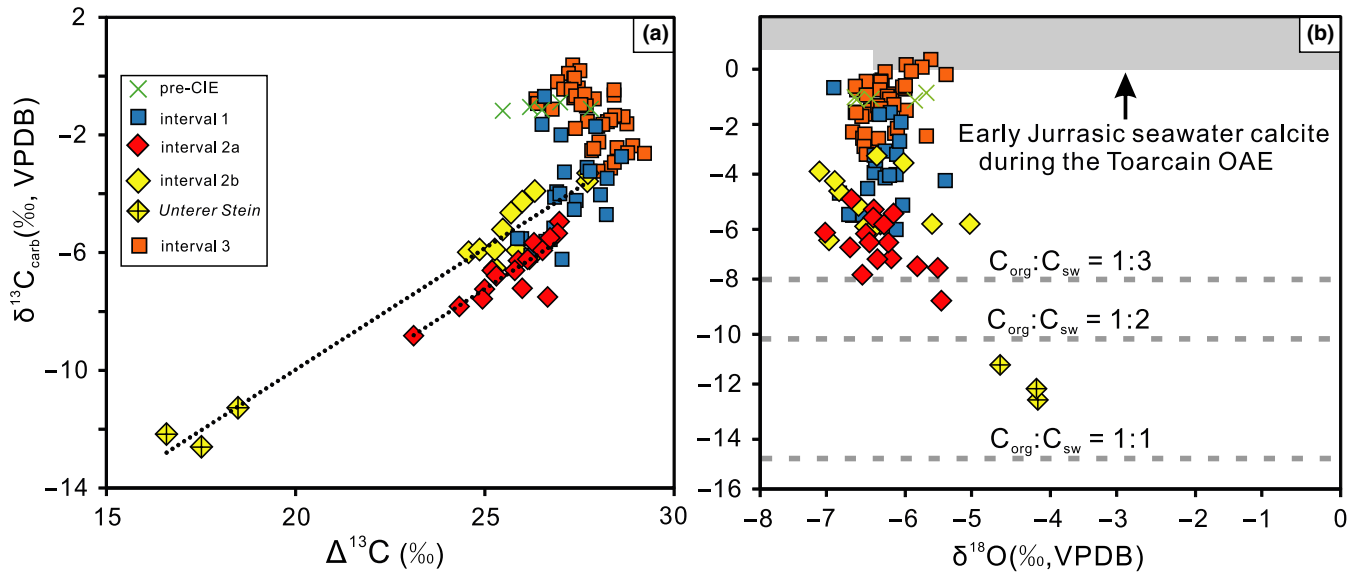


FIGURE 10 Crossplots of $\delta^{13}\text{C}_{\text{carb}}$ vs $\Delta^{13}\text{C}$ (a) and $\delta^{13}\text{C}_{\text{carb}}$ vs $\delta^{18}\text{O}$ (b) for different sedimentary intervals in the Dotternhausen. (a) The interval 2a (black shales) and 2b (Unterer Stein and black shales) show strong correlations between $\delta^{13}\text{C}_{\text{carb}}$ and $\Delta^{13}\text{C}$. (b) An model showing the carbonate carbon contribution between organic matter oxidation (C_{org}) and seawater inorganic carbon (C_{sw}) (cf. Heimann et al., 2010; Konhauser et al., 2017). The isotope composition of early Jurassic seawater calcites during Toarcian OAE were estimated from the belemnites ($\delta^{13}\text{C}_{\text{bel}}$: ~ 0 to $+2\text{‰}$ and $\delta^{18}\text{O}_{\text{bel}}$: ~ -6 to 0‰ ; Ullmann, Thibault, Ruhl, Hesselbo, & Korte, 2014) and platform limestone ($\delta^{13}\text{C}_{\text{limestone}}$: $\sim +1$ to $+2\text{‰}$ and $\delta^{18}\text{O}_{\text{limestone}}$: ~ -8 to -5‰ ; Han, Hu, Kemp, & Li, 2018)

that is, oxygenic photosynthesis, and ultimately trigger the progressive recovery to the end of the Toarcian CIE observed in the overlying interval 3 (Figure 7).

5.3.3 | Implication for ecosystem structure on local-scale carbon-cycle perturbation

A previous study has shown that co-varying $\delta^{13}\text{C}_{\text{carb}}$ and $\delta^{13}\text{C}_{\text{org}}$ imply that organic carbon in marine sediments is mainly derived from primary (photosynthetic) production without substantial post-depositional alteration (cf. Jiang et al., 2012). Here, it is shown that an abrupt carbon-cycle perturbation by intense metabolisms of GSB has the capacity of decoupling the primary carbon isotopic signals. In Earth's history, the dramatic rise in GSB activity is not only limited to Toarcian OAE epicontinental seas (Pancost et al., 2004; Röhl, Schmid-Röhl, Oschmann, Frimmel, & Schwark, 2001; Sælen, Tyson, Telnæs, & Talbot, 2000; Schwark & Frimmel, 2004; van Breugel, Baas, Schouten, Mattioli, & Sinninghe Damsté, 2006; Xu et al., 2018), but also significant in a number of ancient marine realms during the end-Ordovician, end-Devonian, end-Permian and end-Triassic mass-extinction events, which were, at least in part, forced by an increase in H_2S in the seawater (e.g., Joachimski et al., 2001; Riccardi, Kump, Arthur, & D'Hondt, 2007; Richoz et al., 2012). Decoupled $\delta^{13}\text{C}_{\text{carb}}-\delta^{13}\text{C}_{\text{org}}$ signals across these mass extinctions broadly coincide with enhanced GSB activities (van de Schootbrugge & Gollner, 2013, and references therein), which

implies the potential role of GSB in perturbing coeval carbon cycling. Thus, to investigate the possible mechanisms for decoupling $\delta^{13}\text{C}_{\text{carb}}-\delta^{13}\text{C}_{\text{org}}$ in sedimentary rocks, carbon-cycle turnover arising from a sharp proliferation of GSB may play a major role and should not be neglected.

5.4 | Tethys-wide but locally variable second-order perturbations of the Toarcian carbon cycle

Theoretically, coupled $\delta^{13}\text{C}_{\text{carb}}-\delta^{13}\text{C}_{\text{org}}$ signatures are expected in all existing Toarcian OAE sedimentary sections due to the global scale of this event (described in Section 5.3.1). Opposed to this expectation, however, decoupled $\delta^{13}\text{C}_{\text{carb}}-\delta^{13}\text{C}_{\text{org}}$ signals (yellow areas in Figure 11a and yellow squares in Figure 11b) are also found in other Toarcian OAE profiles, such as Bilong Co (eastern Tethys: Fu et al., 2016), Sancerre (northwestern Tethys: Hermoso et al., 2012), and Nianduo (southeastern Tethys: Han, Hu, Kemp, & Li, 2018), apart from the Dotternhausen one. This indicates that second-order carbon-cycle perturbations pervasively existed in anoxic/euxinic restricted basins and unrestricted marginal seas throughout Tethyan margin across the Toarcian OAE. Both, the Bilong Co and Sancerre sections, show coupled $\delta^{13}\text{C}_{\text{carb}}-\delta^{13}\text{C}_{\text{org}}$ below and above the decoupling interval (blue and orange areas in Figure 11a; blue and orange squares in Figure 11b), similar to the Dotternhausen profile. By contrast, the Nianduo CIE profile does not exhibit such coupled $\delta^{13}\text{C}_{\text{carb}}-\delta^{13}\text{C}_{\text{org}}$ intervals (Figure 11c),

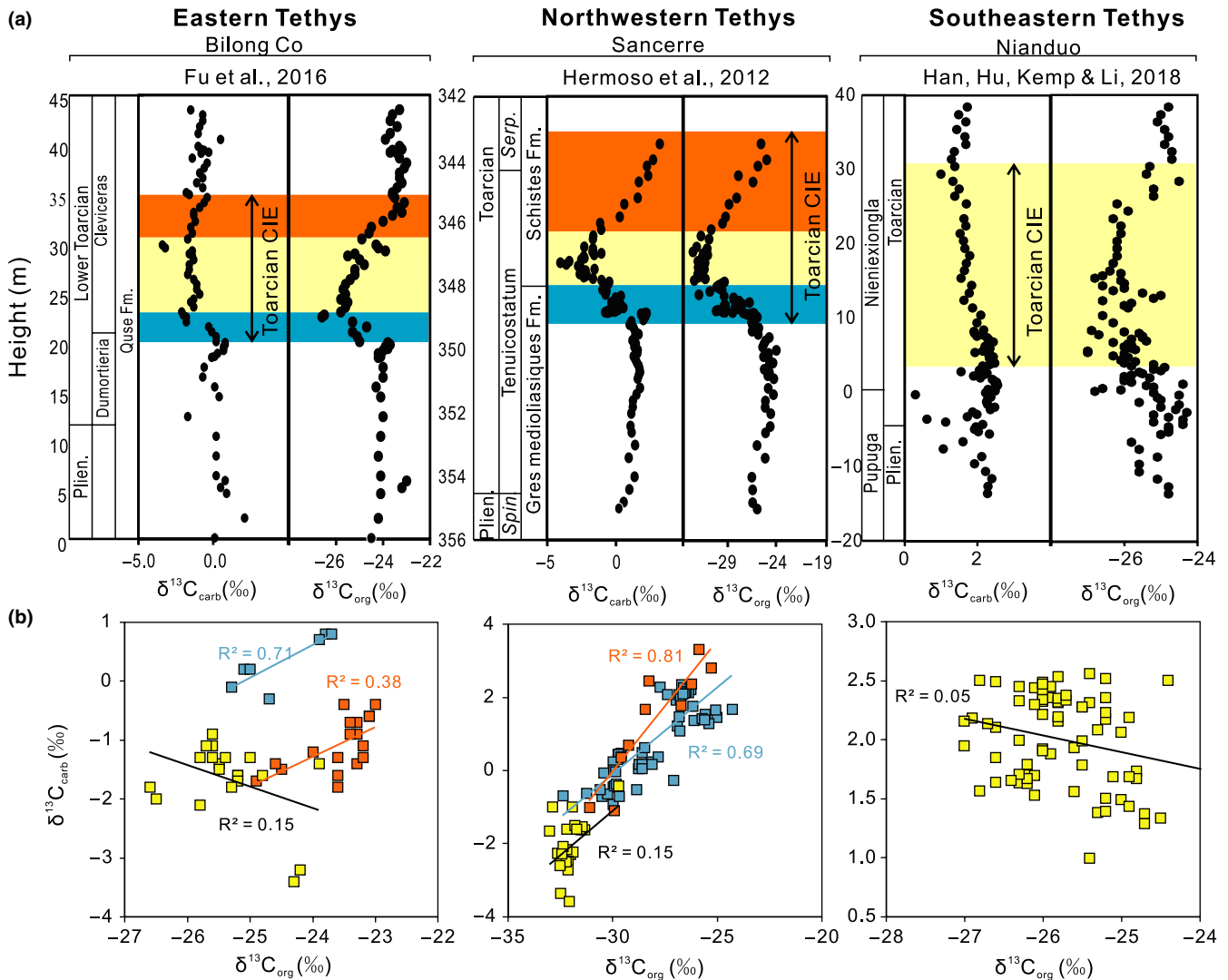


FIGURE 11 $\delta^{13}\text{C}_{\text{carb}}-\delta^{13}\text{C}_{\text{org}}$ decoupling signals (yellow areas in panel (a) and yellow squares in panel (b)) from geographically distinct localities (Bilong Co in eastern Tethys, Fu et al., 2016; Sancerre in northwestern Tethys, Hermoso et al., 2012; Nianduo in southeastern Tethys, Han et al., 2018) are identified across Toarcian CIE shown in panel A. Blue and orange colors in both panel A and B standing for the observed coupled $\delta^{13}\text{C}_{\text{carb}}-\delta^{13}\text{C}_{\text{org}}$ signals across Toarcian CIE are comparable to the marked interval 1 and 3 in the studied Dotternhausen section. Fm., formation; Plien., Pliensbachian; Serp., Serpentinum; Spin., Spinatum

which for the southeastern Tethys implies persistent local carbon-cycling disturbances throughout the entire Toarcian OAE. It should be noted that the $\delta^{13}\text{C}_{\text{carb}}$ profiles of the various Toarcian sedimentary sections throughout the entire Toarcian CIE are strikingly different from one another, and so are the $\delta^{13}\text{C}_{\text{org}}$ profiles, respectively (Figures 7 and 11). Interestingly, $\delta^{13}\text{C}_{\text{org}}$ and $\delta^{13}\text{C}_{\text{carb}}$ throughout the decoupled sections of the various profiles also behave very differently, even when deposited in similar regions of the Tethys Ocean. For example, $\delta^{13}\text{C}_{\text{org}}$ in the decoupled part of the Sancerre section (NW-Tethys) is characterized by relatively constant values, whereas $\delta^{13}\text{C}_{\text{carb}}$ values strongly decrease and then increase again. In the decoupled part of the Dotternhausen section (NW-Tethys) $\delta^{13}\text{C}_{\text{org}}$ values are increasing, while the corresponding $\delta^{13}\text{C}_{\text{carb}}$ values are decreasing (Figures 7 and 11). This

difference in the C isotope stratigraphies of the two sections may be tied to the hydrographically restricted conditions (McArthur, 2019; McArthur et al., 2008; Ruvalcaba Baroni et al., 2018) that prevented water mass exchange between the two basins. However, further detailed work beyond the scope of this study is needed to understand the $\delta^{13}\text{C}_{\text{carb}}-\delta^{13}\text{C}_{\text{org}}$ decoupling patterns observed in the various Toarcian OAE sections.

6 | CONCLUSION

The black shale facies in the Dotternhausen section was deposited in a redox stratified marine environment and was not significantly impacted by terrestrial-sourced organic carbon, thermal maturity,

and hydrothermal fluids. Two prominent decoupled $\delta^{13}\text{C}_{\text{carb}}$ - $\delta^{13}\text{C}_{\text{org}}$ signals superimpose the Toarcian CIE in the Dotternhausen section, southwest Germany. The stratigraphically first $\delta^{13}\text{C}_{\text{carb}}$ - $\delta^{13}\text{C}_{\text{org}}$ decoupling (shown in black shales in interval 2a) was of a small magnitude and most likely caused by a carbon-cycle disturbance from the onset of GSB metabolic activity. The second and in magnitude much larger decoupling in interval 2b resulted from a GSB bloom, but was further exaggerated by early diagenetic effects. Thereby, dissimilatory respiration of SRB led to the formation of ^{12}C -enriched authigenic calcites within the sediment throughout organic matter remineralization. This process amplified the $\delta^{13}\text{C}_{\text{carb}}$ - $\delta^{13}\text{C}_{\text{org}}$ decoupling between the diagenetic carbonate (Unterer Stein) and the remaining organic matter. The $\delta^{13}\text{C}_{\text{carb}}$ and $\delta^{13}\text{C}_{\text{org}}$ profiles from geographically distinct Toarcian OAE localities (e.g., Bilong Co, Nianduo, and Sancerre) in the Tethys region show strong variability in their $\delta^{13}\text{C}_{\text{carb}}$ - $\delta^{13}\text{C}_{\text{org}}$ decoupling signals, which indicates the substantial impact of local carbon-cycle perturbations on the global carbon cycle during the Toarcian CIE.

ACKNOWLEDGMENTS

We are grateful for the help and technical support from Elmar Reitter and Bernd Steinhilber in the laboratory. We thank Holcim GmbH Dotternhausen for access to their quarry and for providing drillcore materials for this study. Y.W. thanks the China Scholarship Council (CSC) for his financial support. We are grateful to the two anonymous reviewers and to the Editor N. Planavsky for their comments and suggestions that highly improved the original manuscript. We would also like to thank the Editor K. Konhauser for handling this manuscript. Open access funding enabled and organized by Projekt DEAL.

CONFLICT OF INTEREST

The authors declare no conflict of interest and no compelling financial interests.

ORCID

Yunfeng Wang  <https://orcid.org/0000-0001-6818-1061>

REFERENCES

- Ader, M., Macouin, M., Trindade, R. I. F., Hadrien, M., Yang, Z. Y., Sun, Z. M., & Besse, J. (2009). A multilayered water column in the Ediacaran Yangtze platform? Insights from carbonate and organic matter paired $\delta^{13}\text{C}$. *Earth and Planetary Science Letters*, 288, 213–227. <https://doi.org/10.1016/j.epsl.2009.09.024>
- Albut, G., Babechuk, M. G., Kleinhans, I. C., Bengler, M., Beukes, N. J., Steinhilber, B., ... Schoenberg, R. (2018). Modern rather than Mesoarchaeon oxidative weathering responsible for the heavy stable Cr isotopic signatures of the 2.95 Ga old Ijzermijn iron formation (South Africa). *Geochimica et Cosmochimica Acta*, 228, 157–189. <https://doi.org/10.1016/j.gca.2018.02.034>
- Aries, S., Valladon, M., Polvé, M., & Dupré, B. (2007). A routine method for oxide and hydroxide interference corrections in ICP-MS chemical analysis of environmental and geological samples. *Geostandards Newsletter*, 24, 19–31. <https://doi.org/10.1111/j.1751-908X.2000.tb00583.x>
- Babechuk, M. G., Widdowson, M., Murphy, M., & Kamber, B. S. (2015). A combined Y/Ho, high field strength element (HFSE) and Nd isotope perspective on basal weathering, Deccan Traps, India. *Chemical Geology*, 396, 25–41. <https://doi.org/10.1016/j.chemgeo.2014.12.017>
- Baudin, F., Herbin, J.-P., & Vandenbroucke, M. (1990). Mapping and geochemical characterization of the Toarcian organic matter in the Mediterranean Tethys and Middle East. *Advances in Organic Geochemistry*, 16, 677–687. [https://doi.org/10.1016/0146-6380\(90\)90109-D](https://doi.org/10.1016/0146-6380(90)90109-D)
- Bjerrum, C. J., Surlyk, F., Callomon, J. H., & Slingerland, R. L. (2001). Numerical paleoceanographic study of the Early Jurassic transcontinental Laurasian Seaway. *Paleoceanography*, 16, 390–404. <https://doi.org/10.1029/2000pa000512>
- Bour, I., Mattioli, E., & Pittet, B. (2007). Nannofacies analysis as a tool to reconstruct paleoenvironmental changes during the Early Toarcian anoxic event. *Palaeogeography, Palaeoclimatology, Palaeoecology*, 249, 58–79. <https://doi.org/10.1016/j.palaeo.2007.01.013>
- Caruthers, A. H., Gröcke, D. R., & Smith, P. L. (2011). The significance of an Early Jurassic (Toarcian) carbon-isotope excursion in Haida Gwaii (Queen Charlotte Islands), British Columbia, Canada. *Earth and Planetary Science Letters*, 307, 19–26. <https://doi.org/10.1016/j.epsl.2011.04.013>
- Cohen, A. S., Coe, A. L., Harding, S. M., & Schwark, L. (2004). Osmium isotope evidence for the regulation of atmospheric CO_2 by continental weathering. *Geology*, 32, 157–160. <https://doi.org/10.1130/g20158.1>
- Danise, S., Twitchett, R. J., & Little, C. T. S. (2015). Environmental controls on Jurassic marine ecosystems during global warming. *Geology*, 43, 263–266. <https://doi.org/10.1130/g36390.1>
- Dembicki, H. Jr (2009). Three common source rock evaluation errors made by geologists during prospect or play appraisals. *AAPG bulletin*, 93, 341–356. <https://doi.org/10.1306/10230808076>
- Guillaume, D., & Yannick, D. (2012). Modeling evidences for global warming, Arctic seawater freshening, and sluggish oceanic circulation during the Early Toarcian anoxic event. *Paleoceanography and Paleoclimatology*, 27, PA2211. <https://doi.org/10.1029/2012PA002283>
- de Kock, M. O., Beukes, N. J., Adeniyi, E. O., Cole, D., Gotz, A. E., Geel, C., & Ossa Ossa, F. (2017). Deflating the shale gas potential of South Africa's Main Karoo basin. *South African Journal of Science*, 113, 1–12. <https://doi.org/10.17159/sajs.2017/20160331>
- Fantasia, A., Föllmi, K. B., Adatte, T., Spangenberg, J. E., & Montero-Serrano, J.-C. (2018). The early toarcian oceanic anoxic event: Paleoenvironmental and paleoclimatic change across the Alpine Tethys (Switzerland). *Global and Planetary Change*, 162, 53–68. <https://doi.org/10.1016/j.gloplacha.2018.01.008>
- Francois, R. (1988). A study on the regulation of the concentrations of some trace metals (Rb, Sr, Zn, Pb, Cu, V, Cr, Ni, Mn and Mo) in Saanich Inlet sediments, British Columbia, Canada. *Marine Geology*, 83, 285–308. [https://doi.org/10.1016/0025-3227\(88\)90063-1](https://doi.org/10.1016/0025-3227(88)90063-1)
- French, K. L., Sepulveda, J., Trabucho-Alexandre, J., Gröcke, D. R., & Summons, R. E. (2014). Organic geochemistry of the early Toarcian oceanic anoxic event in Hawsker Bottoms, Yorkshire, England. *Earth and Planetary Science Letters*, 390, 116–127. <https://doi.org/10.1016/j.epsl.2013.12.033>
- Frimmel, A. (2003). *Hochauflösende Untersuchungen von Biomarkern an epikontinentalen Schwarzschiefern des Unteren Toarciums (Posidonienschiefer, Lias e) von SW-Deutschland (in German with English abstract)*. Retrieved from <https://publikationen.uni-tuebingen.de/xmlui/handle/10900/48450>
- Frimmel, A., Oschmann, W., & Schwark, L. (2004). Chemostratigraphy of the Posidonia Black Shale, SW Germany I. Influence of sea-level variation on organic facies evolution. *Chemical Geology*, 206, 199–230. <https://doi.org/10.1016/j.chemgeo.2003.12.007>
- Fu, X., Wang, J., Feng, X., Wang, D., Chen, W., Song, C., & Zeng, S. (2016). Early Jurassic carbon-isotope excursion in the Bilong Co Basin (Tibet), the eastern Tethys: Implications for the Toarcian Oceanic anoxic

- event. *Chemical Geology*, 442, 62–72. <https://doi.org/10.1016/j.chemgeo.2016.09.007>
- Govindaraju, K., & Roelandts, I. (1989). 1988 compilation report on trace elements in six ANRT rock reference samples: diorite DR-N, serpentine UB-N, bauxite BX-N, disthene DT-N, granite GS-N and potash feldspar FK-N. *Geostandards Newsletter*, 13, 5–67. <https://doi.org/10.1111/j.1751-908X.1989.tb00465.x>
- Han, Z., Hu, X., Kemp, D. B., & Li, J. (2018). Carbonate-platform response to the Toarcian Oceanic Anoxic Event in the southern hemisphere: Implications for climatic change and biotic platform demise. *Earth and Planetary Science Letters*, 489, 59–71. <https://doi.org/10.1016/j.epsl.2018.02.017>
- Heimann, A., Johnson, C. M., Beard, B. L., Valley, J. W., Roden, E. E., Spicuzza, M. J., & Beukes, N. J. (2010). Fe, C, and O isotope compositions of banded iron formation carbonates demonstrate a major role for dissimilatory iron reduction in ~2.5 Ga marine environments. *Earth and Planetary Science Letters*, 294, 8–18. <https://doi.org/10.1016/j.epsl.2018.07.044>
- Hermoso, M., Minoletti, F., & Pellenard, P. (2013). Black shale deposition during Toarcian super-greenhouse driven by sea level. *Climate of the Past*, 9, 2703–2712. <https://doi.org/10.5194/cp-9-2703-2013>
- Hermoso, M., Minoletti, F., Rickaby, R. E., Hesselbo, S. P., Baudin, F., & Jenkyns, H. C. (2012). Dynamics of a stepped carbon-isotope excursion: Ultra high-resolution study of Early Toarcian environmental change. *Earth and Planetary Science Letters*, 319, 45–54. <https://doi.org/10.1016/j.epsl.2011.12.021>
- Hesselbo, S. P., Gröcke, D. R., Jenkyns, H. C., Bjerrum, C. J., Farrimond, P., Bell, H. S. M., & Green, O. W. (2000). Massive dissociation of gas hydrate during a Jurassic oceanic anoxic event. *Nature*, 406, 392–395. <https://doi.org/10.1038/35019044>
- Hesselbo, S. P., Jenkyns, H. C., Duarte, L. V., & Oliveira, L. C. V. (2007). Carbon-isotope record of the Early Jurassic (Toarcian) Oceanic Anoxic Event from fossil wood and marine carbonate (Lusitanian Basin, Portugal). *Earth and Planetary Science Letters*, 253, 455–470. <https://doi.org/10.1016/j.epsl.2006.11.009>
- Hinrichs, K. U. (2002). Microbial fixation of methane carbon at 2.7 Ga: Was an anaerobic mechanism possible? *Geochemistry, Geophysics, Geosystems*, 3, 1–10. <https://doi.org/10.1029/2001GC000286>
- Hurse, T. J., Kappler, U., & Keller, J. (2008). *Using anoxygenic photosynthetic bacteria for the removal of sulfide from wastewater*. https://doi.org/10.1007/978-1-4020-6863-8_22
- Izumi, K., Kemp, D. B., Itamiya, S., & Inui, M. (2018). Sedimentary evidence for enhanced hydrological cycling in response to rapid carbon release during the early Toarcian oceanic anoxic event. *Earth and Planetary Science Letters*, 481, 162–170. <https://doi.org/10.1016/j.epsl.2017.10.030>
- Jenkyns, H. C. (1988). The early Toarcian (Jurassic) anoxic event; stratigraphic, sedimentary and geochemical evidence. *American Journal of Science*, 288, 101–151. <https://doi.org/10.2475/ajs.288.2.101>
- Jenkyns, H. C. (2010). Geochemistry of oceanic anoxic events. *Geochemistry, Geophysics, Geosystems*, 11(3). <https://doi.org/10.1029/2009gc002788>
- Jenkyns, H. C., Jones, C. E., Gröcke, D. R., Hesselbo, S. P., & Parkinson, D. N. (2002). Chemostratigraphy of the Jurassic System: Applications, limitations and implications for palaeoceanography. *Journal of the Geological Society*, 159, 351–378. <https://doi.org/10.1144/0016-764901-130>
- Jiang, G., Wang, X., Shi, X., Xiao, S., Zhang, S., & Dong, J. (2012). The origin of decoupled carbonate and organic carbon isotope signatures in the early Cambrian (ca. 542–520 Ma) Yangtze platform. *Earth and Planetary Science Letters*, 317–318, 96–110. <https://doi.org/10.1016/j.epsl.2011.11.018>
- Joachimski, M. M., Ostertag-Henning, C., Pancost, R. D., Strauss, H., Freeman, K. H., Littke, R., ... Racki, G. (2001). Water column anoxia, enhanced productivity and concomitant changes in $\delta^{13}\text{C}$ and $\delta^{34}\text{S}$ across the Frasnian-Famennian boundary (Kowala–Holy Cross Mountains/Poland). *Chemical Geology*, 175, 109–131. [https://doi.org/10.1016/S0009-2541\(00\)00365-X](https://doi.org/10.1016/S0009-2541(00)00365-X)
- Kamber, B. S., Webb, G. E., & Gallagher, M. (2014). The rare earth element signal in Archaean microbial carbonate: information on ocean redox and biogenicity. *Journal of the Geological Society*, 171, 745–763. <https://doi.org/10.1144/jgs2013-110>
- Kemp, D. B., Coe, A. L., Cohen, A. S., & Schwark, L. (2005). Astronomical pacing of methane release in the Early Jurassic period. *Nature*, 437, 396–399. <https://doi.org/10.1038/nature04037>
- Konhäuser, K. O., Planavsky, N. J., Hardisty, D. S., Robbins, L. J., Warchola, T. J., Haugaard, R., ... Lyons, T. W. (2017). Iron formations: A global record of Neoproterozoic to Palaeoproterozoic environmental history. *Earth-Science Reviews*, 172, 140–177. <https://doi.org/10.1016/j.earscirev.2017.06.012>
- Knoll, A. H., Hayes, J. M., Kaufman, A. J., Swett, K., & Lambert, I. B. (1986). Secular variation in carbon isotope ratios from Upper Proterozoic successions of Svalbard and East Greenland. *Nature*, 321, 832–838. <https://doi.org/10.1038/321832a0>
- Kuhn, O., & Etter, W. (1994). Der Posidonienschiefer der Nordschweiz: Lithostratigraphie, Biostratigraphie und Fazies. *Eclogae Geologicae Helveticae*, 87, 113–138.
- Kuypers, M. M., Pancost, R. D., & Damste, J. S. S. (1999). A large and abrupt fall in atmospheric CO_2 concentration during Cretaceous times. *Nature*, 399, 342–345. <https://doi.org/10.1038/20659>
- Li, D., Zhang, X., Hu, D., Chen, X., Huang, W., Zhang, X., ... Shen, Y. (2018). Evidence of a large $\delta^{13}\text{C}_{\text{carb}}$ and $\delta^{13}\text{C}_{\text{org}}$ depth gradient for deep-water anoxia during the late Cambrian SPICE event. *Geology*, 47, 115–118. <https://doi.org/10.1130/G45709.1>
- Little, C. T., & Benton, M. J. (1995). Early Jurassic mass extinction: A global long-term event. *Geology*, 23, 495–498. [https://doi.org/10.1130/0091-7613\(1995\)023<0495:EJMEAG>2.3.CO;2](https://doi.org/10.1130/0091-7613(1995)023<0495:EJMEAG>2.3.CO;2)
- Maloof, A. C., Porter, S. M., Moore, J. L., Dudás, F. Ö., Bowring, S. A., Higgins, J. A., ... Eddy, M. P. (2010). The earliest Cambrian record of animals and ocean geochemical change. *Geological Society of America Bulletin*, 122, 1731–1774. <https://doi.org/10.1130/b30346.1>
- Mattioli, E., Pittet, B., Suan, G., & Mailliot, S. (2008). Calcareous nanoplankton changes across the early Toarcian oceanic anoxic event in the western Tethys. *Paleoceanography*, 23, PA3208. <https://doi.org/10.1029/2007PA001435>
- McArthur, J. M. (2019). Early Toarcian black shales: A response to an oceanic anoxic event or anoxia in marginal basins? *Chemical Geology*, 522, 71–83. <https://doi.org/10.1016/j.chemgeo.2019.05.028>
- McArthur, J. M., Algeo, T. J., van de Schootbrugge, B., Li, Q., & Howarth, R. J. (2008). Basinal restriction, black shales, Re-Os dating, and the Early Toarcian (Jurassic) oceanic anoxic event. *Paleoceanography*, 23, PA4217. <https://doi.org/10.1029/2008PA001607>
- McLennan, S. M. (2001). Relationships between the trace element composition of sedimentary rocks and upper continental crust. *Geochemistry, Geophysics, Geosystems*, 2. <https://doi.org/10.1029/2000GC000109>
- McLennan, S. M., Hemming, S., McDaniel, D. K., & Hanson, G. N. (1993). Geochemical approaches to sedimentation, provenance, and tectonics. *Special Papers-Geological Society of America*, 284, 21–40. <https://doi.org/10.1130/spe284-p21>
- Meyer, K. M., Yu, M., Lehrmann, D., van de Schootbrugge, B., & Payne, J. L. (2013). Constraints on Early Triassic carbon cycle dynamics from paired organic and inorganic carbon isotope records. *Earth and Planetary Science Letters*, 361, 429–435. <https://doi.org/10.1016/j.epsl.2012.10.035>
- Montero-Serrano, J.-C., Föllmi, K. B., Adatte, T., Spangenberg, J. E., Tribouillard, N., Fantasia, A., & Suan, G. (2015). Continental weathering and redox conditions during the early Toarcian Oceanic Anoxic Event in the northwestern Tethys: Insight from the Posidonia Shale section in the Swiss Jura Mountains. *Paleogeography*,

- Palaeoclimatology, Palaeoecology*, 429, 83–99. <https://doi.org/10.1016/j.palaeo.2015.03.043>
- Newton, R. J., Reeves, E. P., Kafousia, N., Wignall, P. B., Bottrell, S. H., & Sha, J. G. (2011). Low marine sulfate concentrations and the isolation of the European epicontinental sea during the Early Jurassic. *Geology*, 39, 7–10. <https://doi.org/10.1130/g31326.1>
- Och, L. M., & Shields-Zhou, G. A. (2012). The Neoproterozoic oxygenation event: Environmental perturbations and biogeochemical cycling. *Earth-Science Reviews*, 110, 26–57. <https://doi.org/10.1016/j.earscirev.2011.09.004>
- Ossa Ossa, F. O., Hofmann, A., Wille, M., Spangenberg, J. E., Bekker, A., Poulton, S. W., ... Schoenberg, R. (2018). Aerobic iron and manganese cycling in a redox-stratified Mesoarchean epicontinental sea. *Earth and Planetary Science Letters*, 500, 28–40. <https://doi.org/10.1016/j.epsl.2018.07.044>
- Pancost, R. D., Crawford, N., Magness, S., Turner, A., Jenkyns, H. C., & Maxwell, J. R. (2004). Further evidence for the development of photic-zone euxinic conditions during Mesozoic oceanic anoxic events. *Journal of the Geological Society*, 161, 353–364. <https://doi.org/10.1144/0016764903-059>
- Pearce, C. R., Cohen, A. S., Coe, A. L., & Burton, K. W. (2008). Molybdenum isotope evidence for global ocean anoxia coupled with perturbations to the carbon cycle during the Early Jurassic. *Geology*, 36, 231–234. <https://doi.org/10.1130/g24446a.1>
- Percival, L. M. E., Cohen, A. S., Davies, M. K., Dickson, A. J., Hesselbo, S. P., Jenkyns, H. C., ... Xu, W. (2016). Osmium isotope evidence for two pulses of increased continental weathering linked to Early Jurassic volcanism and climate change. *Geology*, 44, 759–762. <https://doi.org/10.1130/g37997.1>
- Peters, K. E., Walters, C. C., & Moldowan, J. M. (2005). *The biomarker guide: Biomarkers and isotopes in petroleum systems and earth history* (2nd ed.). Cambridge, UK: Cambridge University Press.
- Pinti, D. L., Hashizume, K., Sugihara, A., Massault, M., & Philippot, P. (2009). Isotopic fractionation of nitrogen and carbon in Paleoproterozoic cherts from Pilbara craton, Western Australia: Origin of ^{15}N -depleted nitrogen. *Geochimica et Cosmochimica Acta*, 73, 3819–3848. <https://doi.org/10.1016/j.gca.2009.03.014>
- Raghoebarasingh, A. A., Pol, A., van de Pas-Schoonen, K. T., Smolders, A. J. P., Ettwig Katharina F., Rijpstra, W. I. C., ... & Strous, M. (2006). A microbial consortium couples anaerobic methane oxidation to denitrification. *Nature*, 440, (7086), 918–921. <http://dx.doi.org/10.1038/nature04617>
- Riccardi, A., Kump, L. R., Arthur, M. A., & D'Hondt, S. (2007). Carbon isotopic evidence for chemocline upward excursions during the end-Permian event. *Palaeogeography, Palaeoclimatology, Palaeoecology*, 248, 73–81. <https://doi.org/10.1016/j.palaeo.2006.11.010>
- Richo, S., van De Schootbrugge, B., Pross, J., Püttmann, W., Quan, T. M., Lindström, S., ... Hauenberger, C. A. (2012). Hydrogen sulphide poisoning of shallow seas following the end-Triassic extinction. *Nature Geoscience*, 5, 662–667. <https://doi.org/10.1038/ngeo1539>
- Röhl, H. J., Schmid-Röhl, A., Oschmann, W., Frimmel, A., & Schwark, L. (2001). The Posidonia Shale (Lower Toarcian) of SW-Germany: An oxygen-depleted ecosystem controlled by sea level and palaeoclimate. *Palaeogeography, Palaeoclimatology, Palaeoecology*, 165, 27–52. [https://doi.org/10.1016/S0031-0182\(00\)00152-8](https://doi.org/10.1016/S0031-0182(00)00152-8)
- Röhl, H. J., & Schmid-Röhl, A. (2005). Lower Toarcian (Upper Liassic) black shales of the Central European Epicontinental Basin: A sequence stratigraphic case study from the Sw German posidonia shale. *The Deposition of Organic-Carbon-Rich Sediments: Models, Mechanisms, and Consequences*, 82, 165–189. <https://doi.org/10.2110/pec.05.82.0165>
- Ruebsam, W., Mayer, B., & Schwark, L. (2019). Cryosphere carbon dynamics control Early Toarcian global warming and sea level evolution. *Global and Planetary Change*, 172, 440–453. <https://doi.org/10.1016/j.gloplacha.2018.11.003>
- Ruebsam, W., Müller, T., Kovács, J., Pálffy, J., & Schwark, L. (2018). Environmental response to the early Toarcian carbon cycle and climate perturbations in the northeastern part of the West Tethys shelf. *Gondwana Research*, 59, 144–158. <https://doi.org/10.1016/j.gr.2018.03.013>
- Ruebsam, W., Münzberger, P., & Schwark, P. (2014). Chronology of the Early Toarcian environmental crisis in the Lorraine Sub-Basin (NE Paris Basin). *Earth and Planetary Science Letters*, 404, 273–282. <https://doi.org/10.1016/j.epsl.2014.08.005>
- Ruebsam, W., Reolid, M., & Schwark, L. (2020). $\delta^{13}\text{C}$ of terrestrial vegetation records Toarcian CO_2 and climate gradients. *Scientific reports*, 10, 1–8. <https://doi.org/10.1038/s41598-019-56710-6>
- Ruvalcaba Baroni, I., Pohl, A., van Helmond, N. A., Papadomanolaki, N. M., Coe, A. L., Cohen, A. S., ... Slomp, C. P. (2018). Ocean circulation in the Toarcian (Early Jurassic): A key control on deoxygenation and carbon burial on the European Shelf. *Paleoceanography and Paleoclimatology*, 33, 994–1012. <https://doi.org/10.1029/2018pa003394>
- Sahoo, S. K., Planavsky, N. J., Kendall, B., Wang, X., Shi, X., Scott, C., ... Jiang, G. (2012). Ocean oxygenation in the wake of the Marinoan glaciation. *Nature*, 489, 546–549. <https://doi.org/10.1038/nature11445>
- Sælen, G., Tyson, R. V., Telnæs, N., & Talbot, M. R. (2000). Contrasting watermass conditions during deposition of the Whitby Mudstone (Lower Jurassic) and Kimmeridge Clay (Upper Jurassic) formations, UK. *Palaeogeography, Palaeoclimatology, Palaeoecology*, 163, 163–196. [https://doi.org/10.1016/S0031-0182\(00\)00150-4](https://doi.org/10.1016/S0031-0182(00)00150-4)
- Schouten, S., van Kaam-Peters, H. M., Rijpstra, W. I. C., Schoell, M., & Damste, J. S. S. (2000). Effects of an oceanic anoxic event on the stable carbon isotopic composition of early Toarcian carbon. *American Journal of Science*, 300, 1–22. <https://doi.org/10.2475/ajs.300.1.1>
- Schwark, L., & Frimmel, A. (2004). Chemostratigraphy of the Posidonia Black Shale, SW-Germany. *Chemical Geology*, 206, 231–248. <https://doi.org/10.1016/j.chemgeo.2003.12.008>
- Shields, G., & Veizer, J. (2002). Precambrian marine carbonate isotope database: Version 1.1. *Geochemistry, Geophysics, Geosystems*, 3, 1 of 12–12 of 12. <https://doi.org/10.1029/2001GC000266>
- Song, J., Littke, R., & Weniger, P. (2017). Organic geochemistry of the Lower Toarcian Posidonia Shale in NW Europe. *Organic Geochemistry*, 106, 76–92. <https://doi.org/10.1016/j.orggeochem.2016.10.014>
- Spötl, C., & Vennemann, T. W. (2003). Continuous-flow isotope ratio mass spectrometric analysis of carbonate minerals. *Rapid Communications in Mass Spectrometry*, 17, 1004–1006. <https://doi.org/10.1002/rcm.1010>
- Suan, G., Van De Schootbrugge, B., Adatte, T., Fiebig, J., & Oschmann, W. (2015). Calibrating the magnitude of the Toarcian carbon cycle perturbation. *Paleoceanography*, 30, 495–509. <https://doi.org/10.1002/2014pa002758>
- Svensen, H., Planke, S., Chevallier, L., Malthes-Sørensen, A., Corfu, F., & Jamtveit, B. (2007). Hydrothermal venting of greenhouse gases triggering Early Jurassic global warming. *Earth and Planetary Science Letters*, 256, 554–566. <https://doi.org/10.1016/j.epsl.2007.02.013>
- Takahashi, S., Kaiho, K., Oba, M., & Kakegawa, T. (2010). A smooth negative shift of organic carbon isotope ratios at an end-Permian mass extinction horizon in central pelagic Panthalassa. *Palaeogeography, Palaeoclimatology, Palaeoecology*, 292, 532–539. <https://doi.org/10.1016/j.palaeo.2010.04.025>
- Them, T. R., Gill, B. C., Selby, D., Grocke, D. R., Friedman, R. M., & Owens, J. D. (2017). Evidence for rapid weathering response to climatic warming during the Toarcian Oceanic Anoxic Event. *Scientific Reports*, 7, 5003. <https://doi.org/10.1038/s41598-017-05307-y>
- Trecalli, A., Spangenberg, J., Adatte, T., Föllmi, K. B., & Parente, M. (2012). Carbonate platform evidence of ocean acidification at the onset of the early Toarcian oceanic anoxic event. *Earth and Planetary*

- Science Letters*, 357–358, 214–225. <https://doi.org/10.1016/j.epsl.2012.09.043>
- Tribouillard, N., Algeo, T. J., Lyons, T., & Riboulleau, A. (2006). Trace metals as paleoredox and paleoproductivity proxies: An update. *Chemical Geology*, 232, 12–32. <https://doi.org/10.1016/j.chemgeo.2006.02.012>
- Ullmann, C. V., Thibault, N., Ruhl, M., Hesselbo, S. P., & Korte, C. (2014). Effect of a Jurassic oceanic anoxic event on belemnite ecology and evolution. *Proceedings of the National Academy of Sciences of the United States of America*, 111, 10073–10076. <https://doi.org/10.1073/pnas.1320156111>
- Ulrich, T., Kamber, B. S., Woodhead, J. D., & Spencer, L. A. (2010). Long-term observations of isotope ratio accuracy and reproducibility using Quadrupole ICP-MS. *Geostandards and Geoanalytical Research*, 34, 161–174. <https://doi.org/10.1111/j.1751-908X.2010.00046.x>
- van Breugel, Y., Baas, M., Schouten, S., Mattioli, E., & Sinninghe Damsté, J. S. (2006). Isorenieratane record in black shales from the Paris Basin, France: Constraints on recycling of respired CO₂ as a mechanism for negative carbon isotope shifts during the Toarcian oceanic anoxic event. *Paleoceanography*, 21, PA4220. <https://doi.org/10.1029/2006pa001305>
- van de Schootbrugge, B., & Gollner, S. (2013). Altered primary production during mass-extinction events. *The Paleontological Society Papers*, 19, 87–114. <https://doi.org/10.1017/S1089332600002709>
- van de Schootbrugge, B., McArthur, J. M., Bailey, T. R., Rosenthal, Y., Wright, J. D., & Miller, K. G. (2005). Toarcian oceanic anoxic event: An assessment of global causes using belemnite C isotope records. *Paleoceanography*, 20, PA3008. <https://doi.org/10.1029/2004pa001102>
- Watanabe, Y., Naraoka, H., Wronkiewicz, D. J., Condie, K. C., & Ohmoto, H. (1997). Carbon, nitrogen, and sulfur geochemistry of Archean and Proterozoic shales from the Kaapvaal Craton, South Africa. *Geochimica et Cosmochimica Acta*, 61, 3441–3459. [https://doi.org/10.1016/S0016-7037\(97\)00164-6](https://doi.org/10.1016/S0016-7037(97)00164-6)
- Wignall, P. B., Hallam, A., Newton, R. J., Sha, J. G., Reeves, E., Mattioli, E., & Crowley, S. (2006). An eastern Tethyan (Tibetan) record of the Early Jurassic (Toarcian) mass extinction event. *Geobiology*, 4, 179–190. <https://doi.org/10.1111/j.1472-4669.2006.00081.x>
- Xu, W., Ruhl, M., Jenkyns, H. C., Hesselbo, S. P., Riding, J. B., Selby, D., ... Idiz, E. F. (2017). Carbon sequestration in an expanded lake system during the Toarcian oceanic anoxic event. *Nature Geoscience*, 10, 129–134. <https://doi.org/10.1038/ngeo2871>
- Xu, W., Ruhl, M., Jenkyns, H. C., Leng, M. J., Huggett, J. M., Minisini, D., ... Hesselbo, S. P. (2018). Evolution of the Toarcian (Early Jurassic) carbon-cycle and global climatic controls on local sedimentary processes (Cardigan Bay Basin, UK). *Earth and Planetary Science Letters*, 484, 396–411. <https://doi.org/10.1016/j.epsl.2017.12.037>
- Ziegler, P. A. (1988). Evolution of the Arctic-North Atlantic and the Western Tethys. *AAPG Memoir*, 43, 198.

SUPPORTING INFORMATION

Additional supporting information may be found online in the Supporting Information section.

How to cite this article: Wang Y, Ossa Ossa F, Wille M, et al. Evidence for local carbon-cycle perturbations superimposed on the Toarcian carbon isotope excursion. *Geobiology*. 2020;18:682–709. <https://doi.org/10.1111/gbi.12410>

Paleoceanography and Paleoclimatology



RESEARCH ARTICLE

10.1029/2020PA004207

Key Points:

- Molybdenum-based nitrogen fixation was prevalent in the northern European epicontinental shelf during the Toarcian carbon isotope excursion
- Quantitative denitrification and/or anammox caused nitrogen famine in strongly redox-stratified environments during the early Toarcian
- Oxygen-deficient basins on the northern European epicontinental shelf across the Toarcian carbon isotope excursion

Correspondence to:

Y. Wang,
yunfeng.wang@uni-tuebingen.de

Citation:

Wang, Y., Ossa, F. O., Spangenberg, J. E., Wille, M., & Schoenberg, R. (2021). Restricted oxygen-deficient basins on the Northern European epicontinental shelf across the Toarcian carbon isotope excursion interval. *Paleoceanography and Paleoclimatology*, 36, e2020PA004207. <https://doi.org/10.1029/2020PA004207>

Received 25 DEC 2020
 Accepted 18 MAY 2021

Restricted Oxygen-Deficient Basins on the Northern European Epicontinental Shelf Across the Toarcian Carbon Isotope Excursion Interval

Yunfeng Wang¹ , Frantz Ossa Ossa^{1,2} , Jorge E. Spangenberg³ , Martin Wille⁴, and Ronny Schoenberg^{1,2} 

¹Department of Geosciences, University of Tuebingen, Tuebingen, Germany, ²Department of Geology, University of Johannesburg, Johannesburg, South Africa, ³Institute of Earth Surface Dynamics, University of Lausanne, Lausanne, Switzerland, ⁴Institute of Geological Sciences, University of Bern, Bern, Switzerland

Abstract The worldwide recognition of the Toarcian carbon isotope excursion (T-CIE) in organic-rich sedimentary rocks has been linked to an oceanic anoxic event (OAE) which implies the world's deep oceans were anoxic ~183 Ma. The majority of independent redox observations used to build this argument were mainly obtained from T-CIE organic-rich sediments deposited on northern European epicontinental shelf. However, increasing evidence has shown that this shelf had limited connection with the open ocean, making it unsuitable for reconstructing the T-CIE ocean redox structure. To unveil such controversy, we present integrated $\delta^{15}\text{N}_{\text{bulk}}$ and $\delta^{15}\text{N}_{\text{ker}}$ from Dotternhausen profile, Germany, combined with literature data from other T-CIE profiles. Both $\delta^{15}\text{N}_{\text{bulk}}$ and $\delta^{15}\text{N}_{\text{ker}}$ values are predominantly between +0.3 and +2.5‰. These positive near-zero $\delta^{15}\text{N}$ values imply enhanced N_2 fixation by cyanobacteria using molybdenum (Mo)-based nitrogenase to compensate bioavailable N loss following quantitative denitrification and/or anammox in a strongly redox-stratified marine setting. Such N isotope composition contradicts the typical sedimentary $\delta^{15}\text{N}$ values (>3‰) induced by partial water-column denitrification and/or anammox in modern-ocean oxygen minimum zones. We rather propose the existence of local oxygen-deficient basins on northern European epicontinental shelf where dissolved N underwent extensive denitrification and/or anammox causing bioavailable N deficiency. Mo-based diazotrophy thus played a critical role in discriminating N isotope compositions among multiple hydrographically restricted T-CIE marginal basins. Restricted oxygen-depleted environments on the northern European epicontinental shelf unlikely represent the open-ocean redox landscape. The existence of the global OAE thus needs comprehensive redox investigations on Tethys and/or Panthalassa deep-sea T-CIE successions to validate.

1. Introduction

During the Mesozoic era, several particular periods of widespread deposition of organic-rich black shales occurred during extreme perturbations to global climate and ocean redox structure, known as Oceanic Anoxic Events (OAEs). Of these events, the early Jurassic (Toarcian) OAE at ~183 Ma is marked by a specific interval of rapid global warming (Jenkyns, 1988), second-order marine mass extinction (e.g., Harries & Little, 1999; Little & Benton, 1995) and widespread oxygen deficiency (Pearce et al., 2008), manifested in deposits of anoxic marine sediments around the globe. The Toarcian OAE also dictated a significant carbon-cycle perturbation which was along with a negative Toarcian carbon isotope excursion (T-CIE) recorded in terrestrial wood (Hesselbo et al., 2007) and marine organic- and inorganic-carbon reservoirs at a global scale (e.g., Hesselbo et al., 2000). Consequently, the global (deep) oceans were suggested to be anoxic across the T-CIE (e.g., Pearce et al., 2008; Thibault et al., 2018). The hypothesis of the suggested global deep ocean anoxia is, however, challenged by the findings that most of the Toarcian fine-grained organic-rich sedimentary successions were deposited in hydrographically restricted anoxic basins especially in the northern European epicontinental shelf region (e.g., Fantasia et al., 2018; Frimmel et al., 2004; Sælen et al., 2000), which were appreciably isolated from the open ocean (Dickson et al., 2017; McArthur, 2019; McArthur et al., 2008; Remírez & Algeo, 2020). Furthermore, contrasting redox states have been proposed for the European epicontinental shelf seas during the T-CIE, in that the development of anoxia in the bottom waters was largely limited to the northern part of the European epicontinental shelf, while the southern part remained mainly oxygenated (Ruvalcaba Baroni et al., 2018).

© 2021. The Authors.

This is an open access article under the terms of the [Creative Commons Attribution License](https://creativecommons.org/licenses/by/4.0/), which permits use, distribution and reproduction in any medium, provided the original work is properly cited.

In this study, the biogeochemical cycle of nitrogen (N), a redox-sensitive and bio-limiting element, is used in the attempt to unravel the controversy of the Toarcian oceanic redox structure. Before the T-CIE and inferred co-evolved OAE, the oxygenated ocean is expected to have built up a large and steady nitrate (NO_3^-) reservoir. When entering the T-CIE, if sedimentary deposition occurs in open marine environments, the extensive seawater deoxygenation (OAE) would partially consume NO_3^- through water-column denitrification, the most prominent oceanic NO_3^- removal process (Sigman & Fripiat, 2019; Stüeken et al., 2016). Considering that partial denitrification and/or anammox preferentially releases ^{14}N as the form of $\text{N}_2/\text{N}_2\text{O}$ to the atmosphere, resulting in higher $\delta^{15}\text{N}$ values of the residual N pool, organic matter (OM) deposited in open marine environment records such ^{15}N -rich seawater signal through assimilation and imparts $\delta^{15}\text{N}$ values $\geq 3\text{‰}$ in sediments (e.g., Garvin et al., 2009; Gilleaudeau et al., 2020; Stüeken et al., 2016; Tesdal et al., 2013). This is because a large dissolved marine N reservoir is required to record the isotopic fingerprints of its redox-driven cycle in co-deposited sediments (Stüeken et al., 2016). In contrast, if hydrographic water-mass restriction represents the main depositional settings of T-CIE sedimentary rocks, quantitative denitrification and/or anammox is most likely to occur as a result of strongly redox-stratified water column (Schwark & Frimmel, 2004; Wang et al., 2020). Biomass deposited under such conditions is expected to preserve the $\delta^{15}\text{N}$ value of the main input source that is, N_2 fixation (Stüeken et al., 2016). Collectively, whether the northern European T-CIE epicontinental shelf successions were deposited in marine environments well connected to the open ocean or in very restricted environments can thus be reliably validated through evaluating the contemporaneous sedimentary N isotope records. This study reports high resolution of whole rock and separated kerogen $\delta^{15}\text{N}$ ($\delta^{15}\text{N}_{\text{bulk}}$ and $\delta^{15}\text{N}_{\text{ker}}$) data from the well-recognized T-CIE stratigraphic profile of Dotternhausen, southwestern (SW) Germany, to address the evolution of marine N biogeochemical cycling and ultimately shed new light on the expansion of anoxia in the coeval ocean.

2. Geological Background and the Studied Sedimentary Section

Early Jurassic experienced a warm period induced by a global temperature rise, reaching $\sim 6^\circ\text{C}$ – 10°C higher than the present day (Chandler et al., 1992; Dera et al., 2011; Rosales et al., 2018; Svensen et al., 2007). This global warming event was suggested to be linked to the massively released CO_2 owing to the Karoo-Ferrar large igneous province emplacement (Pálffy & Smith, 2000; Svensen et al., 2007) and/or CH_4 released from Gondwanan organic-rich shales or methane clathrates (e.g., Hesselbo et al., 2000; Kemp et al., 2005; McElwain et al., 2005). Across the greenhouse early Jurassic (Toarcian) interval, the hydrological cycle was intensified, followed by the formation of humid climate conditions and the enhanced chemical weathering rates (Brazier et al., 2015; Cohen et al., 2004; Fantasia et al., 2018; Hermoso & Pellenard, 2014; Montero-Serrano et al., 2015; Them et al., 2017). In addition, the majority of the present-day Europe was situated on the northern European epicontinental shelf which deepened toward the southeastern part of the contemporaneous Tethys Ocean (Jenkyns, 2010) (Figure 1a). However, the northern European epicontinental shelf during the Early Toarcian was characterized by multiple isolated basins/sub-basins in which the frequency of the deep-water renewal was to some extent restricted (e.g., McArthur, 2019; McArthur et al., 2008; Röhl et al., 2001). Moreover, the warming event during the early Toarcian tied to the massive emission of the greenhouse gases (Hesselbo et al., 2000; Kemp et al., 2005; Ruebsam et al., 2019, 2020) together with the coeval large-scale tectonic activities for example, the breakup of Pangaea supercontinent, likely jointly led to seawater transgression and deoxygenation in the northwestern Tethyan shallow shelf marine areas. The pervasive deposition of the organic-rich sedimentary rocks may thus be related to the pronounced change in the paleoceanographic and paleoclimatologic conditions during the early Toarcian period (e.g., Baudin et al., 1990; Jenkyns, 2010).

The studied Dotternhausen sedimentary section ($48^\circ 13' 32.6''\text{N}$, $8^\circ 46' 29.8''\text{E}$) is geographically located in the present-day SW Germany, and was deposited in the northern European epicontinental shelf seaway throughout the Early Toarcian interval (Ziegler, 1988) (Figures 1b, and 1c). This sedimentary section belongs to the well-recognized lower Toarcian Posidonia Shales that are enriched in high abundance of well-preserved OM and are widely distributed over Europe (Bour et al., 2007; Fantasia et al., 2018; Montero-Serrano et al., 2015; Song et al., 2017). A lot of previous work thus has been performed on the Posidonia Shales as case studies to understand the early Toarcian carbon cycling, continental weathering, marine deoxygenation and mass extinction (e.g., Montero-Serrano et al., 2015; Röhl et al., 2001; van Acken et al., 2019;

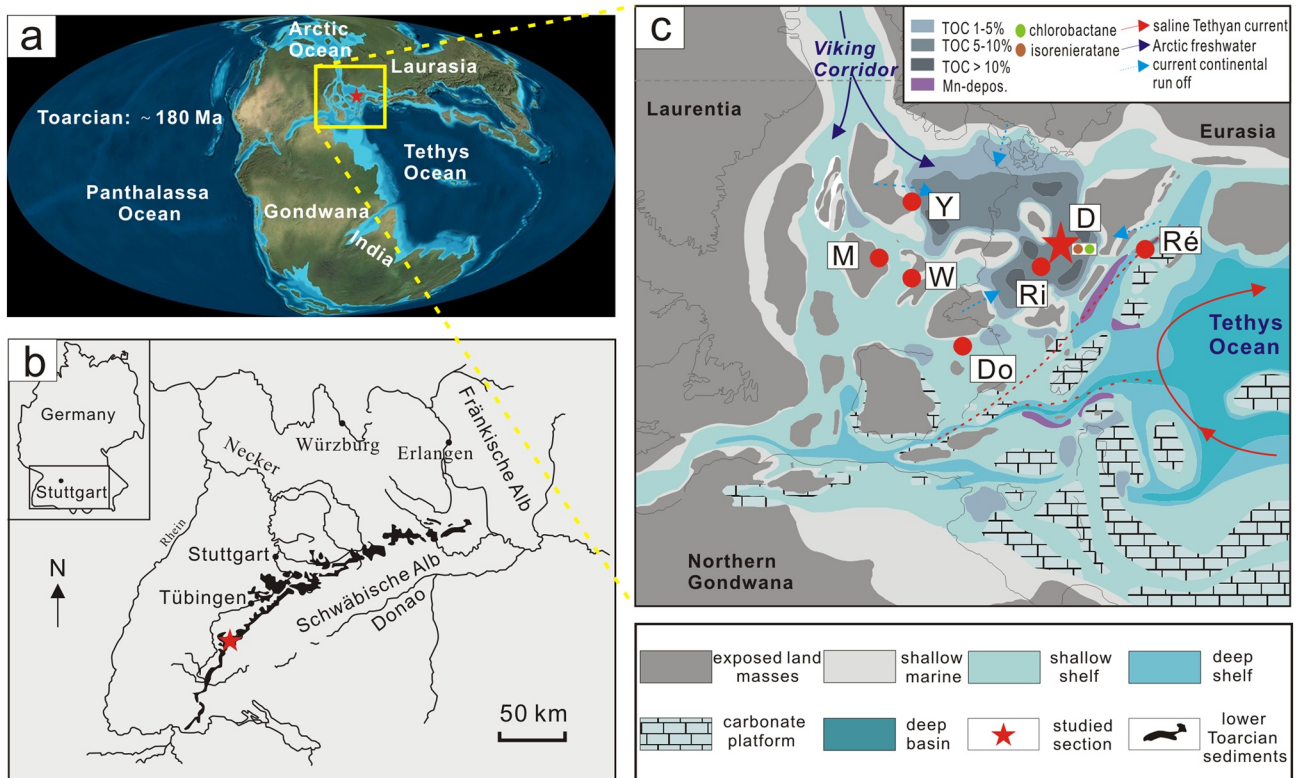


Figure 1. (a) Early Toarcian paleogeographic map with the location of Dotternhausen section (southwestern Germany). (b) Present-day map of southwestern Germany showing the site of the Dotternhausen section (modified from Röhl et al., 2001). (c) Early Toarcian paleogeography of the northern European epicontinental shelf settings (modified from Ruebsam et al., 2018). Red dots denote the Toarcian sedimentary sections spanning the CIE that are compared in this study. Dotternhausen (D; Germany), Rietheim (Ri; Switzerland), Réka Valley (Ré; Hungary), Yorkshire (Y; UK), Winterborne Kingston (W; UK), Mochras (M; UK) and Dogna (Do, Italy).

Wang et al., 2020). This Dotternhausen section has been also extensively studied and been well characterized in terms of lithostratigraphy and biostratigraphy (Röhl et al., 2001; Röhl & Schmid-Röhl, 2005). From the bottom up, this section was divided into three ammonite zones *tenuicostatum*, *falciferum* and *bifrons*, and was further subdivided into several subzones including *elegantulum*, *exaratum*, *elegans*, *falciferum*, *commune*, etc (cf. Röhl et al., 2001). In addition, three lithologic units for the Dotternhausen section have been defined in the light of the distinct abundances of the OM and siliciclastic component and different fabric types (Röhl et al., 2001; van Acken et al., 2019; Wang et al., 2020). They are bioturbated light-gray (organic-lean) shales from the depth of 1,180–980 cm, laminated fine-grained organic-rich shales and marlstones from 980–550 cm, and bituminous light-gray (organic-lean) shales from 550 to 0 cm, respectively (Röhl et al., 2001). The bioturbated light-gray shale unit starting with the limestone bed Spinatum Bank is abundant in benthic fauna and contains two intercalated thin organic-rich black shale beds (Figure 2). The fine-grained organic-rich sedimentary rocks deposited during the T-CIE are depleted in benthic fauna, and marked by high total organic carbon (TOC) concentration. These organic-rich sedimentary rocks were not metamorphosed and only experienced diagenesis in the oil window which is reflected by their persistently high hydrogen index (HI) values (580 mg hydrocarbon (HC)/g TOC on average) and their oil shale character (cf. Frimmel et al., 2004; Röhl et al., 2001; Wang et al., 2020). In the Dotternhausen section, there are three limestone beds, including the Unterer Stein, Steinplatte and Oberer Stein at the depth of ~800, ~680 and ~610 cm, respectively (Figure 2). The Unterer Stein with the thickness of 20–30 cm formed during early diagenesis and can be traced in several European countries such as Germany, Switzerland and France (van de Schootbrugge et al., 2005). It thus can be used as a stratigraphic marker to track more T-CIE sedimentary sections. The studied Dotternhausen sedimentary section has been subdivided into Aschgraue Mergel, Unterer Schiefer, and Mittlerer Schiefer Members in ascending order. The Aschgraue Mergel Member at the base of the Dotternhausen section is composed of organic-lean shales. Within the upward fine-grained

Dotternhausen Section

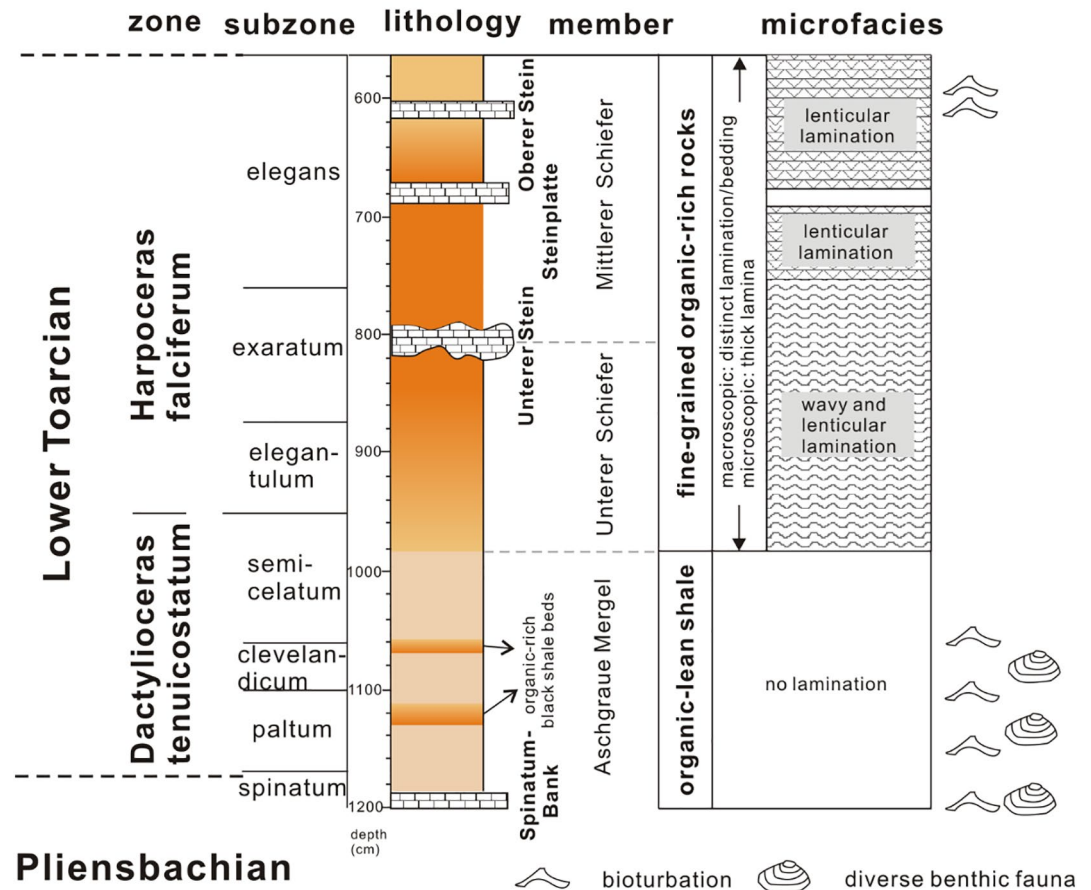


Figure 2. Stratigraphic distribution of lithology, microfacies and lamination types of the Dotternhausen sedimentary section during the Early Toarcian (modified from Röhl et al., 2001).

organic-rich rock facies, Unterer Schiefer and Mittlerer Schiefer Members are partitioned by the Unterer Stein limestone bed. A further description of the Dotternhausen sedimentary section with aspect to its paleontological and sedimentary characteristics can be found in previous studies (cf. Röhl et al., 2001; Röhl & Schmid-Röhl, 2005).

3. Materials and Methods

3.1. Sampling

In this study, the Dotternhausen sedimentary section, SW Germany, from 1,050 to 610 cm in stratigraphic depth containing the T-CIE was investigated. This stratigraphic interval starts with the upper *semicelatum* subzone and ends with the Oberer Stein in the upper *elegans* subzone (Figure 2). In detail, it comprises a lower 0.8 m-thick bioturbated light-gray (organic-lean) shale unit preceding the T-CIE and an upper 3.6 m-thick interbedded organic-rich shale and marlstone unit deposited during the T-CIE. High-resolution sampling at a small spacing (3.5 cm on average) was performed on the organic-lean shales and fine-grained organic-rich sedimentary rocks from the two units in this study. A total of 31 samples were collected and used for further geochemical analyses.

3.2. Analytical Methods

To avoid potential influence from weathered materials and any handling contamination, we cut the collected sedimentary rock samples into 2 cm-thick slabs with a water-cooled saw. The slabs were cleaned and then rinsed by distilled water and analytical grade and glass distilled ethanol and dichloromethane, respectively. Following preparing the cleaned sample slabs, they were dried at 50°C for one day, and then fragmented and powdered using an agate mill. The obtained sample powders were subsequently analyzed for $\delta^{15}\text{N}_{\text{bulk}}$ and $\delta^{15}\text{N}_{\text{ker}}$, and $\delta^{13}\text{C}$ for TOC and extracted kerogen ($\delta^{13}\text{C}_{\text{org}}$ and $\delta^{13}\text{C}_{\text{ker}}$) at the laboratory of the Institute of Earth Surface Dynamics, University of Lausanne. The analytical procedure is based on the previous description provided by Spangenberg and Frimmel (2001), Spangenberg and Herlec (2006), and Spangenberg and Macko (1998).

The measurement of all C and N data was carried out by combined elemental analyzer (Carlo Erba 1,108) and isotope ratio mass spectrometry (Delta V Plus; Thermo Fisher Scientific) (EA-IRMS) under a continuous helium flow condition through a ConFlo III open split interface (cf. Spangenberg et al., 2006, 2014). For TOC, total nitrogen (TN), $\delta^{13}\text{C}_{\text{org}}$, and $\delta^{15}\text{N}_{\text{bulk}}$ analyses, powdered whole rock materials were treated by a drop-wise addition of 10% HCl to remove all inorganic carbon. For the analyses of N_{ker} , $\delta^{13}\text{C}_{\text{ker}}$, and $\delta^{15}\text{N}_{\text{ker}}$, powdered whole rock samples were gradually treated to extract the kerogen fraction that cannot be dissolved in organic solvents, non-oxidizing acids and bases. On the basis of the kerogen extraction procedure described by Durand and Nicaise (1980), this study used Soxhlet extraction method in which mixed methanol and dichloromethane were added to remove bitumen (a soluble fraction in OM), 6 M HCl was added to remove carbonate, sulfide, sulphate, and (hydro)oxide, and a mixed acid composed of 40% HF and 6 M HCl was added to remove siliciclastic fraction. These stepwise treatments were all carried out at the temperature of 65°C–70°C, and were accelerated through using a PTFE-coated magnetic stirrer. After removing the supernatant, the residues were thoroughly washed and purified using deionized water and ultrapure water produced by Direct-Q UV3 Millipore®, respectively, and then dried at the temperature of 40°C. Following drying the solid residues, mineralogical analysis performed by a Thermo Scientific ARL X-TRA Diffractometer showed that all the silicate fraction in the whole rock samples has been removed completely.

The measured stable C and N isotope compositions are reported using delta (δ) notation in per mil relative to their standards which are Vienna Pee Dee Belemnite and atmospheric nitrogen (Air-N₂), respectively. They are thus defined as: $\delta^{13}\text{C} = ((^{13}\text{C}/^{12}\text{C})_{\text{sample}} / (^{13}\text{C}/^{12}\text{C})_{\text{VPDB}} - 1) \times 1,000$ and $\delta^{15}\text{N} = ((^{15}\text{N}/^{14}\text{N})_{\text{sample}} / (^{15}\text{N}/^{14}\text{N})_{\text{Air-N}_2} - 1) \times 1,000$. In this study almost all the C and N isotope data were performed in duplicate, and the analytical reproducibility of the repeated sample measurements for the C and N isotope values conducted by the EA-IRMS was, respectively, better than $\pm 0.1\%$ and $\pm 0.3\%$. The TOC abundance for the whole-rock samples, and the abundance of the TN_{bulk} for whole-rock samples and of N_{ker} for kerogen extracts were obtained from the peak areas of the major isotopes through the use of the calibrations for the $\delta^{13}\text{C}_{\text{org}}$, $\delta^{15}\text{N}_{\text{bulk}}$, and $\delta^{15}\text{N}_{\text{ker}}$ values, respectively. The analytical repeatability was better than ± 0.2 wt.% for the contents of TOC, TN_{bulk} and N_{ker} .

4. Results and Discussion

4.1. Evaluation of Primary Nitrogen Isotopic Signals

Continental run-off of OM from land plants may provide an additional source of N and may influence the isotope composition of marine sediments. In this study, the Dotternhausen sedimentary section from 1,050 to 980 cm is composed of organic-lean shales deposited prior to the T-CIE (Figure 2). These shale samples contain a considerable component of land plant-derived OM supported by low HI value (<400 mg HC/g TOC) and high oxygen index values (up to 100 mg CO₂/g TOC) (cf. Frimmel et al., 2004; Wang et al., 2020). In contrast, from 986 to 600 cm of this section, the OM in T-CIE fine-grained organic-rich sedimentary rocks (Figure 2) was primarily of marine origin (Frimmel et al., 2004; Wang et al., 2020) and thus likely reflect N biogeochemical processes in marine environments during the T-CIE.

The $\delta^{15}\text{N}$ of sedimentary rocks is a robust proxy to record the primary biomass signal of living organisms if it is not substantially imprinted by allochthonous inorganic N, diagenesis, metamorphism or metasomatism (e.g., Ader et al., 2006; Stüeken et al., 2016). Nitrogen in the sedimentary rocks is primarily present in organic- and clay-bound forms (mainly as ammonium (NH₄⁺)). The presence of a large fraction of inorganic N

Table 1
Carbon and Nitrogen Data for the Dotternhausen Samples

Depth [cm]	TOC (wt.%)	$\delta^{13}\text{C}_{\text{org}}$ (‰, VPDB)	TN _{bulk} (wt.%)	(C/N) _{bulk} (mol/mol)	$\delta^{15}\text{N}_{\text{bulk}}$ (‰, Air-N ₂)	$\delta^{13}\text{C}_{\text{ker}}$ (‰, VPDB)	TN _{ker} (wt.%)	$\delta^{15}\text{N}_{\text{ker}}$ (‰, Air-N ₂)	(C/N) _{ker} (mol/mol)	$\Delta^{15}\text{N}_{\text{bulk-ker}}$ (‰)
621	6.3	-27.7	0.21	35.7	2.3	-27.6	0.86	1.5	56.2	0.8
635	12.5	-27.6	0.28	52.2	2.1	-28.1	0.79	1.6	52.2	0.5
648	16.8	-27.6	0.43	45.7	2.8	-28.3	1.29	2.5	42.0	0.3
669.5	10.6	-28.5	0.33	37.5	2.5	-28.8	0.98	2.0	58.9	0.5
687	11.7	-28.2	0.32	42.5	2.1	-28.3	1.04	1.8	56.6	0.3
705	18.0	-28.4	0.37	57.0	2.1	-28.9	1.20	2.2	55.5	-0.1
729	18.5	-29.2	0.33	65.9	4.0	-29.8	1.31	1.9	46.9	2.1
743	16.1	-30.6	0.14	52.2	2.0	-31.0	1.15	2.2	51.9	-0.2
760	21.9	-31.0	0.41	62.0	2.0	-31.6	1.32	2.0	52.0	-0.1
770	27.0	-32.0	0.53	59.7	2.2	-32.4	1.34	2.4	51.0	-0.2
775	17.7	-30.0	0.39	53.1	1.9	-29.7	1.29	1.2	54.4	0.7
782	10.9	-32.3	0.31	40.4	2.2	-32.6	1.07	2.0	49.4	0.2
785	16.4	-30.5	0.39	48.5	1.9	-30.7	1.25	1.1	51.1	0.9
790	22.8	-30.8	0.43	61.5	1.7	-31.4	1.13	0.3	53.6	1.5
792	14.8	-31.0	0.32	53.4	1.6	-31.7	0.52	1.1	53.6	0.5
817	19.1	-31.9	0.37	60.8	3.3	-32.4	1.09	1.4	52.2	1.9
819.5	19.1	-31.9	0.35	63.7	3.1	-32.2	1.26	1.3	52.1	1.7
822	20.9	-32.3	0.28	85.6	3.1	-32.6	1.27	1.6	56.1	1.5
825	17.9	-32.0	0.24	85.3	5.7	-32.7	1.13	1.6	49.1	4.1
836	12.2	-33.1	0.31	46.1	4.7	-33.4	1.04	2.0	50.6	2.7
859	17.2	-32.7	0.23	86.9	2.1	-33.3	1.13	2.1	51.3	0.0
871	15.4	-32.0	0.27	66.2	1.2	-32.4	1.18	2.0	50.7	-0.8
898	13.2	-32.1	0.39	39.4	1.0	-32.5	0.90	2.0	47.8	-1.0
919	16.4	-32.0	0.34	56.0	1.1	-32.5	1.13	1.9	48.7	-0.7
940	7.0	-32.2	0.15	53.4	0.9	-32.7	0.43	2.2	49.7	-1.4
964	12.4	-31.6	0.29	49.5	1.5	-32.2	1.02	2.2	52.2	-0.7
986	8.7	-29.2	0.20	50.7	0.8	-29.6	0.64	1.7	47.2	-0.8
1,003	0.8	-27.4	0.06	14.6	2.2	-27.5	0.35	2.0	53.4	0.2
1,020	0.6	-26.9	0.08	8.9	1.9	-27.0	0.29	1.6	48.8	0.2
1,030	0.6	-27.5	0.08	8.6	2.4	-27.4	0.28	1.6	50.0	0.8
1,040	0.6	-27.2	0.08	8.9	1.9	-26.4	0.28	1.6	53.4	0.3

(NH₄⁺) can significantly affect organic-bound $\delta^{15}\text{N}$ values, especially in organic-lean sediments (e.g., Schubert & Calvert, 2001). Here, the high TOC content (15.6 wt.% on average) for the studied Dotternhausen T-CIE samples (Table 1) imply the negligible alteration on the primary $\delta^{15}\text{N}$ by inorganic N. The positive correlation between TOC and TN_{bulk} ($R^2 = 0.43$; $p = 0.00$; Figure 3a) observed for the studied T-CIE samples implies that most N was derived from marine organic matter. Furthermore, the lack of correlation between TN_{bulk} and detrital indicator aluminum (Al) concentration (Figure 3b) indicates the N contribution from detrital input does not compromise the robustness of the primary N isotope signal.

The release of NH₄⁺ induced by OM remineralization in diagenetic settings can to some extent influence the whole rock $\delta^{15}\text{N}_{\text{bulk}}$ values. For instance, an obvious increase in $\delta^{15}\text{N}_{\text{bulk}}$ values by ~4‰ will be caused under oxic diagenetic conditions, whereas a minimal alteration on $\delta^{15}\text{N}_{\text{bulk}}$ values is often expected during anoxic

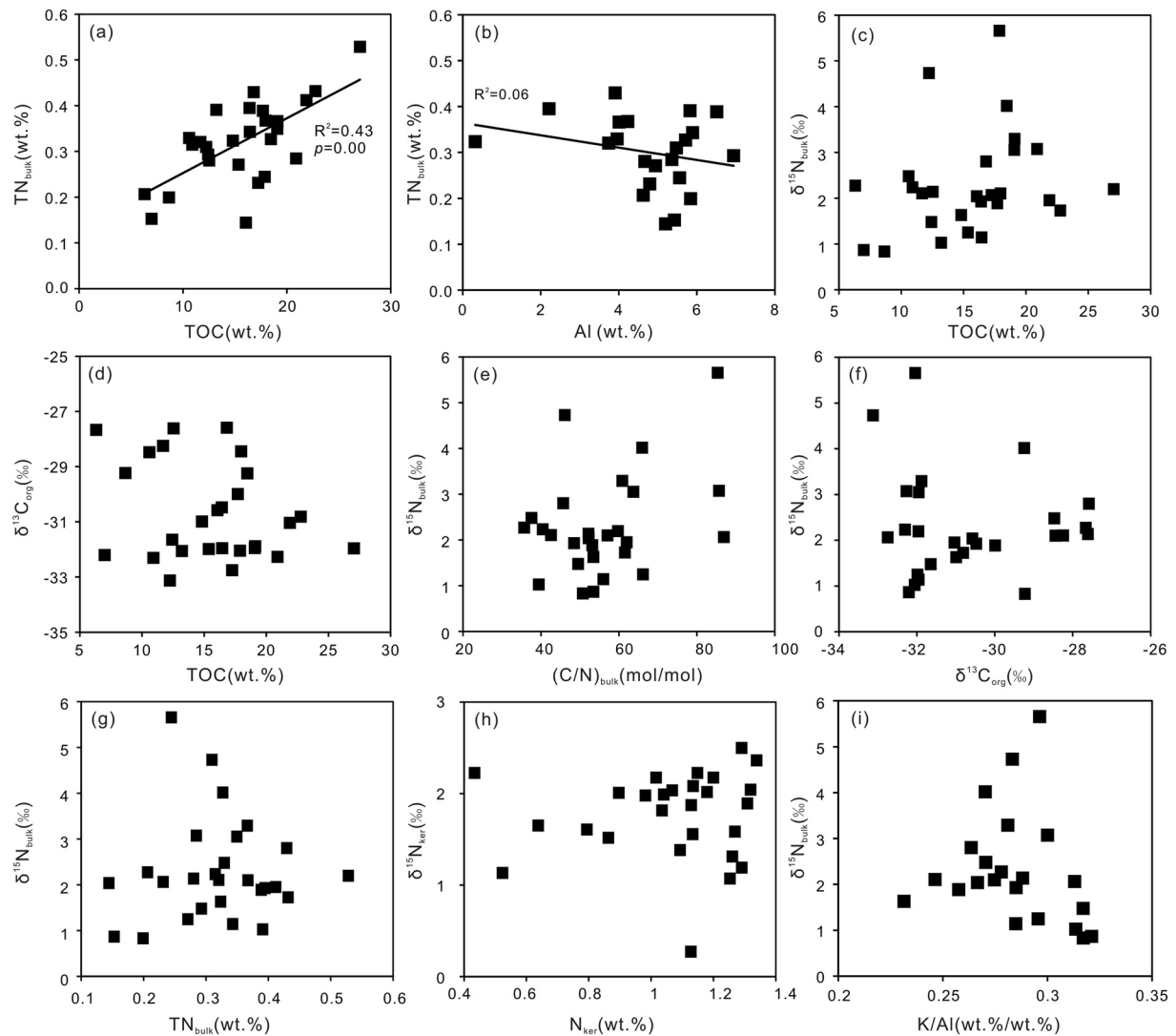


Figure 3. Cross-plots of geochemical data for the Dotternhausen Toarcian carbon isotope excursion samples. Data show: (a) Total nitrogen (TN_{bulk}) versus total organic carbon (TOC), (b) TN_{bulk} versus Al, (c) $\delta^{15}N_{\text{bulk}}$ versus TOC, (d) $\delta^{13}C_{\text{org}}$ versus TOC, (e) $\delta^{15}N_{\text{bulk}}$ versus $(C/N)_{\text{bulk}}$, (f) $\delta^{15}N_{\text{bulk}}$ versus $\delta^{13}C_{\text{org}}$, (g) $\delta^{15}N_{\text{bulk}}$ versus TN_{bulk} , (h) $\delta^{15}N_{\text{ker}}$ versus N_{ker} , and (i) $\delta^{15}N_{\text{bulk}}$ versus K/Al. The data of Al and K concentrations are from Wang et al. (2020).

diagenesis that is accompanied by an isotopic fractionation of $<1\text{‰}$ (Ader et al., 2006; Altabet et al., 1999; Stüeken et al., 2016). In this study, early diagenetic influence on the studied $\delta^{15}N_{\text{bulk}}$ values can be discounted because fine-grained Dotternhausen sedimentary rocks across the T-CIE interval are enriched in TOC, prone to anoxic diagenesis, and were deposited in a strongly redox-stratified basin with oxic surface and euxinic bottom water masses (Röhl et al., 2001; Schwark & Frimmel, 2004; Wang et al., 2020) which further prevented oxic diagenesis. This inference is supported by the absence of negative correlations of $\delta^{15}N_{\text{bulk}}$ versus TOC and $\delta^{13}C_{\text{org}}$ versus TOC (Figures 3c, and 3d) that are often expected following early diagenetic alteration processes (e.g., Wang et al., 2018).

Thermal devolatilization of OM due to burial diagenesis and metamorphism tends to preferential free organic-bound ^{14}N , leading to a $\delta^{15}N_{\text{bulk}}$ increase by 1‰ – 2‰ for greenschist facies, 3‰ – 4‰ for lower amphibolite facies, and up to 6‰ – 12‰ for upper amphibolite facies (e.g., Ader et al., 2006). However, it is constrained that the OM of the Dotternhausen T-CIE samples was well preserved and did not apparently experience thermal volatilization (Wang et al., 2020), which suggests a negligible rise in the studied $\delta^{15}N_{\text{bulk}}$ values. On the other hand, the preferential release of ^{14}N due to thermal volatilization is typically accompanied by positive covariations of $\delta^{15}N_{\text{bulk}}$ versus $(C/N)_{\text{bulk}}$ and $\delta^{15}N_{\text{bulk}}$ versus $\delta^{13}C_{\text{org}}$, and negative

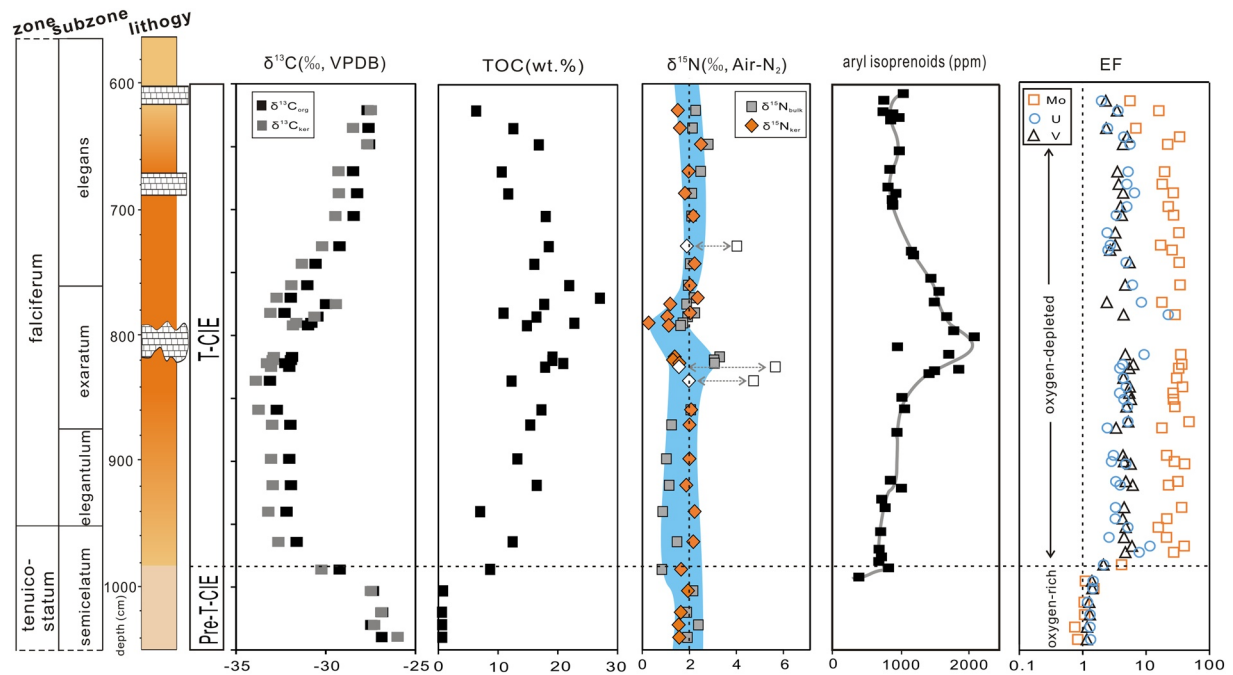


Figure 4. Chemostratigraphic $\delta^{13}\text{C}$, total organic carbon (TOC) content, $\delta^{15}\text{N}$, aryl isoprenoid content and enrichment factors (EFs) of Mo, V and U for Dotternhausen sedimentary section. Reliable N isotope values for the Dotternhausen samples are denoted in the $\delta^{15}\text{N}$ panel using a blue shading. The white diamonds and squares in the $\delta^{15}\text{N}$ panel denote the excluded samples that have large offsets between $\delta^{15}\text{N}_{\text{bulk}}$ and $\delta^{15}\text{N}_{\text{ker}}$ (see 4.1 for detailed discussion). The data of aryl isoprenoid content are from Schwark and Frimmel (2004). The Mo, V, U and aluminum (Al) data are from Wang et al. (2020). EF is calculated relative to upper continental crust (UCC; McLennan, 2001) using the equation of $[(\text{element}/\text{Al})_{\text{sample}}/(\text{element}/\text{Al})_{\text{UCC}}]$.

covariations of $\delta^{15}\text{N}_{\text{bulk}}$ versus TN_{bulk} and $\delta^{15}\text{N}_{\text{ker}}$ versus N_{ker} (Ader et al., 2006, 2016; Kipp et al., 2018; Mettam et al., 2019). The scarcity of such covariations (Figures 3e–3h) again implies the negligible systematic burial diagenetic or metamorphic alteration on the primarily deposited N isotope compositions of the Dotternhausen T-CIE samples. Furthermore, metasomatism can potentially substitute the organic-bound NH_4^+ by externally fluid-sourced potassium ions (K^+), due to equal charge and similar sizes, and change the primary $\delta^{15}\text{N}_{\text{bulk}}$ values (Ader et al., 2016; Stüeken et al., 2016). However, the lack of a relationship between $\delta^{15}\text{N}_{\text{bulk}}$ and K/Al (Figure 3i) rules out this possibility.

In addition, $\delta^{15}\text{N}_{\text{ker}}$ can be used to calibrate and evaluate the preservation extent of the primarily deposited N isotope signal imparted by the originally sinking biomass (e.g., Ader et al., 2016; Kipp et al., 2018; Stüeken et al., 2016, 2017). A majority of the studied samples show an overall minimal offset between $\delta^{15}\text{N}_{\text{bulk}}$ and $\delta^{15}\text{N}_{\text{ker}}$ ($\Delta^{15}\text{N}_{\text{bulk-ker}} = \delta^{15}\text{N}_{\text{bulk}} - \delta^{15}\text{N}_{\text{ker}}$, $0.2 \pm 0.8\text{‰}$; average ± 1 standard deviation), excluding three samples (DH-836, DH-825 and DH-729) with high $\delta^{15}\text{N}_{\text{bulk}}$ values (up to $+5.7\text{‰}$), where the offset is up to $+4.1\text{‰}$ (Figure 4; Table 1). The primary N isotope compositions of these three samples were likely affected by locally small-scale post-depositional modifications (Ader et al., 2016; Kipp et al., 2018; Stüeken et al., 2017) and will thus be excluded for further discussion. By contrast, the minimal $\delta^{15}\text{N}_{\text{bulk}} - \delta^{15}\text{N}_{\text{ker}}$ offset displayed for the rest of the Dotternhausen samples implies that the primary N isotopic signals are well preserved.

4.2. Marine N Biogeochemical Cycling During the Dotternhausen Toarcian Carbon Isotope Excursion

Well preserved primary N isotope compositions of sedimentary OM can serve as an effective proxy to reconstruct the input (e.g., diazotrophy which is an atmospheric N_2 fixation metabolism utilizing metal-based nitrogenase enzymes) and output (e.g., denitrification and/or anammox) fluxes of bioavailable N in marine environments. Diazotrophy relying on molybdenum (Mo)-based nitrogenase is the most representative form of N_2 fixation in natural environments (Stüeken et al., 2016; Tyrrell, 1999). In marine settings with aqueous Mo limitation, N_2 fixation can alternatively use vanadium (V)- or iron (Fe)-based nitrogenase.

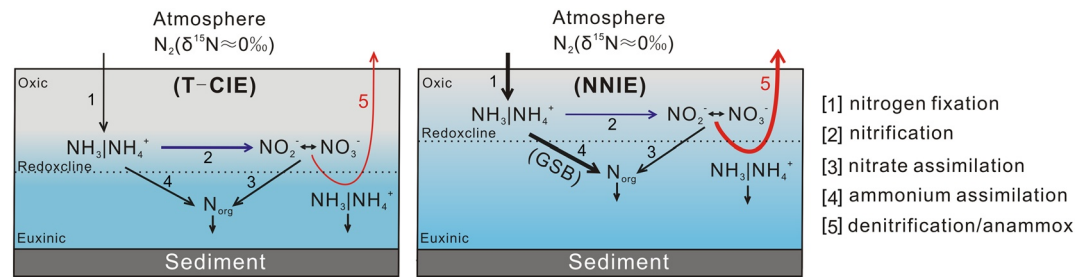


Figure 5. Schematic sketch showing N biogeochemical cycling in the Dotternhausen depositional setting across the Toarcian carbon isotope excursion (T-CIE) interval. During the maximum anoxia at the height of T-CIE (NNIE), thicker black arrows in [1] and [4] indicate enhanced nitrogen fixation and ammonium assimilation, respectively, while thicker red arrow in [5] denotes quantitative denitrification and/or anammox. NNIE: negative nitrogen isotope excursion (see Figure 4). GSB: green sulfur bacteria.

Culture experiments revealed that the expression of Mo- versus alternative-nitrogenase can be discerned by the N isotope values of the produced biomass (Bauersachs et al., 2009; Zhang et al., 2014). In these experiments, Mo-based diazotrophy had biomass $\delta^{15}\text{N}$ values between -4‰ and $+2\text{‰}$, while alternative nitrogenase yields values as low as -7‰ . In the modern ocean, aerobic N cycle is dominated by largely quantitative nitrification and partial denitrification and/or anammox in oxygen minimum zones (OMZs). This process leaves the remaining deep ocean NO_3^- pool higher $\delta^{15}\text{N}$ values with an average of $\sim +5\text{‰}$ (e.g., Sigman & Fripiat, 2019; Tesdal et al., 2013). Biomass preserves this signature in marine sediments. Thus, in ancient sedimentary rocks, $\delta^{15}\text{N}$ values between -4‰ and $+2\text{‰}$ can be confined to the dominant operation of Mo-based diazotrophy, while higher $\delta^{15}\text{N}$ values ($> +3\text{‰}$) evidence water-column partial denitrification and/or anammox (e.g., Garvin et al., 2009; Gilleaudeau et al., 2020; Stüeken et al., 2016).

In the Dotternhausen sedimentary section, the initiation of the T-CIE corresponds to the onset of the prominent enrichment of Mo, V and uranium (U) which are redox-sensitive elements (Figure 4). These elements are more soluble and less particle-reactive under oxygen-rich seawater states, which tends not to express authigenic enrichment in the oxic sediments; on the other hand, these elements are less soluble and more particle-reactive under oxygen-depleted seawater conditions, which can lead to pronounced authigenic accumulation in sediments (Algeo & Maynard, 2004; Tribouillard et al., 2006). The obvious authigenic enrichment of the Mo, V and U in this study thus implies the development of bottom-water euxinic conditions during the deposition of the T-CIE Dotternhausen section. Furthermore, there is a strong correlation between the height of the T-CIE curve and aryl isoprenoid, green sulfur bacteria (GSB) biomarker abundance (see Figure 4; Wang et al., 2020) indicating that the peak of the T-CIE coincides with the highest level of euxinic conditions in the water column. Evidence for this anoxia was traditionally described to reflect the Toarcian OAE (e.g., Pearce et al., 2008; Thibault et al., 2018).

Both $\delta^{13}\text{C}$ for TOC and separated kerogen show similar negative excursion, reaching minimum values of -33.1‰ and -33.4‰ , respectively (Figure 4; Table 1). The $\delta^{15}\text{N}$ values predominantly range between $+0.3$ and $+2.5\text{‰}$ (average ± 1 standard deviation; $\delta^{15}\text{N}_{\text{bulk}} = +2.0 \pm 0.6\text{‰}$ and $\delta^{15}\text{N}_{\text{ker}} = +1.8 \pm 0.5\text{‰}$) (Figure 4; Table 1). Across the T-CIE, the increasing bottom-water euxinia facilitated the emergence of water-column denitrification and/or anammox at the redoxcline (Figure 5). However, the reliable $\delta^{15}\text{N}$ values between $+0.3$ and $+2.5\text{‰}$ found in the uppermost *tenuicostatum* and lower *falciferum* zones (Figure 4) do not reflect the isotope effect of water-column partial denitrification and/or anammox (traditionally $> +3\text{‰}$; cf. Garvin et al., 2009; Gilleaudeau et al., 2020; Stüeken et al., 2016). By contrast, such a N isotope signal is in accordance with Mo-based diazotrophy likely under N-limited conditions. The severe scarcity of bioavailable N in the coeval depositional environment was driven by quantitative denitrification and/or anammox which was accompanied by the lack of an isotopic effect. The other possibility is that the concentration of dissolved N may have been high in anoxic bottom waters similar to the situation in the modern Black Sea (Ader et al., 2016; Fulton et al., 2012; Stüeken et al., 2016). However, the lack of N exchange between bottom and surface waters may have limited the availability of this dissolved deep N pool to organisms in surface waters and likely caused N scarcity. Cyanobacteria may thus have enhanced the rate of N_2 fixation to compensate this bioavailable N famine, here marked by the lack of any large isotopic variability. A small

$\delta^{15}\text{N}$ depletion to $\sim 0\text{‰}$ is found in the middle of the *exaratum* subzone (Figure 4). This depletion correlates with the highest level of bottom-water euxinia (Schwark & Frimmel, 2004; Wang et al., 2020) and may be associated with enhanced Mo-based diazotrophic activity through which more atmospheric N_2 would have been fixed ($\sim 0\text{‰}$) (Figure 5). Alternatively, this small negative $\delta^{15}\text{N}$ excursion is also coincident with highest abundance of aryl isoprenoid biomarkers, leading to elevated contribution of ^{14}N -enriched GSB biomass (Fogel & Cifuentes, 1993; Schwark & Frimmel, 2004) (Figures 4 and 5). Nonetheless, N famine occurred in surface waters as a result of N loss to the atmosphere (quantitative denitrification and/or anammox) and/or lack of mixing between bottom and surface waters during the deposition of the Dotternhausen T-CIE interval. In view of this, atmospheric N_2 was substantially fixed through Mo-based diazotrophs in order to keep pace with this seawater N scarcity.

4.3. Can the Northern European Epicontinental Shelf Settings Help to Validate an Evolved Oceanic Anoxic Event During the Toarcian Carbon Isotope Excursion?

T-CIE sedimentary profiles in the northern European epicontinental shelf are commonly marked by high abundance in TOC (e.g., Jenkyns, 2010). In addition to hydrographically restricted conditions (e.g., modern Black Sea), organic-rich sediments are also distributed in modern upwelling (unrestricted)-induced OMZ settings where partial denitrification and/or anammox is at play (Lam & Kuypers, 2011). By contrast, the studied T-CIE fine-grained organic-rich sedimentary rocks were deposited in a characteristic marine environment with enhanced water-column quantitative denitrification and/or anammox (see above). This finding convincingly manifests that the Dotternhausen fine-grained organic-rich rock deposition happened in a hydrographically restricted regime with minimal exchanges between bottom and surface waters during the T-CIE. Such hydrographic water-mass restriction heavily impeded bioavailable N replenishment from the bottom waters or open ocean and only accommodated an extremely limited NO_3^- inventory in surface waters. The restricted amount of NO_3^- was quantitatively consumed when the seawater became extensively euxinic during the T-CIE (Schwark & Frimmel, 2004). The reduced species of NH_4^+ acquired through enhanced N_2 fixation therewith succeeded NO_3^- as the dominant biologically available N form. Typically, under NH_4^+ -replete conditions, biotic assimilation imparts a large isotope fractionation ($-27\text{‰} - -4\text{‰}$) depending on the NH_4^+ abundance, followed by the formation of low $\delta^{15}\text{N}$ values of biomass (e.g., Higgins et al., 2012; Stüeken et al., 2016). However, this possibility is markedly inconsistent with the T-CIE $\delta^{15}\text{N}$ values ($+0.3\text{‰} - +2.5\text{‰}$) of the Dotternhausen section (Figure 4). It further indicates that the ecosystem assimilating this newly fixed N was too small to outbalance the $\delta^{15}\text{N}$ values of the preserved biomass as a consequence of a restricted setting. An analog exhibiting such a restricted marine environment is the Black Sea across the Holocene during which the prominently prevalent biological N_2 fixation was accompanied by biomass $\delta^{15}\text{N}$ values of $\sim 0\text{‰} - +2\text{‰}$ stimulated by the deficit in bioavailable N (Fulton et al., 2012; Tyrrell, 1999) owing to (near-) complete consumption of NO_3^- . This scenario has also been proposed for ancient Archean and mid-Proterozoic marine environments (Ossa Ossa et al., 2019; Stüeken et al., 2016).

Additionally, whole rock $\delta^{15}\text{N}$ data compiled from multiple shallow shelf T-CIE sedimentary successions including Rietheim (Switzerland), Réka Valley (Hungary), Yorkshire (UK), Winterborne Kingston (UK) and Mochras (UK) in the northern European epicontinental shelf range between -4‰ and $+2\text{‰}$ (Figure 6). However, the pelagic T-CIE profile from Dogna in Italy exhibits a slightly larger variation in $\delta^{15}\text{N}_{\text{bulk}}$ values between -3‰ and $+4\text{‰}$ (Figure 6). Environmental redox conditions during the deposition of the pelagic T-CIE Dogna sedimentary succession were proposed to have been unstable (Dickson et al., 2017). Nevertheless, $\delta^{15}\text{N}$ values up to $+4\text{‰}$ observed in this profile may also be tied to NO_3^- assimilation or partial denitrification and/or anammox in OMZs elsewhere in a likely oxygenated Tethyan Sea (see review from Ader et al., 2016). It is thus worth noting that the $\delta^{15}\text{N}$ records of other T-CIE profiles located in the shallow shelf settings fall in the Mo-based diazotrophic range. This N_2 fixation isotope record contradicts the possibility of existing water-column partial denitrification and/or anammox of marginal marine basins connected to the open ocean ($\delta^{15}\text{N}$ values traditionally $> +3\text{‰}$; e.g., Ader et al., 2016; Garvin et al., 2009; Gilleaudeau et al., 2020; Stüeken et al., 2016), but is in line with redox-controlled N biogeochemical cycle in hydrographically restricted environments.

To confirm the scenario for restricted marine settings, organic-rich sediment Mo/TOC mass ratio was used to constrain the degree of hydrographically restricted water-mass conditions of T-CIE sections deposited

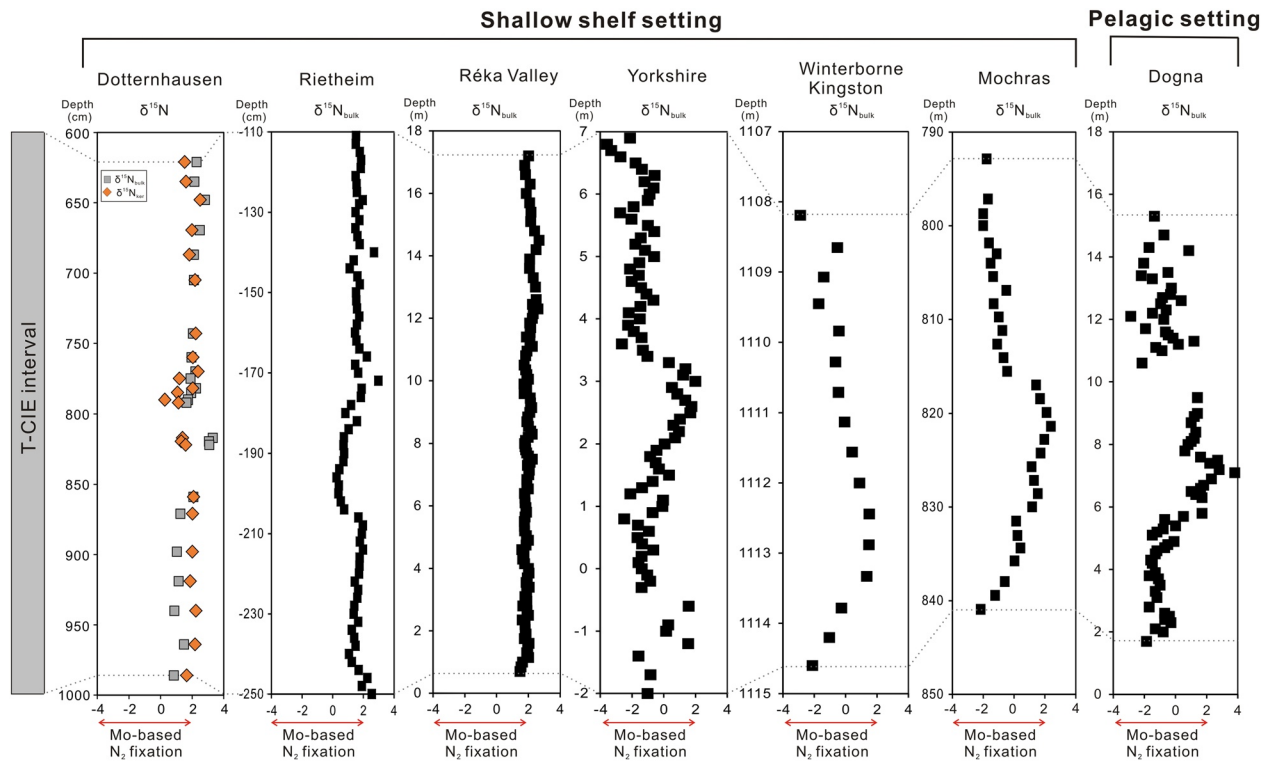


Figure 6. Comparison of $\delta^{15}\text{N}$ records among multiple Toarcian carbon isotope excursion sections. The $\delta^{15}\text{N}_{\text{bulk}}$ data of Rietheim (Switzerland) and Réka Valley (Hungary) sections are from Montero-Serrano et al. (2015) and Ruebsam et al. (2018), respectively. The $\delta^{15}\text{N}_{\text{bulk}}$ data of Yorkshire (represented by Hawsker Bottom; UK), Winterborne Kingston (UK), Mochras (UK) and Dogna (Italy) sections are from Jenkyns et al. (2001).

in the northern European epicontinental shelf. This proxy relies on the observation that the slope of the Mo versus TOC regression line is low at $\sim 4.5 \mu\text{g}\cdot\text{g}^{-1}\cdot\text{wt}\cdot\%^{-1}$ (Figure 7a) in modern Black Sea organic-rich sediments deposited under severe hydrographic restriction with limited water-mass renewal (Algeo & Lyons, 2006). The occurrence of such a low Mo versus TOC regression line slope is due to basin-scale aqueous

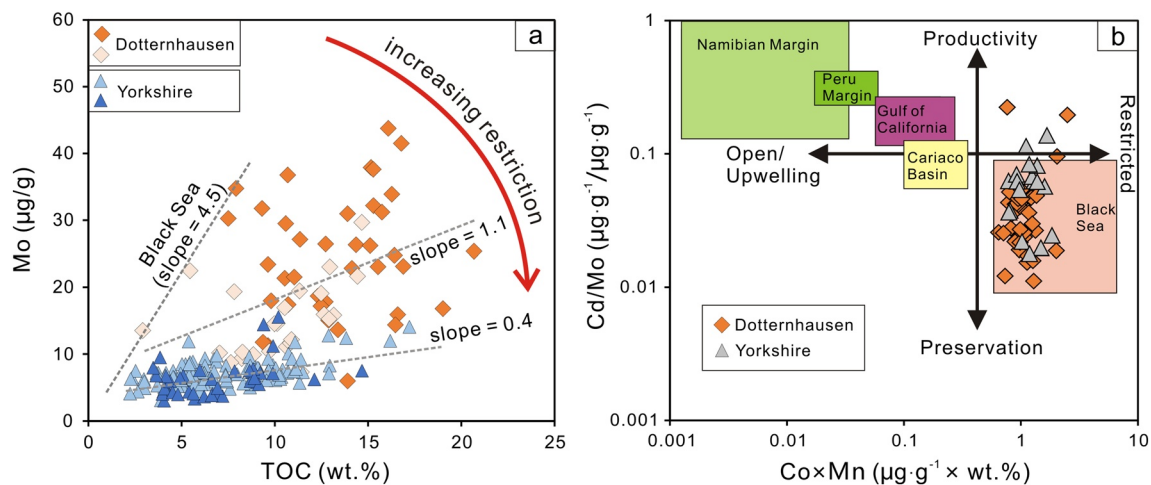


Figure 7. Cross-plots of Molybdenum (Mo) versus total organic carbon contents (a) and cadmium (Cd)/Mo versus cobalt (Co) × manganese (Mn) (b) for Dotternhausen and Yorkshire Toarcian carbon isotope excursion organic-rich samples. (a) The lower the slope the more depleted is the aqueous Mo reservoir due to hydrographically restricted water-mass circulation in coeval depositional settings (Algeo & Lyons, 2006). (b) the values of Cd/Mo and Co × Mn for modern organic-rich sediments from distinct depositional settings follow Sweere et al. (2016). Heavy and light blue triangles in a denoting the Yorkshire sample data are from Pearce et al. (2008) and Thibault et al. (2018), respectively. Gray triangles in b denoting the Yorkshire sample data are from McArthur (2019). Heavy orange diamonds in a and b, and light ones in a denoting Dotternhausen sample data are from Wang et al. (2020) and Dickson et al. (2017), respectively.

Mo drawdown to the sediment along with limited resupply. When hydrographic restriction condition decreased, the increase in open ocean water mass renewal and Mo replenishment led to high slope values in organic-rich marine sediments. Slopes in Mo versus TOC space for T-CIE sedimentary successions are very variable with values between 0.4 and $1.1 \mu\text{g}\cdot\text{g}^{-1}\cdot\text{wt}\cdot\%^{-1}$, implying that for example the depositional environment of the Yorkshire succession was more restricted than that of Dotternhausen (Figure 7a). Furthermore, both slope values are lower than $\sim 4.5 \mu\text{g}\cdot\text{g}^{-1}\cdot\text{wt}\cdot\%^{-1}$ (Figure 7a), supporting that their depositional settings were even more restricted than the modern Black Sea (Figure 7a). Given the drawdown of dissolved Mo is very fast when adequate amounts of aqueous hydrogen sulphide are present (Algeo & Maynard, 2004; Reinhard et al., 2013), the persistently high Mo enrichment throughout the entire Dotternhausen T-CIE section (Figure 4) points to limited but permanent Mo feeding from a larger oxic Mo reservoir that is, open ocean (Algeo & Lyons, 2006). The lack of evidence for quantitative Mo drawdown in pelagic Tethyan black shales of the Dogna sedimentary succession indicates that Mo likely remained dissolved in coeval oxic seawaters while their light $\delta^{98}\text{Mo}$ values (Dickson et al., 2017) further support that the water column, at least at the site of deposition, was not anoxic and sulfidic (euxinic) during the T-CIE. This may explain why the Dogna sedimentary succession did not record the N isotopic effect of water-column denitrification and/or anammox at the site of the deposition—though the water-column of deposition was neither euxinic nor sulfidic oxygen-depleted OMZ.

In addition, hydrographic conditions can also be evaluated using a cross-plot of sedimentary cadmium (Cd)/Mo versus manganese×cobalt (Mn×Co) since distinct hydrographic regimes can be effectively constrained by modern high-TOC marine sediment Cd/Mo and Co×Mn values (Figure 7b; cf. Sweere et al., 2016, 2020). High Cd uptake in organic material relative to Mo often promotes high Cd/Mo ratios (>0.1) in organic-rich sediments in upwelling (unrestricted) regions of the modern ocean (Conway & John, 2015). In restricted settings, oxygen deficit is in favor of Cd and Mo deposition but relatively weak marine productivity limits organic-driven output channel of Cd, resulting in low sedimentary Cd/Mo ratios (<0.1). The contents of Co and Mn in rivers and/or surface seawaters are significantly enriched compared to open-ocean sub-surface waters which feed upwelling systems, and thus the supply of both elements is typically higher in restricted basins (Sweere et al., 2016 and references therein). The different behaviors of these elements eventually promote high Co×Mn values ($>0.4 \mu\text{g}\cdot\text{g}^{-1}\times\text{wt}\cdot\%$) in organic-rich sediments that are deposited under restricted settings, whereas low Co×Mn values ($<0.4 \mu\text{g}\cdot\text{g}^{-1}\times\text{wt}\cdot\%$) in the counterpart from upwelling (unrestricted) settings. An empirical comparison between elemental data from the representative T-CIE sedimentary successions with the modern marine sediment records is further indicative of hydrographically restricted water-mass conditions for the northern European epicontinental shelf seas (Figure 7b).

Collectively, combined N isotope and elemental concentration data of sedimentary successions deposited during the T-CIE add an important insight in the evolution of the ocean redox structure during the early Jurassic. These data support that the deoxygenated marine conditions commonly identified in several T-CIE localities from the northern European epicontinental shelf do not reflect the redox structure of the coeval Tethyan ocean, but rather indicate the development of oxygen-deficient basins. However, testing whether the global deep-ocean anoxia existed during the T-CIE requires robust redox evaluation (e.g., by trace element geochemistry and Fe speciation) of deep open ocean sedimentary successions.

5. Conclusion

Combined $\delta^{15}\text{N}_{\text{bulk}}$ and $\delta^{15}\text{N}_{\text{ker}}$ data obtained from the well-recognized T-CIE sedimentary section of Dotternhausen, SW Germany, are used to investigate the N biogeochemical cycle and its isotopic effect during the Early Toarcian marine deoxygenation. The $\delta^{15}\text{N}_{\text{bulk}}$ and $\delta^{15}\text{N}_{\text{ker}}$ values range predominantly between $+0.3\text{‰}$ and $+2.5\text{‰}$, implying enhanced N_2 fixation by cyanobacteria using Mo-based nitrogenase enzyme to keep pace with bioavailable N loss as a result of quantitative denitrification and/or anammox in a strongly redox-stratified marine environment lacking exchanges between bottom and surface water masses. This inference is further confirmed by the sedimentary N isotope records ranging between -4‰ and $+2\text{‰}$ from other northern European epicontinental shallow-shelf sections. The N_2 -fixing signal exhibited in these T-CIE sections contradicts the typical sedimentary $\delta^{15}\text{N}$ values ($>3\text{‰}$) induced by partial water-column denitrification and/or anammox in marginal marine settings well connected to the open ocean. Instead, this study proposes the development of oxygen-deficient basins on the northern European epicontinental shelf.

In such hydrographically restricted marine environments, dissolved N pool suffered extensive denitrification and/or anammox which led to severe bioavailable N scarcity and thus stimulated Mo-based diazotrophic activity. These oxygen-depleted restricted settings situated on the northern European epicontinental shelf cannot thus be considered for evaluating the redox landscape of the coeval open ocean during the T-CIE. A robust redox evaluation of sedimentary successions deposited in both Tethyan and Panthalassan oceans is thus still missing for validating the putative global deep ocean anoxia across the T-CIE interval.

Data Availability Statement

Geochemical data for this research are available in the Zenodo repository at <https://zenodo.org/record/4778565#.YKe1LqgzaUl>.

Acknowledgments

We would like to thank LafargeHolcim GmbH Dotternhausen for providing drill core material and its Head of the Fossil Museum Dr. Annette Schmid-Röhl for scientific discussion. Yunfeng Wang would like to thank the China Scholarship Council (201706400079) for the financial support. Frantz Ossa Ossa and Ronny Schoenberg acknowledge financial support by the German Research Foundation (DFG) project SCHO1071/11-1. We are greatly indebted to Eva Stüeken and the two anonymous reviewers for their constructive comments that greatly helped to improve the quality of the manuscript. Open access funding enabled and organized by Projekt DEAL.

References

- Ader, M., Cartigny, P., Boudou, J. P., Oh, J. H., Petit, E., & Javoy, M. (2006). Nitrogen isotopic evolution of carbonaceous matter during metamorphism: Methodology and preliminary results. *Chemical Geology*, 232(3–4), 152–169. <https://doi.org/10.1016/j.chemgeo.2006.02.019>
- Ader, M., Thomazo, C., Sansjofre, P., Busigny, V., Papineau, D., Laffont, R., et al. (2016). Interpretation of the nitrogen isotopic composition of Precambrian sedimentary rocks: Assumptions and perspectives. *Chemical Geology*, 429, 93–110. <https://doi.org/10.1016/j.chemgeo.2016.02.010>
- Algeo, T. J., & Lyons, T. W. (2006). Mo–total organic carbon covariation in modern anoxic marine environments: Implications for analysis of paleoredox and paleohydrographic conditions. *Paleoceanography*, 21, PA1016. <https://doi.org/10.1029/2004pa001112>
- Algeo, T. J., & Maynard, J. B. (2004). Trace-element behavior and redox facies in core shales of Upper Pennsylvanian Kansas-type cyclothems. *Chemical Geology*, 206(3–4), 289–318. <https://doi.org/10.1016/j.chemgeo.2003.12.009>
- Altabet, M. A., Pilskaln, C., Thunell, R., Pride, C., Sigman, D., Chavez, F., & Francois, R. (1999). The nitrogen isotope biogeochemistry of sinking particles from the margin of the Eastern North Pacific. *Deep Sea Research Part I: Oceanographic Research Papers*, 46(4), 655–679. [https://doi.org/10.1016/S0967-0637\(98\)00084-3](https://doi.org/10.1016/S0967-0637(98)00084-3)
- Baudin, F., Herbin, J.-P., & Vandenbroucke, M. (1990). Mapping and geochemical characterization of the Toarcian organic matter in the Mediterranean Tethys and Middle East. *Organic Geochemistry*, 16(4–6), 677–687. [https://doi.org/10.1016/0146-6380\(90\)90109-d](https://doi.org/10.1016/0146-6380(90)90109-d)
- Bauersachs, T., Schouten, S., Compaoré, J., Wollenzien, U., Stal, L. J., & Sinninghe Damsté, J. S. (2009). Nitrogen isotopic fractionation associated with growth on dinitrogen gas and nitrate by cyanobacteria. *Limnology & Oceanography*, 54(4), 1403–1411. <https://doi.org/10.4319/lo.2009.54.4.1403>
- Bour, I., Mattioli, E., & Pittet, B. (2007). Nanofacies analysis as a tool to reconstruct paleoenvironmental changes during the Early Toarcian anoxic event. *Palaeogeography, Palaeoclimatology, Palaeoecology*, 249(1–2), 58–79. <https://doi.org/10.1016/j.palaeo.2007.01.013>
- Brazier, J. M., Suan, G., Tacail, T., Simon, L., Martin, J. E., Mattioli, E., & Balter, V. (2015). Calcium isotope evidence for dramatic increase of continental weathering during the Toarcian oceanic anoxic event (Early Jurassic). *Earth and Planetary Science Letters*, 411, 164–176. <https://doi.org/10.1016/j.epsl.2014.11.028>
- Chandler, M. A., Rind, D., & Ruedy, R. (1992). Pangaeian climate during the Early Jurassic: GCM simulations and the sedimentary record of paleoclimate. *GSA Bulletin*, 104(5), 543–559. [https://doi.org/10.1130/0016-7606\(1992\)104<0543:pcdtej>2.3.co;2](https://doi.org/10.1130/0016-7606(1992)104<0543:pcdtej>2.3.co;2)
- Cohen, A. S., Coe, A. L., Harding, S. M., & Schwark, L. (2004). Osmium isotope evidence for the regulation of atmospheric CO₂ by continental weathering. *Geology*, 32(2), 157–160. <https://doi.org/10.1130/g20158.1>
- Conway, T. M., & John, S. G. (2015). The cycling of iron, zinc and cadmium in the North East Pacific Ocean—Insights from stable isotopes. *Geochimica et Cosmochimica Acta*, 164, 262–283. <https://doi.org/10.1016/j.gca.2015.05.023>
- Dera, G., Brigaud, B., Monna, F., Laffont, R., Pucéat, E., Deconinck, J. F., et al. (2011). Climatic ups and downs in a disturbed Jurassic world. *Geology*, 39(3), 215–218. <https://doi.org/10.1130/g31579.1>
- Dickson, A. J., Gill, B. C., Ruhl, M., Jenkyns, H. C., Porcelli, D., Idiz, E., et al. (2017). Molybdenum-isotope chemostratigraphy and paleoceanography of the Toarcian Oceanic Anoxic Event (Early Jurassic). *Paleoceanography*, 32, 813–829. <https://doi.org/10.1002/2016pa003048>
- Durand, B., & Nicaise, G. (1980). Procedures for kerogen isolation. In B. Durand (Ed.), *Kerogen insoluble organic matter from sedimentary rocks*. 35–53: Editions Technip.
- Fantasia, A., Föllmi, K. B., Adatte, T., Spangenberg, J. E., & Montero-Serrano, J.-C. (2018). The Early Toarcian oceanic anoxic event: Paleoenvironmental and paleoclimatic change across the Alpine Tethys (Switzerland). *Global and Planetary Change*, 162, 53–68. <https://doi.org/10.1016/j.gloplacha.2018.01.008>
- Fogel, M. L., & Cifuentes, L. A. (1993). Isotope Fractionation during Primary Production. In M. H. Engel, & S. A. Macko (Eds.), *Organic Geochemistry*. (73–98). Springer, Boston, MA. https://doi.org/10.1007/978-1-4615-2890-6_3
- Frimmel, A., Oschmann, W., & Schwark, L. (2004). Chemostratigraphy of the Posidonia Black Shale, SW Germany: I. Influence of sea-level variation on organic facies evolution. *Chemical Geology*, 206(3–4), 199–230. <https://doi.org/10.1016/j.chemgeo.2003.12.007>
- Fulton, J. M., Arthur, M. A., & Freeman, K. H. (2012). Black Sea nitrogen cycling and the preservation of phytoplankton δ¹⁵N signals during the Holocene. *Global Biogeochemical Cycles*, 26, GB2030. <https://doi.org/10.1029/2011GB004196>
- Garvin, J., Buick, R., Anbar, A. D., Arnold, G. L., & Kaufman, A. J. (2009). Isotopic evidence for an aerobic nitrogen cycle in the latest Archean. *Science*, 323(5917), 1045–1048. <https://doi.org/10.1126/science.1165675>
- Gilleaudeau, G. J., Sahoo, S. K., Ostrander, C. M., Owens, J. D., Poulton, S. W., Lyons, T. W., & Anbar, A. D. (2020). Molybdenum isotope and trace metal signals in an iron-rich Mesoproterozoic ocean: A snapshot from the Vindhyan Basin, India. *Precambrian Research*, 343, 105718. <https://doi.org/10.1016/j.precamres.2020.105718>
- Harries, P. J., & Little, C. T. S. (1999). The early Toarcian (Early Jurassic) and the Cenomanian–Turonian (Late Cretaceous) mass extinctions: Similarities and contrasts. *Palaeogeography, Palaeoclimatology, Palaeoecology*, 154(1–2), 39–66. [https://doi.org/10.1016/S0031-0182\(99\)00086-3](https://doi.org/10.1016/S0031-0182(99)00086-3)

- Hermoso, M., & Pellenard, P. (2014). Continental weathering and climatic changes inferred from clay mineralogy and paired carbon isotopes across the early to middle Toarcian in the Paris Basin. *Palaeogeography, Palaeoclimatology, Palaeoecology*, 399, 385–393. <https://doi.org/10.1016/j.palaeo.2014.02.007>
- Hesselbo, S. P., Gröcke, D. R., Jenkyns, H. C., Bjerrum, C. J., Farrimond, P., Bell, H. S. M., & Green, O. W. (2000). Massive dissociation of gas hydrate during a Jurassic oceanic anoxic event. *Nature*, 406, 392–395. <https://doi.org/10.1038/35019044>
- Hesselbo, S. P., Jenkyns, H. C., Duarte, L. V., & Oliveira, L. C. V. (2007). Carbon-isotope record of the Early Jurassic (Toarcian) Oceanic Anoxic Event from fossil wood and marine carbonate (Lusitanian Basin, Portugal). *Earth and Planetary Science Letters*, 253(3–4), 455–470. <https://doi.org/10.1016/j.epsl.2006.11.009>
- Higgins, M. B., Robinson, R. S., Husson, J. M., Carter, S. J., & Pearson, A. (2012). Dominant eukaryotic export production during ocean anoxic events reflects the importance of recycled NH_4^+ . *Proceedings of the National Academy of Sciences*, 109(7), 2269–2274. <https://doi.org/10.1073/pnas.1104313109>
- Jenkyns, H. C. (1988). The early Toarcian (Jurassic) anoxic event; stratigraphic, sedimentary and geochemical evidence. *American Journal of Science*, 288(2), 101–151. <https://doi.org/10.2475/ajs.288.2.101>
- Jenkyns, H. C. (2010). Geochemistry of oceanic anoxic events. *Geochemistry, Geophysics, Geosystems*, 11(3), Q03004. <https://doi.org/10.1029/2009gc002788>
- Jenkyns, H. C., Gröcke, D. R., & Hesselbo, S. P. (2001). Nitrogen isotope evidence for water mass denitrification during the early Toarcian (Jurassic) oceanic anoxic event. *Paleoceanography*, 16(6), 593–603. <https://doi.org/10.1029/2000pa000558>
- Kemp, D. B., Coe, A. L., Cohen, A. S., & Schwark, L. (2005). Astronomical pacing of methane release in the Early Jurassic period. *Nature*, 437, 396–399. <https://doi.org/10.1038/nature04037>
- Kipp, M. A., Stüeken, E. E., Yun, M., Bekker, A., & Buick, R. (2018). Pervasive aerobic nitrogen cycling in the surface ocean across the Paleoproterozoic Era. *Earth and Planetary Science Letters*, 500, 117–126. <https://doi.org/10.1016/j.epsl.2018.08.007>
- Lam, P., & Kuypers, M. M. (2011). Microbial nitrogen cycling processes in oxygen minimum zones. *Annual review of marine science*, 3, 317–345. <https://doi.org/10.1146/annurev-marine-120709-142814>
- Little, C. T. S., & Benton, M. J. (1995). Early Jurassic mass extinction: A global long-term event. *Geology*, 23(6), 495–498. [https://doi.org/10.1130/0091-7613\(1995\)023<0495:ejmeag>2.3.co;2](https://doi.org/10.1130/0091-7613(1995)023<0495:ejmeag>2.3.co;2)
- McArthur, J. M. (2019). Early Toarcian black shales: A response to an oceanic anoxic event or anoxia in marginal basins? *Chemical Geology*, 522, 71–83. <https://doi.org/10.1016/j.chemgeo.2019.05.028>
- McArthur, J. M., Algeo, T. J., van de Schootbrugge, B., Li, Q., & Howarth, R. J. (2008). Basinal restriction, black shales, Re-Os dating, and the Early Toarcian (Jurassic) oceanic anoxic event. *Paleoceanography*, 23(4), PA4217. <https://doi.org/10.1029/2008pa001607>
- McElwain, J. C., Wade-Murphy, J., & Hesselbo, S. P. (2005). Changes in carbon dioxide during an oceanic anoxic event linked to intrusion into Gondwana coals. *Nature*, 435(7041), 479–482. <https://doi.org/10.1038/nature03618>
- McLennan, S. M. (2001). Relationships between the trace element composition of sedimentary rocks and upper continental crust. *Geochemistry, Geophysics, Geosystems*, 2(4), 1021. <https://doi.org/10.1029/2000GC000109>
- Mettam, C., Zerkle, A. L., Claire, M. W., Prave, A. R., Poulton, S. W., & Junium, C. K. (2019). Anaerobic nitrogen cycling on a Neoproterozoic ocean margin. *Earth and Planetary Science Letters*, 527, 115800. <https://doi.org/10.1016/j.epsl.2019.115800>
- Montero-Serrano, J. C., Föllmi, K. B., Adatte, T., Spangenberg, J. E., Tribouillard, N., Fantasia, A., & Suan, G. (2015). Continental weathering and redox conditions during the early Toarcian Oceanic anoxic event in the northwestern Tethys: Insight from the Posidonia Shale section in the Swiss Jura Mountains. *Palaeogeography, Palaeoclimatology, Palaeoecology*, 429, 83–99. <https://doi.org/10.1016/j.palaeo.2015.03.043>
- Ossa Ossa, F., Hofmann, A., Spangenberg, J. E., Poulton, S. W., Stüeken, E. E., Schoenberg, R., et al. (2019). Limited oxygen production in the Mesoproterozoic ocean. *Proceedings of the National Academy of Sciences*, 116(14), 6647–6652. <https://doi.org/10.1073/pnas.1818762116>
- Pálfy, J., & Smith, P. L. (2000). Synchrony between Early Jurassic extinction, oceanic anoxic event, and the Karoo-Ferrar flood basalt volcanism. *Geology*, 28(8), 747–750. [https://doi.org/10.1130/0091-7613\(2000\)28<747:SBEJEO>2.0.CO;2](https://doi.org/10.1130/0091-7613(2000)28<747:SBEJEO>2.0.CO;2)
- Pearce, C. R., Cohen, A. S., Coe, A. L., & Burton, K. W. (2008). Molybdenum isotope evidence for global ocean anoxia coupled with perturbations to the carbon cycle during the Early Jurassic. *Geology*, 36(3), 231–234. <https://doi.org/10.1130/g24446a.1>
- Reinhard, C. T., Planavsky, N. J., Robbins, L. J., Partin, C. A., Gill, B. C., Lalonde, S. V., et al. (2013). Proterozoic ocean redox and biogeochemical stasis. *Proceedings of the National Academy of Sciences*, 110(14), 5357–5362. <https://doi.org/10.1073/pnas.1208622110>
- Remírez, M. N., & Algeo, T. J. (2020). Paleosalinity determination in ancient epicontinental seas: A case study of the T-OAE in the Cleveland Basin (UK). *Earth-Science Reviews*. 201. <https://doi.org/10.1016/j.earscirev.2019.103072>
- Röhl, H.-J., & Schmid-Röhl, A. (2005). Lower Toarcian (Upper Liassic) black shales of the Central European Epicontinental Basin: A sequence stratigraphic case study from the SW German Posidonia Shale. In N. B. Harris (Ed.), *The Deposition of Organic-Carbon-Rich Sediments: Models, Mechanisms, and Consequences*, 82, 165–189. Society for Sedimentary Geology Special Publication. <https://doi.org/10.2110/pec.05.82.0165>
- Röhl, H.-J., Schmid-Röhl, A., Oschmann, W., Frimmel, A., & Schwark, L. (2001). The Posidonia Shale (Lower Toarcian) of SW-Germany: an oxygen-depleted ecosystem controlled by sea level and palaeoclimate. *Palaeogeography, Palaeoclimatology, Palaeoecology*, 165(1–2), 27–52. [https://doi.org/10.1016/s0031-0182\(00\)00152-8](https://doi.org/10.1016/s0031-0182(00)00152-8)
- Rosales, I., Barnolas, A., Goy, A., Sevillano, A., Armendáriz, M., & López-García, J. M. (2018). Isotope records (C-O-Sr) of late Pliensbachian-early Toarcian environmental perturbations in the westernmost Tethys (Majorca Island, Spain). *Palaeogeography, Palaeoclimatology, Palaeoecology*, 497, 168–185. <https://doi.org/10.1016/j.palaeo.2018.02.016>
- Ruebsam, W., Mayer, B., & Schwark, L. (2019). Cryosphere carbon dynamics control early Toarcian global warming and sea level evolution. *Global and Planetary Change*, 172, 440–453. <https://doi.org/10.1016/j.gloplacha.2018.11.003>
- Ruebsam, W., Müller, T., Kovács, J., Pálfy, J., & Schwark, L. (2018). Environmental response to the early Toarcian carbon cycle and climate perturbations in the northeastern part of the West Tethys shelf. *Gondwana Research*, 59, 144–158. <https://doi.org/10.1016/j.gr.2018.03.013>
- Ruebsam, W., Reolid, M., & Schwark, L. (2020). $\delta^{13}\text{C}$ of terrestrial vegetation records Toarcian CO_2 and climate gradients. *Scientific Reports*, 10, 117. <https://doi.org/10.1038/s41598-019-56710-6>
- Ruvalcaba Baroni, I., Pohl, A., van Helmond, N. A. G. M., Papadomanolaki, N. M., Coe, A. L., Cohen, A. S., et al. (2018). Ocean circulation in the Toarcian (Early Jurassic): A key control on deoxygenation and carbon burial on the European Shelf. *Paleoceanography and Paleoclimatology*, 33(9), 994–1012. <https://doi.org/10.1029/2018PA003394>
- Sælen, G., Tyson, R. V., Telnæs, N., & Talbot, M. R. (2000). Contrasting watermass conditions during deposition of the Whitby Mudstone (Lower Jurassic) and Kimmeridge clay (upper Jurassic) formations, UK. *Palaeogeography, Palaeoclimatology, Palaeoecology*, 163(3–4), 163–196. [https://doi.org/10.1016/S0031-0182\(00\)00150-4](https://doi.org/10.1016/S0031-0182(00)00150-4)

- Schubert, C. J., & Calvert, S. E. (2001). Nitrogen and carbon isotopic composition of marine and terrestrial organic matter in Arctic Ocean sediments: Implications for nutrient utilization and organic matter composition. *Deep Sea Research Part I: Oceanographic Research Papers*, 48(3), 789–810. [https://doi.org/10.1016/S0967-0637\(00\)00069-8](https://doi.org/10.1016/S0967-0637(00)00069-8)
- Schwark, L., & Frimmel, A. (2004). Chemostratigraphy of the Posidonia Black Shale, SW-Germany: II. Assessment of extent and persistence of photic-zone anoxia using aryl isoprenoid distributions. *Chemical Geology*, 206(3–4), 231–248. <https://doi.org/10.1016/j.chemgeo.2003.12.008>
- Sigman, D. M., & Fripiat, F. (2019). Nitrogen isotope in the ocean. In J. Kirk Cochran H. J. Bokuniewicz & P. L. Yager (Eds.), *Encyclopedia of Ocean Sciences*, 3rd ed. 1, 263–278. <https://doi.org/10.1016/B978-0-12-409548-9.11605-7>
- Song, J., Littke, R., & Weniger, P. (2017). Organic geochemistry of the lower Toarcian Posidonia Shale in NW Europe. *Organic Geochemistry*, 106, 76–92. <https://doi.org/10.1016/j.orggeochem.2016.10.014>
- Spangenberg, J. E., Bagnoud-Velásquez, M., Boggiani, P. C., & Gaucher, C. (2014). Redox variations and bioproductivity in the Ediacaran: Evidence from inorganic and organic geochemistry of the Corumbá Group, Brazil. *Gondwana Research*, 26(3–4), 1186–1207. <https://doi.org/10.1016/j.gr.2013.08.014>
- Spangenberg, J. E., & Frimmel, H. E. (2001). Basin-internal derivation of hydrocarbons in the Witwatersrand Basin, South Africa: Evidence from bulk and molecular $\delta^{13}\text{C}$ data. *Chemical Geology*, 173(4), 339–355. [https://doi.org/10.1016/S0009-2541\(00\)00283-7](https://doi.org/10.1016/S0009-2541(00)00283-7)
- Spangenberg, J. E., & Herlec, U. (2006). Hydrocarbon biomarkers in the Topla-Mežica zinc–lead deposits, Northern Karavanke/Drau Range, Slovenia: Palaeoenvironment at the site of ore formation. *Economic Geology*, 101(5), 997–1021. <https://doi.org/10.2113/gsecongeo.101.5.997>
- Spangenberg, J. E., Jacomet, S., & Schibler, J. (2006). Chemical analyses of organic residues in archaeological pottery from Arbon Bleiche 3, Switzerland—evidence for dairying in the late Neolithic. *Journal of Archaeological Science*, 33(1), 1–13. <https://doi.org/10.1016/j.jas.2005.05.013>
- Spangenberg, J. E., & Macko, S. A. (1998). Organic geochemistry of the San Vicente Mississippi Valley-type zinc–lead district, eastern Pucará Basin, Peru. *Chemical Geology*, 146(1–2), 1–23. [https://doi.org/10.1016/S0009-2541\(97\)00158-7](https://doi.org/10.1016/S0009-2541(97)00158-7)
- Stüeken, E. E., Kipp, M. A., Koehler, M. C., & Buick, R. (2016). The evolution of Earth's biogeochemical nitrogen cycle. *Earth-Science Reviews*, 160, 220–239. <https://doi.org/10.1016/j.earscirev.2016.07.007>
- Stüeken, E. E., Zaloumis, J., Meixnerová, J., & Buick, R. (2017). Differential metamorphic effects on nitrogen isotopes in kerogen extracts and bulk rocks. *Geochimica et Cosmochimica Acta*, 217, 80–94. <https://doi.org/10.1016/j.gca.2017.08.019>
- Svensen, H., Planke, S., Chevallier, L., Malthe-Sørenssen, A., Corfu, F., & Jamtveit, B. (2007). Hydrothermal venting of greenhouse gases triggering Early Jurassic global warming. *Earth and Planetary Science Letters*, 256(3–4), 554–566. <https://doi.org/10.1016/j.epsl.2007.02.013>
- Sweere, T., van den Boorn, S., Dickson, A. J., & Reichart, G. J. (2016). Definition of new trace-metal proxies for the controls on organic matter enrichment in marine sediments based on Mn, Co, Mo and Cd concentrations. *Chemical Geology*, 441, 235–245. <https://doi.org/10.1016/j.chemgeo.2016.08.028>
- Sweere, T. C., Dickson, A. J., Jenkyns, H. C., Porcelli, D., & Henderson, G. M. (2020). Zinc- and cadmium-isotope evidence for redox-driven perturbations to global micronutrient cycles during Oceanic Anoxic Event 2 (Late Cretaceous). *Earth and Planetary Science Letters*, 546, 116427. <https://doi.org/10.1016/j.epsl.2020.116427>
- Tesdal, J. E., Galbraith, E. D., & Kienast, M. (2013). Nitrogen isotopes in bulk marine sediment: Linking seafloor observations with subsurface record. *Biogeosciences*, 10, 101–118. <https://doi.org/10.5194/bg-10-101-2013>
- Them, T. R., Gill, B. C., Selby, D., Gröcke, D. R., Friedman, R. M., & Owens, J. D. (2017). Evidence for rapid weathering response to climatic warming during the Toarcian Oceanic Anoxic Event. *Scientific Reports*, 7, 5003. <https://doi.org/10.1038/s41598-017-05307-y>
- Thibault, N., Ruhl, M., Ullmann, C. V., Korte, C., Kemp, D. B., Gröcke, D. R., & Hesselbo, S. P. (2018). The wider context of the lower Jurassic Toarcian oceanic anoxic event in Yorkshire coastal outcrops, UK. *Proceedings of the Geologists' Association*, 129(3), 372–391. <https://doi.org/10.1016/j.pgeola.2017.10.007>
- Tribouillard, N., Algeo, T. J., Lyons, T., & Riboulleau, A. (2006). Trace metals as paleoredox and paleoproductivity proxies: An update. *Chemical Geology*, 232(1–2), 12–32. <https://doi.org/10.1016/j.chemgeo.2006.02.012>
- Tyrrell, T. (1999). The relative influences of nitrogen and phosphorus on oceanic primary production. *Nature*, 400(6744), 525–531. <https://doi.org/10.1038/22941>
- van Acken, D., Tütken, T., Daly, J. S., Schmid-Röhl, A., & Orr, P. J. (2019). Rhenium-osmium geochronology of the Toarcian Posidonia Shale, SW Germany. *Paleoceanography, Palaeoclimatology, Palaeoecology*, 534, 109294. <https://doi.org/10.1016/j.palaeo.2019.109294>
- van de Schootbrugge, B., McArthur, J. M., Bailey, T. R., Rosenthal, Y., Wright, J. D., & Miller, K. G. (2005). Toarcian oceanic anoxic event: An assessment of global causes using belemnite C isotope records. *Paleoceanography*, 20(3). <https://doi.org/10.1029/2004pa001102>
- Wang, D., Ling, H. F., Struck, U., Zhu, X. K., Zhu, M., He, T., et al. (2018). Coupling of ocean redox and animal evolution during the Ediacaran-Cambrian transition. *Nature Communications*, 9, 2575. <https://doi.org/10.1038/s41467-018-04980-5>
- Wang, Y., Ossa Ossa, F., Wille, M., Schurr, S., Saussele, M., Schmid-Röhl, A., & Schoenberg, R. (2020). Evidence for local carbon-cycle perturbations superimposed on the Toarcian carbon isotope excursion. *Geobiology*, 18, 682–709. <https://doi.org/10.1111/gbi.12410>
- Zhang, X., Sigman, D. M., Morel, F. M. M., & Kraepiel, A. M. L. (2014). Nitrogen isotope fractionation by alternative nitrogenases and past ocean anoxia. *Proceedings of the National Academy of Sciences*, 111(13), 4782–4787. <https://doi.org/10.1073/pnas.1402976111>
- Ziegler, P. A. (1988). Evolution of the Arctic-North Atlantic and the Western Tethys. *AAPG Memoir*. 43, 198.

Zinc geochemical cycling response to the Early Jurassic (Toarcian: ~183 Ma) marine anoxia and its paleoenvironmental significance

Yunfeng Wang^{1*}, Marie-Laure Pons², Angela Coe³, Frantz Ossa Ossa^{1,4}, Martin Wille⁵, and Ronny Schoenberg^{1,4}

¹ Department of Geosciences, University of Tuebingen, 72074 Tuebingen, Germany

² CNRS, Aix Marseille Univ, IRD, INRAE, Coll France, CEREGE, 13545, Aix en Provence, France

³ School of Earth, Environment and Ecosystem Sciences, The Open University, UK

⁴ Department of Geology, University of Johannesburg, 2092 Johannesburg, South Africa

⁵ Institute of Geological Sciences, University of Bern, 3012 Bern, Switzerland

Abstract

The Early Jurassic (Toarcian: ~183 Ma) was accompanied by a widespread marine anoxic event characterized by the deposition of organic-rich sedimentary rocks bearing depleted carbon isotope compositions. These signatures, referred as the negative Toarcian carbon isotope excursion (T-CIE) were widely distributed on the Northern European epicontinental shelf. These organic-rich rocks generally contain high amounts of metal sulfide and organic matter which are major hosts for zinc (Zn), a sulfide-forming and bio-essential element. However, how Zn is cycled throughout the interval of Early Toarcian marine anoxia has not been investigated so far. This study presents $\delta^{66}\text{Zn}_{\text{bulk}}$ data for two T-CIE sections (Yorkshire and Dotternhausen) deposited on the European epicontinental shelf. We demonstrate that these values are independent of local seawater redox and marine productivity, but may be associated with the Zn reservoir composition of the global deep ocean. To provide insights into the Early Toarcian ocean Zn geochemical cycling, this study estimated the two sections' $\delta^{66}\text{Zn}_{\text{auth}}$ values (~+0.54 and +0.62 ‰, respectively) that are within uncertainty identical with that of the present-day global deep ocean seawater (+0.50 ± 0.14 ‰). This observation demonstrates that the Early Toarcian ocean overall approached the modern level of Zn biogeochemical cycling. It is observed that in both Yorkshire and Dotternhausen strata there is one small event of synchronous negative $\delta^{66}\text{Zn}_{\text{bulk}}$ excursion which was linked to ocean oxygenation leading to isotopically heavier Zn sequestration into oxic sediments (e.g., carbonates, iron-manganese (Fe-Mn) oxides). This isotope effect depleted the residual Zn in the global ocean seawater. The ocean redox landscape throughout the T-CIE was also investigated by sedimentary molybdenum (Mo) isotope compositions. Compared to Mo, near-quantitative

sequestration of dissolved Zn from seawater can easily happen under the condition of hydrogen sulfide (H₂S) concentration in excess of Zn abundance. This study conservatively proposed that compared the redox-sensitive Mo isotope system, Zn isotopes have a higher potential as proxy for redox-driven global ocean seawater changes.

1. INTRODUCTION

A few distinct extreme perturbations of the carbon cycle to the global climate occurred during the Mesozoic (250–64 Ma), leading to several temporal intervals of Oceanic Anoxic Events (OAEs) (Takashima et al., 2006; Jenkyns, 2010). The OAEs are typically marked by widespread deposition of organic-rich sedimentary rocks, and associated with rapid warming, expansion of oxygen-poor marine environments and a decrease in floral and faunal diversities (e.g., Danise et al., 2015; Jenkyns, 2010). One of the OAEs happened during the Early Toarcian at ~183 Ma (T-OAE: Jenkyns, 1988), which was commonly accompanied by ~3-7 ‰ negative carbon isotope excursions (T-CIEs) recorded in terrestrial fossil woods, lacustrine sediments, marine carbonate and organic matter around the globe (e.g., Caruthers et al., 2011; Hesselbo et al., 2000, 2007; Xu et al., 2018). This anomalous carbon perturbation was suggested to be linked to the massive release of CO₂ from the Karoo-Ferrar large igneous province emplacement (Pálffy and Smith, 2000; Svensen et al., 2007) and/or the release of CH₄ from Gondwanan organic-rich shales or methane clathrates (e.g., Hesselbo et al., 2000; Kemp et al., 2005; McElwain et al., 2005). The duration of the T-CIE and the coevolved T-OAE are not precisely clear but they may have lasted around several hundred thousand years (Kemp et al., 2005, 2011; Suan et al., 2008). The maintenance of the T-OAE throughout this interval has been attributed to elevated marine productivity during which the rising amount of produced organic matter experienced intensive aerobic remineralization through consuming oxygen from bottom waters (Frimmel et al., 2004; Röhl et al., 2001). The high-rate marine primary productivity was favored by enhanced delivery of nutrient inventories to proximal shelf-sea settings due to an increased hydrological cycle (e.g., Izumi et al., 2018) and warming-induced intensification of continental weathering (e.g., Cohen et al., 2004; Jenkyns, 2010).

The long-lasting marine oxygen deficit across the T-CIE interval is accompanied by extensive burial fluxes of metal sulfide and organic matter into the underlying organic-

rich sedimentary rocks, which is particularly widespread in the north European epicontinental shelf region (e.g., Berner et al., 2013; Frimmel, et al., 2004; Gill et al., 2011; Röhl et al., 2001; Sælen et al., 2000). Metal sulfide and organic matter occupying a high fraction in organic-rich marine sediments are major hosts for zinc (Zn) which is a sulfide-forming and bio-essential element (Hu et al., 2018; Isson et al., 2018; John et al., 2007; Little et al., 2016; Sweere et al., 2020; Vance et al., 2016). The removal of Zn from seawater to organic-rich marine sediments relates to two main fluxes: organically bound metals and metals sulfides (e.g., sphalerite, wurtzite). Uptake of cellular living organisms generally represents the main export mechanism of Zn to the sediment, where it may be buried as part of organic material or fixed as metal sulfides (Little et al., 2015; Weber et al., 2018). This is particularly true for the Mesozoic OAEs during which high rate of primary productivity accelerated the assimilation of Zn into biomass and then the sinking of Zn into the underlying oxygen-depleted sediments. The resultant organic-rich sedimentary rocks thus contain high amounts of Zn (e.g., Montero-Serrano et al., 2015; Sweere et al., 2020; Wang et al., 2020). Recently, organic-rich sedimentary rocks depositing during the Cenomanian-Turonian (Late Cretaceous, ~94 Ma) OAE 2 were used to reconstruct the coevally oceanic Zn-cycle processes (Sweere et al., 2020). In their study, the authors proposed that the disturbance of micronutrient Zn cycling was controlled by fluctuating ocean redox states within the OAE 2 (Sweere et al., 2020). However, in the course of the widespread deposition of T-CIE organic-rich sediments, how oceanic Zn geochemical cycling proceeded in response to the coeval marine anoxia so far remains unexplored. Furthermore, as a traditional seawater redox proxy, whether molybdenum (Mo) cycling in relation to the Early Toarcian marine anoxia is tight to that of Zn has not yet been investigated. To better constrain these processes, this study selected two well-characterized T-CIE sedimentary successions from the Yorkshire coast, northeastern England (Cleveland Basin), and a quarry located in Dotternhausen, Germany (Southern German Basin) (Fig. 1). The analysis of Zn isotope compositions for these two successions was performed to place constraints on the contemporaneous Zn-inventory evolutions and unravel the associated paleoenvironmental perturbations. New high-resolution Mo isotope records for Dotternhausen quarry together with those from the Yorkshire coast were connected to their Zn isotope compositions to attempt to provide new insights into Zn geochemical significance in paleoceanography.

2. SITES AND METHODS

The Early Toarcian sedimentary successions from Yorkshire coast and Dotternhausen quarry were paleogeographically located in the northern European epicontinental shelf-sea settings during the T-CIE (Fig. 1). They provide well-studied T-CIE records starting from the depth of -2.5 to 6.3 m and ~9.8 to ~6.2 m, respectively (Fig. 2). More detailed descriptions of their stratigraphy, paleontology, sedimentology, and petrography can be quantitatively found in Howarth (1973) and Röhl et al. (2001), respectively. The present study sampled organic-lean grey shales deposited before the T-CIE and organic-rich black shales deposited during the T-CIE from both Yorkshire and Dotternhausen sections, respectively (Fig. 2). In addition, a diagenetic limestone bed (Unterer Stein) at the depth of ~8 m in Dotternhausen section (Fig. 2) was also sampled in this study.

2.1. Analyses of element concentration and molybdenum isotope composition

The analyses of major- and trace-elements for the Yorkshire samples in this study followed the protocol of Wang et al. (2020). The measurement of bulk Mo isotope for the Dotternhausen samples followed the method described by Wille et al. (2013). Rock samples were ashed for 15 h at 500 °C to oxidize organic matter fraction. An adequate amount of a ^{100}Mo - ^{97}Mo double spike was added to 50-500 mg powdered sample material prior to sample digestion and Mo-purification. The double-spike method allows for the correction of the instrumental mass bias as well as mass fractionation that may occur in the process of chromatographic Mo-purification (Rudge et al., 2009). Samples were dissolved in Teflon beakers by sequential digestion steps using distilled HF, HNO₃ and HCl acids. Mo was purified using a combination of anion and cation exchange chromatography (i.e., using Dowex 1×8, 200-400 mesh and Dowex 50WX8 200-400 mesh resins, respectively) as described by Wille et al. (2013). Molybdenum isotopic ratios were measured on a multi-collector ICP-MS (ThermoFisher Scientific NeptunePlus) at the University of Tuebingen, Germany. Measurements of the in-house standard ZH-2, a Mo-rich sulfide that ran through all chemical separation steps, yield a long-term reproducibility on $\delta^{98}\text{Mo}$ better than 0.09‰ (2 σ). Results were calibrated using the Johnson Matthey ICP standard and are reported in the σ -notation relative to the NIST3134 standard (Goldberg et al., 2013), which was set to 0.25‰ following a procedure of Nögler et al. (2014):

$$\delta^{98}\text{Mo} = 1.0025 \times ((^{98}\text{Mo}/^{95}\text{Mo})_{\text{sample}} / (^{98}\text{Mo}/^{95}\text{Mo})_{\text{NIST3134}} - 1) \quad (1)$$

where δ is expressed in ‰ by multiplication with a factor of 1000.

2.2. Analyses of zinc isotope composition

For the Zn isotope analyses, fine-grained rock powder was weighted into Teflon beakers and admixed with appropriate amounts of purified ^{64}Zn - ^{67}Zn double spike (DS) isotope tracer solution (in 1 mol L⁻¹ HNO₃) to achieve a spike:sample Zn ratio of 1.22 (Moeller et al., 2012). Samples were digested using 3 mL of concentrated HF-HNO₃ at a 3:1 ratio and placing the closed beakers on hot plates at 110 °C for 48 h. Samples were then taken to dryness, refluxed in 2 mL of 6 M HCl and placed on hot plates at 120 °C for 24 h to dissolve fluorides and convert the samples to chloride form. Samples were dried again and taken up in 1 mL 6 M HCl for chemical separation of Zn. Ion chromatographic purification of Zn was completed using 2 mL of 200–400 mesh BioRad DOWEX AG1X8 anion exchange resin in SpectraChrom columns, followed by smaller columns containing 0.3 mL of the same resin for 2nd purification step. The Zn purification procedures employed in this study followed the protocol of Moeller et al. (2012). The DS technique allows in-run correction of the instrumental mass bias, and accounts for chemical Zn isotopic fractionation effects caused by anion-exchange chromatography (Maréchal et al., 1999). Zinc isotope ratio determinations were performed in medium-resolution mode on a ThermoFisher Scientific NeptunePlus MC-ICP-MS housed at the Isotope Geochemistry laboratories of the Department of Geosciences, University of Tuebingen. Sample uptake by a Cetac ARIDUS II desolvating nebulizer system without N₂ purging minimised potential polyatomic oxide and nitride interferences, while yielding improved atom-to-ion conversion and ion beam stability compared to standard ‘cold spray’ uptake systems. For reporting Zn isotopic data, this study followed the guidelines by Coplen (2011), based on the recommendations by the Commission on Isotopic Abundances and Atomic Weights of the International Union of Pure and Applied Chemistry that are widely consistent with the Système International d’Unités. Sample Zn isotopic compositions were measured as the ‰-differences of their $^{66}\text{Zn}/^{64}\text{Zn}$ isotope abundance ratios relative to that of the isotopically certified reference material IRMM-3702 in δ -values. The data were then recalculated to the no longer available ‘JMC-Lyon’ standard solution as δ -zero anchor by applying an offset of +0.29 ‰ on $\delta^{66}\text{Zn}_{\text{IRMM-3702}}$ values (Moeller et al., 2012). For

ease of reference and comparison to previous Zn isotopic studies we report $\delta^{66}\text{Zn}_{\text{JMC-L}}$ values in Table 1 according to the following equations, and work with the $\delta^{66}\text{Zn}_{\text{JMC-L}}$ values throughout the text and in the figures:

$$\delta^{66}\text{Zn}_{\text{JMC-L}} = 1.0029 \times ((^{66}\text{Zn}/^{64}\text{Zn})_{\text{sample}}/(^{66}\text{Zn}/^{64}\text{Zn})_{\text{IRMM-3702}} - 1)$$

The reproducibility for $\delta^{66}\text{Zn}$ on the IRMM-3702 throughout all analytical sessions during the course of this study was always better than 0.035 ‰ (2 s.d.; 0.017–0.031 ‰). Accuracy was controlled by interleaved analysis of an in-house solution standard prepared from an Alfa Aesar Puratronic Zn wire yielding an average $\delta^{66}\text{Zn}_{\text{JMC-L}}$ of -9.983 ± 0.033 ‰ (2 s.d, $n = 46$), which is in great agreement with the laboratory long-term reproducibility of -9.983 ± 0.037 ‰ ($n = 137$). Two determinations of Zn isotope composition for the USGS reference material BCR-2 yield average $\delta^{66}\text{Zn}_{\text{JMC-L}}$ value of $+0.27 \pm 0.011$ ‰ ($n = 2$; Supplementary Table 1 in Appendix D), which agrees very well with previously published ones (Moynier et al., 2017; Rosca et al., 2019; Kamber and Schoenberg, 2020). Multiple digestions followed by Zn purification of USGS reference materials OU-6 and QS-1 yielded very reproducible $\delta^{66}\text{Zn}_{\text{JMC-L}}$ values of $+0.23 \pm 0.016$ ‰ ($n = 6$) and $+0.32 \pm 0.021$ ‰ ($n = 4$), respectively (Supplementary Table 1 in Appendix D). Given that all standard solutions and rock reference materials reproducibilities were better than 0.040 ‰ ($\delta^{66}\text{Zn}_{\text{JMC-L}}$, 2 s.d), this value was taken as the conservative overall reproducibility (2 s.d) and applied to all data points in this study.

3. RESULTS

3.1. Elemental concentration

The concentrations of selected major element oxides and trace element data of the measured samples from Yorkshire section are reported in Table 1. The detrital indicator element Al in all the Yorkshire samples has a relatively high abundance (mean = 9.14 wt.%) (Table 1) compared to the UCC (8.04 wt.%: McLennan, 2001). Notably, the pre-T-CIE gray bioturbated shale samples (from the depth of -12.07 to -3 m) have higher Al concentrations with the average of 10.89 wt.% than those of the T-CIE laminated black shale samples (from the depth of -1.71 to 6.15 m) (mean = 8.84 wt.%). The concentrations of Mo, uranium (U) and vanadium (V) between the Yorkshire pre-T-CIE and T-CIE samples are very different, which is expected considering they are redox-sensitive elements. Mo, U, and V concentrations for the pre-T-CIE samples

range from 0.7 to 1.5 µg/g (mean = 0.9 µg/g), 3.1 to 3.8 µg/g (mean = 3.5 µg/g) and 134.9 to 158.7 µg/g (mean = 148.0 µg/g), respectively (Table 1), which are on the whole comparable to those of the UCC (Mo: 1.5 µg/g, U: 2.8 µg/g, V: 107 µg/g). By contrast, these element concentrations for the T-CIE samples ranging from 4.2 to 35.9 µg/g (mean = 8.4 µg/g), 4.7 to 17.2 µg/g (mean = 7.2 µg/g), and 150.3 to 299.2 µg/g (mean = 194.8 µg/g), respectively (Table 1), are higher than those of the pre-T-CIE samples and the UCC. The concentrations of bio-essential elements copper (Cu), nickel (Ni) and phosphorus (P) between the Yorkshire pre-T-CIE and T-CIE samples are also different. Cu, Ni and P concentrations for the pre-T-CIE samples range from 29.4 to 38.8 µg/g (mean = 35.7 µg/g), 64.2 to 75.4 µg/g (mean = 75.6 µg/g) and 0.027 to 0.061 wt.% (mean = 0.036 µg/g), respectively (Table 1). Of which the Cu and Ni concentrations are higher than those of the UCC (Cu: 25 µg/g, Ni: 44 µg/g), while the P concentration is lower than that of the UCC (P: 0.07 wt.%). For the T-CIE samples, Cu, Ni and P concentrations are in the range between 41.4 and 151.7 µg/g (mean = 83.6 µg/g), 75.8 and 203.9 µg/g (mean = 99.4 µg/g) and 0.031 and 0.284 wt.% (mean = 0.097 wt.%), respectively (Table 1), which are significantly higher than those of the pre-T-CIE samples and the UCC. The concentration of another bio-limiting element Zn for the Yorkshire pre-T-CIE and T-CIE samples does not show an obvious difference. For the pre-T-CIE samples, Zn concentration ranges from 77.5 to 121.9 µg/g (mean = 102.9 µg/g), whereas the T-CIE samples have the Zn concentration of 77.4 to 224.8 µg/g (mean = 128.0 µg/g) (Table 1). Both mean values are higher than that of the UCC (71 µg/g).

3.2. Molybdenum isotope composition

The measured Mo isotope composition ($\delta^{98}\text{Mo}$) for the Dotternhausen samples are given in Table 1. Its pre-T-CIE samples (from the depth of 1003 to 986 cm) have heavier $\delta^{98}\text{Mo}$ values ranging from 0.99 to 1.46 ‰ with the average of 1.23 ± 0.66 ‰ (2 s.d., $n = 2$) than those of the T-CIE samples (from the depth of 976 to 613 cm) which are in the range between 0.46 and 1.11 ‰ (mean = 0.84 ± 0.32 ‰; $n = 37$) (Table 1). To correct for possible terrigenous-sourced Mo, the isotope composition of the authigenic Mo fraction ($\delta^{98}\text{Mo}_{\text{auth}}$) was calculated using $\text{Mo}_{\text{detrital}} = 1.5$ µg/g, $\text{Al}_{\text{detrital}} = 8.04$ %, and $\delta^{98}\text{Mo}_{\text{detrital}} = + 0.4$ ‰ as the parameters for the UCC endmember (McLennan, 2001; Dahl et al., 2011) by the following equations:

$$f_{\text{detrital}} = (\text{Mo}_{\text{detrital}}/\text{Al}_{\text{detrital}}) \times \text{Al}_{\text{sample}}/\text{Mo}_{\text{sample}}, \text{ and}$$

$$\delta^{98}\text{Mo}_{\text{auth}} = (\delta^{98}\text{Mo} - f_{\text{detrital}} \times \delta^{98}\text{Mo}_{\text{detrital}}) / (1 - f_{\text{detrital}}).$$

The calculated $\delta^{98}\text{Mo}_{\text{auth}}$ values are close to the measured $\delta^{98}\text{Mo}_{\text{bulk}}$ values ($\delta^{98}\text{Mo}_{\text{auth}} = 1.105 \times \delta^{98}\text{Mo}_{\text{bulk}} + 0.0621$; $R^2 = 0.968$; $n = 38$, $p(a) < 0.001$), which may result from the terrigenous Mo comprising only a small fraction of the total Mo in most samples. The $\delta^{98}\text{Mo}_{\text{auth}}$ values for T-CIE samples range from +0.47 to +1.27 ‰ (Table 1) with an average of +0.87 ‰, which is markedly lower than the modern global seawater value of +2.34 ‰ (e.g., Siebert et al., 2003).

3.3. Zinc isotope composition

The Yorkshire pre-T-CIE samples show $\delta^{66}\text{Zn}_{\text{bulk}}$ values varying from +0.18 to +0.23 ‰ with an average of $+0.19 \pm 0.04$ ‰ (2 s.d., $n = 7$), whereas the Dotternhausen pre-T-CIE samples have relatively heavy $\delta^{66}\text{Zn}_{\text{bulk}}$ values that are in the range of +0.29 to +0.38 ‰ averaging $+0.35 \pm 0.06$ ‰ (2 s.d., $n = 7$) (Fig. 2; Table 1). The pre-T-CIE $\delta^{66}\text{Zn}_{\text{bulk}}$ values for both sedimentary sections are, however, comparable to that of the lithogenic average ($\sim 0.27 \pm 0.07$ ‰; Little et al., 2016 and references therein). Across the T-CIE interval, an overall positive excursion of $\delta^{66}\text{Zn}_{\text{bulk}}$ is observed for both Yorkshire and Dotternhausen samples which range from 0.29 to 0.55 ‰ (mean = $+0.41 \pm 0.12$ ‰; 2 s.d., $n = 41$) and from 0.32 to 0.66 ‰ (mean = $+0.52 \pm 0.17$ ‰; 2 s.d., $n = 39$), respectively. A prominent negative $\delta^{66}\text{Zn}_{\text{bulk}}$ excursion in both Yorkshire and Dotternhausen T-CIE strata is observed in Fig 2. The negative shifts towards the similar minimum value of ~ 0.3 ‰ are at the depth of ~ 1.0 m and ~ 8.2 m in the Yorkshire and Dotternhausen sections, respectively (Fig. 2). This negative $\delta^{66}\text{Zn}_{\text{bulk}}$ excursion of the Yorkshire and Dotternhausen sections is exhibited on different lithological facies: organic-rich black shales and a diagenetic limestone concretion (Unterer Stein) (cf. Fig. 2; Röhl et al., 2001).

Assuming the sedimentation rates for the Yorkshire and Dotternhausen T-CIE strata are respectively constant, they can be calculated by the equation

$$\text{sedimentation rates} = \text{distance/duration (D)}$$

where the distance denotes the thickness of T-CIE strata expressed in Yorkshire and Dotternhausen sedimentary sections, and the duration (D) denotes the temporal interval of T-CIE which ranges from ~ 120 to $\sim 1,200$ kyr (Suan et al., 2008; Ogg and Hinnov, 2012). The thickness of the Yorkshire and Dotternhausen T-CIE strata are ~ 8.8 m (from ~ 2.5 m to 6.3 m) and ~ 3.6 m (from ~ 9.8 m to 6.2 m), respectively (Figure 2; Röhl et al., 2001; Pearce et al., 2008; French et al., 2014). After entering the T-CIE

interval, the temporal occurrence of the negative shift in $\delta^{66}\text{Zn}_{\text{bulk}}$ values at the depth of ~1.0 m and ~8.2 m in Yorkshire and Dotternhausen sections can be determined. It respectively lasted $\sim 0.40 \times D$ and $\sim 0.44 \times D$ to arrive at the $\delta^{66}\text{Zn}_{\text{bulk}}$ negative shift observed in Yorkshire and Dotternhausen sections. Therefore, the $\delta^{66}\text{Zn}_{\text{bulk}}$ drop found in these two sedimentary sections occurred nearly concurrently after the onset of the T-CIE.

4. DISCUSSION

4.1. Local marine redox and productivity controls on $\delta^{66}\text{Zn}_{\text{bulk}}$ during the T-CIE?

Sedimentary $\delta^{66}\text{Zn}$ records are dominated by burial pathways which are commonly impacted by seawater redox conditions and marine productivity (e.g., John et al., 2007; John and Conway, 2014; Kunzmann et al., 2013; Little et al., 2016; Isson et al., 2018; Sweere et al., 2018, 2020; Köbberich and Vance, 2019). Temporarily more reducing conditions could have led to a smaller isotopic offset between seawater and sediments, compared to sediments deposited under less reducing conditions, as observed in the present-day continental-margin sediments (Little et al., 2016). The modern ocean sediments deposited in anoxic to mildly sulfidic environments that exhibit higher $\delta^{66}\text{Zn}$ values than sediments from suboxic to anoxic conditions (cf. Little et al., 2016). It has been proposed that marine productivity by living organisms preferentially assimilates light Zn isotopes which are then exported onto the seafloor by the produced biomass, enriching the residual seawater Zn in heavy isotopes (e.g., Kunzmann et al., 2013; Isson et al., 2018). To explore whether these two mechanisms may have controlled the $\delta^{66}\text{Zn}_{\text{bulk}}$ values of the Yorkshire and Dotternhausen organic-rich black shales, enrichment factors (EFs) of redox-sensitive elements Mo, U and V (e.g., Algeo and Maynard, 2004; Algeo and Tribovillard, 2009; Tribovillard et al., 2012) and bio-essential nutrient elements Cu, Ni and P (e.g., Schenau et al., 2005; Tribovillard et al., 2006; Tyrrell, 1999) are employed here. If sedimentary $\delta^{66}\text{Zn}_{\text{bulk}}$ records are dominated by local marine redox states or marine productivity, a correlation between the $\delta^{66}\text{Zn}_{\text{bulk}}$ values and the EFs of redox-sensitive elements or bio-essential nutrient elements is expected. However, our data show no such correlations of $\delta^{66}\text{Zn}_{\text{bulk}}$ versus Mo_{EF} , U_{EF} and V_{EF} (Fig. 3), which indicates negligible local seawater redox control on the $\delta^{66}\text{Zn}_{\text{bulk}}$ patterns of both Yorkshire and Dotternhausen T-CIE samples. Further, the absence of systematic covariations of $\delta^{66}\text{Zn}_{\text{bulk}}$ versus Cu_{EF} , Ni_{EF} and P_{EF} (Fig. 3) implies a minimal

export productivity control on the two T-CIE sections' $\delta^{66}\text{Zn}_{\text{bulk}}$. These observations demonstrate that the perturbations of $\delta^{66}\text{Zn}_{\text{bulk}}$ values across the T-CIE interval are not simply controlled by the coeval basinal-scale marine redox or productivity conditions. Instead, the stratigraphic $\delta^{66}\text{Zn}_{\text{bulk}}$ patterns of the Yorkshire and Dotternhausen T-CIE sedimentary sections are more likely to be related to changes in the global deep-ocean Zn reservoir composition (see section 4.4). The positive $\delta^{66}\text{Zn}_{\text{bulk}}$ excursion for the T-CIE organic-rich black shale samples compared to the pre-T-CIE organic-lean grey shale samples may be caused by a joint control between expanded marine anoxia and/or elevated marine productivity which at the global scale accelerated the removal of light Zn isotopes onto the seafloor and enriched the seawater in ^{66}Zn .

4.2. Determination of the authigenic Zn isotope compositions for T-CIE organic-rich black shales

Considering the possible contamination from terrigenous-sourced Zn, obtaining authigenic Zn isotope composition (expressed by $\delta^{66}\text{Zn}_{\text{auth}}$) through lithogenic correction appears requisite. However, Zn enrichment in marine sediments is difficult to spot, which is unlike Mo. This is because the Zn abundance of the detrital background can be on the order of 10–100 $\mu\text{g/g}$, compared to approximately 1 $\mu\text{g/g}$ for Mo (McLennan, 2001; Rudnick and Gao, 2003), which may give rise to a large bias on the original $\delta^{66}\text{Zn}$ signal of the sediment authigenic component (cf. Vance et al., 2016). It follows that calculating $\delta^{66}\text{Zn}_{\text{auth}}$ values on a sample by sample basis using the traditional Zn–aluminum (Al) systematics (cf. Little et al., 2016) for the Yorkshire and Dotternhausen T-CIE organic-rich black shales seems irrational. To address this issue, this study alternatively used a cross-plot between $\delta^{66}\text{Zn}_{\text{bulk}}$ and Al/Zn (Fig. 4a; Vance et al., 2016). At Al/Zn = 0 on this cross-plot, the concentration of detrital indicator Al is set to be zero, meaning no detrital Zn contribution on the sediment authigenic Zn component (cf. Vance et al., 2016). Thus, $\delta^{66}\text{Zn}_{\text{auth}}$ records can be roughly represented by the intercept on y (here, $\delta^{66}\text{Zn}_{\text{bulk}}$)-axis (Fig. 4a; Vance et al., 2016). In this study, for organic-rich black shale samples of the Yorkshire and Dotternhausen T-CIE sections, the intercepts on y-axis are +0.54 ‰ and +0.63 ‰, respectively (Fig. 4a), which stand for the two sections' $\delta^{66}\text{Zn}_{\text{auth}}$ estimates.

4.3. The modern-like Zn geochemical cycling in the Early Toarcian ocean

In the modern ocean, surface-water $\delta^{66}\text{Zn}$ is spatially heterogeneous and is generally lower than that of the deep waters whose $\delta^{66}\text{Zn}$ is nearly homogeneous with an average of $+0.50 \pm 0.14$ ‰ (2 s.d.; Fig. 5; Conway and John, 2014, 2015; Isson et al., 2018). However, the response of $\delta^{66}\text{Zn}_{\text{auth}}$ for organic-rich sediments deposited in hydrographically open versus restricted marine environments to the homogeneous oceanic Zn inventory behaves discrepantly (Fig. 5; Isson et al., 2018; Little et al., 2016; Vance et al., 2016). Organic-rich sediments of the continental-margin oxygen minimum zone (OMZ) sites represent the only known sink for isotopically light Zn (Little et al., 2016; Vance et al., 2016). Their $\delta^{66}\text{Zn}_{\text{auth}}$ values are generally lighter than in the deep ocean by ~ 0.5 ‰ (Little et al., 2016). By contrast, organic-rich sediments accumulating underneath euxinic deep waters (i.e., in modern Black Sea and Cariaco Basin) favored by the hydrographic water-mass restriction feature heavy Zn isotope records (Fig. 5; Isson et al., 2018; Vance et al., 2016). Their $\delta^{66}\text{Zn}_{\text{auth}}$ values of $\sim +0.5$ to $+0.6$ ‰ are within uncertainty identical to that of the average deep-ocean composition. This observation is because in both Black Sea and Cariaco Basin sulfidic bottom waters the dissolved Zn fed from the outside open ocean 1) has the deficient concentration compared to hydrogen sulfide (H_2S), and 2) suffers near-quantitative removal through precipitation of highly stable Zn sulfide (ZnS) complex (Algeo and Tribouillard, 2009; Isson et al., 2018; Vance et al., 2016; Sweere et al., 2020). Therefore, in euxinic depositional settings, where Zn drawdown is (near-) quantitative, underlying organic-rich sedimentary $\delta^{66}\text{Zn}$ is expected to mirror the original isotope composition of the Zn source in deep seawater (analogous to Mo) (cf. Vance et al., 2016).

In this study, the Yorkshire and Dotternhausen T-CIE organic-rich black shales contain high total organic carbon (TOC) abundance of > 4 wt.% (Pearce et al., 2008; Röhl et al., 2001; Wang et al., 2020). Though their deposition was claimed to be in response to global ocean anoxia (e.g., Pearce et al., 2008; Thibault et al., 2018), a growing body of geochemical evidence has shown that they were in fact deposited in mutually separate, restricted environments (e.g., Dickson et al., 2017; McArthur et al., 2008; McArthur, 2019; Remírez and Algeo, 2020; Wang et al., 2021). Furthermore, the Yorkshire and Dotternhausen T-CIE organic-rich black shales display persistently high abundances of authigenic redox-sensitive elements (i.e., Mo, U, and V; Fig. 2) and green sulfur bacteria (GSB) biomarker (French et al., 2014; Frimmel et al., 2004; Schwark and Frimmel, 2004). This indicates that oxygen-depleted benthic water mass

containing aqueous H₂S has diffused into the photic zone in both the Cleveland Basin (Yorkshire coast) and the Southern German Basin (Dotternhausen quarry) during the T-CIE interval. Taken together, these T-CIE organic-rich sedimentary rocks accumulated under redox-stratified seawater conditions which splits the water column into thin oxic surface and thick euxinic bottom. Such restriction and redox nature for the Early Toarcian Cleveland Basin and Southern German Basin are visibly comparable to those of the modern analogs, i.e., Black Sea and Cariaco Basin which are restricted basins having aqueous H₂S in their bottom waters (Algeo and Tribovillard, 2009 and references therein). It follows that the $\delta^{66}\text{Zn}_{\text{auth}}$ records for the T-CIE euxinic organic-rich black shales from the Yorkshire coast of Cleveland Basin and the Dotternhausen quarry of Southern German Basin can reflect the coeval local deep seawater Zn isotope signal. Given the persistent existence of the authigenic Zn enrichment for the organic-rich sediments in both sedimentary sections through the entire T-CIE interval (Fig. 2), Zn replenishment into their depositional environments has to be dependent on water-mass renewal from a large Zn reservoir, i.e., open ocean. The contemporaneous local deep seawater Zn isotope signal (reflected by $\delta^{66}\text{Zn}_{\text{auth}}$) can thus stand for the global average deep-ocean composition. Here, the $\delta^{66}\text{Zn}_{\text{auth}}$ estimates for the T-CIE black shale samples of Yorkshire (+0.54 ‰) and Dotternhausen (+0.63 ‰) sections (Fig. 4) are indiscernible from that of the modern global deep water ($\delta^{66}\text{Zn}$: +0.50 ± 0.14 ‰: Conway and John, 2014, 2015; Isson et al., 2018). This finding therefore indicates that the Zn biogeochemical cycling in the Early Toarcian ocean during the T-CIE interval had overall reached the present-day level. By contrast, the Cenomanian-Turonian OAE 2 interval exhibiting very fluctuating global deep-ocean Zn isotope signals (~-0.09 to +0.85 ‰ with a mean of ~-0.33 ‰) due to ocean redox perturbations (Sweere et al., 2020) significantly differ from that of the modern ocean ($\delta^{66}\text{Zn}$: +0.50 ± 0.14 ‰: Conway and John, 2014, 2015; Isson et al., 2018). The difference in global deep-ocean $\delta^{66}\text{Zn}$ composition between the T-OAE (~183 Ma) and the OAE 2 (~94 Ma) further imparts a non-linear evolutionary trend for ocean Zn cycling over geologic time.

4.4. A short-lived ocean oxygenation recorded by a negative Zn isotope excursion?

Zinc itself is not redox-sensitive, but dissolved Zn has a high affinity for S ligands and is easily complexed by aqueous H₂S in sulfidic pore waters or seawater. The

Zn-H₂S complex preferentially incorporates light Zn isotope (Fujii et al., 2011), enriching the ambient microenvironments in ⁶⁶Zn, when removal is non-quantitative (Little et al., 2016; Sweere et al., 2020; Vance et al., 2016). This process widely exists in the modern continental-margin OMZ settings in which the formation of authigenic Zn sulfide in the underlying organic-rich sediments is suggested to be the driver of the present-day heavy isotope composition of deep seawater (cf. Little et al., 2016). On the other hand, Zn also has an affinity for oxic sediments (i.e., iron-manganese (Fe-Mn) (oxyhydr)oxides, carbonates) which display Zn isotope composition of 0.4–0.5 ‰ higher than that of the average deep ocean (Fig. 5; Little et al., 2014a, b; Pichat et al., 2003). The nearly homogeneous Zn isotope composition of the modern deep ocean is set by Zn balance between input and output fluxes to and from the ocean (cf. Conway and John, 2014; Sweere et al., 2020). The steady-state global ocean Zn cycle may be altered by changes in the input and output fluxes in concert with global environmental perturbations. A significant increase in Zn input flux into the ocean system from allochthonous Zn sources such as riverine discharge, hydrothermal fluids, eolian dust, all ≤ 0.3 ‰ (Fig. 5; Lemaitre et al., 2020; Little et al., 2016), can contribute to a decrease of the deep-ocean Zn isotope composition (cf. Sweere et al., 2018), and vice versa. Further, a substantial change in the proportion of Zn removal into the continental-margin OMZ organic-rich sediments and the oxic sediments that constitute the main Zn outputs in the modern ocean can also alter the deep-ocean δ⁶⁶Zn (cf. Sweere et al., 2018, 2020). Specifically, a relative increase in the removal flux of Zn from seawater into continental-margin organic-rich sediments compared to Zn burial in oxic sediments would cause a shift toward higher δ⁶⁶Zn values of the global ocean and vice versa.

To understand the possible existence of remarkable variations in deep-ocean δ⁶⁶Zn throughout the T-CIE interval, lithogenic-corrected δ⁶⁶Zn_{auth} of the studied Yorkshire and Dotternhauen T-CIE sedimentary rocks are theoretically required (see section 4.3). Considering the possible existence of a significant bias on calculated δ⁶⁶Zn_{auth} values (see section 4.2), this study alternatively employed a cross-plot between δ⁶⁶Zn_{bulk} and Al to evaluate the detrital contribution on the primary authigenic Zn isotope signals. A lack of any marked covariation between δ⁶⁶Zn_{bulk} and Al (Fig. 4b) indicates that the δ⁶⁶Zn_{bulk} values for the two T-CIE sections are actually controlled by the authigenic sedimentary Zn suffering negligible influence from detrital input. For the diagenetic limestone samples from the Dotternhausen section, the δ⁶⁶Zn_{bulk} directly represents

their $\delta^{66}\text{Zn}_{\text{auth}}$ signals due to their low Al concentrations (Wang et al., 2020). However, these diagenetic limestone $\delta^{66}\text{Zn}_{\text{bulk}}$ values can only be representative of the local-scale Zn cycling in the South German Basin rather than that of the global-scale deep ocean. Collectively, deep-ocean Zn-cycle perturbation trends, if present, during the T-CIE interval, can thus be reflected by organic-rich black shale $\delta^{66}\text{Zn}_{\text{bulk}}$ records, though its exact Zn isotope signature may not be mirrored.

The synchronous negative $\delta^{66}\text{Zn}_{\text{bulk}}$ excursion (see section 3.3) observed in the Yorkshire and Dotternhausen T-CIE stratigraphic profiles corresponds to distinct lithological facies that are black shales and a diagenetic limestone bed (Unterer Stein), respectively (Fig. 2). The observed negative $\delta^{66}\text{Zn}_{\text{bulk}}$ shift in organic-rich black shales of the Yorkshire section represents an oceanic Zn-cycle event. It is unlikely that the $\delta^{66}\text{Zn}_{\text{bulk}}$ drop results from an increasing input flux from allochthonous isotopically light Zn sources into the contemporaneous ocean. This is because there is no significant increase in the Zn/Al values during this short negative Zn isotope excursion interval (Fig. 2). Instead, the negative shift in $\delta^{66}\text{Zn}_{\text{bulk}}$ is most likely to be caused by one ocean oxygenation event which lead to a global decrease in the proportion of Zn removal into organic-rich continental-margin sediments relative to oxic sediments. Given the two sections' negative $\delta^{66}\text{Zn}_{\text{bulk}}$ excursion occurred concurrently, this ocean oxygenation may in part accelerate the delivery of electron acceptor (e.g., sulfate) onto sediment-seawater interface occurring in the South German Basin. This process may thus favor the formation of the diagenetic limestone bed (Unterer Stein) observed in the Dotternhausen section (Fig. 2). Its negative $\delta^{66}\text{Zn}_{\text{bulk}}$ shift may thus be related to the coeval decreased deep-ocean $\delta^{66}\text{Zn}$ or the basinal-scale released light Zn isotopes from organic matter remineralization during diagenesis, or both.

Short-lived ocean oxygenation events during the T-CIE interval have also been documented by ichnological records which have pointed out that episodic oxygen fluctuations indeed developed in basinal bottom waters of the Tethys Ocean and Panthalassa Ocean (Izumi et al., 2012; Fernández-Martínez et al., 2021; Rodríguez-Tovar, 2021). Nonetheless, the current uncertainty in the interpretation of the transient negative $\delta^{66}\text{Zn}_{\text{bulk}}$ excursion may be further improved by (i) providing detailed ichnological records for the Yorkshire and Dotternhausen T-CIE sedimentary sections, to better constrain short-term oxygen fluctuations; (ii) analyzing Zn isotope data for T-CIE sedimentary rocks from other sites, to complementarily constrain the coeval deep-ocean seawater $\delta^{66}\text{Zn}$ more accurately.

4.5. Zinc has a higher potential to track redox-driven ocean chemistry variation than Mo

The Mo isotope composition of euxinic organic-rich sediments is a widely used proxy to record global ocean Mo isotope signature in Earth's history (e.g., Cheng et al., 2016; Dickson et al., 2012; Goldberg et al., 2016; Kendall et al., 2017). However, caution should be exercised when using euxinic organic-rich sediment Mo isotopes to reconstruct the coeval seawater $\delta^{98}\text{Mo}$. At a threshold aqueous H_2S concentration of $> 11 \mu\text{M}$, almost all dissolved molybdate anion (MoO_4^{2-}) is converted to tetrathiomolybdate (MoS_4^{2-}) and quantitatively scavenged into the underlying sediment, yielding sediment $\delta^{98}\text{Mo}$ equal to that of the seawater source (Algeo and Lyons, 2006; Helz et al., 2011). When aqueous H_2S is below this threshold, incomplete transformation of MoO_4^{2-} to MoS_4^{2-} followed by non-quantitative Mo removal leads to a significant Mo isotope fractionation from the ambient seawater, which is recorded by the sediment (Poulson et al., 2006; Neubert et al., 2008). These two scenarios are well represented by the modern hydrographically restricted Black Sea and Cariaco Basin, respectively, in which the Mo supply to their sulfidic bottom water is mainly derived from the open ocean. Black Sea euxinic sediments carry the averaged global ocean $\delta^{98}\text{Mo}$ of $+2.34 \text{ ‰}$ due to the high H_2S abundance of $> 11 \mu\text{M}$ in its bottom water (Barling et al., 2001; Erickson and Helz, 2000; Neubert et al., 2008). By contrast, $\delta^{98}\text{Mo}$ records for euxinic sediments from Cariaco Basin are much lighter (mostly between 1 and 2 ‰) due to its low water column H_2S concentration (Arnold et al., 2004; Brüske et al., 2020; Helz et al., 1996). In addition to redox control, the lighter $\delta^{98}\text{Mo}$ for Cariaco Basin euxinic sediments may also arise from a local Fe–Mn (oxyhydr)oxides particulate shuttle which adsorbs and delivers a large fraction of light Mo isotopes to the sediment (cf. Scholz et al., 2017). Any paleo-approach attempting to identify a trigger for a shift to lighter Mo isotope values in organic-rich sediments needs to assess whether the particulate Mo delivery with Fe–Mn (oxyhydr)oxides can be ruled out. Otherwise, Mo isotope fractionation associated with this shuttle may disturb the determination of seawater redox variations. In this study, the incomparable Mo isotope in terms of authigenic values and stratigraphic trends for the Yorkshire and Dotternhausen T-CIE organic-rich sedimentary rocks (Fig. 2) cannot simultaneously reflect the coeval global ocean seawater chemical composition and variation. Instead, these Mo isotopic discrepancies are indicative of the existence of isotopic offset from the contemporaneous seawater, at least for one of the two sites. This Mo isotopic offset

between seawater and sediments can be related to low concentration of water-column H_2S ($< 11 \mu\text{M}$) and/or the operation of a local Fe–Mn (oxyhydr)oxide shuttle. Though the aqueous H_2S concentration is difficult to determine in the coeval depositional settings, the indeed presence of a local Fe–Mn (oxyhydr)oxide shuttle (Fig. 6; Algeo and Tribovillard, 2009) disallows the $\delta^{98}\text{Mo}$ interpretation to be a result of a global driver.

Authigenic Zn isotope for organic-rich sediments also has the capability of recording the global ocean isotope composition, if a fixed isotopic offset from seawater during Zn removal can be determined (Vance et al., 2016; Sweere et al., 2020; section 4.3). Lacking a net Zn isotope fractionation from seawater is expected in most sulfidic environments in which near-quantitative precipitation of dissolved Zn always occurs. This is in marked contrast to Mo since near-quantitative Zn removal only requires excess concentrations of aqueous H_2S relative to Zn (Sweere et al., 2020; Yan et al., 2018) instead of the H_2S abundance of $> 11 \mu\text{M}$. Furthermore, a local Fe–Mn (oxyhydr)oxide particulate shuttle, if present, does not significantly influence the Zn isotope composition of the authigenic components in the sediment, though preferentially adsorbed heavy Zn isotopes by this shuttle may be transported onto the seafloor. This is likely because most of dissolved Zn has been preferentially combined by aqueous H_2S , leaving insignificant Zn available for the adsorption onto Fe–Mn (oxyhydr)oxide particulates. The phenomenon is well expressed by the modern Cariaco Basin whose Zn supply mainly derives from the open ocean (i.e., Atlantic) deep waters (Isson et al., 2018). Near-quantitative Zn sequestration occurring in the Cariaco Basin renders the authigenic $\delta^{66}\text{Zn}$ of the underlying euxinic sediments capture the present-day deep ocean signature (Isson et al., 2018), regardless of the active operation of a Fe–Mn (oxyhydr)oxide shuttle (Algeo and Tribovillard, 2009). The scenario is further exhibited by this studied Early Toarcian Yorkshire and Dotternhausen organic-rich sedimentary rocks. They deposited in separate persistently euxinic environments and suffered distinct influence of local Fe–Mn (oxyhydr)oxide shuttling during the T-CIE interval (Fig. 6; Dickson et al., 2017; McArthur et al., 2008; McArthur, 2019; Wang et al., 2020), but still display comparable authigenic Zn isotope records and stratigraphic Zn isotope trends (Fig. 2). The observations imply that near-quantitative Zn removal with minimal isotopic effects between seawater and sediments easily occurs under excessive H_2S conditions.

Frequent redox perturbations in the ocean happen in Earth's history, which is characteristic of significantly changes in seawater Mo and Zn isotope compositions (e.g., Kendall et al., 2017; Sweere et al., 2018, 2020). Expanded oceanic anoxia leads to a secular decrease in isotope composition of Mo but increase in isotope composition of Zn in seawater and vice versa (e.g., Kendall et al., 2017; Sweere et al., 2018, 2020). Such oceanic redox variations are to date abundantly investigated by the use of authigenic Mo isotope records of organic-rich sedimentary rocks (e.g., Cheng et al., 2016; Dickson et al., 2012; Goldberg et al., 2016). Notably, if this redox-sensitive element removal from seawater into the sediment is non-quantitative owing to $< 11 \mu\text{M}$ H_2S concentration and/or is partly accelerated by an active operation of Fe–Mn (oxyhydr)oxide shuttle, the possibly resultant isotope fractionations may complicate the reliable explanation of the sediment authigenic Mo isotope compositions. In this instance, authigenic Zn isotope for such organic-rich sedimentary rocks may take this opportunity serving as an alternative proxy to trace the contemporaneous oceanic redox changes.

5. CONCLUSION

The $\delta^{66}\text{Zn}_{\text{bulk}}$ data for two Early Toarcian Yorkshire and Dotternhausen sedimentary sections deposited on the European epicontinental shelf are presented in this study. The $\delta^{66}\text{Zn}_{\text{bulk}}$ values for the T-CIE organic-rich samples are not controlled by local marine redox state or productivity, but are likely related to the global deep-ocean Zn reservoir composition. To better constrain the ocean Zn geochemical cycle during the T-CIE interval, the estimated $\delta^{66}\text{Zn}_{\text{auth}}$ values for the Yorkshire and Dotternhausen sections were determined ($\sim +0.54$ and $+0.62$ ‰, respectively) and found to be comparable to that of the modern global deep seawater ($+0.50 \pm 0.14$ ‰). This finding implies the Early Toarcian ocean overall had the present-day level of Zn biogeochemical cycling. Notably, a small negative $\delta^{66}\text{Zn}_{\text{bulk}}$ excursion concurrently occurred in both Yorkshire and Dotternhausen strata, and was interpreted to reflect an ocean oxygenation event. Sedimentary Mo isotope composition was also used to explore the global ocean redox variations during the T-CIE interval. However, the influence of an active Fe-Mn shuttle on the Mo isotope composition remains unclear, and might affect the effectiveness of this redox proxy. Near-quantitative aqueous Zn drawdown is inclined to occur under conditions where H_2S abundance exceeds that of

Zn, which is unlike Mo that needs a threshold H₂S concentration of > 11 μM to be quantitatively sequestered. This study puts forward that, relative to redox-sensitive Mo, Zn has a higher potential to track redox-driven changes in global ocean chemistry.

References

- Algeo, T.J. and Lyons, T.W., 2006. Mo–total organic carbon covariation in modern anoxic marine environments: Implications for analysis of paleoredox and paleohydrographic conditions. *Paleoceanography*, 21(1). <https://doi.org/10.1029/2004PA001112>.
- Algeo, T.J. and Maynard, J.B., 2004. Trace-element behavior and redox facies in core shales of Upper Pennsylvanian Kansas-type cyclothems. *Chemical geology*, 206(3-4), 289-318.
- Algeo, T.J. and Tribovillard, N., 2009. Environmental analysis of paleoceanographic systems based on molybdenum–uranium covariation. *Chemical Geology*, 268(3-4), 211-225.
- Arnold, G.L., Anbar, A.D., Barling, J. and Lyons, T.W., 2004. Molybdenum isotope evidence for widespread anoxia in mid-Proterozoic oceans. *Science*, 304(5667), 87-90.
- Barling, J., Arnold, G.L. and Anbar, A.D., 2001. Natural mass-dependent variations in the isotopic composition of molybdenum. *Earth and Planetary Science Letters*, 193(3-4), 447-457.
- Brüske, A., Weyer, S., Zhao, M.Y., Planavsky, N.J., Wegwerth, A., Neubert, N., Dellwig, O., Lau, K.V. and Lyons, T.W., 2020. Correlated molybdenum and uranium isotope signatures in modern anoxic sediments: implications for their use as paleo-redox proxy. *Geochimica et Cosmochimica Acta*, 270, 449-474.
- Caruthers, A.H., Gröcke, D.R. and Smith, P.L., 2011. The significance of an Early Jurassic (Toarcian) carbon-isotope excursion in Haida Gwaii (Queen Charlotte Islands), British Columbia, Canada. *Earth and Planetary Science Letters*, 307(1-2), 19-26.
- Cheng, M., Li, C., Zhou, L., Algeo, T.J., Zhang, F., Romaniello, S., Jin, C.S., Lei, L.D., Feng, L.J. and Jiang, S.Y., 2016. Marine Mo biogeochemistry in the context of dynamically euxinic mid-depth waters: a case study of the lower Cambrian Niutitang shales, South China. *Geochimica et Cosmochimica Acta*, 183, 79-93.
- Cohen, A.S., Coe, A.L., Harding, S.M. and Schwark, L., 2004. Osmium isotope evidence for the regulation of atmospheric CO₂ by continental weathering. *Geology*, 32(2), 157-160.
- Conway, T.M. and John, S.G., 2014. The biogeochemical cycling of zinc and zinc isotopes in the North Atlantic Ocean. *Global Biogeochemical Cycles*, 28(10), 1111-1128.
- Conway, T.M. and John, S.G., 2015. The cycling of iron, zinc and cadmium in the North East Pacific Ocean—Insights from stable isotopes. *Geochimica et Cosmochimica Acta*, 164, 262-283.

- Coplen, T.B., 2011. Guidelines and recommended terms for expression of stable-isotope-ratio and gas-ratio measurement results. *Rapid Communications in Mass Spectrometry*, 25(17), 2538-2560.
- Danise, S., Twitchett, R.J. and Little, C.T., 2015. Environmental controls on Jurassic marine ecosystems during global warming. *Geology*, 43(3), 263-266.
- Dahl, T.W., Canfield, D.E., Rosing, M.T., Frei, R.E., Gordon, G.W., Knoll, A.H. and Anbar, A.D., 2011. Molybdenum evidence for expansive sulfidic water masses in ~750 Ma oceans. *Earth and Planetary Science Letters*, 311(3-4), 264-274.
- Dickson, A.J. and Cohen, A.S., 2012. A molybdenum isotope record of Eocene Thermal Maximum 2: Implications for global ocean redox during the early Eocene. *Paleoceanography*, 27(3). <https://doi.org/10.1029/2012PA002346>.
- Dickson, A.J., Gill, B.C., Ruhl, M., Jenkyns, H.C., Porcelli, D., Idiz, E., Lyons, T.W. and van den Boorn, S.H., 2017. Molybdenum-isotope chemostratigraphy and paleoceanography of the Toarcian Oceanic Anoxic Event (Early Jurassic). *Paleoceanography*, 32(8), 813-829.
- Erickson, B.E. and Helz, G.R., 2000. Molybdenum (VI) speciation in sulfidic waters: stability and lability of thiomolybdates. *Geochimica et Cosmochimica Acta*, 64(7), 1149-1158.
- Fernández-Martínez, J., Rodríguez-Tovar, F.J., Piñuela, L., Martínez-Ruiz, F. and García-Ramos, J.C., 2021. Bottom-and pore-water oxygenation during the early Toarcian Oceanic Anoxic Event (T-OAE) in the Asturian Basin (N Spain): Ichnological information to improve facies analysis. *Sedimentary Geology*, 419. <https://doi.org/10.1016/j.sedgeo.2021.105909>.
- French, K.L., Sepúlveda, J., Trabucho-Alexandre, J., Gröcke, D.R. and Summons, R.E., 2014. Organic geochemistry of the early Toarcian oceanic anoxic event in Hawsker Bottoms, Yorkshire, England. *Earth and Planetary Science Letters*, 390, 116-127.
- Frimmel, A., Oschmann, W. and Schwark, L., 2004. Chemostratigraphy of the Posidonia Black Shale, SW Germany: I. Influence of sea-level variation on organic facies evolution. *Chemical Geology*, 206(3-4), 199-230.
- Fujii, T., Moynier, F., Pons, M.L. and Albarède, F., 2011. The origin of Zn isotope fractionation in sulfides. *Geochimica et Cosmochimica Acta*, 75(23), 7632-7643.
- Gill, B.C., Lyons, T.W. and Jenkyns, H.C., 2011. A global perturbation to the sulfur cycle during the Toarcian Oceanic Anoxic Event. *Earth and Planetary Science Letters*, 312(3-4), 484-496.
- Goldberg, T., Gordon, G., Izon, G., Archer, C., Pearce, C.R., McManus, J., Anbar, A.D. and Rehkämper, M., 2013. Resolution of inter-laboratory discrepancies in Mo isotope data: an intercalibration. *Journal of Analytical Atomic Spectrometry*, 28(5), 724-735.
- Goldberg, T., Poulton, S.W., Wagner, T., Kolonic, S.F. and Rehkämper, M., 2016. Molybdenum drawdown during cretaceous oceanic anoxic event 2. *Earth and Planetary Science Letters*, 440, 81-91.

- Helz, G.R., Bura-Nakić, E., Mikac, N. and Ciglencčki, I., 2011. New model for molybdenum behavior in euxinic waters. *Chemical Geology*, 284(3-4), 323-332.
- Helz, G.R., Miller, C.V., Charnock, J.M., Mosselmans, J.F.W., Patrick, R.A.D., Garner, C.D. and Vaughan, D.J., 1996. Mechanism of molybdenum removal from the sea and its concentration in black shales: EXAFS evidence. *Geochimica et Cosmochimica Acta*, 60(19), 3631-3642.
- Hesselbo, S.P., Gröcke, D.R., Jenkyns, H.C., Bjerrum, C.J., Farrimond, P., Bell, H.S.M. and Green, O.R., 2000. Massive dissociation of gas hydrate during a Jurassic oceanic anoxic event. *Nature*, 406(6794), 392-395.
- Hesselbo, S.P., Jenkyns, H.C., Duarte, L.V. and Oliveira, L.C., 2007. Carbon-isotope record of the Early Jurassic (Toarcian) Oceanic Anoxic Event from fossil wood and marine carbonate (Lusitanian Basin, Portugal). *Earth and Planetary Science Letters*, 253(3-4), 455-470.
- Howarth, M.K., 1973. The stratigraphy and ammonite fauna of the upper Liassic Grey Shales of the Yorkshire coast. *Bull. Br. Mus. Nat. Hist. Geol.*, 24, 235-277.
- Hu, S.Y., Evans, K., Rempel, K., Guagliardo, P., Kilburn, M., Craw, D., Grice, K. and Dick, J., 2018. Sequestration of Zn into mixed pyrite-zinc sulfide framboids: A key to Zn cycling in the ocean?. *Geochimica et Cosmochimica Acta*, 241, 95-107.
- Isson, T.T., Love, G.D., Dupont, C.L., Reinhard, C.T., Zumberge, A.J., Asael, D., Gueguen, B., McCrow, J., Gill, B.C., Owens, J. and Rainbird, R.H., 2018. Tracking the rise of eukaryotes to ecological dominance with zinc isotopes. *Geobiology*, 16(4), 341-352.
- Izumi, K., Kemp, D.B., Itamiya, S. and Inui, M., 2018. Sedimentary evidence for enhanced hydrological cycling in response to rapid carbon release during the early Toarcian oceanic anoxic event. *Earth and Planetary Science Letters*, 481, 162-170.
- Izumi, K., Miyaji, T. and Tanabe, K., 2012. Early Toarcian (Early Jurassic) oceanic anoxic event recorded in the shelf deposits in the northwestern Panthalassa: Evidence from the Nishinakayama Formation in the Toyora area, west Japan. *Palaeogeography, Palaeoclimatology, Palaeoecology*, 315, 100-108.
- Jenkyns, H.C., 1988. The early Toarcian (Jurassic) anoxic event; stratigraphic, sedimentary and geochemical evidence. *American Journal of Science*, 288(2), 101-151.
- Jenkyns, H.C., 2010. Geochemistry of oceanic anoxic events. *Geochemistry, Geophysics, Geosystems*, 11(3). <https://doi.org/10.1029/2009GC002788>.
- John, S.G. and Conway, T.M., 2014. A role for scavenging in the marine biogeochemical cycling of zinc and zinc isotopes. *Earth and Planetary Science Letters*, 394, 159-167.
- John, S.G., Geis, R.W., Saito, M.A. and Boyle, E.A., 2007. Zinc isotope fractionation during high-affinity and low-affinity zinc transport by the marine diatom *Thalassiosira oceanica*. *Limnology and Oceanography*, 52(6), 2710-2714.

- Kamber, B.S. and Schoenberg, R., 2020. Evaporative loss of moderately volatile metals from the superheated 1949 Ma Sudbury impact melt sheet inferred from stable Zn isotopes. *Earth and Planetary Science Letters*, 544. <https://doi.org/10.1016/j.epsl.2020.116356>.
- Kemp, D.B., Coe, A.L., Cohen, A.S. and Schwark, L., 2005. Astronomical pacing of methane release in the Early Jurassic period. *Nature*, 437(7057). <https://doi.org/10.1016/j.epsl.2020.116356>.
- Kemp, D.B., Coe, A.L., Cohen, A.S. and Weedon, G.P., 2011. Astronomical forcing and chronology of the early Toarcian (Early Jurassic) oceanic anoxic event in Yorkshire, UK. *Paleoceanography*, 26(4). <https://doi.org/10.1029/2011PA002122>.
- Kendall, B., Dahl, T.W. and Anbar, A.D., 2017. The stable isotope geochemistry of molybdenum. *Reviews in Mineralogy and Geochemistry*, 82(1), 683-732.
- Köbberich, M. and Vance, D., 2019. Zn isotope fractionation during uptake into marine phytoplankton: Implications for oceanic zinc isotopes. *Chemical Geology*, 523, 154-161.
- Kunzmann, M., Halverson, G.P., Sossi, P.A., Raub, T.D., Payne, J.L. and Kirby, J., 2013. Zn isotope evidence for immediate resumption of primary productivity after snowball Earth. *Geology*, 41(1), 27-30.
- Lemaitre, N., de Souza, G.F., Archer, C., Wang, R.M., Planquette, H., Sarthou, G. and Vance, D., 2020. Pervasive sources of isotopically light zinc in the North Atlantic Ocean. *Earth and Planetary Science Letters*, 539. <https://doi.org/10.1016/j.epsl.2020.116216>.
- Little, S.H., Sherman, D.M., Vance, D. and Hein, J.R., 2014a. Molecular controls on Cu and Zn isotopic fractionation in Fe–Mn crusts. *Earth and Planetary Science Letters*, 396, 213-222.
- Little, S.H., Vance, D., Lyons, T.W. and McManus, J., 2015. Controls on trace metal authigenic enrichment in reducing sediments: insights from modern oxygen-deficient settings. *American Journal of Science*, 315(2), 77-119.
- Little, S.H., Vance, D., McManus, J. and Severmann, S., 2016. Key role of continental margin sediments in the oceanic mass balance of Zn and Zn isotopes. *Geology*, 44(3), 207-210.
- Little, S.H., Vance, D., Walker-Brown, C. and Landing, W.M., 2014b. The oceanic mass balance of copper and zinc isotopes, investigated by analysis of their inputs, and outputs to ferromanganese oxide sediments. *Geochimica et Cosmochimica Acta*, 125, 673-693.
- Maréchal, C. and Albarède, F., 2002. Ion-exchange fractionation of copper and zinc isotopes. *Geochimica et Cosmochimica Acta*, 66(9), 1499-1509.
- McArthur, J.M., 2019. Early Toarcian black shales: A response to an oceanic anoxic event or anoxia in marginal basins?. *Chemical Geology*, 522, 71-83.

- McArthur, J.M., Algeo, T.J., Van de Schootbrugge, B., Li, Q. and Howarth, R.J., 2008. Basinal restriction, black shales, Re-Os dating, and the Early Toarcian (Jurassic) oceanic anoxic event. *Paleoceanography*, 23(4). <https://doi.org/10.1029/2008PA001607>.
- McElwain, J.C., Wade-Murphy, J. and Hesselbo, S.P., 2005. Changes in carbon dioxide during an oceanic anoxic event linked to intrusion into Gondwana coals. *Nature*, 435(7041), 479-482.
- McLennan, S.M., 2001. Relationships between the trace element composition of sedimentary rocks and upper continental crust. *Geochemistry, Geophysics, Geosystems*, 2(4). <https://doi.org/10.1029/2000GC000109>.
- Moeller, K., Schoenberg, R., Pedersen, R.B., Weiss, D. and Dong, S., 2012. Calibration of the new certified reference materials ERM-AE633 and ERM-AE647 for copper and IRMM-3702 for zinc isotope amount ratio determinations. *Geostandards and Geoanalytical Research*, 36(2), 177-199.
- Montero-Serrano, J.C., Föllmi, K.B., Adatte, T., Spangenberg, J.E., Tribovillard, N., Fantasia, A. and Suan, G., 2015. Continental weathering and redox conditions during the early Toarcian Oceanic Anoxic Event in the northwestern Tethys: Insight from the Posidonia Shale section in the Swiss Jura Mountains. *Palaeogeography, Palaeoclimatology, Palaeoecology*, 429, 83-99.
- Moynier, F., Vance, D., Fujii, T. and Savage, P., 2017. The isotope geochemistry of zinc and copper. *Reviews in Mineralogy and Geochemistry*, 82(1), 543-600.
- Nägler, T.F., Anbar, A.D., Archer, C., Goldberg, T., Gordon, G.W., Greber, N.D., Siebert, C., Sohrin, Y. and Vance, D., 2014. Proposal for an international molybdenum isotope measurement standard and data representation. *Geostandards and Geoanalytical Research*, 38(2), 149-151.
- Neubert, N., Nägler, T.F. and Böttcher, M.E., 2008. Sulfidity controls molybdenum isotope fractionation into euxinic sediments: Evidence from the modern Black Sea. *Geology*, 36(10), 775-778.
- Ogg, J.G. and Hinnov, L.A., 2012. Jurassic (Chapter 26). In: Gradstein, F.M., Ogg, J.G., Schmitz, M., Ogg, G. (eds.), *The Geologic Time Scale 2012*, Elsevier, Amsterdam, 731-791.
- Pálffy, J. and Smith, P.L., 2000. Synchrony between Early Jurassic extinction, oceanic anoxic event, and the Karoo-Ferrar flood basalt volcanism. *Geology*, 28(8), 747-750.
- Pearce, C.R., Cohen, A.S., Coe, A.L. and Burton, K.W., 2008. Molybdenum isotope evidence for global ocean anoxia coupled with perturbations to the carbon cycle during the Early Jurassic. *Geology*, 36(3), 231-234.
- Percival, L.M., Cohen, A.S., Davies, M.K., Dickson, A.J., Hesselbo, S.P., Jenkyns, H.C., Leng, M.J., Mather, T.A., Storm, M.S. and Xu, W., 2016. Osmium isotope evidence for two pulses

- of increased continental weathering linked to Early Jurassic volcanism and climate change. *Geology*, 44(9), 759-762.
- Pichat, S., Douchet, C. and Albarède, F., 2003. Zinc isotope variations in deep-sea carbonates from the eastern equatorial Pacific over the last 175 ka. *Earth and Planetary Science Letters*, 210(1-2), 167-178.
- Poulson, R.L., Siebert, C., McManus, J. and Berelson, W.M., 2006. Authigenic molybdenum isotope signatures in marine sediments. *Geology*, 34(8), 617-620.
- Remírez, M.N. and Algeo, T.J., 2020. Carbon-cycle changes during the Toarcian (Early Jurassic) and implications for regional versus global drivers of the Toarcian oceanic anoxic event. *Earth-Science Reviews*, 209. <https://doi.org/10.1016/j.earscirev.2020.103283>.
- Rodríguez-Tovar, F.J., 2021. Ichnology of the Toarcian Oceanic Anoxic Event: An underestimated tool to assess palaeoenvironmental interpretations. *Earth-Science Reviews*, <https://doi.org/10.1016/j.earscirev.2021.103579>.
- Rosca, C., Schoenberg, R., Tomlinson, E.L. and Kamber, B.S., 2019. Combined zinc-lead isotope and trace-metal assessment of recent atmospheric pollution sources recorded in Irish peatlands. *Science of the Total Environment*, 658, 234-249.
- Röhl, H.J., Schmid-Röhl, A., Oschmann, W., Frimmel, A. and Schwark, L., 2001. The Posidonia Shale (Lower Toarcian) of SW-Germany: an oxygen-depleted ecosystem controlled by sea level and palaeoclimate. *Palaeogeography, Palaeoclimatology, Palaeoecology*, 165(1-2), 27-52.
- Rudge, J.F., Reynolds, B.C. and Bourdon, B., 2009. The double spike toolbox. *Chemical Geology*, 265(3-4), 420-431.
- Rudnick, R.L., Gao, S., Holland, H.D. and Turekian, K.K., 2003. Composition of the continental crust. *The Crust*, 3, 1-64.
- Sælen, G., Tyson, R.V., Telnæs, N. and Talbot, M.R., 2000. Contrasting watermass conditions during deposition of the Whitby Mudstone (Lower Jurassic) and Kimmeridge Clay (Upper Jurassic) formations, UK. *Palaeogeography, Palaeoclimatology, Palaeoecology*, 163(3-4), 163-196.
- Schenau, S.J., Reichart, G.J. and De Lange, G.J., 2005. Phosphorus burial as a function of paleoproductivity and redox conditions in Arabian Sea sediments. *Geochimica et Cosmochimica Acta*, 69(4), 919-931.
- Scholz, F., Siebert, C., Dale, A.W. and Frank, M., 2017. Intense molybdenum accumulation in sediments underneath a nitrogenous water column and implications for the reconstruction of paleo-redox conditions based on molybdenum isotopes. *Geochimica et Cosmochimica Acta*, 213, 400-417.

- Schwark, L. and Frimmel, A., 2004. Chemostratigraphy of the Posidonia Black Shale, SW-Germany: II. Assessment of extent and persistence of photic-zone anoxia using aryl isoprenoid distributions. *Chemical Geology*, 206(3-4), 231-248.
- Siebert, C., Nägler, T.F., von Blanckenburg, F. and Kramers, J.D., 2003. Molybdenum isotope records as a potential new proxy for paleoceanography. *Earth and Planetary Science Letters*, 211(1-2), 159-171.
- Suan, G., Pittet, B., Bour, I., Mattioli, E., Duarte, L.V. and Mailliot, S., 2008. Duration of the Early Toarcian carbon isotope excursion deduced from spectral analysis: consequence for its possible causes. *Earth and Planetary Science Letters*, 267(3-4), 666-679.
- Svensen, H., Planke, S., Chevallier, L., Malthe-Sørensen, A., Corfu, F. and Jamtveit, B., 2007. Hydrothermal venting of greenhouse gases triggering Early Jurassic global warming. *Earth and Planetary Science Letters*, 256(3-4), 554-566.
- Sweere, T.C., Dickson, A.J., Jenkyns, H.C., Porcelli, D., Elrick, M., van den Boorn, S.H. and Henderson, G.M., 2018. Isotopic evidence for changes in the zinc cycle during Oceanic Anoxic Event 2 (Late Cretaceous). *Geology*, 46(5), 463-466.
- Sweere, T.C., Dickson, A.J., Jenkyns, H.C., Porcelli, D. and Henderson, G.M., 2020. Zinc- and cadmium-isotope evidence for redox-driven perturbations to global micronutrient cycles during Oceanic Anoxic Event 2 (Late Cretaceous). *Earth and Planetary Science Letters*, 546, <https://doi.org/10.1016/j.epsl.2020.116427>.
- Takashima, R., Nishi, H., Yamanaka, T., Tomosugi, T., Fernando, A.G., Tanabe, K., Moriya, K., Kawabe, F. and Hayashi, K., 2011. Prevailing oxic environments in the Pacific Ocean during the mid-Cretaceous Oceanic Anoxic Event 2. *Nature Communications*, 2(1), 1-5.
- Thibault, N., Ruhl, M., Ullmann, C.V., Korte, C., Kemp, D.B., Gröcke, D.R. and Hesselbo, S.P., 2018. The wider context of the Lower Jurassic Toarcian oceanic anoxic event in Yorkshire coastal outcrops, UK. *Proceedings of the Geologists' Association*, 129(3), 372-391.
- Tribovillard, N., Algeo, T.J., Baudin, F. and Riboulleau, A., 2012. Analysis of marine environmental conditions based on molybdenum–uranium covariation—Applications to Mesozoic paleoceanography. *Chemical Geology*, 324, 46-58.
- Tribovillard, N., Algeo, T.J., Lyons, T. and Riboulleau, A., 2006. Trace metals as paleoredox and paleoproductivity proxies: an update. *Chemical Geology*, 232(1-2), 12-32.
- Tyrrell, T., 1999. The relative influences of nitrogen and phosphorus on oceanic primary production. *Nature*, 400(6744), 525-531.
- Vance, D., Little, S.H., Archer, C., Cameron, V., Andersen, M.B., Rijkenberg, M.J. and Lyons, T.W., 2016. The oceanic budgets of nickel and zinc isotopes: the importance of sulfidic environments as illustrated by the Black Sea. *Philosophical Transactions of the Royal Society A*, 374. <http://dx.doi.org/10.1098/rsta.2015.0294>.

- Wang, Y., Ossa Ossa, F., Spangenberg, J.E., Wille, M. and Schoenberg, R., 2021. Restricted oxygen-deficient basins on the northern European epicontinental shelf across the Toarcian carbon isotope excursion interval. *Paleoceanography and Paleoclimatology*. <https://doi.org/10.1029/2020PA004207>.
- Wang, Y., Ossa Ossa, F., Wille, M., Schurr, S., Saussele, M.E., Schmid-Röhl, A. and Schoenberg, R., 2020. Evidence for local carbon-cycle perturbations superimposed on the Toarcian carbon isotope excursion. *Geobiology*, 18(6), 682-709.
- Weber, T., John, S., Tagliabue, A. and DeVries, T., 2018. Biological uptake and reversible scavenging of zinc in the global ocean. *Science*, 361(6397), 72-76.
- Wille, M., Nebel, O., Van Kranendonk, M.J., Schoenberg, R., Kleinhanns, I.C. and Ellwood, M.J., 2013. Mo–Cr isotope evidence for a reducing Archean atmosphere in 3.46–2.76 Ga black shales from the Pilbara, Western Australia. *Chemical Geology*, 340, 68-76.
- Xu, W., Ruhl, M., Jenkyns, H.C., Leng, M.J., Huggett, J.M., Minisini, D., Ullmann, C.V., Riding, J.B., Weijers, J.W., Storm, M.S. and Percival, L.M., 2018. Evolution of the Toarcian (Early Jurassic) carbon-cycle and global climatic controls on local sedimentary processes (Cardigan Bay Basin, UK). *Earth and Planetary Science Letters*, 484, 396-411.
- Yan, B., Zhu, X., He, X. and Tang, S., 2019. Zn isotopic evolution in early Ediacaran ocean: A global signature. *Precambrian Research*, 320, 472-483.

Figures and Figure Captions

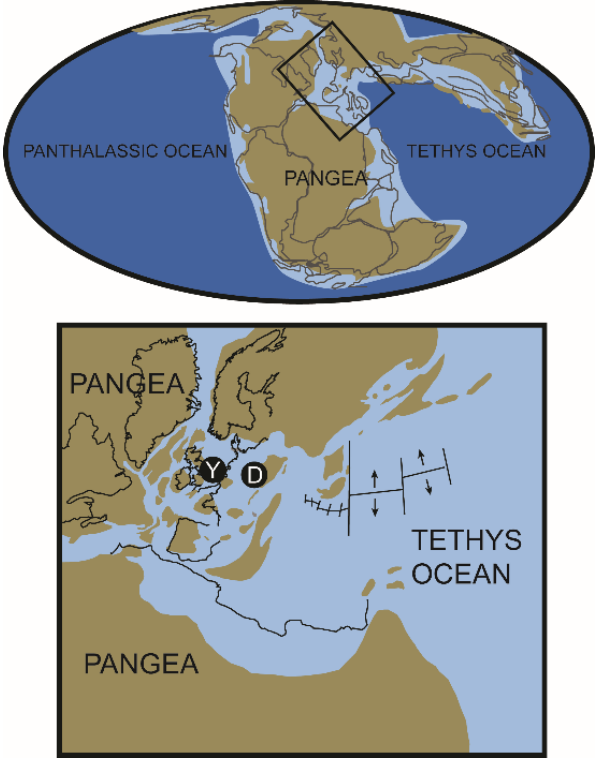


Figure 1. Paleogeographic maps for the Early Jurassic and the North European and Northwestern Tethyan regions specifically, after Gill et al. (2011) and Percival et al. (2016). Locations of this studied sample sites are noted as black circles: Yorkshire (Y), England and Dotternhausen (D), Germany.

Yorkshire

Dotternhausen

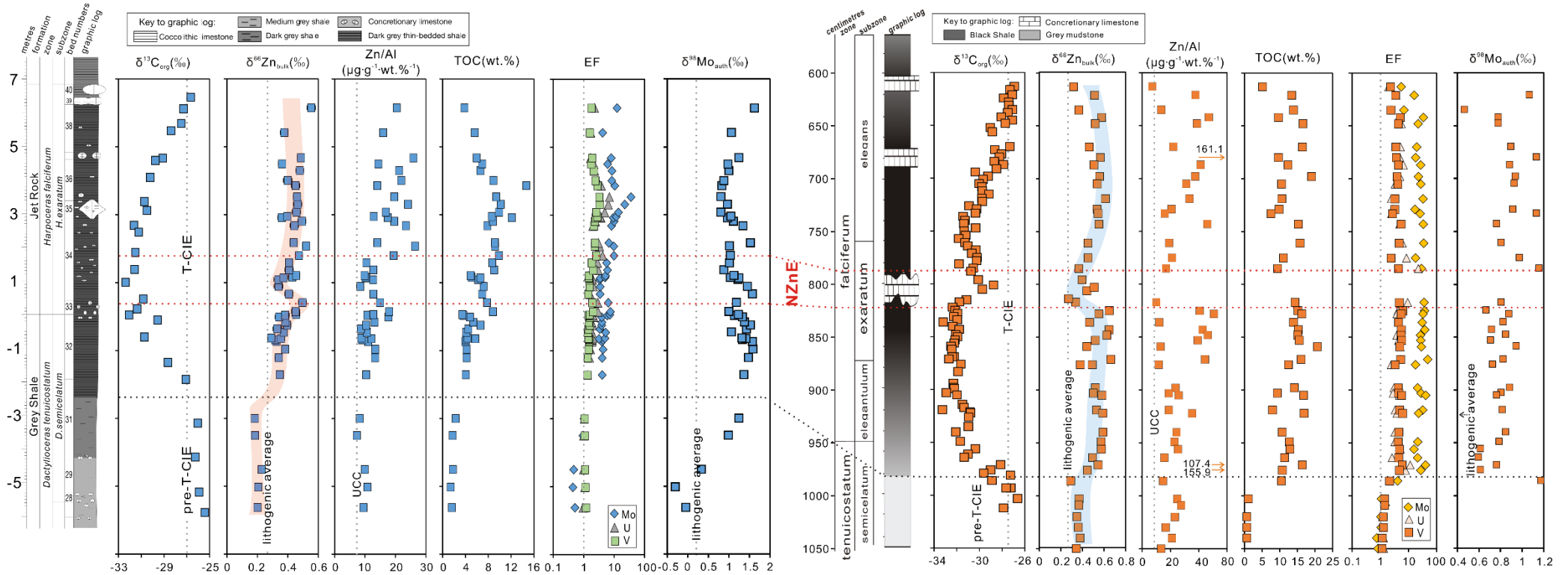


Figure 2. Chemostratigraphic $\delta^{13}C_{org}$, $\delta^{66}Zn_{bulk}$, Zn/Al, TOC content, enrichment factors (EFs) of Mo-U-V elements, and $\delta^{98}Mo_{auth}$ for the Yorkshire and Dotternhausen sedimentary sections throughout the pre-T-CIE and T-CIE intervals. The interval bracketed by two dashed red lines denotes the negative bulk Zn isotope excursion (NZnE). The $\delta^{13}C_{org}$, TOC and $\delta^{98}Mo_{auth}$ data for the Yorkshire samples are from Pearce et al. (2008).

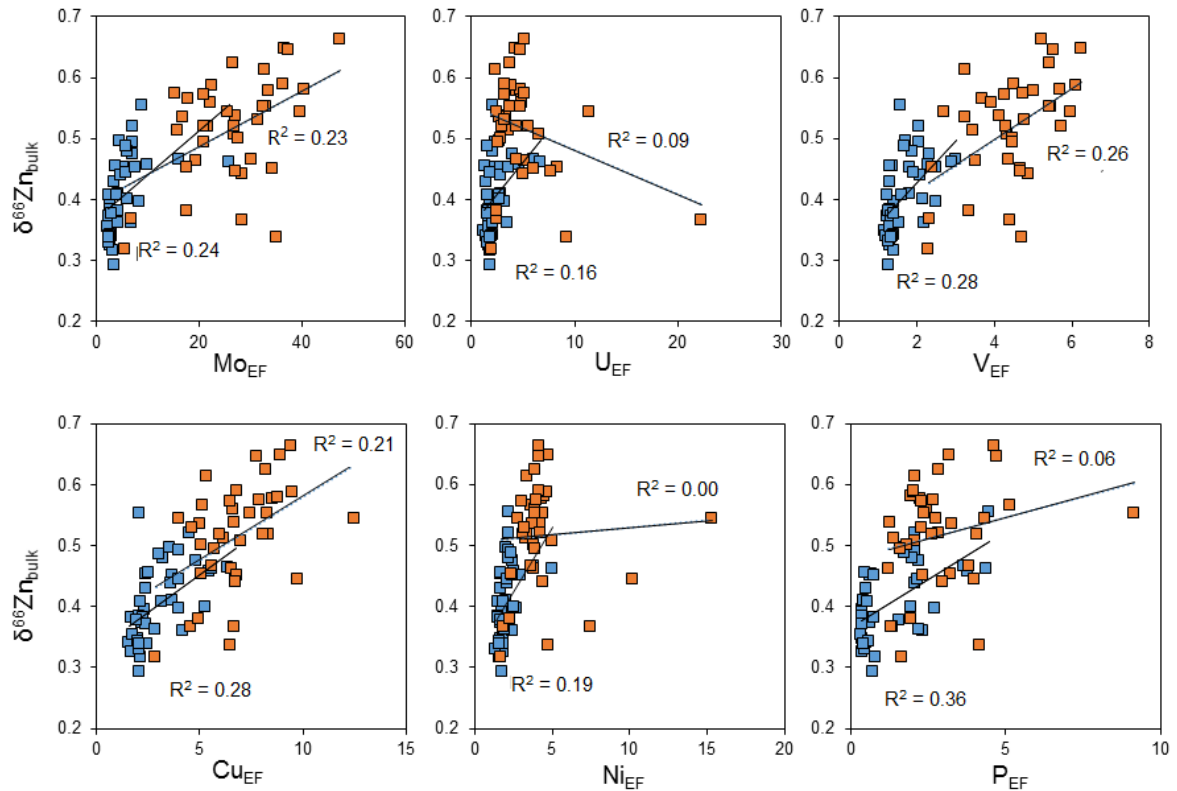


Figure 3. Cross-plots between $\delta^{66}\text{Zn}_{\text{bulk}}$ and enrichment factors (EFs) of redox-sensitive elements Mo, U and V, and bio-essential nutrient elements Cu, Ni and P for the Yorkshire (blue rectangles) and Dotternhausen (orange rectangles) T-CIE organic-rich black shale samples. The EF is calculated relative to upper continental crust (UCC; McLennan, 2001) using the equation of $[(\text{element}/\text{Al})_{\text{sample}}/(\text{element}/\text{Al})_{\text{UCC}}]$. R^2 represents the coefficient of the determination of the covariation.

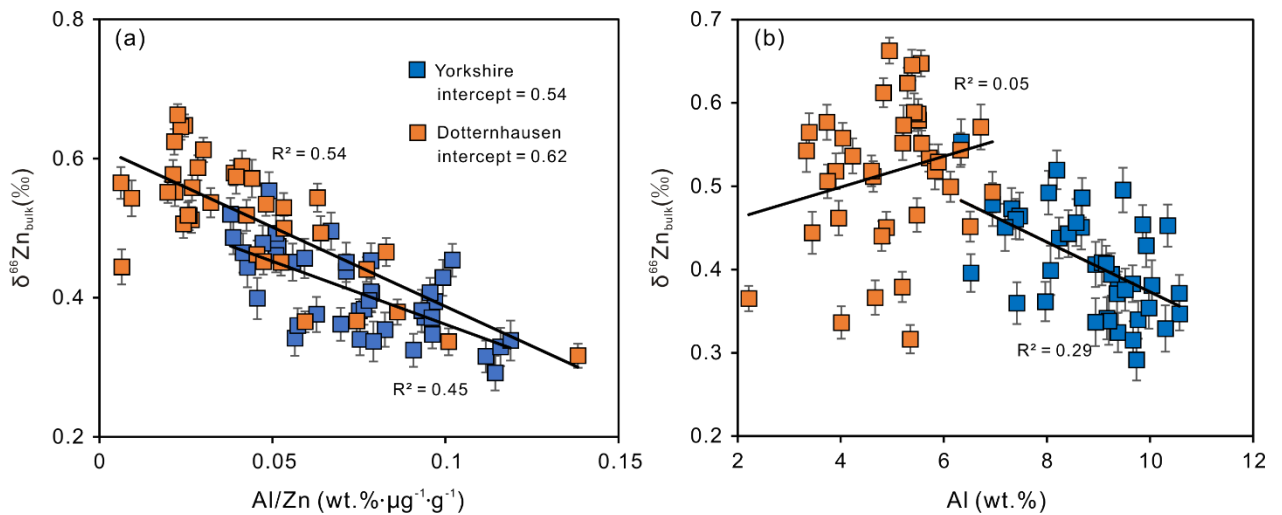


Figure 4. Cross-plots of (a) $\delta^{66}\text{Zn}_{\text{bulk}}$ versus Al/Zn and (b) $\delta^{66}\text{Zn}_{\text{bulk}}$ versus Al for Yorkshire and Dotternhausen T-CIE organic-rich black shale samples. In a, the intercepts at Al/Zn = 0 of correlation trends provide the $\delta^{66}\text{Zn}_{\text{auth}}$ estimates. R^2 represents the coefficient of the determination of the covariation.

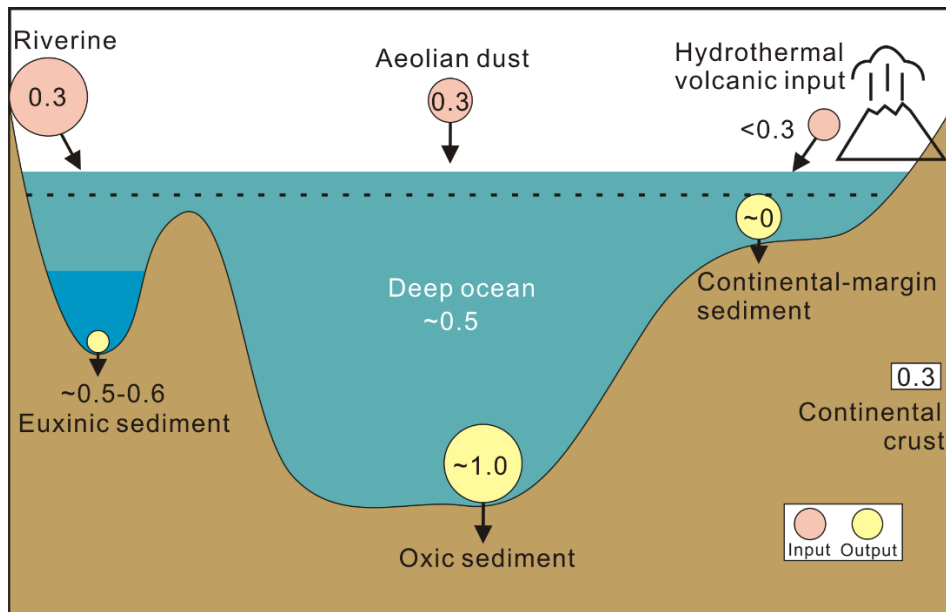


Figure 5. A sketch showing Zn inputs and outputs in the modern ocean (modified after Sweere et al., 2018). The associated Zn isotope systems are based on data from Conway and John (2014, 2015), Little et al. (2014b, 2016), Vance et al. (2016) and Isson et al. (2018). The size of circles stands for the relative Zn flux sizes, and numbers are their Zn isotope compositions in per mil (‰).

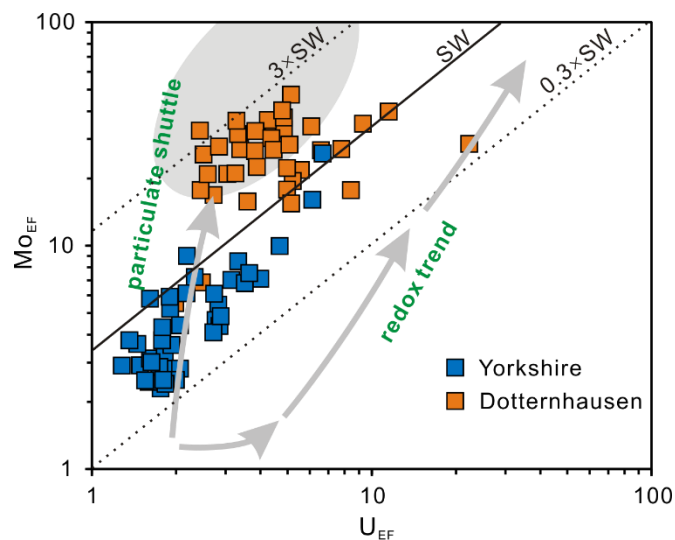


Figure 6. Cross-plots of Mo_{EF} versus U_{EF} for the Yorkshire and Dotternhausen organic-rich black shale samples. The seawater lines show Mo/U molar ratio equal to the seawater value (SW) and to multiples thereof ($3 \times SW$, $0.3 \times SW$). The pattern of Mo and U EFs is compared to the model behaviours proposed by Algeo and Tribouillard (2009). The Yorkshire and Dotternhausen samples obviously display evidence for the operation of an active particulate shuttle.

Table 1 $\delta^{66}\text{Zn}_{\text{bulk}}$ values for the Yorkshire and Dotternhausen samples, $\delta^{98}\text{Mo}$ and $\delta^{98}\text{Mo}_{\text{auth}}$ values for the Dotternhausen samples, and selected major-trace element concentrations for the Yorkshire samples

Dotternhausen					Yorkshire											
Depth [cm]	$\delta^{66}\text{Zn}_{\text{bulk}}$ (‰, JMC-L)	2 s.e.	$\delta^{98}\text{Mo}$ (‰)	$\delta^{98}\text{Mo}_{\text{auth}}$ (‰)	Name	Depth [m]	$\delta^{66}\text{Zn}_{\text{bulk}}$ (‰, JMC-L)	2 s.e.	Zn [$\mu\text{g/g}$]	Mo [$\mu\text{g/g}$]	U [$\mu\text{g/g}$]	V [$\mu\text{g/g}$]	Cu [$\mu\text{g/g}$]	Ni [$\mu\text{g/g}$]	P [wt.%]	Al [wt.%]
613	0.32	0.017	1.11	1.27	Tpa00-44	-12.07	0.18	0.019	103.5	0.7	3.1	158.7	38.0	75.4	0.030	11.56
621	0.51	0.018	1.03	1.07	Tte00-53	-8.07	0.17	0.024	121.9	0.7	3.4	158.6	36.4	71.3	0.061	10.57
635	0.37	0.021	0.46	0.47	Tte00-58	-5.62	0.20	0.022	106.2	0.8	3.5	157.6	35.3	65.7	0.030	11.20
642	0.58	0.021	0.77	0.78	Tte00-59	-5.02	0.20	0.019	115.1	0.6	3.8	144.9	34.6	64.2	0.039	10.68
648	0.52	0.021	0.76	0.78	Tse00-60	-4.5	0.23	0.021	108.8	0.7	3.6	144.8	29.4	78.1	0.027	11.00
670	0.46	0.021	0.87	0.90	Tse00-62	-3.5	0.18	0.020	77.5	1.4	3.5	136.3	38.8	71.3	0.032	10.63
680	0.56	0.023	1.10	1.14	Tse00-63	-3	0.18	0.022	87.1	1.5	3.7	134.9	37.4	75.1	0.034	10.56
687	0.51	0.020	0.87	0.89	Tse00-65	-1.71	0.35	0.020	110.0	5.7	4.7	166.7	66.1	99.9	0.034	10.57
698	0.56	0.018	0.92	0.94	Tse00-66	-1.21	0.34	0.023	129.7	5.3	5.0	157.7	47.9	90.1	0.045	9.77
705	0.54	0.021	0.91	0.93	Tse00-67	-1.0	0.38	0.0	124.9	5.5	5.3	163.8	49.8	93.8	0.033	9.38
719	0.61	0.018	1.20	1.23	TC05-C04	-0.73	0.32	0.024	103.3	5.0	5.8	165.6	50.6	95.0	0.031	9.38
729	0.53	0.016	0.89	0.92	TC05-C03	-0.68	0.32	0.023	86.6	5.7	6.1	181.0	65.6	87.3	0.067	9.67
733	0.54	0.020	1.11	1.14	Tse00-15	-0.65	0.35	0.025	120.9	4.3	6.1	176.7	56.1	103.3	0.031	9.98
743	0.55	0.020	0.76	0.77	TC05-C02	-0.63	0.29	0.025	85.2	6.5	6.5	165.0	63.0	94.7	0.060	9.74
761	0.45	0.019	0.80	0.81	Tse00-68	-0.46	0.37	0.022	112.4	7.5	6.5	174.0	73.5	97.9	0.059	10.57
775	0.45	0.018	0.95	0.98	TC05-C01	-0.36	0.33	0.028	88.9	4.7	5.7	175.2	67.9	77.3	0.041	10.30
785	0.37	0.015	1.13	1.16	Tse97-36	-0.25	0.39	0.025	95.4	4.9	5.9	173.9	68.3	91.5	0.031	9.25
796	0.39	0.019			TC05-B04	-0.16	0.38	0.022	126.4	5.2	5.9	170.0	63.8	83.8	0.033	9.66
801	0.48	0.021			TC05-B03	-0.01	0.34	0.025	162.2	4.8	6.6	172.0	58.6	82.3	0.046	9.16
805	0.44	0.021			TC05-B02	0.04	0.38	0.030	107.7	8.1	6.2	173.4	72.0	84.5	0.069	10.03
815	0.31	0.019			TC05-B01	0.06	0.45	0.025	131.8	10.1	6.8	192.7	78.4	97.8	0.061	10.34
817	0.34	0.019	0.80	0.81	Tex97-32	0.15	0.45	0.027	155.3	8.8	8.5	209.5	100.3	102.4	0.049	8.67
825	0.65	0.016	0.66	0.67	Tex 97-28	0.42	0.50	0.027	141.6	8.2	9.1	217.3	104.3	108.1	0.14	9.47
828	0.55	0.015	0.87	0.88	Tex00-13	0.67	0.41	0.027	113.7	4.2	4.8	150.3	61.0	76.2	0.032	8.94
836	0.47	0.020	0.82	0.83	TC05-A03	0.89	0.34	0.029	77.4	4.3	6.4	171.2	71.5	93.3	0.033	9.20
843	0.65	0.018	0.71	0.72	TC05-A02	1.09	0.34	0.029	112.9	4.0	5.7	162.9	58.8	81.6	0.033	8.94
848	0.62	0.018	0.83	0.85	Tex00-71	1.14	0.37	0.023	97.4	4.4	5.9	169.6	69.6	98.0	0.031	9.36
853	0.52	0.019	0.70	0.71	Tex00-14	1.16	0.43	0.026	100.0	6.7	5.0	172.8	75.3	91.0	0.044	9.92
859	0.44	0.018	0.93	0.95	TC05-A01	1.21	0.45	0.024	96.6	7.0	4.7	173.5	77.5	91.8	0.041	9.85
871	0.66	0.016	0.82	0.83	Tse97-08	1.38	0.41	0.027	115.5	7.4	9.0	220.1	104.0	100.2	0.035	9.07
876	0.38	0.018	0.71	0.73	Tex00-72	1.59	0.41	0.021	95.8	7.0	8.6	199.5	91.4	96.1	0.045	9.15
898	0.52	0.022	0.87	0.89	Tex01-02	1.8	0.47	0.025	141.7	9.71	10.2	226.4	110.2	100.9	0.14	7.31
903	0.50	0.018	0.80	0.81	Tex00-16	2.08	0.52	0.023	216.3	10.74	9.0	224.3	115.9	100.6	0.15	8.19
905	0.58	0.018	0.76	0.77	Tex00-73	2.18	0.44	0.025	115.5	7.45	8.3	230.1	92.2	96.7	0.15	8.24
919	0.53	0.021	0.81	0.82	Tex00-74	2.68	0.44	0.028	196.7	9.29	5.5	217.2	104.5	100.0	0.16	8.41
922	0.59	0.018	0.84	0.85	Tex06-01	2.81	0.49	0.026	157.4	10.85	6.5	222.5	100.4	97.7	0.15	8.03
940	0.59	0.023	0.77	0.79	Tex06-06	2.92	0.36	0.025	129.5	9.42	9.1	218.3	97.0	100.0	0.15	7.42
949	0.57	0.027	0.61	0.62	Tex06-08	2.95	0.40	0.023	83.8	10.37	7.6	216.6	81.8	96.9	0.15	6.52
956	0.57	0.024	0.59	0.60	Tex06-16	3.08	0.46	0.028	144.4	15.94	14.0	264.6	145.8	119.0	0.28	8.57
964	0.49	0.024	0.76	0.77	Tex97-27	3.31	0.46	0.028	180.1	22.40	15.9	299.2	147.5	156.7	0.24	7.47
971	0.54	0.026	0.61	0.62	Tex97-39	3.53	0.46	0.024	145.1	35.69	17.2	286.5	128.4	203.9	0.28	7.39
976	0.44	0.025	0.99	1.18	Tex06-28	3.86	0.45	0.028	100.8	10.1	9.1	241.2	151.7	118.2	0.047	7.19
986	0.29	0.021	1.46	---	Tex06-38	4.01	0.40	0.030	176.9	9.18	7.7	232.9	132.8	115.1	0.14	8.07
1003	0.37	0.025			Tex00-25	4.3	0.48	0.026	147.1	7.95	5.3	175.8	70.1	85.0	0.12	6.94
1009	0.37	0.024			Tex00-24	4.5	0.36	0.024	114.3	6.56	5.7	166.3	70.7	87.4	0.15	7.97
1020	0.35	0.020			Tex00-22	4.68	0.49	0.024	224.8	9.40	4.9	196.4	82.2	114.2	0.13	8.68
1030	0.36	0.020			Tex97-46	5.42	0.38	0.025	151.8	5.35	5.4	179.7	58.7	90.4	0.13	9.52
1040	0.38	0.022			Tex00-81	6.15	0.55	0.027	129.3	10.66	4.8	135.2	41.4	75.8	0.25	6.34
1050	0.34	0.022														

Internal precision of a sample run is reported as 2 standard error (2 s.e.).

Appendix D

Analytical methods

Yorkshire and Dotternhausen sample powders

Dotternhausen samples of this study include organic-lean gray shales (from the depth of 1,012 to 986 cm), organic-rich black shales (from the depth of 986 to 613 cm) and diagenetic limestones (Figure 1.2) at a high resolution with an average spacing of 3.5 cm. Outcrop samples were taken on a freshly quarried surface avoiding the long-term influence from surface weathering and contamination by vegetation. Powders of outcrop and drillcore samples were prepared using a diamondmounted driller and dried at 60°C for further analyses. Yorkshire sample powders including the organic-lean gray shales (from the depth of -12.07 to -3 m) and organic-rich black shales (from the depth of -1.71 to 6.15 m) samples (Figure 1.2) used in this study were prepared at The Open University (Pearce et al., 2008).

Elemental analyses

Major element analyses for Yorkshire and Dotternhausen samples

100 mg sample powders were mixed with 500 mg of Merck Spectromelt® A12 and were heated to 1,050 °C for 30 min using Oxiflux system to prepare homogeneous glass beads. These beads were then dissolved in polypropylene bottles using 100 g of ~2 % HNO₃ to a dilution factor of ~1,000 and then were diluted with 2 % M HNO₃ to obtain a final dilution factor of 1:150,000 for major element concentration measurement. Loss on ignition (LOI) was determined on a separate ~100 mg sample aliquot by the weight loss after 60 min of heating in a furnace at 1,050 °C. Analyses were carried out on a Thermo Fisher Scientific iCap-Qc quadrupole inductively coupled plasma mass spectrometer (Q-ICP-MS) using a similar experimental design as described in detail below for the trace element determinations. Calibration for sample unknowns used the powder reference materials W-2a (United States Geological Survey; USGS) prepared as above and using the major element values reported in Govindaraju and Roelandts (1989). Secondary quality control standards were also prepared from the international reference materials (QS-1, OU-6, SCo-1, and AGV-2), and the precision range of major elements relative to the recommended values from

GeoReM. Data are reported as elemental concentrations expressed in weight percent (wt.%), and generally, uncertainties for major elements are better than 1 wt.% (1σ).

Trace element analyses for Dotternhausen and Yorkshire samples

~200 mg of dried powder materials was weighted and ashed in a furnace at 500 °C for 15 hr to oxidize organic matter. These ashed sample powders were re-weighed immediately upon cooling to determine the loss of weight during the ashing process. ~25 mg of ashed powders was weighed and digested in a 4 ml (4:1) HF-HNO₃ volumetric mixture on hot plates at 120 °C for 2 days. Following digestion, the dissolved sample mixtures were evaporated, and the residues were reacted with 2 ml 6 m HCl at 120 °C for 24 hr to dissolve potential fluorides. Upon drying the samples, they were taken up in 1 ml 14.5 m HNO₃, heated to 120 °C for 1 hr and dried again to volatilize excess fluorine and chlorine. This last step was repeated to ensure full conversion of the samples to nitric form. The samples were then taken up in 1 ml 5 m HNO₃ and gravimetrically diluted to ~30 ml 2 % HNO₃ stock solutions with a nominal dilution factor of ~1,000. Powders of rock reference materials used for calibration and quality control were also digested using this procedure. For analyses, all stock solutions were then further diluted with 2 % HNO₃ to a nominal, gravimetric dilution factor of ~10,000. This 2 % HNO₃, as an internal standard during ICP-MS analysis, contains a mixed spike of ⁶Li (~3 ng/g), In (~1 ng/g), Re (~1 ng/g), and Bi (~1 ng/g). All samples were measured using a Thermo Fisher Scientific iCap-Qc ICP-MS coupled to an ESI SC-2 DX autosampler with an ESI Fast uptake system equipped with a 4 ml sample loop. All sample liquids were introduced from the loop using the iCap-Q peristaltic pump (at 30–35 rpm) and aspirated with a PFA nebulizer into a Peltier-cooled cyclonic spray chamber. The nebulizer and cool gas flow rates were typically ~1 and 14 L/min, respectively, and the interface was configured with Ni sampler cone, with a Cu core and Ni skimmer cone with a high-matrix insert.

The analytical procedure was analogous to that described in previous studies (Albut et al., 2018; Babechuk et al., 2015; Kamber et al., 2014). Oxide/hydroxide interference rates of Ba on Eu, Nd on the MREE to HREE (Gd, Tb, Dy, Er), Zr, on Ag, and the isobaric overlap of ¹⁶⁰Dy on ¹⁶⁰Gd were quantified ahead of each experiment. Remaining interference “rates” were determined according to a previous quantification scaled to the daily Nd oxide on Gd production rate (Aries et al., 2000; Ulrich et al., 2010). A daily measurement of the ⁶Li/⁷Li ratio in unspiked USGS standard AGV-2 was

also applied to determine a correction factor for the contribution of natural ^6Li in sample unknowns. Experimental sequences contained measurements of the internal standard-bearing carrier acid, procedural blanks, rock calibration (W-2a), and quality control standard (OU-6, QS-1, BCR-2, BHVO-2, BIR-1, and IF-G), sample unknowns, and a final batch of standards. Repeated measurement of a monitor solution (mixture of dissolved rock standards) was made every 5–7 samples for external drift correction remaining after internal standard spike correction. Following the introduction of each sample liquid into the ICP-MS, the sample uptake probe and tubing were rinsed with 5 % HNO_3 . Additional washing with acid blank bracketed monitor samples or was placed between samples known or expected to have contrasting matrices or analyte abundance. In the course of experiments, analyte isotopes were measured in the iCap-Q STD mode, typically with five repeats of 25–30 sweeps at 3 channels (0.1 amu spacing) and analyte dwell times ranging from 10–30 ms. Mean analyte intensities were corrected offline for blank, isobaric interferences, and signal drift. Corrected intensities were calibrated using the average response of repeated measurements (5–8) of the USGS reference material W-2a at different dilution factors (~10,000, ~20,000, and ~40,000), which was prepared from at least three separate powder digestions. The calibration lines that show tighter ranges were constructed using the laboratory's preferred analyte concentrations for the W-2a standard. The overall intermediate method precision and accuracy are monitored using the repeated measurements of reference materials (OU-6, QS-1, BCR-2, BHVO-2, BIR-1, and IF-G), representing a range in analyte concentrations and sample matrices. The method precision, estimated from the 1 r.s.d of the mean, is better than 3 % for most elements.

Analyses of TOC and carbonate contents for Dotternhausen samples

Powdered mudstone and shale samples was decarbonized in 15-ml centrifuge tubes by drop-wise addition of 16 % HCl at room temperature to remove all inorganic carbon (TIC). The residual samples were then centrifuged for 10 min at 246 g, decanted and again mixed with approximately 10 ml Milli-Q H_2O . This procedure was repeated 7–10 times until the samples were neutralized. Upon complete drying of the samples, between 5 and 70 mg of decalcified samples were weighed into tin-capsules. TOC concentrations were performed with a VARIO EL Elemental Analyzer at Center for Applied Geosciences, University of Tuebingen. Acetanilide standard ($\text{C}_8\text{H}_9\text{NO}$, 71.9 % Carbon, 10.36 % Nitrogen) was analyzed at the beginning, middle, and end of each

sample set. All the measured TOC contents were reported as a weight percent (wt.%) of the total fraction, and the external reproducibility is better than 1 wt.% (1σ). Decalcifying procedures refer to organic carbon isotopic analysis (see below). For the carbonate content measurement, the treatment procedures for the studied samples are described below for $\delta^{13}\text{C}_{\text{carb}}$. An almost perfect linear correlation ($R^2 = 0.9917$) between samples weight (for samples between 10 and 150 mg CaCO_3) and the 2nd peak area on the Finnigan MAT 252 gas source mass spectrometer (for further details see Spötl and Vennemann, 2003) allows for the calculation of the carbonate content in each specific sample. These calculated carbonate contents were then divided by total sample weights and multiplied with 100 to obtain the carbonate contents of the bulk samples in %.

Bulk isotopic analyses

Carbon and oxygen isotope compositions for Dotternhausen samples

Carbonate fractions of the selected Dotternhausen samples were measured for their carbon and oxygen isotope compositions using a Finnigan MAT 252 gas source mass spectrometer combined with a Thermo-Finnigan Gasbench II/CTC Combi-Pal autosampler at the Isotope Geochemistry Laboratory, University of Tuebingen. Both devices are connected using the continuous flow technique with a He stream as carrier gas. ~50 mg gray mudstone and shale powders, and ~5 mg diagenetic limestone powders were loaded into 10-ml glass vials, sealed with a rubber septum. The vials were then placed in an aluminum tray and heated to 90 °C. 20 drops of 99 % phosphoric acid were added into the vials, after purging them with pure He gas. After 90 min' reaction time, the released CO_2 was transferred to the mass spectrometer using a He carrier gas via a GC gas column to separate other components. The collected CO_2 was analyzed relative to international reference materials (NBS18 and NBS19) and an internal laboratory tank gas standard, which was calibrated against the in-house Lasser marble reference material. All measured values are given in per mille (‰) notation relative to the Vienna PeeDee belemnite standard reference material (VPDB) for $\delta^{13}\text{C}$ and VPDB for $\delta^{18}\text{O}$. They are thus defined as: $\delta^{13}\text{C} = ((^{13}\text{C}/^{12}\text{C})_{\text{sample}}/(^{13}\text{C}/^{12}\text{C})_{\text{VPDB}} - 1) \times 1000$ and $\delta^{18}\text{O} = ((^{18}\text{O}/^{16}\text{O})_{\text{sample}}/(^{18}\text{O}/^{16}\text{O})_{\text{VPDB}} - 1) \times 1000$. The repeatability and intermediate precision of the analyses were monitored by replicate measurements of the laboratory standard Lasser marble and the NBS18

($\delta^{13}\text{C}_{\text{carb}} = -5 \text{ ‰}$, $\delta^{18}\text{O} = -22.96 \text{ ‰}$) and NBS19 ($\delta^{13}\text{C}_{\text{carb}} = 1.95 \text{ ‰}$, $\delta^{18}\text{O} = -2.20 \text{ ‰}$). All analyzed results have a reproducibility of $\pm 0.1 \text{ ‰}$ (1σ) for both $\delta^{13}\text{C}_{\text{carb}}$ and $\delta^{18}\text{O}$.

Analyses of $\delta^{13}\text{C}_{\text{org}}$ were conducted on an Elemental Analyzer NC2500 connected to a Thermo Quest Delta Plus XL mass spectrometer in continuous flow online-mode at the Isotope Geochemistry Laboratory, University of Tuebingen. ~100 mg of sample powders was decalcified in 15-ml centrifuge tubes by drop-wise addition of 16 % HCl to remove TIC. Decalcified samples containing 0.05 mg carbon were weighed in tin capsules and combusted at 1,050 °C in an oxidation tube and at 650 °C in a reduction tube, before they were cooled in a watertrap and transferred through a GC gas column into the mass spectrometer. Sample organic carbon was measured relative to an internal acetanilide standard which is calibrated against an in-house (e.g., Laaser marble) and international reference material (USGS24, $\delta^{13}\text{C}_{\text{org}} = -16.00 \text{ ‰}$). $\delta^{13}\text{C}_{\text{org}}$ results have an external reproducibility of $\pm 0.1 \text{ ‰}$ (1σ) for shales and $\pm 0.2 \text{ ‰}$ (1σ) for limestones.

Nitrogen data for Dotternhausen samples

To avoid potential influence from weathered materials and any handling contamination, we cut the collected sedimentary rock samples into 2-cm-thick slabs with a water-cooled saw. The slabs were cleaned and then rinsed by distilled water and analytical grade and glass distilled ethanol and dichloromethane, respectively. Following preparing the cleaned sample slabs, they were dried at 50 °C for 1 day, and then fragmented and powdered using an agate mill. The obtained sample powders were subsequently analyzed for $\delta^{15}\text{N}_{\text{bulk}}$ and $\delta^{15}\text{N}_{\text{ker}}$, and $\delta^{13}\text{C}$ for organic carbon and extracted kerogen ($\delta^{13}\text{C}_{\text{org}}$ and $\delta^{13}\text{C}_{\text{ker}}$) at the laboratory of the Institute of Earth Surface Dynamics (IDYST), University of Lausanne. The analytical procedure is based on the previous description provided by Spangenberg and Frimmel (2001), Spangenberg and Herlec (2006), and Spangenberg and Macko (1998).

The measurement of all C and N data was carried out by combined elemental analyser (Carlo Erba 1108; Milan, Italy) and isotope ratio mass spectrometry (Delta V Plus; Thermo Fisher Scientific, Bremen, Germany) (EA-IRMS) under a continuous helium flow condition through a ConFlo III open split interface (cf. Spangenberg et al., 2006, 2014). For TOC, total nitrogen (TN), $\delta^{13}\text{C}_{\text{org}}$, and $\delta^{15}\text{N}_{\text{bulk}}$ analyses, powdered whole rock materials were treated by a drop-wise addition of 10 % HCl. For the analyses of N_{ker} , $\delta^{13}\text{C}_{\text{ker}}$, and $\delta^{15}\text{N}_{\text{ker}}$, powdered whole rock samples were gradually

treated to extract the kerogen fraction that cannot be dissolved in organic solvents, non-oxidizing acids and bases. On the basis of the kerogen extraction procedure described by Durand and Nicaise (1980), this study used Soxhlet extraction method in which mixed methanol and dichloromethane were added to remove bitumen (a soluble fraction in OM), 6 M HCl was added to remove carbonate, sulfide, sulfate, and (hydro)oxide, and a mixed acid composed of 40 % HF and 6 M HCl was added to remove siliciclastic fraction. These stepwise treatments were all carried out at the temperature of 65–70 °C, and were accelerated through using a PTFE-coated magnetic stirrer. After removing the supernatant, the residues were thoroughly washed and purified using deionized water and ultrapure water produced by Direct-Q UV3 Millipore®, respectively, and then dried at the temperature of 40 °C. Following drying the solid residues, mineralogical analysis performed by a Thermo Scientific ARL X-TRA Diffractometer showed that all the silicate fraction in the whole rock samples has been removed completely.

The measured stable N isotope composition is reported using delta (δ) notation in per mil relative to its standard which is atmospheric nitrogen in the air (Air-N₂). It is thus defined as: $\delta^{15}\text{N} = ((^{15}\text{N}/^{14}\text{N})_{\text{sample}} / (^{15}\text{N}/^{14}\text{N})_{\text{Air-N}_2} - 1) \times 1000$. In this study almost all N isotope data were performed in duplicate, and the analytical reproducibility of the repeated sample measurements for the N isotope values conducted by the EA-IRMS was better than ± 0.3 %. The TOC abundance for the whole-rock samples, and the abundance of the TN_{bulk} for whole-rock samples and of N_{ker} for kerogen extracts were obtained from the peak areas of the major isotopes through the use of the calibrations for the $\delta^{13}\text{C}_{\text{org}}$, $\delta^{15}\text{N}_{\text{bulk}}$, and $\delta^{15}\text{N}_{\text{ker}}$ values, respectively. The analytical repeatability was better than ± 0.2 wt.% for the contents of TOC, TN_{bulk} and N_{ker}.

Molybdenum isotope compositions for Dotternhausen samples

The measurement of bulk Mo isotope for the Dotternhausen samples followed the method described by Wille et al. (2013). Sedimentary rock samples were ashed for 15 hr at 500 °C to oxidize organic matter fraction. An adequate amount of a ¹⁰⁰Mo-⁹⁷Mo double spike was added to 50-500 mg powdered sample material prior to sample digestion and Mo-purification. The double-spike method allows for the correction of the instrumental mass bias as well as mass fractionation that may occur in the process of chromatographic Mo-purification (Rudge et al., 2009). Samples were dissolved in Teflon beakers by sequential digestion steps using distilled HF, HNO₃ and HCl acids.

Mo was purified using a combination of anion and cation exchange chromatography (i.e., using Dowex 1x8, 200-400 mesh and Dowex 50WX8 200-400 mesh resins, respectively) as described by Wille et al. (2013). Molybdenum isotopic ratios were measured on a multi-collector ICP-MS (ThermoFisher Scientific NeptunePlus) at the University of Tuebingen. Measurements of the in-house standard ZH-2, a Mo-rich sulfide that ran through all chemical separation steps, yield a long-term reproducibility on $\delta^{98}\text{Mo}$ better than 0.09 ‰ (2σ). Results were calibrated using the Johnson Matthey ICP standard, and are reported in the σ -notation relative to the NIST3134 standard (Goldberg et al., 2013), which was set to 0.25 ‰ for better comparison with earlier published data (Nägler et al., 2014):

$$\delta^{98}\text{Mo} = 1.0025 \times ((^{98}\text{Mo}/^{95}\text{Mo})_{\text{sample}}/(^{98}\text{Mo}/^{95}\text{Mo})_{\text{NIST3134}} - 1)$$

where δ is expressed in ‰ by multiplication with a factor of 1000.

Zinc isotope compositions for Yorkshire and Dotternhausen samples

For the Zn isotope analyses, fine-grained rock powder was weighted into Teflon beakers and admixed with appropriate amounts of purified ^{64}Zn – ^{67}Zn double spike (DS) isotope tracer solution (in 1 mol L⁻¹ HNO₃) to achieve a DS proportion of 0.6 to the total amount of Zn in the mixture (Moeller et al., 2012). Samples were digested through adding 3 mL of concentrated HF–HNO₃ at a 3:1 ratio and placing the closed beakers on hot plates at 110 °C for 48 hr. Samples were then taken to dryness, refluxed in 2 mL of 6 M HCl and placed on hot plates at 120 °C for 24 hr to dissolve fluorides and convert the samples to chloride form. Samples were dried again and taken up in 1 mL 6 M HCl for chemical separation of Zn. Ion chromatographic purification of Zn was completed using 2 mL of 100–200 mesh BioRad DOWEX AG1X8 anion exchange resin in SpectraChrom columns, followed by smaller columns containing 0.3 mL of the same resin for 2nd purification step. The Zn purification procedures employed in this study followed the protocol of Moeller et al. (2012). The DS technique allows in-run correction of the instrumental mass bias, and account for chemical Zn isotopic fractionation effects caused by anion-exchange chromatography (Maréchal et al., 1999). Zinc isotope ratio determinations were performed in medium-resolution mode on a ThermoFisher Scientific NeptunePlus MC-ICP-MS housed at the Isotope Geochemistry laboratories of the Department of Geosciences, University of Tuebingen. Sample uptake by a Cetac ARIDUS II desolvating nebulizer system without

N₂ purging minimised potential polyatomic oxide and nitride interferences, while yielding improved atom-to-ion conversion and ion beam stability compared to standard ‘cold spray’ uptake systems. For reporting Zn isotopic data, this study followed the guidelines by Coplen (2011), based on the recommendations by the Commission on Isotopic Abundances and Atomic Weights of the International Union of Pure and Applied Chemistry that are widely consistent with the *Système International d’Unités*. Sample Zn isotopic compositions were measured as the ‰-differences of their ⁶⁶Zn/⁶⁴Zn isotope abundance ratios relative to that of the isotopically certified reference material IRMM-3702 in δ-values. The data were then recalculated to the no longer available ‘JMC-Lyon’ standard solution as δ-zero anchor by applying an offset of +0.29 ‰ on δ⁶⁶Zn/⁶⁴Zn_{IRMM-3702} values (Moeller et al., 2012). For ease of reference and comparison to previous Zn isotopic studies we report δ⁶⁶Zn_{JMC-L} values in Table 1 (Appendix C) according to the following equations, and work with the δ⁶⁶Zn_{JMC-L} values throughout the text and in the figures:

$$\delta^{66}\text{Zn}_{\text{JMC-L}} = 1.0029 \times ((^{66}\text{Zn}/^{64}\text{Zn})_{\text{sample}} / (^{66}\text{Zn}/^{64}\text{Zn})_{\text{IRMM-3702}} - 1)$$

where δ is expressed in ‰ by multiplication with a factor of 1000.

The reproducibility for δ⁶⁶Zn on the IRMM-3702 throughout all analytical sessions during the course of this study was always better than 0.035 ‰ (2 s.d.; 0.017–0.031 ‰). Accuracy was controlled by interleaved analysis of an in-house solution standard prepared from an Alfa Aesar Puratronic Zn wire yielding an average δ⁶⁶Zn_{JMC-L} of -9.983 ± 0.033 ‰ (2 s.d, n = 46), which is in great agreement with the laboratory long-term reproducibility of -9.983 ± 0.037 ‰ (n = 137). Two determinations of Zn isotope composition for the USGS reference material BCR-2 yield average δ⁶⁶Zn_{JMC-L} value of $+0.27 \pm 0.011$ ‰ (n = 2; see Supplementary Table 1), which agrees very well with previously published ones (Moynier et al., 2017; Rosca et al., 2019; Kamber and Schoenberg, 2020). Multiple digestions followed by Zn purification of USGS reference materials OU-6 and QS-1 yielded very reproducible δ⁶⁶Zn_{JMC-L} values of $+0.23 \pm 0.016$ ‰ (n = 6) and $+0.32 \pm 0.021$ ‰ (n = 4), respectively (see Supplementary Table 1). Given that all standard solutions and rock reference materials reproducibilities were better than 0.040 ‰ (δ⁶⁶Zn_{JMC-L}, 2 s.d), this value was taken as the conservative overall reproducibility (2 s.d) and applied to all data points in this study.

Supplementary Table 1 Zn isotope compositions for rock standard references

Rock standards	$\delta^{66}\text{Zn}_{\text{bulk}}$ (‰, JMC-L)	2 s.e.
OU-6	0.23	0.018
	0.22	0.017
	0.24	0.017
	0.24	0.021
	0.22	0.025
	0.22	0.028
Average	0.23	2 s.d. 0.016
QS-1	0.33	0.019
	0.31	0.023
	0.31	0.024
	0.33	0.029
Average	0.32	2 s.d. 0.021
BCR-1	0.26	0.018
	0.27	0.015
Average	0.27	2 s.d. 0.011

Internal precision of a sample run is reported as 2 standard error (2 s.e.).
 Reproducibility of the same sample is reported as 2 standard deviation (2 s.d.).

References

- Aries, S., Valladon, M., Polvé, M. and Dupré, B., 2000. A routine method for oxide and hydroxide interference corrections in ICP-MS chemical analysis of environmental and geological samples. *Geostandards Newsletter*, 24(1), pp.19-31.
- Babechuk, M.G., Widdowson, M., Murphy, M. and Kamber, B.S., 2015. A combined Y/Ho, high field strength element (HFSE) and Nd isotope perspective on basalt weathering, Deccan Traps, India. *Chemical Geology*, 396, pp.25-41.
- Coplen, T.B., 2011. Guidelines and recommended terms for expression of stable-isotope-ratio and gas-ratio measurement results. *Rapid Communications in Mass Spectrometry*, 25(17), pp.2538-2560.
- Durand, B. and Nicaise, G., 1980. Procedures for Kerogen Isolation. In *Kerogen: Insoluble organic matter from sedimentary rocks*, pp.35-53. Editions Technip Paris.
- Goldberg, T., Gordon, G., Izon, G., Archer, C., Pearce, C.R., McManus, J., Anbar, A.D. and Rehkämper, M., 2013. Resolution of inter-laboratory discrepancies in Mo isotope data: an intercalibration. *Journal of Analytical Atomic Spectrometry*, 28(5), pp.724-735.
- Govindaraju, K. and Roelandts, I., 1989. 1988 compilation report on trace elements in six ANRT rock reference samples: diorite DR-N, serpentine UB-N, bauxite BX-N, disthene DT-N, granite GS-N and potash feldspar FK-N. *Geostandards Newsletter*, 13(1), pp.5-67.
- Kamber, B.S. and Schoenberg, R., 2020. Evaporative loss of moderately volatile metals from the superheated 1949 Ma Sudbury impact melt sheet inferred from stable Zn isotopes. *Earth and Planetary Science Letters*, 544, p.116356.
- Kamber, B.S., Webb, G.E. and Gallagher, M., 2014. The rare earth element signal in Archaean microbial carbonate: information on ocean redox and biogenicity. *Journal of the Geological Society*, 171(6), pp.745-763.

- Maréchal, C.N., Télouk, P. and Albarède, F., 1999. Precise analysis of copper and zinc isotopic compositions by plasma-source mass spectrometry. *Chemical Geology*, 156(1-4), pp.251-273.
- Moeller, K., Schoenberg, R., Pedersen, R.B., Weiss, D. and Dong, S., 2012. Calibration of the new certified reference materials ERM-AE633 and ERM-AE647 for copper and IRMM-3702 for zinc isotope amount ratio determinations. *Geostandards and Geoanalytical Research*, 36(2), pp.177-199.
- Moynier, F., Vance, D., Fujii, T. and Savage, P., 2017. The isotope geochemistry of zinc and copper. *Reviews in Mineralogy and Geochemistry*, 82(1), pp.543-600.
- Rosca, C., Schoenberg, R., Tomlinson, E.L. and Kamber, B.S., 2019. Combined zinc-lead isotope and trace-metal assessment of recent atmospheric pollution sources recorded in Irish peatlands. *Science of the Total Environment*, 658, pp.234-249.
- Rudge, J.F., Reynolds, B.C. and Bourdon, B., 2009. The double spike toolbox. *Chemical Geology*, 265(3-4), pp.420-431.
- Spangenberg, J.E., Bagnoud-Velásquez, M., Boggiani, P.C. and Gaucher, C., 2014. Redox variations and bioproductivity in the Ediacaran: Evidence from inorganic and organic geochemistry of the Corumbá Group, Brazil. *Gondwana Research*, 26(3-4), pp.1186-1207.
- Spangenberg, J.E. and Frimmel, H.E., 2001. Basin-internal derivation of hydrocarbons in the Witwatersrand Basin, South Africa: evidence from bulk and molecular $\delta^{13}\text{C}$ data. *Chemical Geology*, 173(4), pp.339-355.
- Spangenberg, J.E. and Herlec, U., 2006. Hydrocarbon biomarkers in the Topla-Mezica zinc-lead deposits, northern Karavanke/Drau range, Slovenia: paleoenvironment at the site of ore formation. *Economic Geology*, 101(5), pp.997-1021.
- Spangenberg, J.E., Jacomet, S. and Schibler, J., 2006. Chemical analyses of organic residues in archaeological pottery from Arbon Bleiche 3, Switzerland—evidence for dairying in the late Neolithic. *Journal of Archaeological Science*, 33(1), pp.1-13.
- Spangenberg, J.E. and Macko, S.A., 1998. Organic geochemistry of the San Vicente zinc-lead district, eastern Pucará Basin, Peru. *Chemical Geology*, 146(1-2), pp.1-23.
- Spötl, C. and Vennemann, T.W., 2003. Continuous-flow isotope ratio mass spectrometric analysis of carbonate minerals. *Rapid Communications in Mass Spectrometry*, 17(9), pp.1004-1006.
- Ulrich, T., Kamber, B.S., Woodhead, J.D. and Spencer, L.A., 2010. Long-term observations of isotope ratio accuracy and reproducibility using quadrupole ICP-MS. *Geostandards and Geoanalytical Research*, 34(2), pp.161-174.
- Wille, M., Nebel, O., Van Kranendonk, M.J., Schoenberg, R., Kleinhanns, I.C. and Ellwood, M.J., 2013. Mo–Cr isotope evidence for a reducing Archean atmosphere in 3.46–2.76 Ga black shales from the Pilbara, Western Australia. *Chemical Geology*, 340, pp.68-76.